Advances on innovative protein-based complexes with promising functionality, nutrient retention and encapsulation capacity

Edited by
Xiao Feng, Xi Yu, Shuai Chen, Ruican Wang and Hualu Zhou

About Frontiers

Frontiers is more than just an open access publisher of scholarly articles: it is a pioneering approach to the world of academia, radically improving the way scholarly research is managed. The grand vision of Frontiers is a world where all people have an equal opportunity to seek, share and generate knowledge. Frontiers provides immediate and permanent online open access to all its publications, but this alone is not enough to realize our grand goals.

Frontiers journal series

The Frontiers journal series is a multi-tier and interdisciplinary set of open-access, online journals, promising a paradigm shift from the current review, selection and dissemination processes in academic publishing. All Frontiers journals are driven by researchers for researchers; therefore, they constitute a service to the scholarly community. At the same time, the *Frontiers journal series* operates on a revolutionary invention, the tiered publishing system, initially addressing specific communities of scholars, and gradually climbing up to broader public understanding, thus serving the interests of the lay society, too.

Dedication to quality

Each Frontiers article is a landmark of the highest quality, thanks to genuinely collaborative interactions between authors and review editors, who include some of the world's best academicians. Research must be certified by peers before entering a stream of knowledge that may eventually reach the public - and shape society; therefore, Frontiers only applies the most rigorous and unbiased reviews. Frontiers revolutionizes research publishing by freely delivering the most outstanding research, evaluated with no bias from both the academic and social point of view. By applying the most advanced information technologies, Frontiers is catapulting scholarly publishing into a new generation.

What are Frontiers Research Topics?

Frontiers Research Topics are very popular trademarks of the *Frontiers journals series*: they are collections of at least ten articles, all centered on a particular subject. With their unique mix of varied contributions from Original Research to Review Articles, Frontiers Research Topics unify the most influential researchers, the latest key findings and historical advances in a hot research area.

Find out more on how to host your own Frontiers Research Topic or contribute to one as an author by contacting the Frontiers editorial office: frontiersin.org/about/contact

Advances on innovative protein-based complexes with promising functionality, nutrient retention and encapsulation capacity

Topic editors

Xiao Feng — Nanjing University of Finance and Economics, China
Xi Yu — Macau University of Science and Technology, SAR China
Shuai Chen — Wuhan University, China
Ruican Wang — Nankai University, China
Hualu Zhou — University of Georgia, United States

Table of
contents

Editorial: Advances on innovative protein-based complexes with promising functionality, nutrient retention and encapsulation capacity

Shuai Chen[1], Xiao Feng[2] and Xi Yu[3]*

[1]School of Public Health, Wuhan University, Wuhan, China, [2]School of Food Science and Engineering, Nanjing University of Finance and Economics, Nanjing, China, [3]Faculty of Medicine, Macau University of Science and Technology, Macau, Macau SAR, China

KEYWORDS

protein-based complex, encapsulation, emulsion, protein functionality, nutrient retention

Editorial on the Research Topic
Advances on innovative protein-based complexes with promising functionality, nutrient retention and encapsulation capacity

Protein-based complexes are of great interest in food industry and research, such as protein gels, protein-stabilized emulsions, protein-based carriers of bioactive compounds, etc. Proteins derived from different resources with different processing technology have different structure and properties, which enables their application in nutrient retention, delivery, improved digestibility and other functionalities. Emerging technologies, micro- and macronutrients, and new protein resources have been exploited for protein-based complex research. This Research Topic aims to provide a platform for researchers to share their state-of-the-art innovations on the preparation, evaluation and application of protein-based complexes, especially those with improved encapsulation efficiency, nutrient retention, anti-nutritional factor removal, etc., compared to currently available work. In addition to emerging technologies, innovative proteins (e.g., insect, yeast, pseudocereal), hydrocolloids, soluble fibers, and ligand receptors are also of great interest. This Research Topic includes the development of innovative protein-based complexes, improved functionality of protein-based complexes, protein-based complexes for nutrient delivery, nutrient preservation of protein-based complexes during food processing and *in vitro* digestion, reduction of antinutrients and unpleasant compounds from protein-based foods.

The binding behavior of protein and bioactive compound can affect the functional properties of their complexes. For example, β-carotene improved DPPH radical scavenging activity, foaming capacity, and emulsifying stability of soybean protein isolate (Zhang, Zhao et al.). The binding with quercetin changed the secondary structure of soybean protein isolate, resulting in a partially unfolded and more flexible structure. Meanwhile, modification by quercetin enhanced the foaming and emulsifying capacities of soybean protein isolate (Zhang, Hou et al.). The addition of polysaccharides had an important effect on the properties and functions of protein-based complexes. Chitosan oligosaccharide modification not only delayed the oxidation of myofibrillar protein but also promoted myofibrillar protein to show better solubility, foaming, and foaming stability (Cong et al.). Dong et al. found that

the addition of octenyl succinic anhydride modified starch (OSAS) improved hydrophobicity and emulsifying capacity of the soy protein (SP)-(-)-epigallocatechin-3-gallate (EGCG) complexes. Emulsion gels is a novel complex that prepared from proteins, polysaccharides and lipids, which can be used as solid fat replacers. κ-carrageenan (κC), high-acyl gellan (HA), konjac glucomannanon (KGM), pea protein isolate (PPI) and sunflower seed oil were used to prepare the emulsion gels (Hou et al.). The presence of polysaccharides enhanced the hardness, storage modulus and resistance against deformation of emulsion gel, where PPI/κC system exhibited superior hardness with a similar level of pig back fat.

Some authors reported novel application scenarios for various proteins. Yan et al. reviewed the application of zein-based nano-systems for the delivery of bioactive compounds. Recent advances on using zein-based encapsulation and protection systems were systematically reviewed and discussed, offering insights and inspirations for future developers. Wang et al. made improvements on whey protein with the aid of hesperidin, to enhance their performances as emulsion stabilizer. The antioxidant capacity of the complex was improved as well. The work offers new thoughts on the combined and synergistic utilization of proteins and natural bioactive compounds.

Some of the papers investigated the undiscovered functions of traditional proteins. Sun, Xu et al. revealed that fermented soymilk has antioxidative and anti-inflammatory effect on mice, providing references on the utilization of fermented products of traditional proteins. The in-depth characterization is also important for the investigation of these large biomolecules. The structure-function relationship can be better understood with the help of modern imaging techniques. Sun, Li et al. reviewed the recent advances on the characterization of various biomacromolecules in foods with the aid of small-angle X-ray scattering, summarizing the pros and cons of this advanced imaging technique for unveiling the mystery of various large molecules in food materials.

Author contributions

SC, XF, and XY prepared, checked and revised the manuscript, and approved the submitted version. All authors contributed to the article and approved the submitted version.

Funding

Conflict of interest

The authors declare that the research was conducted in the absence of any commercial or financial relationships that could be construed as a potential conflict of interest.

Publisher's note

All claims expressed in this article are solely those of the authors and do not necessarily represent those of their affiliated organizations, or those of the publisher, the editors and the reviewers. Any product that may be evaluated in this article, or claim that may be made by its manufacturer, is not guaranteed or endorsed by the publisher.

Changes on the conformational and functional properties of soybean protein isolate induced by quercetin

Yating Zhang[1]*[†], Ruiyang Hou[1†], Beibei Zhu[2], Guangwei Yin[2], Jian Zhang[3], Wenqi Zhao[1], Junxi Zhang[1], Taoran Li[1], Zifan Zhang[1], Hongwu Wang[1] and Zheng Li[2]*

[1]School of Public Health and Health Sciences, Tianjin University of Traditional Chinese Medicine, Tianjin, China, [2]College of Chinese Medicine Pharmaceutical Engineering, Tianjin University of Traditional Chinese Medicine, Tianjin, China, [3]Key Laboratory of Industrial Fermentation Microbiology, Ministry of Education, Tianjin University of Science and Technology, Tianjin, China

The conformational changes and functional properties of SPI induced by quercetin was investigated via fourier transform infrared (FTIR) spectroscopy, fluorescence spectroscopy, circular dichroism (CD) spectroscopy and molecular docking. A decrease in the fluorescence intensity and a blue shift in the maximum wavelength were observed due to the binding process with fluorescent residues. The analysis of Stern-Volmer equation showed that the fluorescence quenching induced by quercetin took the form of static quenching, and the binding stoichiometry between SPI and quercetin was 1:1. The values of ΔH and ΔS were both positive illustrating that hydrophobic interaction was the primary binding force between quercetin and SPI. Results of FTIR and CD indicated that the binding with quercetin changed the secondary structure of SPI, resulting in a partially unfolded and more flexible structure. SDS-PAGE confirmed there was no covalent interaction between the two constituents. Molecular docking demonstrated that there were stable configurations and high matching degrees in both 11S and 7S proteins with quercetin via hydrogen bonds and hydrophobic interactions. Meanwhile, modification by quercetin enhanced the foaming and emulsifying capacities of SPI. These findings might provide theory reference for elucidation the mechanism of polyphenols-proteins interaction and development of related food additive products in future.

KEYWORDS

soybean protein isolate, quercetin, multi-spectroscopic techniques, molecular docking, interaction

Highlights

1. A systematic study is pressly needed on changes in structure and function of SPI with quercetin.
2. Fluorescence quenching induced by quercetin took the form of static quenching.
3. The binding stoichiometry between SPI and quercetin was 1:1.
4. SPI-quercetin complex binded stably by hydrogen bonds and hydrophobic interactions.
5. Binding with quercetin led a more flexible structure and better functional properties of SPI.

Introduction

Soy protein isolated is known as high-quality protein and widely used in food industry due to its excellent functional properties, high nutritional value, and low cost (1). However, the compact globular structure of SPI leads to the poor solubility and emulsifying properties. And SPI is characterized by weak electrostatic and spatial attraction, and it usually forms unstable emulsions (1, 2). It is easily affected by the processing conditions, such as low pH, high temperature, and ionic environment, which greatly restricted its application in actual production. Many strategies have been made to improve the functional properties of soy protein, including physical methods (3, 4) and chemical methods (4, 5) as well as (6). Recently, It was found that the non-covalent interaction of polyphenols with whey protein could cause the exposure of tryptophan residues, the unfolding of proteins and the decrease of the surface hydrophobicity (7). Consequently, considerable improvement of the functional properties was observed including digestibility, solubility, and foaming capacity. According to Yaohui et al., hydrophobic force and hydrogen bonds were the main interaction forces between SPI and EGCG. Due to the high affinity of EGCG, the structure of SPI became looser and exposed more active groups, thus leading to an improvement of the foaming, emulsifying, and antioxidant properties (8).

Quercetin belongs to polyphenols, which is abundant in numerous fruits and vegetables such as celery, parsley, onions, and blueberry (9). A number of health benefits have been reported for quercetin, including antioxidant (10), anti-inflammatory (11), and anti-aging properties (12). The antioxidant function of quercetin is mainly reflected to enter cells, occupy oxidative damage, and save dying cells. In addition, it is believed that it works mainly by destroying cell structures (13, 14). Mechanistic studies on anti-aging properties revealed that quercetin alleviated senescence by promoting the proliferation of cells and restoring the heterochromatin architecture in WS hMSCs (12). Moreover, quercetin has shown promising antiviral properties, cardioprotective effects (15) as well as potential prophylactic and therapeutic effects

against cancers due to its non-mutagenic properties and relatively low toxicity (16). The chemotherapeutic results of quercetin have been confirmed for many human cancers cells, for instance, colorectal cancer (17). Although quercetin have so many biological activities, the solubility is extremely low due to its high hydrophobicity, which greatly limits the application in food and biomedical industries In aqueous solution, the solubility of quercetin decreased with increasing temperature and pH, especially at alkaline pH (18). Additionally, its chemical instability, permeability and oral bioavailability are also poor, and it swiftly exits the circulation before reaching the target organs (19, 20). Recently, researchers developed some stabilization strategies to improve the solubility and biological activity of polyphenols, via the formation of hydrogels, microencapsulation (16), self-assembling polymeric micelles (21), and structural modification such as glycosylation, acylation (22). Although there are several options to address the low applicability of polyphenols, the disadvantages still exist, such as the process of microencapsulation is complicated and during emulsifying, high temperatures in thermal gelation might destroy their bioactivities (23). Current studies have shown that the formation of complexes with other substances such as proteins and polysaccharides is a good choice to make full use of quercetin (24–26). The construction of the SPI-EGCG complex could also improve the gelation rates of protein significantly (27). As compared with SPI alone, the gel formed by the composite had a better network structure, mechanical strength, water holding capacity, and rheological properties (27). Studies revealed that the interaction force of EGCG with 11S and 7S proteins was hydrogen bonding, electrostatic interaction and hydrophobic interaction (10). It has been found that the biological effects of polyphenols could be affected to varying degrees by the presence of protein, in turn, the structural and functional properties of protein has also been influenced by polyphenols. Yang et al. (28) prepared binary complexes with EGCG and 11S/7S proteins that could withstand a certain ionic strength, meanwhile, the physicochemical and functional properties of SPI was also improved. Wang et al. found the stability and radical scavenging activity of quercetin could be improved when used soy protein isolated (SPI) particles after cold-gelation as a protective carrier (29). Ao et al. compared the strength of the interaction between SPI and food polyphenols and found the SPI-polyphenols binding patterns were closely related to the variety of polyphenols (30).

To our knowledge, the interaction of EGCG and various proteins has attracted considerable attention of various researchers and been well-understood. Nevertheless, more systematic study about the structural changes and functional properties of SPI leading by quercetin is necessary. Based on these scientific findings, current research was conducted to characteristic the conformational changes and interaction mechanism of SPI induced by quercetin via a series of spectroscopy methods and molecular docking and the

improvement on the functional properties of SPI-quercetin complex. The study aims to get further insights into the effect of polyphenols on the structural and functional properties of SPI, thus, offering as a reference for the development of novel protein additives with good functional properties and improved health benefits in future.

Materials and methods

Materials

Quercetin hydrate (HEOWNS, purity ≥99%) was purchased from (Tianjin Heowns Biochem LLC, Tianjin, China), and sodium hydroxide (purity ≥96%) and sodium chloride (purity ≥99.5%) were purchased from Tianjin Jiangtian Chemical Technology Co., LTD (Tianjin, China). Phosphoric acid (purity ≥85%), methanol (purity ≥99.5%) and ethanol (purity ≥99.7%) were purchased from Tianjin Fengchuan Chemical Reagent Technology Co., LTD (Tianjin, China). SurePAGE, Bis-Tris, 10 × 8 (C35222108, 4–12%, 12 wells, 10/pk), Tris-MOPS-SDS Running Buffer Powder (C31382105) and PAGE-MASTER Protein Standard Plus (C2106004) were purchased from GenScript (860 Centennial Ave., Piscataway, NJ 08854, USA). Dimercaptoethanol (purity 99%), Coomassie Brilliant blue R250 (CAS:6104-59-2, Assay ≥90%) and Bromophenol blue (CAS:115-39-9) were purchased from biosharp (Labgic Technology Co., Ltd., Hefei, Anhui Province, China).

Preparation of soybean protein isolate—quercetin conjugates

Soybean protein isolate was extracted from low-denature defatted meal using alkali solution and acid precipitation method (31) and freeze-dried to powders. The freeze-dried soybean protein isolate powders were fully dissolved in deionized water at a concentration of 1.0×10^{-4} mol/L. Quercetin solution was prepared in ethanol at the concentration of 1.0×10^{-3} mol/L. Afterwards, The quercetin solution was slowly added to 30 ml SPI solutions, and vortexed for 1 min. The molar ratios of SPI and quercetin were set as 1:0, 1:0.2, 1:0.4, 1:0.6, 1:0.8, 1:1.

Binding rate analysis

To provide binding information between SPI and Que, binding rate of SPI-quercetin (%) were determined according to the method of Liu et al. (32) with slight modification. All samples were adjusted to pH 4.60 to precipitate the protein-quercetin complexes. The samples were then centrifuged for 5 min at 13,000 rpm, and the absorbance of the supernatant

was measured at 373 nm using a UV-Vis spectrophotometer. A standard curve was used to calculate the concentration of quercetin in the solution. Binding rate of SPI-quercetin was calculated using equation:

$$Binding\ rate\ (\%) = \left(1 - \frac{C_{free}}{C_{all}}\right) \times 100\% \qquad (1)$$

Intrinsic fluorescence spectroscopy

The fluorescence determination at different temperatures (298K, 308K, and 318K) was carried out using the fluorescence spectroscopy (33). Set the excitation wavelength at 280 nm, the slits of the excitation and emission wavelengths at 5 nm, and the scanning speed at 1,500 nm/min. The emission spectra were adjusted between 300 and 500 nm. Blanks were subtracted from SPI aqueous solutions and deionized water. The following has been determined based on Stern-Volmer analysis:

$$\frac{F_0}{F} = 1 + K_q \tau_0\ [Q] = 1 + K_{SV}\ [Q] \qquad (2)$$

Here, F_0 represents fluorescence intensities of the protein solution without quercetin, and F represents fluorescence intensities of the protein with different ratios of quercetin; kq is the bimolecular quenching rate constant; τ_0 is the average lifetime of the complexes without quercetin (the fluorescence lifetime of tryptophan is 3×10^{-9}; [Q] is the concentration of the quercetin in system; K_{SV} is the Stern-Volmer quenching constant.

The binding parameters between quercetin and protein can be analyzed by the logarithmic equation:

$$\log\left(\frac{F_0 - F}{F}\right) = \log K_a + n \log\ [QT] \qquad (3)$$

Here, K_a represents to the binding constant between quercetin and SPI; n is the binding stoichiometry.

Determined the non-covalent interaction of SPI-quercetin binding from thermodynamic parameters, which were calculated by the Van't Hoff equation:

$$\ln K_a = -\frac{\Delta H}{RT} + \frac{\Delta S}{R} \qquad (4)$$

$$\Delta G = \Delta H - T\Delta S \qquad (5)$$

Here, R is the gas constant [8.314 J•(mol•K)$^{-1}$]; T is the absolute temperature.

Fourier-transform infrared (FTIR) spectroscopy

Fourier transform infrared spectroscopy (FTIR) was used to monitor the conformational changes of SPI before and

after binding with Que. All samples were prepared according to Section Preparation of Soybean Protein Isolate—Quercetin Conjugates and freeze-dried to powders. A prefabricated sample powder (1 mg) was mixed with KBr (200 mg) and compressed into a transparent flake. The spectrometer (Bruker, Germany) was applied to get FTIR spectra at 4 cm^{-1} resolution, and scanned 64 times for each group at 25 °C, against a background spectrum recorded from the KBr pellet (34).

Circular dichroism (CD) spectroscopy

The CD spectra of SPI samples with the absence and presence of quercetin at different ratios were measured using a circular dichromatic spectrometer (J-810, Japan). The CD spectra scanning was in the far-UV region (190–250 nm) at room temperature in a 1 cm length quartz cuvette. The scanning speed and bandwidth were set to 50 nm/min and 1.0 nm, respectively. Three parallel groups of samples are required for all samples (35). The content of secondary structures of SPI was calculated with CDSSTR software supported by CDPro software package.

Sodium dodecyl sulfate-polyacrylamide gel electrophoresis (SDS-PAGE)

Effect of different ratios of quercetin on the molecular properties of soybean protein was evaluated using SDS-PAGE electrophoresis according to method of Wu et al. (36) with minor modifications. Briefly, the samples were diluted 1:1 with the (Laemmli) sample buffer (0.0625 mM Tris-HCl, 2% SDS, 10% glycerol, 5% 2-mercaptoethanol, 0.0025% bromophenol blue), and then heated the systems at 95 °C for 3 min. The aliquots were loaded on 4% stacking gel and 12% separating gel, adjusted the voltage, and sustained 150 volts for 1 h. The gels were stained with Coomassie Brilliant Blue R-250 dye liquor overnight after electrophoresis (5% methanol, 7.5% acetic acid) for 30 min. Subsequently, the gels were distained with decolorizing solution (acetic acid: deionized water = 3:37) and observed by gel imaging analysis system.

Molecular docking

A docking compound, quercetin, was obtained from the PubChem database (https://pubchem.ncbi.nlm.nih.gov/). After hydrogenation, optimization, and energy minimization, the structural information was imported into the Schrodinger software and used as a ligand. Crystal structure of SPI target protein downloaded from protein database (http://www.rcsb.org/). Since SPI is primarily composed of 7S and 11S globulin, two target proteins were selected. The protein structures

were processed using the Maestro 12.7 platform. The protein preparation wizard was used to process the proteins, to remove crystallization waters, to add hydrogen atoms that were missing, and to repair the bonds and peptides. Lastly, optimize structures and minimize energy consumption. Glide of Schrodinger Maestro was used for molecular docking. Using LigPre's default settings, quercetin was prepared, and then imported into Glide to generate active sites in the SPI grid. The SP method was used for molecular docking and screening (37, 38).

The interactions between the compound and the target protein were analyzed, and the interaction modes between the compound and the protein residues were obtained, including hydrogen bonds, π-π interactions, and hydrophobic interactions, etc. The docking score of compounds was used to predict whether the compound to be screened had similar activity to the positive compound.

Emulsifying activity index (EAI) and emulsifying stability index (ESI)

The Emulsifying activity index (EAI) and emulsifying stability index (ESI) were measured according to the method of Yating Zhang et al. with slight modification (1). The complexes of SPI and quercetin with molar ratio of 1:0.6 were prepared according to Section Preparation of Soybean Protein Isolate—Quercetin Conjugates and mixed with soybean oil (3:1, v/v). The mixture was homogenized at 15,000 rpm for 1 min and 50 μL of the coarse emulsions were mixed in 5 mL of 0.1% (w/v) SDS solution immediately. The absorbance was measured at 500 nm. The EAI and ESI were obtained using the following formulas:

$$EAI(m^2/g) = \frac{2 \times 2.303 \times A_0 \times 100}{C \times L \times \theta \times 10000} \qquad (6)$$

$$ESI\ (\%) = \frac{A_t}{A_0} \times 100 \qquad (7)$$

Here, A_0 is the absorbance of the coarse emulsion at 0 min after homogenization. C is the concentration of protein (mg/ml), L is the optical path length of the colorimetric dish, and θ is the oil proportion of the emulsions. A_t is the absorbance of the emulsions measured at 5, 10, 20, and 30 min, respectively.

Foaming capacity (FC) and foaming stability (FS) index

Measurement of Foaming capacity (FC) and Foaming stability (FS) was following the method described by Yaohui You et al with slight modification (8). SPI and SPI-quercetin complexes (100 ml) were whipped by a high speed dissolvers (IKA T25, Instrument Co., LTD, German) at 10,000 r/min for

FIGURE 1
The binding rate (%) of SPI-quercetin (Que) at different ratio.
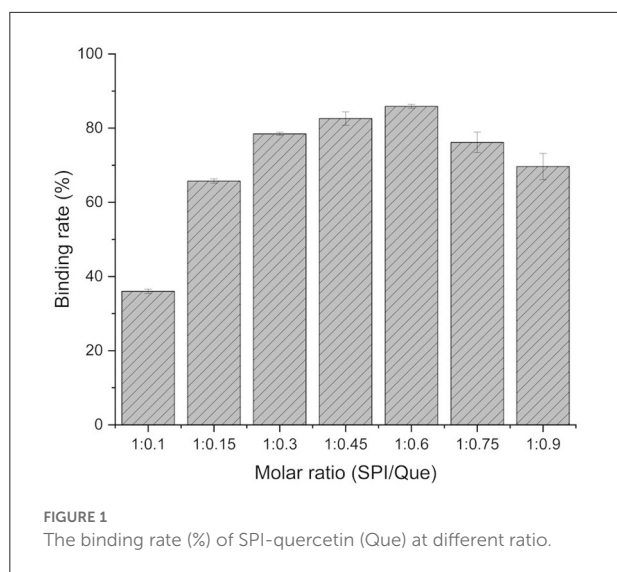
1 min. The volume of foam was recorded at 0, 10, 20, 30, 40, 50 min, respectively. The FC and FS were calculated as follows:

$$FC\,(\%) \;=\; \frac{V_1 - V_0}{V_0} \times 100 \tag{8}$$

$$FS\,(\%) \;=\; \frac{V_t}{V_1} \times 100 \tag{9}$$

Here, V_0 is the beginning volume of the mixture, V_1 is the volume after high speed dispersion (0 min), and V_t is the volume after different quiescence time.

Statistical analysis

All the experiments were conducted in triplicate and the results were expressed as mean ± standard deviation. All data were subjected to analysis of variance (ANOVA) and Duncan's multiple range test using SPSS at the significance level of $P < 0.05$. The figures in this article were created using Origin 2019b.

Results

Binding rate of SPI-quercetin

Result of SPI-quercetin binding rate is shown in Figure 1. The binding rate ranged from 36.03 to 85.86% and mainly concentrated in 70–82%. When the mole ratio of SPI to quercetin was 1:0.6, the binding rate reached the highest level (85.86%). This result indicated that there was an effective combination between SPI and Que. Furthermore, the research of Antonio et al. showed similar results to our findings (39).

Fluorescence spectrum analysis

Fluorescence quenching is widely used to study the protein-polyphenol interactions and can provide the detailed information of the combination. The fluorescence quenching pattern of SPI containing different amounts of quercetin are shown in Figure 2. The maximum fluorescence emission wavelength (λ_{max}) of SPI is about 330 nm. The fluorescence intensity of SPI decreased significantly ($p < 0.05$) as the concentration of quercetin increased in the system, and the maximum wavelength (λ_{max}) showed a blue shift ($p < 0.05$). These phenomena indicated an interaction between SPI and Que, and tryptophan in protein molecule transferred toward hydrophobic environment (40).

To accurately locate the interaction mechanism, the Stern-Volmer equation was used to analyze the data. As shown in Table 1, there was a strong linear relationship between the concentration of quercetin and F_0/F ($R^2 > 0.96$) at different temperatures (298K, 318K, 338K). The value of kq was much higher than maximal diffusion collision quenching constant, 2.0×10^{10} L•mol^{-1}s^{-1} (41) suggesting that the fluorescence quenching induced by quercetin took the form of static quenching (33). According to Table 1, the binding stoichiometry was approximately only 1, manifesting that quercetin interacted with SPI at a 1:1 M ratio regardless of thermal treatments.

Small organic molecules always combined with protein to form a supramolecular complex by electrostatic force, hydrogen bonding force, van der Waals force or hydrophobic force. Different interaction forces existed between different molecules. The nature and magnitude of the thermodynamic parameters associated with various individual kinds of molecular interactions have been characterized by Ross and Subramanian (42). The thermodynamic parameters of the combination between quercetin and SPI were shown in Table 1. The calculated values of ΔG were −27.25, −29.07, and −31.23 kJ mol^{-1} at 25, 45 and 65°C, respectively, which revealed the spontaneity binding of quercetin and SPI. The values of ΔH and ΔS were 4.4 kJ mol^{-1} and on average 91.4 J mol^{-1} K^{-1}, respectively. According to Ross et al. (42), when ΔH > 0, ΔS > 0, predominant are the hydrophobic interactions; when ΔH < 0, ΔS < 0, Vander Waals forces and hydrogen bonds dominate; ΔH < 0, ΔS > 0 indicates the domination of electrostatic forces. The values of ΔH and ΔS in this study were both positive illustrating that hydrophobic interaction was the primary binding force between quercetin and SPI. The positive value of ΔH was possibly dictated by the following endothermic factors: (1) quercetin molecules partly destroy the hydrophobic hydration structure of SPI, and (2) the original iceberg structure surrounding quercetin molecules is changed, when quercetin molecules insert into the hydrophobic pockets of SPI (43). The value of ΔS was also positive, which might be related to the release of combined water molecules from the molecule pocket, the hydration layer on the surface of the SPI particles
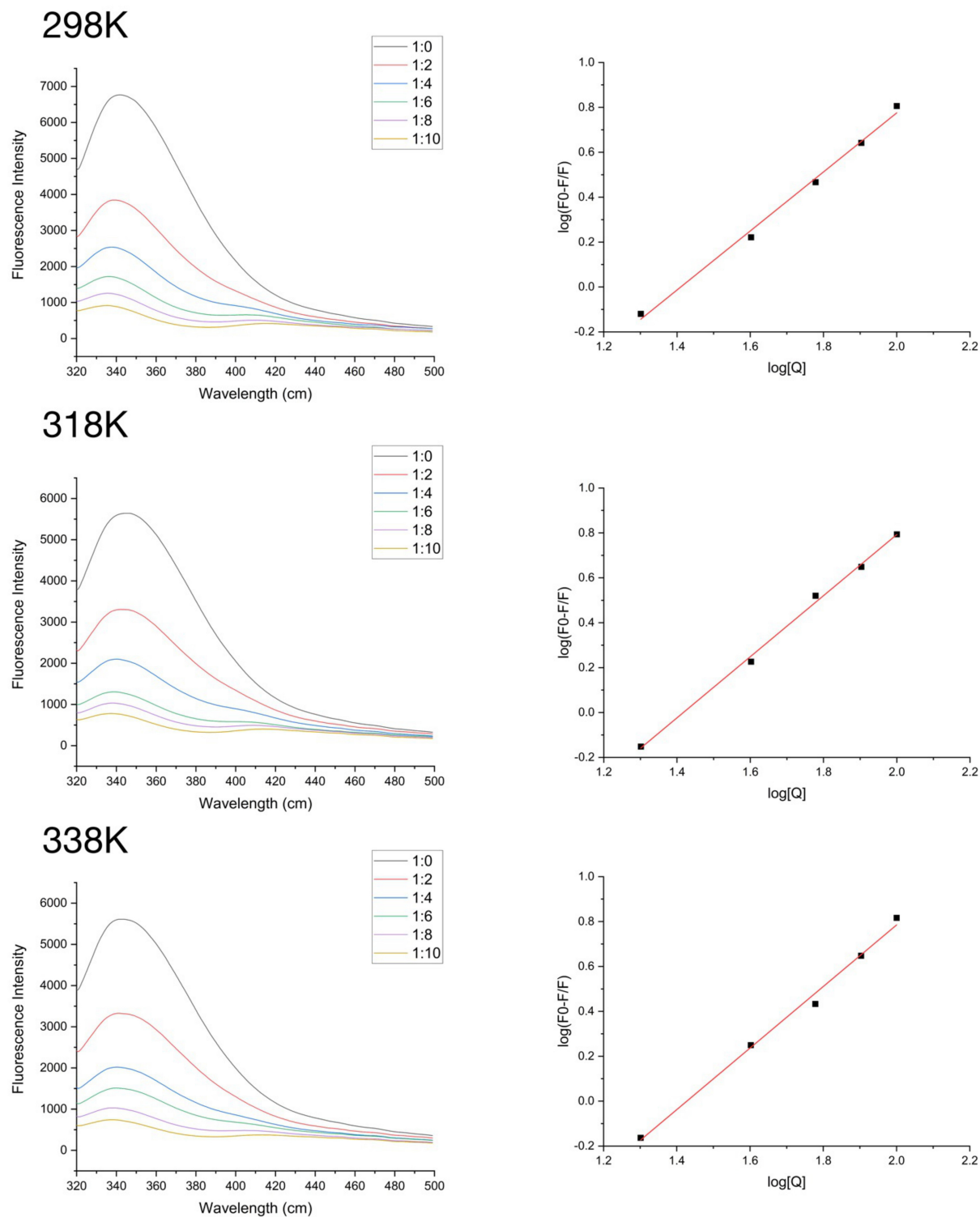
FIGURE 2
At 298K, 318K, and 338K, the fluorescence intensity of SPI and quercetin (Que) complexes in the range of 320−500 nm and the logarithmic equation fitting curve.

TABLE 1 The quenching constants, binding constants, and thermodynamic parameters for SPI-quercetin complexes at 298K, 318K, and 338K.

T/K	KSV/105 L·mol^{-1}	kq/1,014 L·mol^{-1}s^{-1}	Ka/105 L·mol^{-1}	n	ΔH/kJ·mol^{-1}	ΔG/kJ·mol^{-1}	ΔS/kJ·mol^{-1}·K^{-1}
298	0.63 ± 0.60	0.21 ± 0.20	3.06 ± 0.20	1.31 ± 0.06	4.04	−27.25	91.46
318	0.63 ± 0.40	0.21 ± 0.10	2.75 ± 0.22	1.36 ± 0.04		−29.07	91.42
338	0.64 ± 0.70	0.21 ± 0.20	2.83 ± 0.23	1.37 ± 0.06		−31.23	92.41
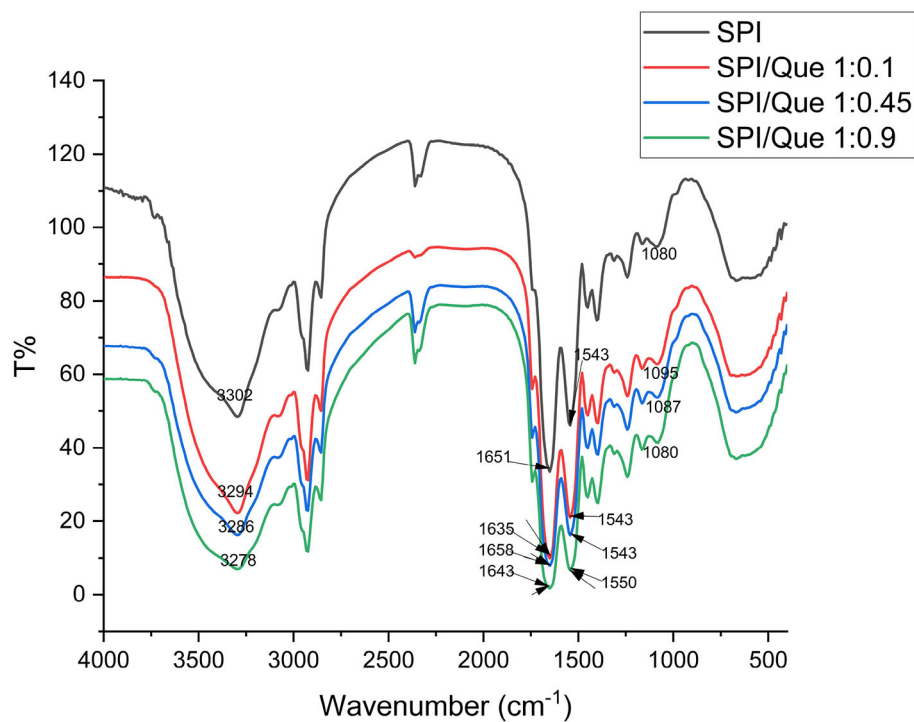
FIGURE 3
Fourier transform infrared spectra of SPI and SPI-quercetin complexes with different molar ratio (1:0.1, 1:0.45, 1:0.9) at 298K. The corresponding wavelength of the characteristic peaks were marked in this figure.

and the iceberg structure surrounding the hydrophobic parts of quercetin to buffer medium (29). Furthermore, the value of ΔH was much lower than the interaction energy of the chemical bond (>100 kJ/mol) suggesting that the interaction force between quercetin and SPI was a weak intermolecular force.

Fourier-transform infrared (FTIR) analysis

Structure of proteins can be determined from the infrared spectra of their amide bands. To get further structural change information about SPI before and after the addition of quercetin, the FTIR profiles were recorded in Figure 3.

The broad band around 3,000–3,500 cm^{-1} indicated the O-H or N–H stretching vibration. and the absorption peak showed a significant blue shift with the increasement of quercetin ratio, indicating that SPI was affected through the formation of

hydrogen bonds (44). The amide I band located around 1,600–1,700 cm^{-1}, mainly relating to C=O stretch. The amide II band located <1,548 cm^{-1}, associating with the vibrations of N–H bending and C–N stretching. 1,600 cm^{-1} is the characteristic peak of C=O stretching vibration (45).

Changes were also found with the amide I band located at 1,651 cm^{-1}. A significant blue shift in amide I band was observed, and the peak strength increased (Figure 3). This phenomenon might be explained by the fact that the hydrogen bond between SPI and quercetin enhanced with the increasement of quercetin content in the same solvent and temperature conditions. In conclusion, the characteristic peaks of SPI in the range of 4,000–1,000 cm^{-1} showed varying degrees of blue shift, indicating that the secondary structure of SPI changes under the influence of different concentrations of quercetin, which was likely to be provided by hydrogen bonds or hydrophobic interaction (46). In combination with

our fluorescence spectrum analysis results, it could be roughly concluded that hydrophobic interaction and hydrogen bonding acted as the main binding forces between SPI and quercetin, which was in accordance with the conclusion of Y. Wang et al. (29).

Circular dichroism (CD) analysis

CD is considered as a sensitive technique which could monitor the conformational changes of proteins or proteins binding with ligands (47). In this study, circular dichroism was used to characterize the secondary structure changes of SPI in the absence and presence of quercetin with different ratios (Figure 4). The contents of the α-helix, β-sheet, β-turns, and random coils calculated by the CDPro software were listed in Table 2. According to Figure 4, the CD spectra profiles of all samples (Figure 4) showed a broad negative band at around 200–235 nm, suggesting that SPI was rich in random coil structures. The negative ellipticities of SPI around 210–220 nm decreased after quercetin addition at different ratios ($p < 0.05$), revealing that the decrease of α-helix was accompanied by an increase in β-sheet and β-turn compared with that of SPI (Table 2) (33, 35). The result is consistent with previous findings of Katouzian et al about the interaction of bovine α-lactalbumin and oleuropein (48). It could be speculated that the addition of quercetin caused the transition of SPI conformation from order to disorder due to hydrogen bonding and hydrophobic interaction. Consequently, the interaction of SPI-quercetin mixture resulted in the formation of a partially unfolded and more flexible complex, further supporting the conclusion of Section Fourier-Transform Infrared (FTIR) Analysis (49).

SDS-PAGE analysis of SPI and que

SDS-PAGE analysis was used to monitor the molecular weights of SPI and quercetin mixtures to determine whether a covalent bond formed. As shown in Figure 5, compared with the molecular weight of SPI alone, those of SPI-quercetin mixtures remained almost unchanged with the addition of different amounts of Que. Additionally, there was no new band was observed in Figure 5, indicating there was no covalent bond formed in the complex systems in this study. The results of SDS-PAGE corroborated the conclusion of Section Fluorescence Spectrum Analysis, which revealed that the bonds between SPI and quercetin were mainly non-covalent (50).

Analysis of molecule docking

SPI contains a variety of globulin components, among which 11S and 7S are the main components (51). The best
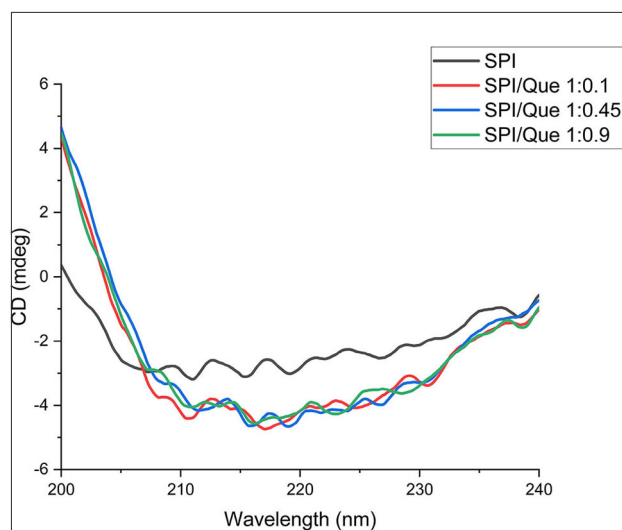
FIGURE 4
Circular dichroism spectra of SPI and SPI-quercetin complexes with different molar ratios (1:0.1, 1:0.45, 1:0.9) in the wavelength range of 200−240 nm.

TABLE 2 Percentage of different secondary structures in SPI and SPI-quercetin complexes.

Sample	α-helix (%)	β-sheet (%)	β-turn (%)	Random coil (%)
SPI	20.40	24.60	20.30	34.70
SPI/Quercetin 1:0.1	19.60	25.40	23.90	31.10
S/Quercetin 1:0.45	18.40	29.80	28.40	28.60
S/Quercetin 1:0.9	14.40	32.10	31.40	22.10

docking models of 7S (Figures 7A–C) and 11S (Figures 6A–C) components of SPI with quercetin were conducted, respectively. The results showed that there were good binding effect and high matching between quercetin and the target proteins with binding energies of −7.25 and −6.38 kcal/mol, respectively (Table 3). Pymol 2.5 software was used to visualize the docking compound and protein complex to determine the binding mode of the two components. In 11S component, the binding of the amino acid and the matching posture of ligands to protein pockets were observed. The active amino acid residues of quercetin were bound to 11S, including ASN-348, ARG-404, PRO-467, ALA-427, PRO-353, MET-350, ALA-349, PRO-467, etc. Several hydrogen bond donor receptors were found in quercetin. The hydrogen bonds with ASN-348, ARG-404, and ARG-459 amino acids were short, testifying the binding ability was strong, which played a crucial role in stabilizing small molecules. Figure 6B also showed that quercetin matched the pocket of 11S globulin very well, and the benzene ring could form a good hydrophobic interaction with the groove.

The active amino acid residues of quercetin binding to 7S globulin were MET-97, ASN-45, ASP-41, SER-267, ARG-356, GLN-104, etc. quercetin could form four hydrogen bonds

with MET-97, ASN-45, ASP-41 and SER-267, and the hydrogen bonds distance was short suggesting the bonding ability was strong. According to Figure 7B, quercetin also had a high matching degree with 7S, and the benzene ring could form a good hydrophobic interaction with the protein's central cavity. In summary, quercetin compounds had good binding patterns and docking scores with the active sites of the two main proteins constituting in SPI, which meant quercetin was a potentially active small molecule. Both 11S and 7S had hydrogen bonding and hydrophobic interactions with the quercetin ligand, in agreement with the findings of multiple spectroscopies above.
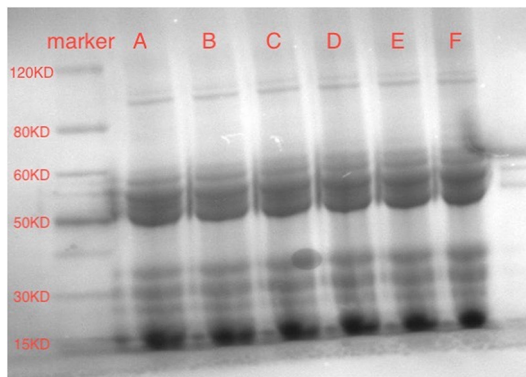
FIGURE 5
SDS-PAGE of SPI-quercetin complexes: **(A)** SPI sample; **(B)** SPI+20 μM quercetin complex; **(C)** SPI+40 μM quercetin complex; **(D)** SPI+60 μM quercetin complex; **(E)** SPI+80 μM quercetin complex; **(F)** SPI+100 μM Que.

Emulsifying properties

Emulsifying capacity is the ability to rapidly form a stable interface at the oil-water interface, which is defined as emulsion activity index (EAI). Emulsifying stability (ESI) refers to the ability to maintain the emulsion state and prevent the separation (8). EAI and ESI of SPI and SPI- quercetin complexes are presented in Figures 8A,B. The initial EAI (0 min) of SPI-quercetin increased comparing with that of native SPI,
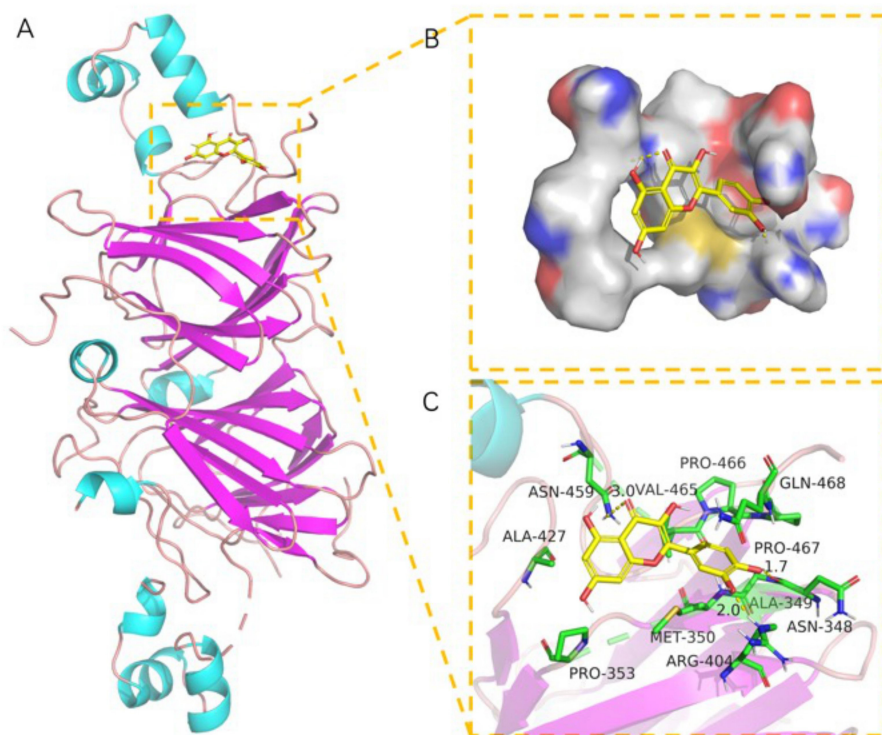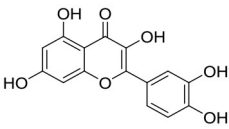
FIGURE 6
The binding mode of 11S with quercetin: **(A)** The 3D structure of complex. **(B)** The surface of active site. **(C)** The detail binding mode of complex. The backbone of protein was rendered in tube and colored in bright blue. quercetin compound is rendering by yellow.

TABLE 3 The selected compounds of docking results.

Target ID	Compounds	Docking Score (kcal/mol)	Combination Type
11S (1fxz)	Quercetin	−7.25	Hydrogen bonds
7S (3aup)		−6.38	Hydrophobic interactive

Binding energy function (52). $:G_{bind} = C_{lipo-lipo} \sum f(\gamma_{ir}) + C_{hbond-neut-neut} \sum g(\gamma) h(\alpha) + C_{hbond-charge-charge} \sum g(\gamma) h(\alpha) + C_{max-metal-ion} \sum f(\gamma_{lm}) + C_{rotb} H_{robt} + C_{polar-phob} V_{polar-phob} + C_{coul} E_{coul} + C_{vdW} E_{vdW} + solvationterms.$

FIGURE 7
The binding mode of 7S with quercetin: **(A)** The 3D structure of complex. **(B)** The surface of active site. **(C)** The detail binding mode of complex. The backbone of protein and quercetin compound were colored at the same.
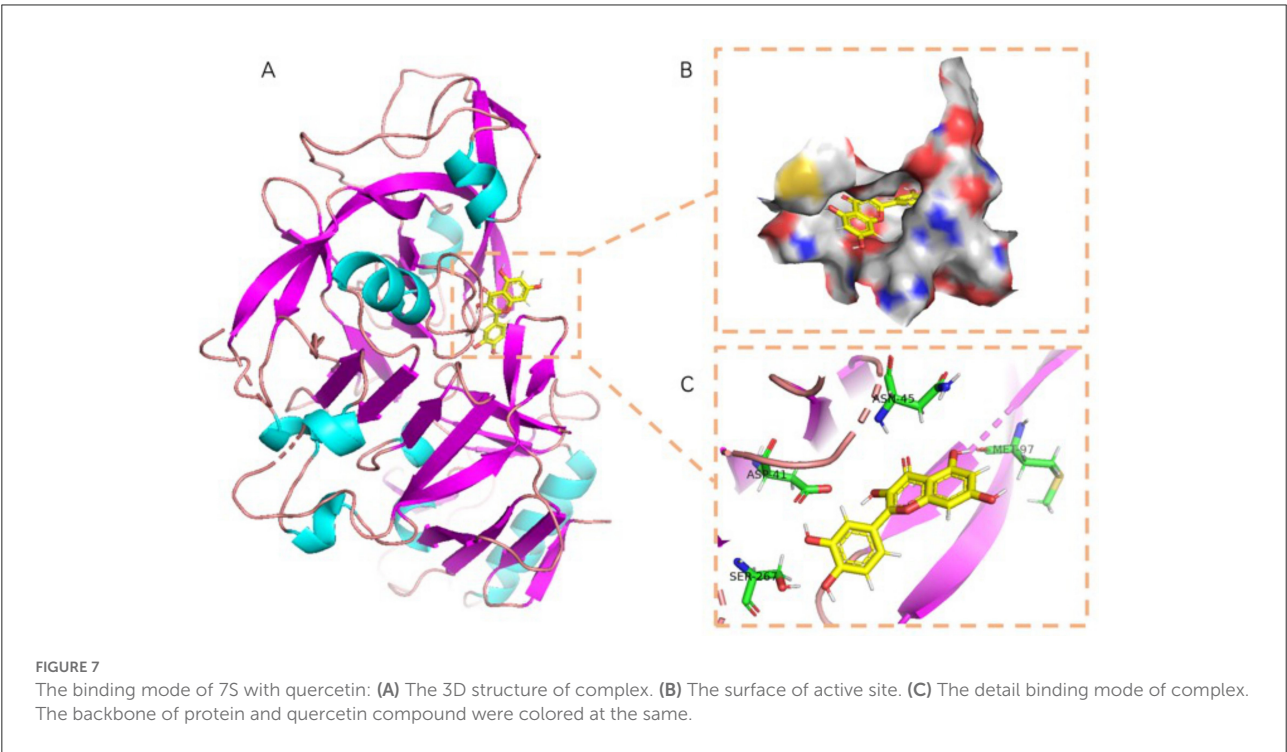
while there was little variation in the ESI. This revealed that modification with quercetin could improve the emulsifying capacity of SPI, which was in consistent with Meng et al. (53), who found the addition of GA, CA, and EGCG increased the EAI comparing to control WPI. However, it was found excess negative zeta potential of polyphenol would hinder proteins to maintain the interface stability due to increased repulsion (54), that might be the reason for the change of ESI.

Foaming properties

The foaming behavior of SPI was related to the rapidly adsorption and film forming capacity at the air-water interface (53). The foaming capacity (FC) and foaming stability (FS) of SPI and SPI-quercetin complexes are shown in Figures 8C,D. Both the FC and FS of SPI showed a slight increase after the

addition of quercetin within 30 min, while a rapid increase was observed at 30 min and 40 min. According to the conformational analysis above, protein with partially unfolded and more flexible structure could be more effective to diffuse to the air-water interface and reduce the surface tension of the air bubbles, which improved the foaming behavior (55). In addition, Morfo Zembyla confirmed that the stabilized system was also probably attribute to the electrostatic attraction between the oppositely-charged polyphenol particles and protein at the interface, although a more order and stable structure was induced by quercetin (56).

Conclusion

In this work, conformational changes and functional properties of SPI modified by quercetin has been investigated.
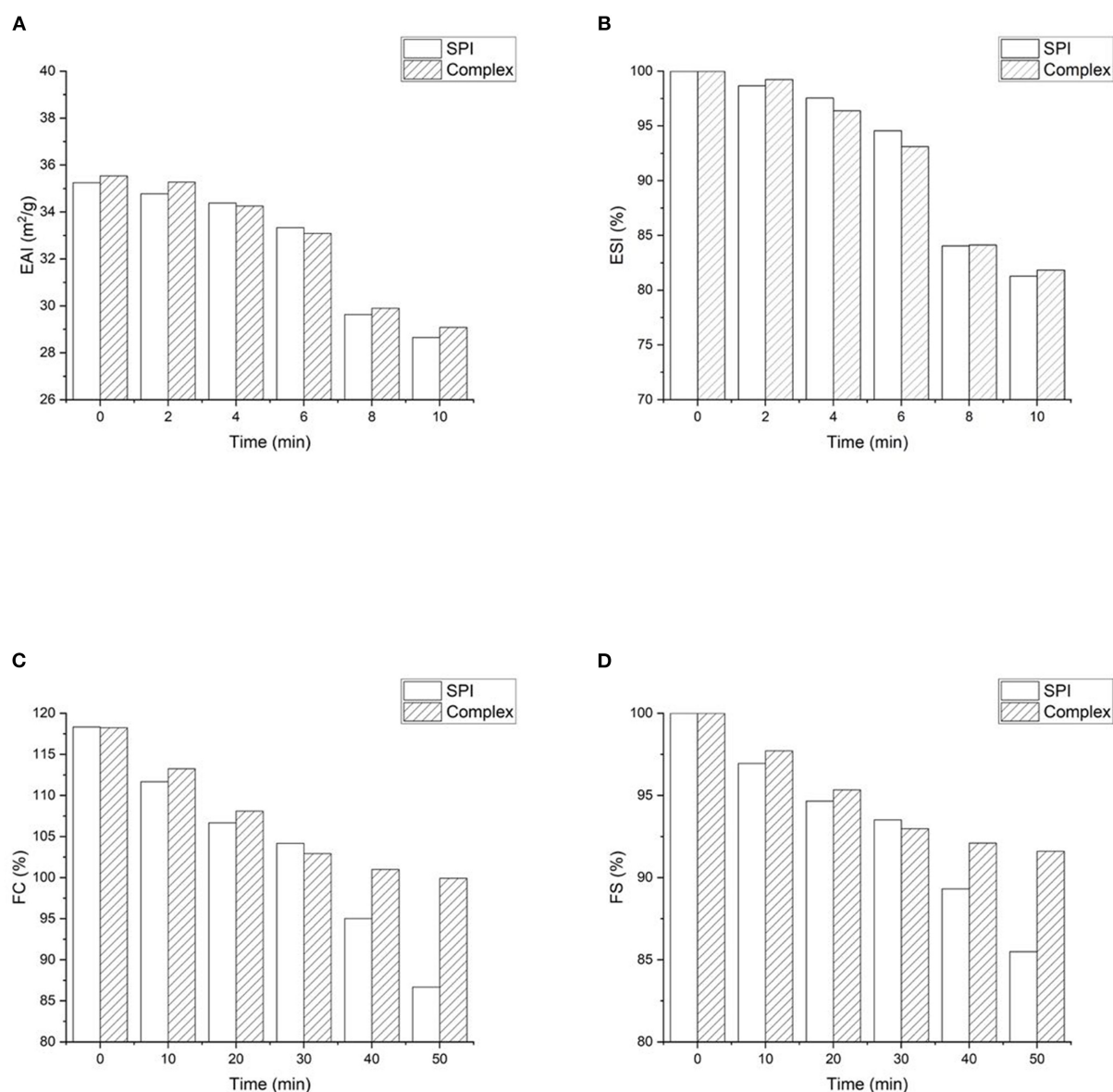
FIGURE 8
Functional properties of SPI-quercetin complex: **(A)** Foaming capacity (FC); **(B)** foaming stability (FS); **(C)** Emulsifying activity index (EAI); **(D)** emulsifying stability index (ESI).

Fluorescence data demonstrated that quercetin induced the static quenching on the fluorescence activity of SPI, leading to the structure changes of SPI, which was confirmed by CD spectroscopy and FTIR results. Further analysis showed that quercetin binded strongly with SPI to form a more flexible structure, primarily through hydrogen bonding and hydrophobic forces with the binding stoichiometry approximately equal to 1. After binding with quercetin, the structure of SPI became looser and flexible, which led to an improvement of its emulsifying and foaming properties. Although more investigation needs to be conducted,

these findings in this study were expected to serve as a theoretical reference for the development of novel plant protein-polyphenols complex products and their application in the food industry in future.

Data availability statement

The original contributions presented in the study are included in the article/Supplementary Material,

further inquiries can be directed to the corresponding author/s.

Author contributions

YZ: funding acquisition, project administration, supervision, writing and editing, and resources. RH: data curation, writing-original draft, investigation, and validation. WZ: investigation, data curation, writing, methodology, and validation. BZ: resources, conceptualization, and supervision. JuZ: investigation and validation. GY and JiZ: project administration. TL and ZZ: investigation. HW: funding acquisition, project administration, and supervision. ZL: funding acquisition, resources, and supervision. All authors contributed to the article and approved the submitted version.

Funding

Conflict of interest

The authors declare that the research was conducted in the absence of any commercial or financial relationships that could be construed as a potential conflict of interest.

Publisher's note

All claims expressed in this article are solely those of the authors and do not necessarily represent those of their affiliated organizations, or those of the publisher, the editors and the reviewers. Any product that may be evaluated in this article, or claim that may be made by its manufacturer, is not guaranteed or endorsed by the publisher.

Supplementary material

The Supplementary Material for this article can be found online at: https://www.frontiersin.org/articles/10.3389/fnut.2022.966750/full#supplementary-material

References

1. Zhang Y, Tan C, Eric K, Abbas S, Liu F, Zhang X, et al. Effect of limited enzymatic hydrolysis on physico-chemical properties of soybean protein isolate-maltodextrin conjugates. *Int J Food Sci Technol.* (2015) 50:226–32. doi: 10.1111/ijfs.12624

2. Zhong MM, Sun YF, Sun YD, Fang L, Qi BK, Xie FY, et al. Dynamic gastric stability and *in vitro* lipid digestion of soybean protein isolate and three storage protein-stabilized emulsions: effects of ultrasonic treatment. *Food Res Int.* (2021) 149:110666. doi: 10.1016/j.foodres.2021.110666

3. Liang G, Chen W, Qie X, Zeng M, Qin F, He Z, et al. Modification of soy protein isolates using combined pre-heat treatment and controlled enzymatic hydrolysis for improving foaming properties. *Food Hydrocolloids.* (2020) 105:105764. doi: 10.1016/j.foodhyd.2020.105764

4. Ma X, Chi C, Pu Y, Miao S, Liu D. Conjugation of soy protein isolate (SPI) with pectin: effects of structural modification of the grafting polysaccharide. *Food Chem.* (2022) 387:132876. doi: 10.1016/j.foodchem.2022.132876

5. Wang J, Zhao M, Qiu C, Sun W. Effect of malondialdehyde modification on the binding of aroma compounds to soy protein isolates. *Food Res Int.* (2018) 105:150–58. doi: 10.1016/j.foodres.2017.11.001

6. Shen P, Zhou F, Zhang Y, Yuan D, Zhao Q, Zhao M. Formation and characterization of soy protein nanoparticles by controlled partial enzymatic hydrolysis. *Food Hydrocolloids.* (2020) 105:105844. doi: 10.1016/j.foodhyd.2020.105844

7. Jiang J, Zhang ZP, Zhao J, Liu YF. The effect of non-covalent interaction of chlorogenic acid with whey protein and casein on physicochemical and radical-scavenging activity of *in vitro* protein digests. *Food Chem.* (2018) 268:334–41. doi: 10.1016/j.foodchem.2018.06.015

8. You Y, Yang L, Chen H, Xiong L, Yang F. Effects of (-)-Epigallocatechin-3-gallate on the functional and structural properties of soybean protein isolate. *J Agric Food Chem.* (2021) 69:2306–15. doi: 10.1021/acs.jafc.0c07337

9. Ulusoy HG, Sanlier N. A minireview of quercetin: from its metabolism to possible mechanisms of its biological activities. *Crit Rev Food Sci Nutr.* (2020) 60:3290–303. doi: 10.1080/10408398.2019.1683810

10. Yang Y, Wang Q, Lei L, Li F, Zhao J, Zhang Y, et al. Molecular interaction of soybean glycinin and beta-conglycinin with (-)-epigallocatechin gallate induced by pH changes. *Food Hydrocolloids.* (2020) 108:106010. doi: 10.1016/j.foodhyd.2020.106010

11. Lee GH, Lee SJ, Jeong SW, Kim HC, Park GY, Lee SG, et al. Antioxidative and antiinflammatory activities of quercetin-loaded silica nanoparticles. *Colloids Surf B Biointerfaces.* (2016) 143:511–17. doi: 10.1016/j.colsurfb.2016.03.060

12. Geng LL, Liu ZP, Zhang WQ, Li W, Wu ZM, Wang W, et al. Chemical screen identifies a geroprotective role of quercetin in premature aging. *Protein Cell.* (2019) 10:417–35. doi: 10.1007/s13238-018-0567-y

13. Faraji S, Nowroozi N, Nouralishahi A, Shabani Shayeh J. Electrospun poly-caprolactone/graphene oxide/quercetin nanofibrous scaffold for wound dressing: evaluation of biological and structural properties. *Life Sci.* (2020) 257:118062. doi: 10.1016/j.lfs.2020.118062

14. He Z, Zhang X, Song Z, Li L, Chang H, Li S, et al. Quercetin inhibits virulence properties of *Porphyromas gingivalis* in periodontal disease. *Sci Rep.* (2020) 10:18313. doi: 10.1038/s41598-020-74977-y

15. Diao Y, Yu X, Zhang C, Jing Y. Quercetin-grafted chitosan prepared by free radical grafting: characterization and evaluation of antioxidant and antibacterial properties. *J Food Sci Technol.* (2020) 57:2259–68. doi: 10.1007/s13197-020-04263-2

16. Moon H, Lertpatipanpong P, Hong Y, Kim CT, Baek SJ. Nano-encapsulated quercetin by soluble soybean polysaccharide/chitosan enhances anti-cancer, anti-inflammation, anti-oxidant activities. *J Funct Foods.* (2021) 87:104756. doi: 10.1016/j.jff.2021.104756

17. Sadighparvar S, Darband SG, Yousefi B, Kaviani M, Ghaderi-Pakdel F, Mihanfar A, et al. Combination of quercetin and exercise training attenuates depression in rats with 1,2-dimethylhydrazine-induced colorectal cancer: possible involvement of inflammation and BDNF signalling. *Exp Physiol.* (2020) 105:1598–609. doi: 10.1113/EP088605

18. Wang J, Zhao XH. Degradation kinetics of fisetin and quercetin in solutions affected by medium pH, temperature and co-existing proteins. *J Serbian Chem Soc.* (2016) 81:243–53. doi: 10.2298/JSC150706092W

19. Doosti M, Dorraji MSS, Mousavi SN, Rasoulifard MH, Hosseini SH. Enhancing quercetin bioavailability by super paramagnetic starch-based hydrogel grafted with fumaric acid: an *in vitro* and *in vivo* study. *Colloids Surf B Biointerfaces.* (2019) 183:110487. doi: 10.1016/j.colsurfb.2019.110487

20. Manzoor MF, Hussain A, Sameen A, Sahar A, Khan S, Siddique R, et al. Novel extraction, rapid assessment and bioavailability improvement of quercetin: a review. *Ultrasonics Sonochem.* (2021) 78:105686. doi: 10.1016/j.ultsonch.2021.105686

21. Chen LC, Chen YC, Su CY, Hong CS, Ho HO, Sheu MT. Development and characterization of self-assembling lecithin-based mixed polymeric micelles containing quercetin in cancer treatment and an *in vivo* pharmacokinetic study. *Int J Nanomed.* (2016) 11:1557–66. doi: 10.2147/IJN.S103681

22. Wiczkowski W, Szawara-Nowak D, Topolska J. Red cabbage anthocyanins: profile, isolation, identification, antioxidant activity. *Food Res Int.* (2013) 51:303–9. doi: 10.1016/j.foodres.2012.12.015

23. Betz M, Kulozik U. Microencapsulation of bioactive bilberry anthocyanins by means of whey protein gels. In: *11th International Congress on Engineering and Food (ICEF)*. Athens (2011). pp. 2047–56.

24. Wang Q, Wei H, Deng C, Xie C, Huang M, Zheng F. Improving stability and accessibility of quercetin in olive oil-in-soy protein isolate/pectin stabilized O/W emulsion. *Foods.* (2020) 9:123. doi: 10.3390/foods9020123

25. Papakyriakopoulou P, Manta K, Kostantini C, Kikionis S, Banella S, Ioannou E, et al. Nasal powders of quercetin-beta-cyclodextrin derivatives complexes with mannitol/lecithin microparticles for Nose-to-Brain delivery: *in vitro* and *ex vivo* evaluation. *Int J Pharm.* (2021) 607:121016. doi: 10.1016/j.ijpharm.2021.121016

26. Li Y, Gao S, Ji X, Liu H, Liu N, Yang J, et al. Evaluation studies on effects of quercetin with different concentrations on the physicochemical properties and *in vitro* digestibility of Tartary buckwheat starch. *Int J Biol Macromol.* (2020) 163:1729–37. doi: 10.1016/j.ijbiomac.2020.09.116

27. Xu JJ, Guo SY, Li XJ, Jiang ST, Zhong XY, Zheng Z. Gel properties of transglutaminase-induced soy protein isolate-polyphenol complex: influence of epigallocatechin-3-gallate. *J Sci Food Agric.* (2021) 101:3870–9. doi: 10.1002/jsfa.11025

28. Yang YX, Wang QM, Tang YW, Lei L, Zhao JC, Zhang YH, et al. Effects of ionic strength and (-)-epigallocatechin gallate on physicochemical characteristics of soybean 11S and 7S proteins. *Food Hydrocolloids.* (2021) 119:106836. doi: 10.1016/j.foodhyd.2021.106836

29. Wang Y, Wang X. Binding, stability, and antioxidant activity of quercetin with soy protein isolate particles. *Food Chem.* (2015) 188:24–9. doi: 10.1016/j.foodchem.2015.04.127

30. Ao L, Liu P, Wu A, Zhao J, Hu X. Characterization of soybean protein isolate-food polyphenol interaction via virtual screening and experimental studies. *Foods.* (2021) 10:2813. doi: 10.3390/foods10112813

31. Li Y, Liu B, Jiang L, Regenstein JM, Jiang N, Poias V, et al. Interaction of soybean protein isolate and phosphatidylcholine in nanoemulsions: a fluorescence analysis. *Food Hydrocolloids.* (2019) 87:814–29. doi: 10.1016/j.foodhyd.2018.09.006

32. Liu K, Zha XQ, Shen WD, Li QM, Pan LH, Luo JP. The hydrogel of whey protein isolate coated by lotus root amylopectin enhance the stability and bioavailability of quercetin. *Carbohydr Polym.* (2020) 236:116009. doi: 10.1016/j.carbpol.2020.116009

33. Yin Z, Qie X, Zeng M, Wang Z, Qin F, Chen J, et al. Effect of thermal treatment on the molecular-level interactions and antioxidant activities in β-casein and chlorogenic acid complexes. *Food Hydrocolloids.* (2022) 123:107177. doi: 10.1016/j.foodhyd.2021.107177

34. Wei J, Xu D, Yang J, Zhang X, Mu T, Wang Q. Analysis of the interaction mechanism of Anthocyanins (*Aronia melanocarpa* Elliot) with β-casein. *Food Hydrocolloids.* (2018) 84:276–281. doi: 10.1016/j.foodhyd.2018.06.011

35. Condict L, Kaur J, Hung A, Ashton J, Kasapis S. Combined spectroscopic, molecular docking and quantum mechanics study of β-casein and ferulic acid interactions following UHT-like treatment. *Food Hydrocolloids.* (2019) 89:351–9. doi: 10.1016/j.foodhyd.2018.10.055

36. Wu X, Lu Y, Xu H, Lin D, He Z, Wu H, et al. Reducing the allergenic capacity of beta-lactoglobulin by covalent conjugation with dietary polyphenols. *Food Chem.* (2018) 256:427–34. doi: 10.1016/j.foodchem.2018.02.158

37. Fazi R, Tintori C, Brai A, Botta L, Selvaraj M, Garbelli A, et al. Homology model-based virtual screening for the identification of human helicase DDX3 inhibitors. *J Chem Inform Model.* (2015) 55:2443–54. doi: 10.1021/acs.jcim.5b00419

38. Rajeswari M, Santhi N, Bhuvaneswari V. Pharmacophore and virtual screening of JAK3 inhibitors. *Bioinformation.* (2014) 10:157–63. doi: 10.6026/97320630010157

39. Antonio E, Khalil NM, Mainardes RM. Bovine serum albumin nanoparticles containing quercetin: characterization and antioxidant activity. *J Nanosci Nanotechnol.* (2016) 16:1346–53. doi: 10.1166/jnn.2016.11672

40. Cui Z, Kong X, Chen Y, Zhang C, Hua Y. Effects of rutin incorporation on the physical and oxidative stability of soy protein-stabilized emulsions. *Food Hydrocolloids.* (2014) 41:1–9. doi: 10.1016/j.foodhyd.2014.03.006

41. Lakowicz JR, Weber G. Quenching of fluorescence by oxygen - probe for structural fluctuations in macromolecules. *Biochemistry.* (1973) 12:4161–70. doi: 10.1021/bi00745a020

42. Ross PD, Subramanian S. Thermodynamics of protein association reactions: forces contributing to stability. *Biochemistry.* (1981) 20:3096–102. doi: 10.1021/bi00514a017

43. Li X, Chen D, Wang G, Lu Y. Study of interaction between human serum albumin and three antioxidants: ascorbic acid, alpha-tocopherol, and proanthocyanidins. *Eur J Med Chem.* (2013) 70:22–36. doi: 10.1016/j.ejmech.2013.09.033

44. Seczyk L, Swieca M, Kapusta I, Gawlik-Dziki U. Protein-phenolic interactions as a factor affecting the physicochemical properties of white bean proteins. *Molecules.* (2019) 24:408. doi: 10.3390/molecules24030408

45. Wang QM, Tang YW, Yang YX, Zhao JC, Zhang YH, Li L, et al. Interaction between wheat gliadin and quercetin under different pH conditions analyzed by multi-spectroscopy methods. *Spectrochim Acta Part A Mol Biomol Spectrosc.* (2020) 229:117937. doi: 10.1016/j.saa.2019.117937

46. Liu FG, Ma CC, McClements DJ, Gao YX. A comparative study of covalent and non-covalent interactions between zein and polyphenols in ethanol-water solution. *Food Hydrocolloids.* (2017) 63:625–34. doi: 10.1016/j.foodhyd.2016.09.041

47. Kelly SM, Jess TJ, Price NC. How to study proteins by circular dichroism. *Biochim Biophys Acta Proteins Proteomics.* (2005) 1751:119–39. doi: 10.1016/j.bbapap.2005.06.005

48. Katouzian I, Jafari SM, Maghsoudlou Y, Karami L, Eikani MH. Experimental and molecular docking study of the binding interactions between bovine α-lactalbumin and oleuropein. *Food Hydrocolloids.* (2020) 105:105859. doi: 10.1016/j.foodhyd.2020.105859

49. Chen Z, Wang C, Gao X, Chen Y, Kumar Santhanam R, Wang C, et al. Interaction characterization of preheated soy protein isolate with cyanidin-3-O-glucoside and their effects on the stability of black soybean seed coat anthocyanins extracts. *Food Chem.* (2019) 271:266–73. doi: 10.1016/j.foodchem.2018.07.170

50. Zhang Y-J, Zhang N, Zhao X-H. The non-covalent interaction between two polyphenols and caseinate as affected by two types of enzymatic protein crosslinking. *Food Chem.* (2021) 364:130375. doi: 10.1016/j.foodchem.2021.130375

51. Chen G, Wang S, Feng B, Jiang B, Miao M. Interaction between soybean protein and tea polyphenols under high pressure. *Food Chem.* (2019) 277:632–8. doi: 10.1016/j.foodchem.2018.11.024

52. Friesner RA, Banks JL, Murphy RB, Halgren TA, Klicic JJ, Mainz DT, et al. Glide: a new approach for rapid, accurate docking and scoring. 1. Method and assessment of docking accuracy. *J Med Chem.* (2004) 47:1739–49. doi: 10.1021/jm0306430

53. Meng Y, Li C. Conformational changes and functional properties of whey protein isolate-polyphenol complexes formed by non-covalent interaction. *Food Chem.* (2021) 364:129622. doi: 10.1016/j.foodchem.2021.129622

54. Acosta-Dominguez L, Cocotle-Ronzon Y, Alamilla-Beltran L, Hernandez-Martinez E. Effect of a cryogenic treatment in the microstructure, functional and flow properties of soy protein isolate. *Food Hydrocolloids.* (2021) 119:106871. doi: 10.1016/j.foodhyd.2021.106871

55. Suib X, Sunb H, Qi B, Zhang M, Lib Y, Jiang L. Functional and conformational changes to soy proteins accompanying anthocyanins: focus on covalent and non-covalent interactions. *Food Chem.* (2018) 245:871–8. doi: 10.1016/j.foodchem.2017.11.090

56. Zembyla M, Murray BS, Radford SJ, Sarkar A. Water-in-oil Pickering emulsions stabilized by an interfacial complex of water-insoluble polyphenol crystals and protein. *J Colloid Interface Sci.* (2019) 548:88–99. doi: 10.1016/j.jcis.2019.04.010

Study on the binding behavior and functional properties of soybean protein isolate and β-carotene

Yating Zhang[1]*[†], Wenqi Zhao[1][†], Zhuqing Xing[1], Beibei Zhu[2], Ruiyang Hou[1], Junxi Zhang[1], Taoran Li[1], Zifan Zhang[1], Hongwu Wang[1] and Zheng Li[2]*

[1]College of Healthy Science and Engineering, Tianjin University of Traditional Chinese Medicine, Tianjin, China, [2]College of Chinese Medicine Pharmaceutical Engineering, Tianjin University of Traditional Chinese Medicine, Tianjin, China

This study focused on the non-covalent interaction between soybean protein isolate (SPI) and β-carotene (BC). The conformational changes of SPI with β-carotene in varying proportions (BC/SPI: 2%, 4%, 6%, 8%, and 10%) were investigated by multi-spectroscopy and molecular docking. Results showed that the quenching mode is static quenching and binding affinity increased with temperature. The stoichiometry was 1:1, indicating there was only one binding site in SPI. The binding was based on entropy and primarily driven by hydrophobic interactions and its binding constant was in the order of 10^4 L·mol^{-1}. The addition of the β-carotene affected the secondary structure of SPI resulting in an increase in α-Helix and a decrease in random coil and β-turn content, indicating protein aggregated and hydrophobic interactions occurred. Sodium dodecyl sulfate-polyacrylamide gel electrophoresis (SDS-PAGE) verified that no new larger molecular weight substance was formed and no covalent interaction existed. Molecular docking corroborated that electrostatic and hydrophobic interactions were both involved in the formation of complexes, where hydrophobic interaction was the dominant one. Moreover, β-carotene improved 1,1-diphenyl-2-picrylhydrazyl (DPPH) radical scavenging activity, foaming capacity, and emulsifying stability of SPI. These findings provide useful information about the interaction mechanism of SPI and β-carotene, which contributes to the further development and application of SPI products rich in β-carotene in the food industry.

KEYWORDS

soybean protein isolate, β-carotene, multi-spectroscopic techniques, molecular docking, emulsifying properties

Introduction

β-carotene ($C_{40}H_{56}$; BC), a precursor of vitamin A, is a carotenoid widely found in fruits and vegetables. It has plenty of beneficial effects on human health, such as anti-cancer, antioxidants, prevention of cardiovascular disease, and age-related macular degeneration. Therefore, β-carotene is a recognized superior functional food additive (1). However, β-carotene is almost insoluble in water and even hardly dissolved in organic solvents, such as acetone, anhydrous ethanol, dimethyl sulfoxide, and some oils and fats. Additionally, it is easily crystallized at room temperature, and sensitivity to light, heat, and oxygen greatly limits its application in food (2).

Recently, the interaction between β-carotene and proteins, which was conducted to modify the properties of β-carotene to expand its application, has attracted raising interest from researchers. Li et al. (3) studied the interaction of β-carotene and astaxanthin with human serum albumin (HSA) and bovine serum albumins (BSA) under physiological conditions by using multi-spectroscopic techniques. The moderate affinity of the carotenoids and HSA/BSA helps these two carotenoids diffuse from the circulatory system to their target sites. A study by Andresa et al. (4) showed that β-carotene entrapped within protein-coated MCT droplets was more stable than within T80-MCT systems. β-carotene interacted with proteins in emulsions changing their properties and behavior under the gastrointestinal tract, consequently, enhancing the stability/bioaccessibility of β-carotene. Allahdad et al. (5–7) explored the interaction mechanism between β-carotene and whey proteins and caseins to improve the color and taste of milk and the consequences were checked by introducing β-carotene into a hydrated polar solution containing milk protein. They found that although WPI was very effective in protecting β-carotene against photodecomposition *via* insertion into the β-lactoglobulin cavity, the open structure and greater amounts of antioxidative amino acids made casein a better protectant than WPI. The association of β-carotene with milk proteins led to the decrease in electron transfer as opposed to hydrogen transfer to the radical species. To our knowledge, most of the current studies in this field are on animal proteins, and there are few systematic studies on the binding of plant proteins to small molecule active components.

Soybean protein isolate (SPI) is an excellent and cheap plant protein. The varieties and contents of eight amino acids in SPI meet the needs of the human body, which effectively supplemented the essential amino acids (8). SPI is also widely used in the delivery of functional nutrients in food because of its good physicochemical features and nutritional value (5, 9–11). The peptide chains of SPI are rich in hydrophobic amino acid residues and charged amino acid residues, which can bind to functional nutrients through hydrophobic, electrostatic, and hydrogen bonding interactions. SPI can promptly deliver and transport the hydrophobic active substances to the specified

position *in vivo*, thus improving the bioavailability of nutrients and enhancing some functional properties of proteins (12). Nevertheless, when different active ingredients are transported, there are great differences in embedding efficiency, stability, and bioavailability. It was found that the binding mode of active components and protein depended on the type and concentration of proteins, the structure of active components as well as their molecular weight, and so on (13, 14). Covalent and non-covalent interactions are two main interaction ways between proteins and nutrients. According to the existing research of Zhang et al., the non-covalent interactions of SPI are more fundamental in extrusion cooking (15), and Y. Chen et al. further explored the effects of the non-covalent interactions between polyphenols and proteins on the formations of the heterocyclic amines in dry heated soybean protein isolate (16). Moreover, Wang et al. (17) researched the physicochemical properties and emulsifying properties during the formation of soybean protein isolate-hawthorn flavonoids non-covalent complexes to provide a theoretical basis for protein processing and application. However, few systematic studies are probing into the interaction mechanism of soy isolate protein and β-carotene.

Based on these findings, the main objective of this work was to comprehensively study the potential binding behavior between SPI and β-carotene and the effects on their functional properties. Accordingly, multi-spectroscopic techniques, including fluorescence spectroscopy, Fourier transform infrared spectroscopy (FTIR), and circular dichroism (CD) spectroscopy, were used to investigate the non-covalent interaction forces, binding site, and the conformation changing patterns of SPI in the presence of β-carotene. Molecular docking was employed to further reveal the mechanism at the molecular level and verify the experimental results. Meanwhile, changes in various functional properties of SPI after binding with β-carotene were detected. It was expected to get further insights into the effect of functional nutrients on the structural and functional properties of SPI, thus, offering a reference for the development of novel protein additives with good functional properties and improved health benefits in the future.

Materials and methods

Materials

The β-carotene (99.8 %) and DPPH were purchased from Macklin Biochemical Company (Shanghai, China). SurePAGE, Bis-Tris (4–12%, 12 wells, 10/pk), Tris-MOPS-SDS Running Buffer Powder, and PAGE-MASTER Protein Standard Plus were bought from GenScript (860 Centennial Ave., Piscataway, NJ, United States). The Coomassie brilliant blue fast staining solution and SDS-PAGE loading buffer (with DDT) were achieved by Beijing Solarbio Science and Technology Co.,

Ltd., (Beijing, China). Potassium bromide was purchased from Comere Chemical Reagents Co., Ltd., (Tianjin, China) and it is in the spectrum of purity. All the reagents above were of analytical grade except otherwise explained.

Preparation of soybean protein isolate

SPI was extracted according to the method of Y. Zhang (18) and the obtained protein solution was freeze-dried and crushed to yield SPI powder.

The preparation of complexes

Complexes preparation was in accordance with the method of Deng et al. (19), Teng et al. (20), and Zhang et al. (21), and slightly adjusted. The SPI aqueous solution (10^{-5} M) was fully mixed with β-carotene ethanol solution (0.15 mg/ml) in different weight ratios (SPI/BC: 2%, 4%, 6%, 8%, and 10%). Subsequently, the mixed solution was put in a water bath at 273, 298, 318, and 338 K for 30 min, respectively. After insulation, the complex samples were evaporated by a vacuum rotary evaporator (Sheng-ye, RE-52AA, China) until ethanol was completely removed. Afterward, ultrapure water was added to adjust the volume to the original volume. The experiment was carried out under dark conditions during the whole course.

Fluorescence spectroscopy

To explore the interaction mechanisms between SPI and β-carotene, a JASCO FP-7100 spectrofluorometer (Jasco, FP-7100, Japan) was used to record the emission spectra at 300–500 nm with the excitation wavelength at 280 nm, respectively. The excitation and emission slits were set to 20 and 5 nm, and the scan speed was 2,400 nm/min. The SPI–β-carotene solutions were pre-warmed at 273, 298, 318, and 338 K for 30 min.

To further explore the fluorescence quenching mechanism, Stern-Volmer (Equation 1) was applied to fit the fluorescence intensity in λ_{max} at different temperatures.

$$\frac{F_0}{F} = 1 + K_{SV}[\beta] = 1 + k_q \cdot \sigma_0[Q] \qquad (1)$$

Here, F_0 and F are fluorescence intensities in the absence and presence of β-carotene, respectively. [β] is the concentration of quencher, k_q is the biomolecular quenching constant, σ_0 is the average biomolecular fluorescence lifetime without quenchers equaling to 10^{-8} s, and K_{SV} is the Stern-Volmer quenching constant.

A double logarithmic Stern-Volmer equation (Equation 2) was used for detecting the static quenching principle in a liner

range at different temperatures.

$$Lg\frac{F_0 - F}{F} = LgK_a + n \cdot Lg[Q] \qquad (2)$$

Here F_0 and F are fluorescence intensities in the absence and presence of β-carotene, respectively. [Q] is the concentration of quencher, n is the bonding site number of the complex, and K_a is the apparent binding constant.

To find out the thermodynamic parameters of the complex, the Vant-Hoff equation (Equations 3, 4) were put to use to make the liner fit.

$$lnK_a = -\frac{\triangle H^0}{RT} + \frac{\triangle S^0}{R} \qquad (3)$$

$$\triangle G^0 = \triangle H^0 - T \cdot \triangle S^0 \qquad (4)$$

Here K_a is the apparent binding constant. $\triangle H^0$, $\triangle S^0$, and $\triangle G^0$ respond to enthalpy change, entropy change, and Gibbs free energy change, successively. R is gas constant ($R = 8.314J \cdot mol^{-1} \cdot K^{-1}$), and T is standard thermodynamic temperature.

Fourier transform infrared spectroscopy

The infrared spectrum of SPI, BC, and SPI–BC complex was measured by a spectrum instrument (Bruker, Germany). Briefly, the sample powder (1 mg) was mixed with KBr powder (150 mg), ground, and pressed into a transparent flake. A total of 32 scans were taken at 4 cm^{-1} resolution from 4,000 to 400 cm^{-1}. Background interference was eliminated *via* KBr and the work environment was 25°C (22, 23).

Circular dichroism spectroscopy

The method of Chamani et al. (24, 25) with slight retouch was taken to measure the CD spectroscopy of the liquid samples, which was heat preservation at 25°C by JASCO (J-810, Japan). The spectropolarimeter was set in the region from 250 nm to 165 nm at 25°C. The deltax was −0.05 and the N point was 1,701. The concentration was 6 10^{-6} M for all proteins, the mean residue weight was 115 g/mol and a cuvette of 1 mm path length was used. The obtained data were converted to molar ellipticity [θ] (deg·cm^2 ·dmol^{-1}), according to Equation 5.

$$[\theta] = \frac{\theta}{R \times C \times l \times 10} \qquad (5)$$

Where θ is the CD signal in degree at each wavelength, C is protein concentration in mol/L, l is the length of light path (cm), and R is the residue number of SPI.

The final statistics were analyzed by the CDpro software, and the result is shown in **Table 2**.

Sodium dodecyl sulfate polyacrylamide gel electrophoresis

The sodium dodecyl sulfate polyacrylamide gel electrophoresis (SDS-PAGE) of SPI and SPI–BC complex were carried out according to the method of Yan et al. (26). The freeze-dried powder of samples was fully dissolved in 0.5 ml loading buffer to obtain a 100 μM SPI solution and then boiled it for 5 min to unfold the SPI. The sample solution (10 μL) after centrifugation was added to each loading slot successively, and the voltage of laminated gel and separation gel was set as 80 mV and 120 mV, respectively. Coomassie brilliant blue fast staining solutions A and B (v/v = 5:1) were mixed to attain the working solution. The gel was placed into 50 ml boiling deionized water for 5 min and then transferred to a 25 ml boiling working solution for 60 s. Afterward, it was transferred to a decolorizing shaker for 10 min. Finally, the image was obtained by a gel analysis imaging system to analyze molecular weight changes of SPI.

Modular docking simulation

The modular docking was performed according to the method of Nada et al. (27) with a little alteration. The Glide module of Schrödinger (2021) was applied for molecular docking. The 3D structure of β-carotene (Substance SID: 319295400) was obtained from PubChem[1] and then optimized by Chem3D 20.0 *via* minimization of energy. The crystal structure of 7S protein (PDB ID:3AUP) and 11S protein (PDB ID:1FXZ) were acquired from the RCSB Protein Data Bank database[2] and the Protein Preparation Wizard of Maestro 12.7 was conducted to prepare them (28).

The Bind Site Detect and Receptor Grid Generation module was conducted to detect the active binding sites and define the active site grid of target proteins, respectively. After using Ligpre to obtain the Lig Files, ran Ligand and Dock module. All parameters were by default. The final binding conformations were recorded based on the calculated GlideScore and the results were visualized using PyMOL (29).

Determination of DPPH radical scavenging activity

The DPPH radical scavenging activity of the protein solution with or without BC was determined according to the methodology formulated by Yamamoto (30) with slight modification. Different ratios of BC were added to the samples at

25°C, as mentioned in section "The preparation of complexes." First, a 2 ml sample solution was mixed with ethanolic DPPH solution at the same proportion. Moreover, a control group mixed with 2 ml ethanol with sample solution at equal volume was set to exclude the impact of the color of BC at the absorbance value. The mixture was vortexed for 1 min and shaken for 30 min in darkness. A double beam UV–visible spectrophotometer (Mapada, Shanghai) was used to achieve the absorbance at 517 nm. The DPPH radical scavenging activity was reckoned with Equation 6.

$$Radical\ scavenging\ activity\,(\%) \; = \; \left(1 - \frac{A_C}{A_0}\right) \; \times \; 100\% \quad (6)$$

Here, A_C is the absorbance value of the solution with DPPH and A_0 is the value of the blank.

Foaming capacity and foaming stability

The foaming capacity (FC) and foaming stability (FS) were investigated following the means of Yan (31). The samples (50 ml) were agitated by a high-shear mixer at 16,000 rpm for 40 s to produce the foam and the foaming volume was recorded immediately. The foaming capacity (FC) was calculated by Equation 7:

$$FC \; = \; \frac{V_a - V_b}{V_a} \; \times \; 100 \quad (7)$$

where V_a and V_b represent the volumes of the samples with and without whipping, respectively.

Keep the foaming samples standing at room temperature for 20 min and record their volume. Equation 8 was used to calculate the foaming stability (FS).

$$FS \; = \; \frac{V_{F(0)} - V_{F(t)}}{V_{F(0)}} \; \times \; 100 \quad (8)$$

Here $V_{F(0)}$ and $V_{F(t)}$ represent the volumes of the samples standing for 0 min and t min after whipping, respectively.

Emulsifying activity index and emulsifying stability index

The emulsifying activity index (EAI) and emulsifying stability index (ESI) were referred to the technique of Xi et al. (32) with little modification. The sample solution (30 ml) was mixed with 10 ml of soybean oil. Afterward, the mixture was homogenized for 40 s to acquire aimed emulsion. The others operation followed the referenced method. EAI and ESI were calculated by Equations 9, 10.

$$EAI(m^2/g) \; = \; \frac{2 \; \times \; 2.303}{C \; \times \; (1 - \varphi) \; \times \; 10} \quad (9)$$

$$ESI\,(\%) \; = \; \frac{A_{10}}{A_0} \; \times \; 100 \quad (10)$$
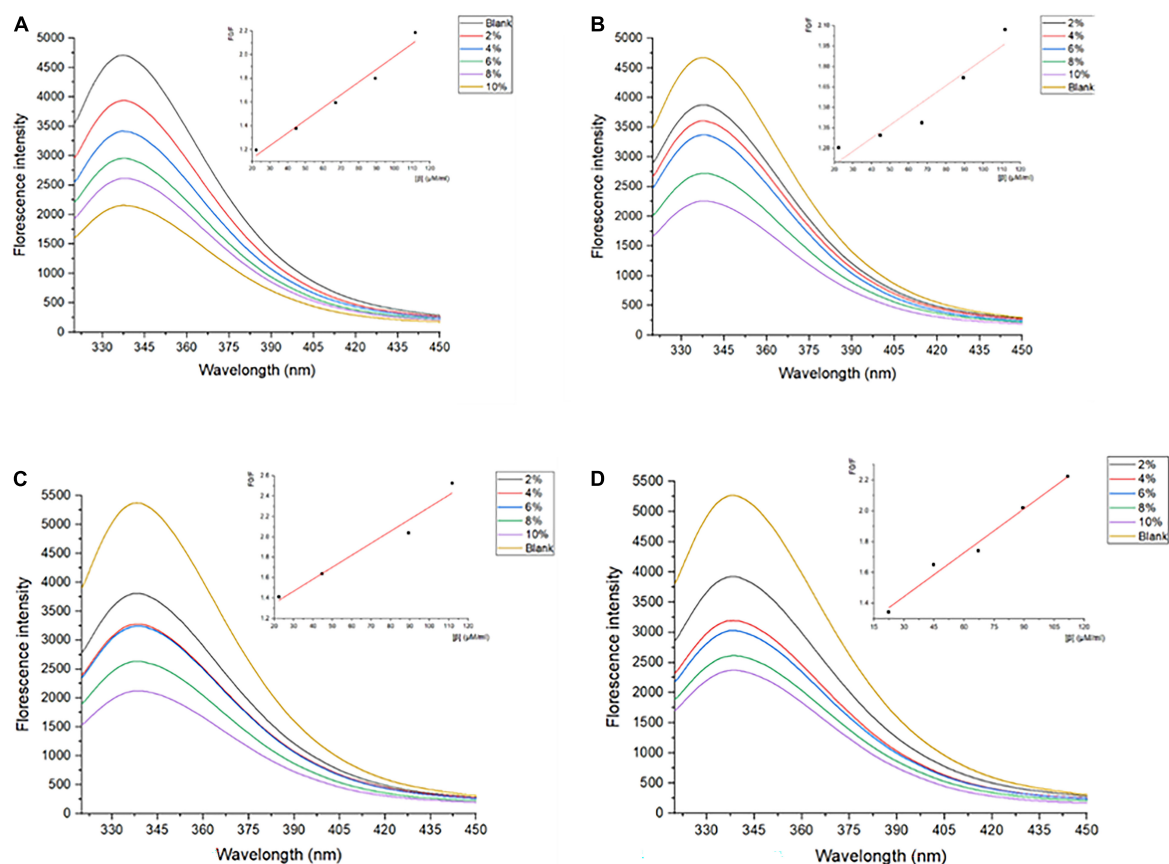
FIGURE 1
Fluorescence spectra of SPI and SPI–BC complexes at different weight ratios (BC/SPI: 2%, 4%, 6%, 8%, and 10%) at **(A)** 273 K, **(B)** 298 K, **(C)** 318 K, and **(D)** 338 K.

Here, C is the protein concentration (mg/mL) in samples, φ is on behalf of the oil phase fraction (v/v) in emulsion, and 100 represents dilution folds.

Statistical analysis

All measurements were conducted three times. One-way ANOVA was used for data analysis by the SPSS 21.0.0.0 software, $p < 0.05$ was considered statistically significant. And the image description was completed by the Origin 9.8.2 software.

Results and discussion

Fluorescence quenching

Generally, tryptophan, tyrosine, and phenylalanine residues in protein scan fluoresce to some extent critically dependent on the folding degree of proteins, especially the tryptophan residues (33). The intrinsic fluorescence spectrum reflects
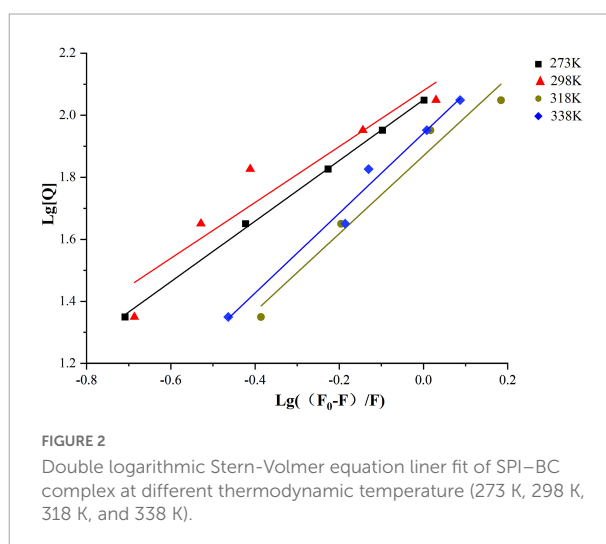
FIGURE 2
Double logarithmic Stern-Volmer equation liner fit of SPI–BC complex at different thermodynamic temperature (273 K, 298 K, 318 K, and 338 K).

the polarity of the microenvironment in which tryptophan resides, and reveals the conformational changes of proteins during the interaction of ligand-protein (34). Therefore, the

measurements of the inner fluorescence spectrum could reveal data on a wide range of molecular activities containing interactions between solvent molecules and fluorophores, rotational diffusion of proteins, distances between sites on biomolecules, conformational changes, and binding interactions (35). As shown in **Figure 1**, the λ_{max} of SPI is 337–339 nm, which is more than 330 nm, indicating that the Trp in SPI was in a polar microenvironment (36), which was similar to the results observed by Allahdad et al. (6, 7). The fluorescence intensity of SPI decreased after interacting with β-carotene, suggesting that fluorescence quenching occurred, which may be due to the shielding effect of β-carotene binding to the protein chain. As shown in **Figures 1A–D**, a blue shift of λ_{max} from 337–339 nm to 335–336 nm was observed with the increase of β-carotene, indicating that the polarity of the microenvironment decreased and hydrophobic interactions were strengthened, which was in accordance with the result of Deng et al. (19). Soy protein and its subunit underwent aggregation due to the addition of β-carotene.

The fluorescence quenching of a fluorophore induced by a variety of molecular interactions can be dynamic, resulting from collisions between the fluorophore and quencher, or static, resulting from the formation of a ground-state complex between the fluorophore and quencher (37). Kq is one of the determining factors of the quenching mechanisms (6).

As shown in **Table 1**, the value of Kq is much larger than the diffusion collision constant 2×10^{10} L/mol·s^{-1}, suggesting a static quenching occurred due to the interaction of SPI and β-carotene (38). Additionally, the quenching constant, K_{SV}, also determined the quenching mechanism. Its values decreased with the increase in temperature, indicating the presence of static quenching (39, 40). Accordingly, it could be confirmed that the SPI–BC complex was formed (41).

Bonding mode analysis

The bonding information including the association constant K_a and the binding stoichiometry were obtained from the double logarithmic regression curve (**Figure 2**) and provided in **Table 1**. The K_a value increased with the increase of temperature, suggesting that the complex had a favorable thermostability in the binding system and the interaction was an endothermic reaction. The value was shown to be closed to 1, which revealed that SPI and β-carotene interacted at the molar ratio of 1:1 (42, 43). As described in section "Fluorescence quenching," different addition ratios of β-carotene caused different changes in the conformation of SPI. Moreover, with the increase of K_a value, the binding affinity also raised, meaning a more stable bonding occurred, indicating an efficient interaction between SPI and BC that could be an excellent carrier *in vivo* being to take shape,

TABLE 1 Effect of temperature on quenching constants and binding parameters of SPI with β-carotene.

T/K	Stern-volmer			Binding parameters			$\Delta H^0/kJ\cdot mol^{-1}$	$\Delta S^0/J\cdot mol^{-1}\cdot K^{-1}$	$\Delta G^0/J\cdot mol^{-1}$	R^2
	$K_{SV}/10^5 L\cdot mol^{-1}$	$kq/10^{13} L\cdot mol^{-1} s^{-1}$	R^2	$K_a/10^5 L\cdot mol^{-1}$	n	R^2				
273	1.07 ± 0.01	1.07 ± 0.01	0.91	0.83 ± 0.01	0.92 ± 0.04	0.90	4,003	32.43	−4,850	0.85
298	0.97 ± 0.02	0.97 ± 0.02	0.98	0.89 ± 0.02	0.97 ± 0.01	0.99			−5,661	
318	0.96 ± 0.03	0.96 ± 0.03	0.98	1.14 ± 0.01	1.05 ± 0.02	0.98			−6,310	
338	0.95 ± 0.07	0.95 ± 0.07	0.96	1.26 ± 0.01	1.10 ± 0.01	0.97			−6,958	
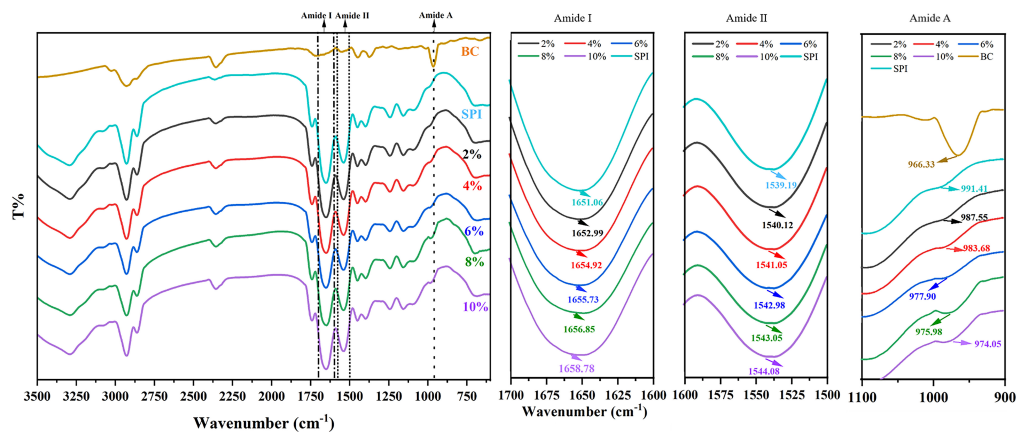
FIGURE 3
Fourier Transform Infrared Spectroscopy SPI and SPI–BC complex at different weight ratios (BC/SPI: 2%, 4%, 6%, 8%, and 10%).

TABLE 2 Secondary structure analysis of CDpro based on circular dichroism spectroscopy data.

Temperature	C_β (μM/ml)	α-helix	β-sheet	β-turn	Random coil
298K	0	14.6%	35.3%	22.5%	27.6%
	22.35	16.3%	33.1%	25.9%	24.7%
	44.70	16.6%	29.7%	31.2%	22.5%
	67.05	17.3%	28.4%	35.1%	19.2%
	89.40	21.5%	25.6%	36.6%	16.3%
	111.7	27.7%	22.8%	35.0%	14.5%
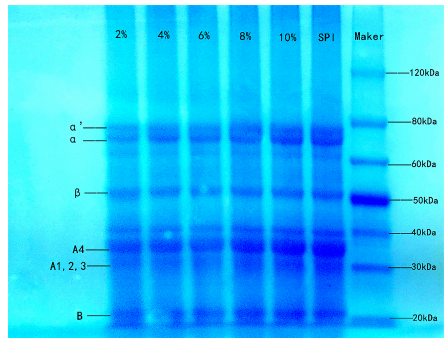
FIGURE 4
Sodium dodecyl sulfate polyacrylamide gel electrophoresis of SPI and SPI–BC complex at different weight ratios (BC/SPI: 2%, 4%, 6%, 8%, and 10%).

which is consistence with the findings of Chamani et al. (44, 45).

Thermodynamic property analysis

There are several non-covalent interactive forces between organic ligands and proteins, including van der Waals forces, hydrophobic interaction, hydrogen bonds, and electrostatic interaction (46). According to the results of Ross and Subramanian, if both $\triangle H^0$ and $\triangle S^0$ are positive, the hydrophobicity is the primary force; if $\triangle H^0$ and $\triangle S^0$ are negative, Van der Waals force and hydrogen bond are the main interaction (47). To confirm the major interactive force between SPI and β-carotene, free-energy change ($\triangle G^0$), enthalpy change ($\triangle H^0$), and entropy change ($\triangle S^0$) were investigated and listed in **Table 1**. As shown, both $\triangle H^0$ and $\triangle S^0$ were positive values indicating that the hydrophobic interaction was the primary driving force. $\triangle H^0 > 0$ indicated that the interaction of SPI and β-carotene was an endothermic reaction, which was entropy driven. This was consistent with the previous analysis of K_a, the effective quenching constant for the available fluorophore, whose value trend was similar to the temperature during static quenching, and contrary to K_{SV} (40). Additionally, $\triangle G^0 < 0$ indicated that the combination of SPI and β-carotene was spontaneous (48), which re-supported the last speculation in section "Bonding mode analysis."

Secondary structure analysis

FTIR spectrometry and circular dichroism spectroscopy were conducted to further determine the alteration in protein
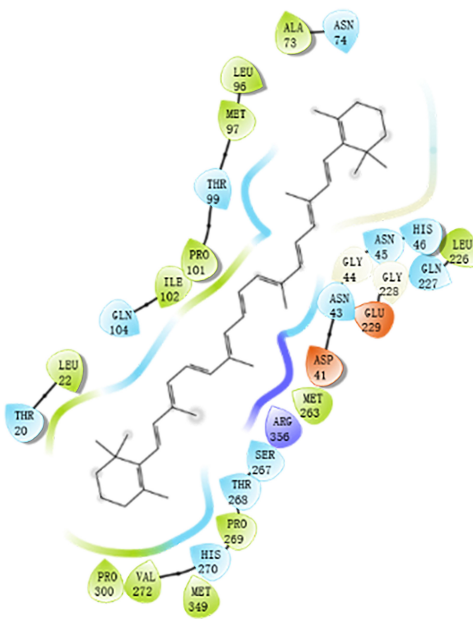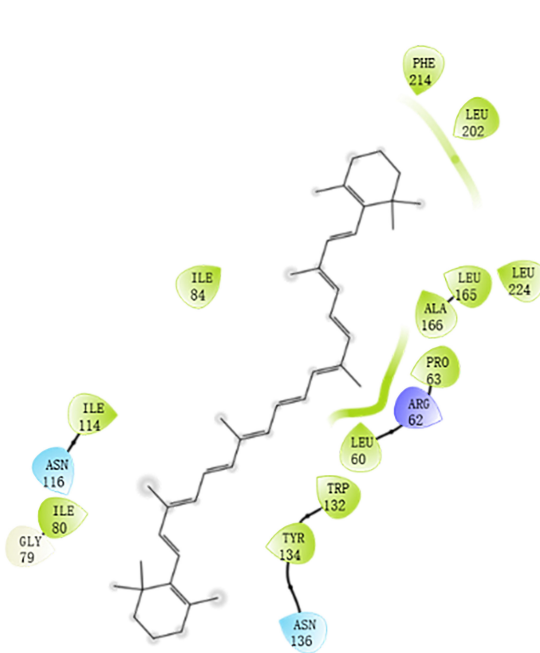
FIGURE 5
Modular docking 2D and 3D conformational at 298K: **(A)** 7S interactions driving force 2D profile; **(B)** 7S docking result 3D model; **(C)** 11S interactions driving force 2D profile; **(D)** 11S docking result 3D model.

secondary structure for the qualitative analysis (49). Amide band, consisting of amide I, amide II, and amide III, is the characteristic band for studying protein structures. The amide I band (1,700–1,600 cm $^{-1}$, C = O tensile vibration) and the amide II band (1,550–1,500 cm $^{-1}$, N–H bending, and C–N stretching) are most commonly used to characterize the structure of proteins (50).

As shown in **Figure 3**, SPI showed characteristic peaks around 1,651 cm^{-1} (amide I band, representative of C = O stretching) and 1,539 cm^{-1} (amide II band, representative of N-H bending, and C–N stretching). The amide I band of SPI was weakened after the addition of β-carotene, indicating that β-carotene altered the C = O bond of SPI (51). Meanwhile, the peak position of the amide I band showed a red shift from 1,651 cm^{-1} to 1,653–1,659 cm^{-1}, suggesting an increase in α-helix. According to the result of circular dichroism spectroscopy (**Table 2**), the α-helix increased from 14.6% to 16.3%, 16.6% to 17.3%, 21.5% to 27.7% with the concentration of β-carotene raised from 0 to 22.35 μM/ml, 44.70 to 67.05 μM/ml, 89.40 to 111.7 μM/ml, respectively, which consisted with the fluorescence analysis and the results of Li et al. (52), which manifested the increase of combination between BC and a hydrophilic group of SPI and hydrophobic interaction.

The amide II band (representative of N-H bending), showed a red shift from 1,539 to 1,540–1,544 cm^{-1}, implying an increase of β-sheet, which is consistent with the results of the amide I band (53). The outcome of circular dichroism spectroscopy (**Table 2**) showed the β-sheet decrease from 35.3% to 33.1%, 29.7% to 28.4%, and 25.6% to 22.8% with the concentration of β-carotene raised from 0 to 22.35 μM/ml, 44.70 to 67.05 μM/ml, and 89.40 to 111.7 μM/ml, respectively, verified the result of amide II. Meanwhile, the changes suggested N–H bond of SPI was altered. Alteration of the amide I and amide II bands indicated a possible electrostatic interaction existed between SPI and β-carotene (54, 55). In addition, accompanied by the addition of β-carotene, the intensity of the peak at 964 cm^{-1} raised to 971–994 cm^{-1}, which represented the addition of β-carotene altered the conformation of SPI. This phenomenon was regarded as concerned with the decrease of the disorder in protein molecules arrangement (56). The increase of α-helix and the converted changes of random coil certified it.

The secondary structure conversion became more obvious accompanying the addition of β-carotene, convergent with the variation trend of Ka. In other words, the more β-carotene added, the higher the binding affinity and the more powerful interaction force demonstrated by hydrophobic interaction were acquired (57).

SDS-PAGE analysis

SDS-PAGE is usually used to analyze the molecular weight composition of protein subunits (58). SPI contains
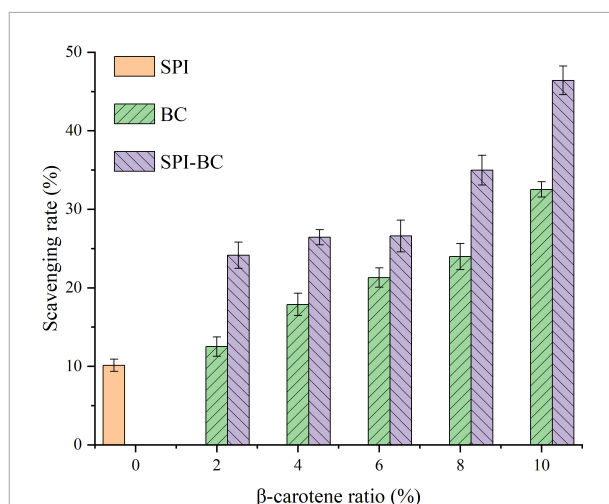
FIGURE 6
DPPH radical scavenging activity of SPI, free BC and SPI–BC complexes at different weight ratio (BC/SPI: 2%, 4%, 6%, 8%, and 10%).

two primary globular proteins: 7S (β-conglycinin) and 11S (glycinin). As shown in **Figure 4**, the SPI–BC complex had intact bands, and no new band was generated compared to native SPI, indicating that there was little impact on SPI molecular weight and no covalent interactions occurred (59). It was speculated that weak intermolecular interactions such as hydrophobic interactions might be the predominated force between SPI and beta-carotene.

Modular docking

In structural molecular biology, molecular docking is an effective technique, which was widely applied to forecast the primary binding modalities of a ligand with a three-dimensionally known protein (60). Thus the 7S and 11S components of SPI were chosen to dock with β-carotene to evaluate the preferred binding sites and the interaction way. The stereoview of the docking experiments is presented in **Figures 5A,B**: 7S; **Figures 5C,D**: 11S.

The topflight binding sites consisting of hydrophobic residues on 7S scoring 1.035 was selected to perform docking. The outcome scored −5.008 with the −4.7903 kJ/mol bonding energy. In the 7S component, hydrophobic interactions dominated the combine and a slight electronic interaction also existed, no H-bond interaction materialized. The specific details are shown in **Table 3**, it was demonstrated that ALA73, MET97, PRO101, ILE102, LEU22, PRO300, VAL272, MET349, PRO269, MET263, and LEU226 bound with BC through hydrophobic interaction, and the electronic interaction consisted of ARG356, ASP41, and GLU229.

TABLE 3   Interactions composition of residues of 7S and 11S.

Protein	Polar	Hydrophobic interaction	Electronic interaction	H-bond
7S	ANS74, THR99, GLN104, THR 20, HIS270, THR263, SER267, ASN43, ASN45, HIS46, GLN27	ALA73, MET97, PRO101, ILE102, LEU22, PRO300, VAL272, MET349, PRO269, MET263, LEU226	ARG356, ASP41, GLU229	None
11S	ASN116, ASN136	ILE80, ILE114, ILE84, PHE241, LEU201. LEU2114, LEU165, ALA166, PRO63, LEU60, TRP132, TYR134	ARG62	None
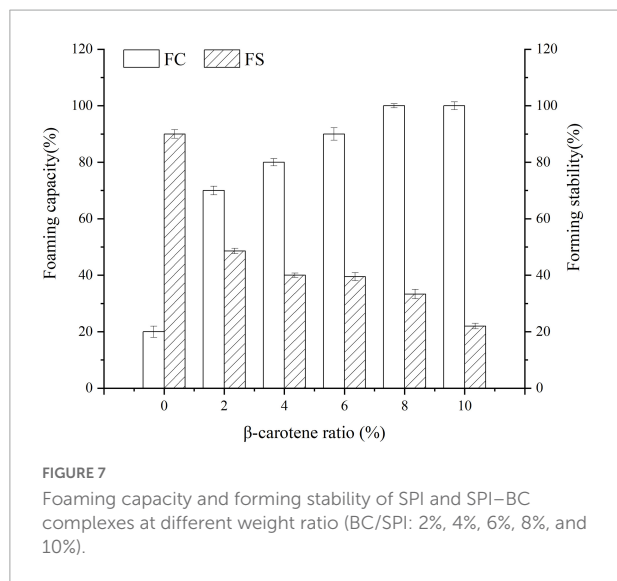
FIGURE 7
Foaming capacity and forming stability of SPI and SPI−BC complexes at different weight ratio (BC/SPI: 2%, 4%, 6%, 8%, and 10%).
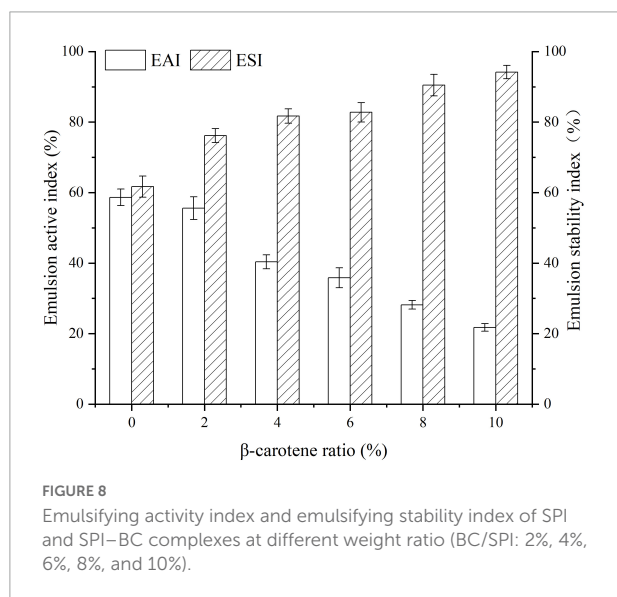
FIGURE 8
Emulsifying activity index and emulsifying stability index of SPI and SPI−BC complexes at different weight ratio (BC/SPI: 2%, 4%, 6%, 8%, and 10%).

In the 11S component, a crystal binding site got the highest score of −4.004 with −3.190 kJ/mol bonding energy. The other consequence was similar to 7S and the details were exhibited in **Figures 5C,D** and **Table 3**, ILE80, ILE114, ILE84, PHE241, LEU201. LEU2114, LEU165,

ALA166, PRO63, LEU60, TRP132, and TYR134 contributed to hydrophobic interaction and only ARG62 made up electronic interaction.

The binding energy was used to assess the binding between the active component and the target, and the binding energy and stability of the ligand–receptor interaction are positively correlated (61). The absolute value of binding energy of 7S was bigger than 11S, meaning that the former had better binding activity and stability, which was consistent with the docking score. Considering the proportion of 7S and 11S is about 3:4 (62), according to the docking result the binding energy was concluded as 4.56 kJ/mol, which was similar to that acquired from fluorescence (4.85 kJ/mol). The fine distinction may cause by the polarity of the solution environment and other components of SPI (6).

Both globulin components bespoke favorable interactions and are mainly influenced by hydrophobic interactions, a potent interaction was formed between SPI and β-carotene, which proved the illations of spectrum analysis.

DPPH radical scavenging activity

The DPPH radical scavenging activity was determined to evaluate the changes in the antioxidant capacity of SPI after binding with β-carotene. As shown in **Figure 6**, the DPPH radical scavenging activity of SPI increased with the increase of BC proportion. Furthermore, the DPPH radical scavenging activity of SPI–BC complex was also higher than free BC, which was consistent with the report of Zhang et al. (21). This may be reasoned by the conformation changes of SPI that the aggregating SPI exposed more free amino groups and the addition of BC improves the affinity of free radicals (59).

Forming capacity and forming stability

Foaming capacity and forming stability were determined to assess the transformations of protein property. As described in **Figure 7**, with the weight ratio of BC/SPI raising, the foaming capacity of the SPI–BC complex increased,

which was consistent with the study of Deng et al. (31). However, the foaming stability of SPI decreased after binding with BC. This phenomenon can be explained by the fact that the hydrophobic interaction between SPI and BC dominated an action that made the surface hydrophobicity and surface tension raise and form an advanced factor to promote foam formation (63), thus improved the foaming capacity of SPI. Nevertheless, it slowed down the molecules migrating from the aqueous phase to the interface and the surface, thus reducing the foaming stability (64).

Emulsifying activity index and emulsifying stability index

Emulsifying activity index (EAI) is influenced by the number of groups exposed and the molecular migration rate, while emulsifying stability index (ESI) is controlled by the thickness of the interface film and the charge on the surface of the droplet (32, 65). As displayed in **Figure 8**, with the increase of β-carotene, the EAI of native SPI dropped. That was possible because several structural residues were buried due to the aggregation of SPI after binding with BC, which made it hard to migrate to oil-water interface (32). Whereas, the change in the ESI of the SPI–BC complex was just the opposite on account of the thick interface film intensified by aggregated SPI (66).

Conclusion

The study found that the combination of SPI and BC was an entropy-driven spontaneous heat-absorbing and can be impacted by changes in ambient variables. The reaction proceeded with being exposed to a polar microenvironment, and the hydrophobic interactions acted as the primary driving force with slight electrostatic interactions. Each SPI molecule has only one binding site for docking with BC, and the stoichiometry is 1:1. After docking with BC, some functional properties of native SPI were enhanced, including DPPH radical scavenging activity, foaming capacity, and emulsifying stability. Infrared spectroscopy, circular dichroism spectroscopy, and fluorescence spectroscopy analysis showed that higher protein aggregation and stronger hydrophobic interactions occurred after the formation of the SPI–BC complex. Although the interaction behavior of SPI and carotene and its effect on protein structure and functional properties were investigated by molecular docking and multispectral analysis, the effect on protein interface properties still needs to be further verified in the process of nutrient delivery. This study is

expected to offer some theoretical references for further development of SPI-based functional products rich in beta-carotene in the future.

Data availability statement

The original contributions presented in this study are included in the article/supplementary material, further inquiries can be directed to the corresponding author/s.

Author contributions

YZ: funding acquisition, project administration, supervision, writing and editing, and resources. WZ: data curation, writing – original draft, investigation, and validation. ZX and HW: project administration and supervision. RH: investigation, data curation, writing, methodology, and validation. BZ: resources, conceptualization, and supervision. JZ: investigation, validation, and project administration. TL and ZZ: investigation. ZL: funding acquisition, resources, and supervision. All authors contributed to the article and approved the submitted version.

Funding

Conflict of interest

The authors declare that the research was conducted in the absence of any commercial or financial relationships that could be construed as a potential conflict of interest.

Publisher's note

References

1. Yonekura L, Nagao A. Intestinal absorption of dietary carotenoids. *Mol Nutr Food Res.* (2007) 51:107–15. doi: 10.1002/mnfr.200600145

2. Popova AV. Spectral characteristics and solubility of β-carotene. *Biophysique.* (2021) 70:53–60.

3. Li X, Wang G, Chen D, Lu Y. Beta-carotene and astaxanthin with human and bovine serum albumins. *Food Chem.* (2015) 179:213–21. doi: 10.1016/j.foodchem.2015.01.133

4. Gomes A, Costa ALR, Cardoso DD, Nathia-Neves G, Meireles MAA, Cunha RL. Interactions of beta-carotene with WPI/Tween 80 mixture and oil phase: effect on the behavior of O/W emulsions during *in vitro* digestion. *Food Chem.* (2021) 341(Pt 2):128–55. doi: 10.1016/j.foodchem.2020.128155

5. Allahdad Z, Varidi M, Zadmard R, Haertle T, Sawyer L, Saboury AA. Efficiency of milk proteins in eliminating practical limitations of beta-carotene in hydrated polar solution. *Food Chem.* (2020) 330:127–218. doi: 10.1016/j.foodchem.2020.127218

6. Allahdad Z, Varidi M, Zadmard R, Saboury AA. Spectroscopic and docking studies on the interaction between caseins and beta-carotene. *Food Chem.* (2018) 255:187–96. doi: 10.1016/j.foodchem.2018.01.143

7. Allahdad Z, Varidi M, Zadmard R, Saboury AA, Haertle T. Binding of beta-carotene to whey proteins: multi-spectroscopic techniques and docking studies. *Food Chem.* (2019) 277:96–106. doi: 10.1016/j.foodchem.2018.10.057

8. Jallinoja P, Niva M, Latvala T. Future of sustainable eating? Examining the potential for expanding bean eating in a meat-eating culture. *Futures.* (2016) 83:4–14. doi: 10.1016/j.futures.2016.03.006

9. Lu Y, Mao L, Zheng H, Chen H, Gao Y. Characterization of β-carotene loaded emulsion gels containing denatured and native whey protein. *Food Hydrocoll.* (2020) 102:105600. doi: 10.1016/j.foodhyd.2019.105600

10. Lu Y, Zhang Y, Yuan F, Gao Y, Mao L. Emulsion gels with different proteins at the interface: structures and delivery functionality. *Food Hydrocoll.* (2021) 116:106637. doi: 10.1016/j.foodhyd.2021.106637

11. Sun X, Cui Q, Li R, Hao L, Liu H, Wang X, et al. Structural and emulsifying properties of soybean protein isolate glycated with glucose based on pH treatment. *J Sci Food Agric.* (2022) 102:4462–72. doi: 10.1002/jsfa.11800

12. Jakobek L. Interactions of polyphenols with carbohydrates, lipids and proteins. *Food Chem.* (2015) 175:556–67. doi: 10.1016/j.foodchem.2014.12.013

13. Zhang J, Liu X, Subirade M, Zhou P, Liang L. A study of multi-ligand beta-lactoglobulin complex formation. *Food Chem.* (2014) 165:256–61. doi: 10.1016/j.foodchem.2014.05.109

14. Zhang R, Han Y, Xie W, Liu F, Chen S. Advances in protein-based nanocarriers of bioactive compounds: from microscopic molecular principles to macroscopical structural and functional attributes. *J Agric Food Chem.* (2022) 70:6354–67. doi: 10.1021/acs.jafc.2c01936

15. Chen FL, Wei YM, Zhang B. Chemical cross-linking and molecular aggregation of soybean protein during extrusion cooking at low and high moisture content. *LWT Food Sci Technol.* (2011) 44:957–62. doi: 10.1016/j.lwt.2010.12.008

16. Chen Y, Xi J. Effects of the non-covalent interactions between polyphenols and proteins on the formations of the heterocyclic amines in dry heated soybean protein isolate. *Food Chem.* (2022) 373:131577. doi: 10.1016/j.foodchem.2021.131557

17. Wang YL, Yang JJ, Dai SC, Tong XH, Tian T, Liang CC, et al. Formation of soybean protein isolate-hawthorn flavonoids non-covalent complexes: linking the physicochemical properties and emulsifying properties. *Ultrason Sonochem.* (2022) 84:105961. doi: 10.1016/j.ultsonch.2022.105961

18. Zhang Y, Tan C, Abbas S, Eric K, Xia S, Zhang X. Modified SPI improves the emulsion properties and oxidative stability of fish oil microcapsules. *Food Hydrocoll.* (2015) 51:108–17. doi: 10.1016/j.foodhyd.2015.05.001

19. Deng XX, Zhang N, Tang CH. Soy protein isolate as a nanocarrier for enhanced water dispersibility, stability and bioaccessibility of -carotene. *J Sci Food Agric.* (2017) 97:2230–7. doi: 10.1002/jsfa.8033

20. Teng Z, Luo Y, Wang Q. Nanoparticles synthesized from soy protein: preparation, characterization, and application for nutraceutical encapsulation. *J Agric Food Chem.* (2012) 60:2712–20. doi: 10.1021/jf205238x

21. Zhang C, Fu Y, Li Z, Li T, Shi Y, Xie H, et al. Application of whey protein isolate fibrils in encapsulation and protection of beta-carotene. *Food Chem.* (2021) 346:128963. doi: 10.1016/j.foodchem.2020.128963

22. Chen S, Ma Y, Dai L, Liao W, Zhang L, Liu J, et al. Fabrication, characterization, stability and re-dispersibility of curcumin-loaded gliadin-rhamnolipid composite nanoparticles using pH-driven method. *Food Hydrocoll.* (2021) 118:8804–12. doi: 10.1016/j.foodhyd.2021.106758

23. Zhang R, Pang X, Lu J, Liu L, Zhang S, Lv J. Effect of high intensity ultrasound pretreatment on functional and structural properties of micellar casein concentrates. *Ultrason Sonochem.* (2018) 47:10–6. doi: 10.1016/j.ultsonch.2018.04.011

24. Chamani J, Moosavi-Movahedi AA. Effect of n-alkyl trimethylammonium bromides on folding and stability of alkaline and acid-denatured cytochrome c: a spectroscopic approach. *J Colloid Interface Sci.* (2006) 297:561–9. doi: 10.1016/j.jcis.2005.11.035

25. Chamani J, Moosavi-Movahedi AA, Hakimelahi GH. Structural changes in β-lactoglobulin by conjugation with three different kinds of carboxymethyl cyclodextrins. *Thermochim Acta.* (2005) 432:106–11. doi: 10.1016/j.tca.2005.04.014

26. Yan S, Xie F, Zhang S, Jiang L, Qi B, Li Y. Effects of soybean protein isolate; polyphenol conjugate formation on the protein structure and emulsifying properties: protein; polyphenol emulsification performance in the presence of chitosan. *Coll Surf A Physicochem Eng Aspects.* (2021) 609:125614. doi: 10.1016/j.colsurfa.2020.125641

27. Nada H, Lee K, Gotina L, Pae AN, Elkamhawy A. Identification of novel discoidin domain receptor 1 (DDR1) inhibitors using E-pharmacophore modeling, structure-based virtual screening, molecular dynamics simulation and MM-GBSA approaches. *Comput Biol Med.* (2022) 142:105217. doi: 10.1016/j.compbiomed.2022.105217

28. Tu Y, Tan L, Lu T, Wang K, Wang H, Han B, et al. Glytabastan B, a coumestan isolated from *Glycine tabacina*, alleviated synovial inflammation, osteoclastogenesis and collagen-induced arthritis through inhibiting MAPK and PI3K/AKT pathways. *Biochem Pharmacol.* (2022) 197:114912. doi: 10.1016/j.bcp.2022.114912

29. Cui M, Zhang K, Wu R, Du J. Exploring the interaction mechanism between antagonist and the jasmonate receptor complex by molecular dynamics simulation. *J Comput Aided Mol Des.* (2022) 36:141–55. doi: 10.1007/s10822-022-00441-w

30. Yamamoto Y, Kato E, Ando A. Increased antioxidative activity of ovalbumin by heat treating in an emulsion of linoleic acid. *Biosci Biotechnol Biochem.* (1996) 60:1430–3. doi: 10.1271/bbb.60.1430

31. Ye JP, Deng LP, Wang YR, McClements DJ, Luo SJ, Liu CM. Impact of rutin on the foaming properties of soybean protein: formation and characterization of flavonoid-protein complexes. *Food Chem.* (2021) 362:130238. doi: 10.1016/j.foodchem.2021.130238

32. Xi C, Kang N, Zhao C, Song H, Liu Y, Zhang T. Effect of reaction temperature on the protein structure and the ability to encapsulate beta-carotene of WPI-dextran conjugates. *J Food Sci.* (2020) 85:1707–16. doi: 10.1111/1750-3841.15141

33. Xu YT, Liu LL. Structural and functional properties of soy protein isolates modified by soy soluble polysaccharides. *J Agric Food Chem.* (2016) 64:7275–84. doi: 10.1021/acs.jafc.6b02737

34. Pallares I, Vendrell J, Aviles FX, Ventura S. Amyloid fibril formation by a partially structured intermediate state of alpha-chymotrypsin. *J Mol Biol.* (2004) 342:321–31. doi: 10.1016/j.jmb.2004.06.089

35. Abdollahpour N, Soheili V, Saberi MR, Chamani J. Investigation of the interaction between human serum albumin and two drugs as binary and ternary systems. *Eur J Drug Metab Pharmacokinet.* (2016) 41:705–21. doi: 10.1007/s13318-015-0297-y

36. Vivian JT, Callis PR. Mechanisms of tryptophan fluorescence shifts in proteins. *Biophys J.* (2001) 80:2093–109. doi: 10.1016/S0006-3495(01)76183-8

37. Lakowicz JR. *Principles of Fluorescence Spectroscopy.* Boston, MA: Springer (2006). doi: 10.1007/978-0-387-46312-4

38. Li Y, Gao F, Gao F, Shan F, Bian J, Zhao C. Study on the interaction between 3 flavonoid compounds and alpha-amylase by fluorescence spectroscopy and enzymatic kinetics. *J Food Sci.* (2009) 74:C199–203. doi: 10.1111/j.1750-3841.2009.01080.x

39. Li H, Zhai B, Sun J, Fan Y, Zou J, Cheng J, et al. Ultrasound-assisted extraction of total saponins from aralia taibaiensis: process optimization, phytochemical characterization, and mechanism of alpha-glucosidase inhibition. *Drug Des Dev Ther.* (2022) 16:83–105. doi: 10.2147/DDDT.S345592

40. Sadeghzadeh F, Entezari AA, Behzadian K, Habibi K, Amiri-Tehranizadeh Z, Asoodeh A, et al. Characterizing the binding of angiotensin converting enzyme i inhibitory peptide to human hemoglobin: influence of electromagnetic fields. *Protein Pept Lett.* (2020) 27:1007–21. doi: 10.2174/1871530320666200425203636

41. Hosseinzadeh M, Nikjoo S, Zare N, Delavar D, Beigoli S, Chamani J. Characterization of the structural changes of human serum albumin upon

interaction with single-walled and multi-walled carbon nanotubes: spectroscopic and molecular modeling approaches. *Res Chem Intermed.* (2018) 45:401–23. doi: 10.1007/s11164-018-3608-5

42. Cao JR, Li FW, Li YY, Chen HP, Liao XJ, Zhang Y. Hydrophobic interaction driving the binding of soybean protein isolate and chlorophyll: improvements to the thermal stability of chlorophyll. *Food Hydrocoll.* (2021) 113:106456. doi: 10.1016/j.foodhyd.2020.106465

43. Silva CEL, Hudson EA, Agudelo ÁJP, da Silva LHM, Pinto MS, do Carmo Hespanhol M, et al. β-carotene and milk protein complexation: a thermodynamic approach and a photo stabilization study. *Food Bioprocess Technol.* (2017) 11:610–20. doi: 10.1007/s11947-017-2028-7

44. Khashkhashi-Moghadam S, Ezazi-Toroghi S, Kamkar-Vatanparast M, Jouyaeian P, Mokaberi P, Yazdyani H, et al. Novel perspective into the interaction behavior study of the cyanidin with human serum albumin-holo transferrin complex: spectroscopic, calorimetric and molecular modeling approaches. *J Mol Liquids.* (2022) 356:119042. doi: 10.1016/j.molliq.2022.119042

45. Marjani N, Dareini M, Asadzade-Lotfabad M, Pejhan M, Mokaberi P, Amiri-Tehranizadeh Z, et al. Evaluation of the binding effect and cytotoxicity assay of 2-Ethyl-5-(4-methylphenyl) pyramido pyrazole ophthalazine trione on calf thymus DNA: spectroscopic, calorimetric, and molecular dynamics approaches. *Luminescence.* (2022) 37:310–22. doi: 10.1002/bio.4173

46. Li Z, Zhao L, Sun Q, Gan N, Zhang Q, Yang J, et al. Study on the interaction between 2,6-dihydroxybenzoic acid nicotine salt and human serum albumin by multi-spectroscopy and molecular dynamics simulation. *Spectrochim Acta A Mol Biomol Spectrosc.* (2022) 270:120868. doi: 10.1016/j.saa.2022.120868

47. Ross PD, Subramanian S. Thermodynamics of protein association reactions: forces contributing to stability. *Biochemistry.* (1981) 20:3069–102. doi: 10.1021/bi00514a017

48. He Z, Xu M, Zeng M, Qin F, Chen J. Interactions of milk α- and β-casein with malvidin-3-O-glucoside and their effects on the stability of grape skin anthocyanin extracts. *Food Chem.* (2016) 199:314–22. doi: 10.1016/j.foodchem.2015.12.035

49. Zhang R, Han Y, McClements DJ, Xu D, Chen S. Production, characterization, delivery, and cholesterol-lowering mechanism of phytosterols: a review. *J Agric Food Chem.* (2022) 70:2483–94. doi: 10.1021/acs.jafc.1c07390

50. Jilie K, Shaoning Y. Fourier transform infrared spectroscopic analysis of protein secondary structures. *Acta Biochim Biophys Sin.* (2007) 39:549–59. doi: 10.1111/j.1745-7270.2007.00320.x

51. Wang C, Jiang L, Wei D, Li Y, Sui X, Wang Z, et al. Effect of secondary structure determined by FTIR spectra on surface hydrophobicity of soybean protein isolate. *Proc Eng.* (2011) 15:4819–27. doi: 10.1016/j.proeng.2011.08.900

52. Li LJ, He MY, Wang N, Li MD, Wu CL, Li Y, et al. Spectroscopic analysis of the effect of vitamin B-12-soy protein isolate on the soy protein isolate structure. *J Mol Liquids.* (2021) 325:115148. doi: 10.1016/j.molliq.2020.115148

53. Litvinov RI, Faizullin DA, Zuev YF, Weisel JW. The α-helix to β-sheet transition in stretched and compressed hydrated fibrin clots. *Biophys J.* (2012) 103:1020–7. doi: 10.1016/j.bpj.2012.07.046

54. Jung C. Insight into protein structure and protein-ligand recognition by Fourier transform infrared spectroscopy. *J Mol Recognit.* (2000) 13:325–51. doi: 10.1002/1099-1352(200011/12)13:6<325::AID-JMR507>3.0.CO;2-C

55. Zhao Y, Wang X, Li D, Tang H, Yu D, Wang L, et al. Effect of anionic polysaccharides on conformational changes and antioxidant properties of protein-polyphenol binary covalently-linked complexes. *Process Biochem.* (2020) 89:89–97. doi: 10.1016/j.procbio.2019.10.021

56. Gu F-L, Kim JM, Abbas S, Zhang X-M, Xia S-Q, Chen Z-X. Structure and antioxidant activity of high molecular weight Maillard reaction products from casein–glucose. *Food Chem.* (2009) 120:505–11. doi: 10.1016/j.foodchem.2009.10.044

57. Dareini M, Amiri Tehranizadeh Z, Marjani N, Taheri R, Aslani-Firoozabadi S, Talebi A, et al. A novel view of the separate and simultaneous binding effects of docetaxel and anastrozole with calf thymus DNA: experimental and *in silico* approaches. *Spectrochim Acta A Mol Biomol Spectrosc.* (2020) 228:117528. doi: 10.1016/j.saa.2019.117528

58. Li R, Cui Q, Wang G, Liu J, Chen S, Wang X, et al. Relationship between surface functional properties and flexibility of soy protein isolate-glucose conjugates. *Food Hydrocoll.* (2019) 95:349–57. doi: 10.1016/j.foodhyd.2019.04.030

59. Feng J, Schroën K, Fogliano V, Berton-Carabin C. Antioxidant potential of non-modified and glycated soy proteins in the continuous phase of oil-in-water emulsions. *Food Hydrocoll.* (2021) 114:106564. doi: 10.1016/j.foodhyd.2020.106564

60. Gao HX, Liang HY, Chen N, Shi B, Zeng WC. Potential of phenolic compounds in *Ligustrum robustum* (Rxob.) blume as antioxidant and lipase inhibitors: multi-spectroscopic methods and molecular docking. *J Food Sci.* (2022) 87:651–63. doi: 10.1111/1750-3841.16020

61. Simayi J, Nuermaimaiti M, Wumaier A, Khan N, Yusufu M, Nuer M, et al. Analysis of the active components and mechanism of Shufeng Jiedu capsule against COVID-19 based on network pharmacology and molecular docking. *Medicine.* (2022) 101:e28286 doi: 10.1097/MD.0000000000028286

62. John H, Chandra P, Giri SK, Sinha LK. Effect of processing methods on 11S/7S protein and nitrogen solubility index of soy protein isolate. *J Instit Eng Series A.* (2021) 102:989–94. doi: 10.1007/s40030-021-00564-7

63. Pan MZ, Meng XJ, Jiang LZ, Yu DY, Liu TY. Effect of cosolvents (polyols) on structural and foaming properties of soy protein isolate. *Czech J Food Sci.* (2017) 35:57–66. doi: 10.17221/35/2016-CJFS

64. Guzey D, McClements DJ, Weiss J. Adsorption kinetics of BSA at air–sugar solution interfaces as affected by sugar type and concentration. *Food Res Int.* (2003) 36:649–60. doi: 10.1016/S0963-9969(03)00004-8

65. Guzey D, McClements DJ. Impact of electrostatic interactions on formation and stability of emulsions containing oil droplets coated by β−lactoglobulin-pectin complexes. *J Agric Food Chem.* (2007) 55:475–85. doi: 10.1021/jf062342f

66. Jiang L, Chen S, Li Y, Wu C, Wang J, Zhang Z, et al. Effects of complexation with anthocyanin on the structural and functional properties of denatured soybean protein. *Food Sci.* (2018) 39:20–7.

Zein-based nano-delivery systems for encapsulation and protection of hydrophobic bioactives: A review

Xiaojia Yan[1], Moting Li[1], Xingfeng Xu[2], Xuebo Liu[1] and
Fuguo Liu[1]*

[1]College of Food Science and Engineering, Northwest A&F University, Xianyang, China, [2]College of
Food Science and Engineering, Qingdao Agricultural University, Qingdao, China

Zein is a kind of excellent carrier materials to construct nano-sized delivery systems for hydrophobic bioactives, owing to its unique interfacial behavior, such as self-assembly and packing into nanoparticles. In this article, the chemical basis and preparation methods of zein nanoparticles are firstly reviewed, including chemical crosslinking, emulsification/solvent evaporation, antisolvent, pH-driven method, etc., as well as the pros and cons of different preparation methods. Various strategies to improve their physicochemical properties are then summarized. Lastly, the encapsulation and protection effects of zein-based nano-sized delivery systems (e.g., nanoparticles, nanofibers, nanomicelles and nanogels) are discussed, using curcumin as a model bioactive ingredient. This review will provide guidance for the in-depth development of hydrophobic bioactives formulations and improve the application value of zein in the food industry.

KEYWORDS

zein, self-assembly, nanoparticle, delivery, curcumin

Introduction

Zein is the main storage protein in maize and accounts for 30%–60% of total protein content (1). It contains more than 50% of non-polar amino acids, including leucine, proline, alanine, phenylalanine, valine and isoleucine, but lacks basic and acidic amino acids (2). The unbalance of amino acid composition leads to the low nutritional value of zein. However, zein readily self-assembles into various structures depending on the solvents and the processing conditions, and it has been extensively studied in terms of encapsulating and delivering bioactive ingredients, which can be well–reflected in the yearly increase in number of publications related to the terms "zein & encapsulation" and "zein & delivery", as shown in Figure 1. About half of the publications on zein are related to research for encapsulation and delivery over the past 3 years.

GRAPHICAL ABSTRACT
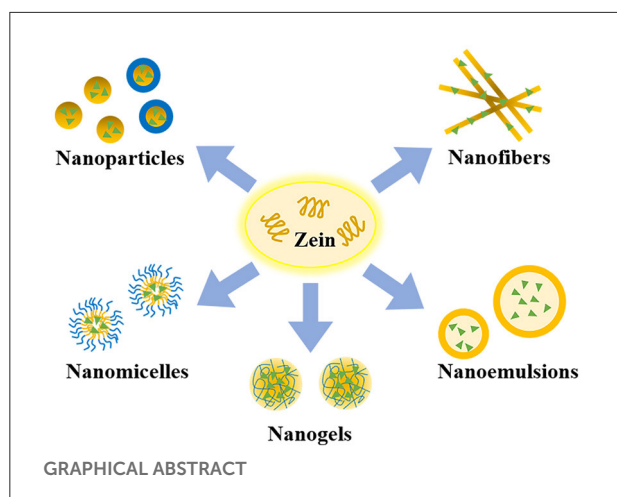
In the past two decades, researchers have successively proposed that the construction of nano-sized delivery systems to encapsulate active ingredients can maximize their health effects, which is mainly attributed to (i) the high specific surface area of nanocarriers can increase the solubility and dissolution rate of actives; (ii) its nanoscale size enables the actives to circulate in the system for a longer time, improves actives distribution in the body as well as allows targeted release and increases biofilm permeability (3). Based on this, the solubility and bioavailability of hydrophobic active ingredients can be effectively enhanced with the help of nanocarriers. Common nano-sized delivery systems include nanoparticles, nanofibers, nanomicelles, solid lipid nanoparticles and nanoemulsion. Biopolymers are alternative materials for constructing nanocarriers because of their good biocompatibility, and Zein-based nano-sized delivery systems loaded with hydrophobic active ingredients have been constructed. For example, maytansine-loaded zein nanoparticles enhanced tumor targeting for non-small cell lung cancer (A549 cells) and reduced the toxic side effects of maytansine (4). Curcumin-loaded zein nanofibers showed enhanced antibacterial activity and the inhibition efficiency increased with the increase of curcumin content (5). Dispersibility of curcumin encapsulated in whey protein isolate (WPI)-zein composite nanoparticles was significantly improved (6). Zein-hyaluronic acid composite nanoparticles prepared through layer-by-layer assembly technique effectively improved the light, thermal and storage stability of curcumin and quercetagetin (7). With the help of nano-delivery system, the water solubility and chemical stability of encapsulated lutein were significantly improved, and the bioaccessibility (32.11%) was much higher than that of free lutein (16.21%) (8). In addition, many studies on hydrophobic active ingredients, such as quercetin, resveratrol, rutin, β-carotene, Vitamin D3, retinol encapsulated in zein-based nanocarriers have been reported (9–14).

In this review, we mainly introduce the chemical basis of zein and various preparation methods of zein nanoparticles, and summarize recent reports on zein-based composite nanoparticles, using curcumin as a model bioactive ingredient. In addition to zein nanoparticles, other types of zein delivery systems are also discussed, including nanofiber, nanomicelles, etc.

Chemical basis of zein

Composition and general properties

According to the difference in molecular weight and solubility, zein can be divided into four categories: α-, β-, γ-, δ-zein. Among them, α-zein accounts for 70%–85% of the total zein content, with a molecular weight of 19–22 kDa, and it is soluble in 70%–95% ethanol aqueous solution. β-zein is composed of α-zein linked by disulfide bonds, so its molecular weight is high. It is soluble in 60%–90% ethanol aqueous solution (15). Generally, Except for a certain concentration of alcohol solution, zein can also be dissolved in alkaline solutions with pH ≥ 11.5 (16, 17), and solutions with high concentration urea and other reducing agents (18). Although zein has poor water solubility, unbalanced amino acid composition and low nutritional value, its unique solubility makes it easy to self-assemble into zein micro/nanoparticles. Therefore, zein is an ideal carrier material for hydrophobic bioactive ingredients. It is also more anti-digestive than other proteins, which is one of the advantages as an oral delivery carrier.

Molecular structure

The self-assembling mechanism of zein is closely related to its structure. Several molecular models for the tertiary structure of α-zein have been proposed, including cylinder model, ribbon-like model, hairpin model and superhelical structural model (19).

The cylinder model is based on analysis of the repeat sequence units and α-helix content of zein dissolved in 70% methanol aqueous solution (20). There are 50%–60% α-helices in zein molecules, and the rest are turn and random coils. Each primary structure of a zein molecule consists of 20 amino acid residues repeated 9 times. Analysis of the physical properties (hydration potential, polarity, turn, helix formation tendency) indicates that the amino acid sequence containing repeat fragments consists of α-helixes with turn regions on both sides. The helix regions are composed of numerous polar amino acids and several hydrophobic amino acid residues, and the turn regions are rich in glutamine. In the structural model of zein, nine adjacent, topologically antiparallel homologous helices
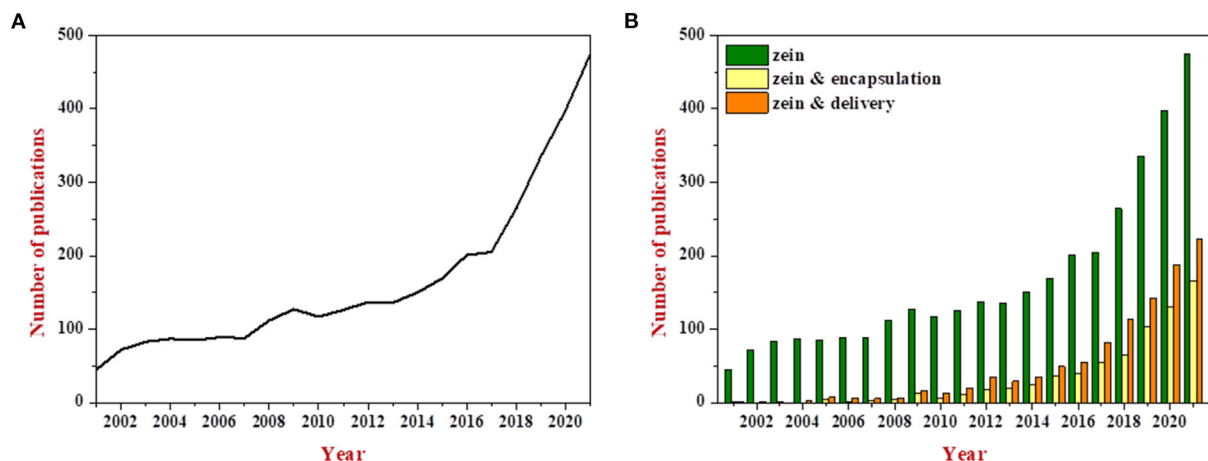
FIGURE 1
Evolution of number of publications related to the term "zein" during the years 2001 to 2021 **(A)**; Comparison of the number of publications related to the terms "zein" vs. "zein & encapsulation" and "zein & delivery" **(B)**. All the data were obtained through the Web of Science system.

cluster form a cylindrical surface connected by polar glutamine residues (Figure 2A). The structure is stabilized by van der Waals force and intramolecular and intermolecular hydrogen bonds. Glutamine-rich turns are located between the helical structures and the cylindrical cap, facilitating the intermolecular stacking into a plane by the interaction between the side chains. The structure model can explain the dense, membrane-enveloped deposits formed by proteins in maize seeds.

To modify the cylinder model, the structure of zein dissolved in 70% ethanol aqueous solution was further analyzed by small angle X-ray scattering (SAXS) (21). In the ribbon-like model, zein is composed of 9–10 adjacent, topologically antiparallel homologous helices clustered, presenting a slender rectangular prism structure with an axial ratio of 6:1, and its three dimensions are 13, 3 and 1.2 nm (Figure 2B). The two-dimensional intermolecular hydrophobic aggregation makes the side chains in the helixes accumulate into a hydrophobic surface, forming a structure with hydrophilic ends and hydrophobic sides, which greatly improves the structural stability of α-zein. The two-dimensional ribbon-like model has been widely used to explain the different orientations of zein molecules on hydrophilic/hydrophobic surfaces and the self-assembly of zein from single molecule to nanoparticles.

In addition, the hairpin model based on nuclear magnetism resonance (NMR), SAXS and Fourier transform infrared spectroscopy (FTIR) is also composed of a series of helix structures as shown in Figure 2C (22). Different from the above two models, these helix structures are connected and extended in the form of rings, sheets or loops, so zein can fold or extend in other ways in different solvent environments. At the same time, it is thought to be related to the fibrillation ability of zein.

FIGURE 2
Proposed 3-D structural models of α-zein. Cylindrical model **(A)**; ribbon-like model (22 kDa) **(B)**; hairpin model (19 kDa) **(C)**; super helical structural model (19 kDa) **(D)**. "R" means repeat unit. Reprinted from (19) with permission from Elsevier.
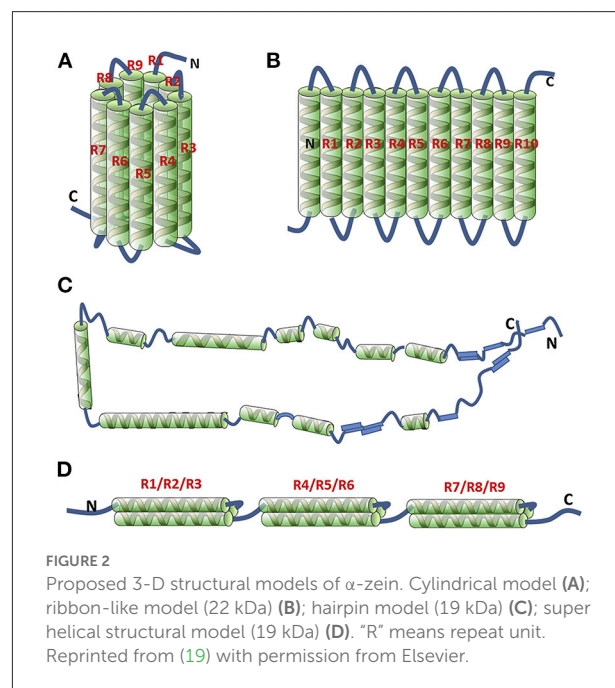
In 2006, a model consisting of three superhelix structures was built by using three antiparallel helix segments connected by a glutamine-rich turn, as shown in Figure 2D (23).

Despite the differences in the molecular models above, it is generally believed that α-zein is a slender conformation formed by a large number of α-helix structures. The three-dimensional structure of zein is affected by different factors, especially solvent type (24). Compared with the folded structure model, the slightly larger sizes of α-zein in acetic acid, 70% and

80% ethanol aqueous solutions indicate that α-zein structure is locally unfolded in these solutions. The CD data demonstrate the secondary structure of α-zein do not change significantly, either in acetic acid or in 70% and 80% ethanol aqueous solutions, which may be because local unfolding mostly occurs in the coil region. The size of α-zein in acetic acid is larger than that in ethanol aqueous solutions, indicating that the expansion and swelling degree of α-zein is greater in the presence of acid. With the increase of zein concentration, α-zein dissolved in acetic acid behaves like polyelectrolyte dissolved in an excellent solvent, and its particle size decreases slightly. Moreover, α-zein dissolved in ethanol aqueous solutions behaves like polymer dissolved in θ solvent (alcohol solution). The conformation and dissolution behaviors of α-zein both differ among different solvents, which may be attributed to three causes: (i) According to the similarity-intermiscibility theory, the dissolution behavior of α-zein should be related to the polarity of solvent. It is known that the hydrophilic index of water, acetic acid and ethanol is 9.0, 6.2, and 5.2 respectively referring to the solvent miscibility table, indicating the hydrophilic index is very close between acetic acid and 70% or 80% ethanol aqueous solutions. The hydrophilic index of α-zein with a molecular weight of 19 and 22 KDa is 4.70 and 4.80 respectively (25), so the similarity-intermiscibility theory should not be the main reason accounting for the difference of solvent quality. (ii) The differences can be related to the hydrophilicity/hydrophobicity of the protein surface. Partial unfolding of zein may change the solvent accessible area of zein surface and hydration. As local unfolding of α-zein is severer in acetic acid, the solvent accessible area is larger, thus promoting the dissolution of α-zein. (iii) Protein surface protonation can also inhibit protein aggregation. Protonation of zein reduces hydrophobicity and improves stability of zein solution through the long-range electrostatic repulsion induced by the positive charge on the protein surface and the existence of acetic acid solvation layer. Because -COOH in acetic acid releases free hydrogen ions more easily than -OH in ethanol, zein in acetic acid is more prone to protonation.

Fabrication of zein-based nanoparticles and its challenges

The construction of zein particles based on unique solubility behavior of zein can be traced back to the 1990s. Zein particles were used as coating materials first in pharmaceutical industry, and then in drug delivery system (26). The preparation methods of zein particles have become rich and various, and can be broadly summarized as chemical crosslinking, antisolvent precipitation, supercritical antisolvent, antisolvent dialysis, pH driving, spray drying, and electrohydrodynamic atomization. Advantages and disadvantages of these methods have been summarized in Table 1.

TABLE 1   Advantages and disadvantages of the methods for preparing zein nanoparticles.

Methods	Advantages	Disadvantages
Chemical crosslinking	Load with hydrophobic actives	Produce micro-scale particles
		Certain safety hazard caused by introduction of toxic crosslinking agent
Emulsification/solvent evaporation	Encapsulate hydrophobic, hydrophilic and amphiphilic actives	Produce micro-scale particles
Antisolvent precipitation	Low cost	Utilization of numerous alcohols
	Easy to operate	Discontinuous and unscalable process
Supercritical antisolvent	Easy to operate	Toxic solvent residues
	Continuous and large-scale production	High cost, specific equipment required
	Produce particles with controllable size and shape	
	Friendly to temperature-sensitive actives	
Antisolvent dialysis	Low cost	Time-consuming
	Optimization of antisolvent precipitation	
pH-driven	Low cost	Susceptibility of encapsulated actives to strong alkaline
	Easy to operate	
	Avoid of organic solvents	
Electrohydrodynamic atomization	Reduce preparation time	Specific equipment required
	Production of uniform particles	

Chemical crosslinking

Glutaraldehyde mediated crosslinking reaction between zein and other molecules (e.g., proteins, polysaccharides, polyphenols) or zein molecules themselves is one of the early methods for zein particles formation. This method originated in the 1980s (27, 28). Glutaraldehyde is a colorless and transparent oily liquid with a pungent odor. It is a commonly homo-bifunctional crosslinking agent that combines with phenol, imidazole, hydroxyl and amino through the aldehyde groups at both ends of its molecule. The crosslinking reaction between molecules endows zein a stronger aggregation trend when exposed to water solutions owing to the distinct surface hydrophobicity of zein, and increases its molecular weight,

which promotes the self-assembly of zein into particles. However, zein particles formed by chemical crosslinking are usually micro-scale. The general process for the formation of zein particles loaded with hydrophobic active ingredients (e.g., curcumin) by chemical crosslinking was shown in Figure 3A. Curcumin as a model bioactive ingredient is firstly dissolved in an ethanol aqueous solution, then mixed with a small amount of a glutaraldehyde aqueous solution, and finally zein is added to cause a cross-linking reaction, resulting in the formation of internally encapsulated curcumin particles. Noticeably, the water volume accompanying glutaraldehyde aqueous solution added must be strictly controlled because the presence of a large amount of water will lead to the aggregation and precipitation of zein, thereby inhibiting the crosslinking efficiency. After the reaction, it was highly diluted with polyvinylpyrrolidone (PVP) solution and centrifugation, followed by ultrasound and freeze-drying to obtain zein particles.

There are some defects in the chemical crosslinking method. First, crosslinking reaction may produce adverse effects on the activity of ingredients encapsulated inside zein particles. Secondly, chemical crosslinking involves toxic agents, such as glutaraldehyde, which has a strong irritant effect on eyes, skin and mucous membrane, causing certain safety risks for the production process and the final products. Therefore, it is imperative to develop alternative green, safe and environmental-friendly chemical crosslinking agents.

Emulsification/solvent evaporation

With emulsification/solvent evaporation, the zein-ethanol aqueous solution and the oil phase containing miscible surfactants are emulsified to form the water-in-oil emulsion as a template for carrier preparation. The internal aqueous phase of the emulsion can be solidified into rigid particles by solvent evaporation. Crosslinking agents (e.g., glutaraldehyde) are added before solvent evaporation to obtain crosslinked particles, which can moderately reduce the size of particles. The operation process of emulsification/solvent evaporation is shown in Figure 3B. Briefly, curcumin as a model active ingredient and zein are co-dissolved in an ethanol aqueous solution, emulsified with oil phase, and then a crosslinking agent is added into the emulsion. With the evaporation of ethanol, zein and curcumin inside emulsion droplets are subsequently solidified into rigid crosslinked particles (29). Finally, zein particles loaded with curcumin are obtained by filtration and removal of residual oil using suitable solvents. Emulsification/solvent evaporation method has been used to prepare zein particles loaded with aceclofenac, and their particle size ranges from 30 to 300 μm, which is suitable for oral administration.

Antisolvent methods

Antisolvent precipitation method

Antisolvent precipitation, also known as liquid-liquid dispersion or phase separation, has been widely used for the preparation of zein nanoparticles by changing the polarity of solvents surrounding zein. As shown in Figure 3C, zein and curcumin are firstly dissolved in an ethanol aqueous solution (60%–95%, high solubility), which is then poured into or added dropwise into numerous water (as antisolvent) under magnetic stirring, so that the ethanol concentration decreased rapidly, resulting in supersaturation and precipitation of zein. Combined with the self-assembly characteristics, zein molecules aggregate into particles, and most of the curcumin spontaneously enters the hydrophobic core of zein particles. Subsequently, the ethanol is removed by rotary evaporation. Solvent polarity seriously affects the properties of zein particles. Ethanol, methanol and isopropanol can be used to prepare zein nanoparticles. The size of zein particles prepared from 80% alcohol solutions ranks by the alcohol type as ethanol>isopropanol>methanol, which may be due to the difference of solvent evaporation rate and zein solubility (30). In addition to the alcohol type, the initial concentration of alcohol and zein, the shear rate, the ratio of alcohol to water, pH, mixing mode and other added substances all can affect the particle properties.

Supercritical antisolvent method

In addition to using water as an antisolvent for the preparation of zein nanoparticles, supercritical fluid CO_2 is also possible, due to its immiscibility with most polymers. The simple processing procedure of supercritical antisolvent method is that the co-solvent in atomized droplets is extracted by supercritical CO_2 after the feedstock is continuously injected into supercritical CO_2. Since most of the polymers are insoluble in CO_2, the solubility of polymers decreases gradually, thus forming nuclei and gradually growing into nanoparticles or microparticles (31). The technology requires that the polymer be dissolved in one or more solvents (co-solvent), and these solvents can be miscible with supercritical CO_2. Advantage of supercritical antisolvent method is that the critical temperature (31.1°C) and pressure (7.38 MPa) of CO_2 can be easily achieved, and it is friendly to thermo-sensitive bioactives, so that they would not be degraded in the process of particle formation. As reported, supercritical CO_2 has been used to form a micro/nano-particle delivery system for foods (32), so as to improve the physicochemical properties and health effects of active ingredients. Zein particles formed by supercritical CO_2 antisolvent method were used to encapsulate lysozyme, which improved the antibacterial activity of lysozyme (33). Lutein/zein nanoparticles prepared by supercritical CO_2 realized the controlled release of lutein (34).

Zein concentration, CO_2 flow rate, alcohol type and concentration all affect the formation of zein particles. It is
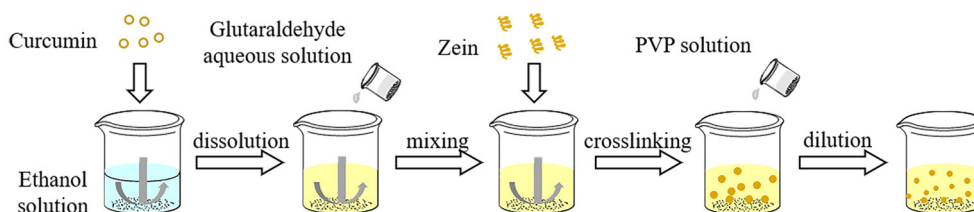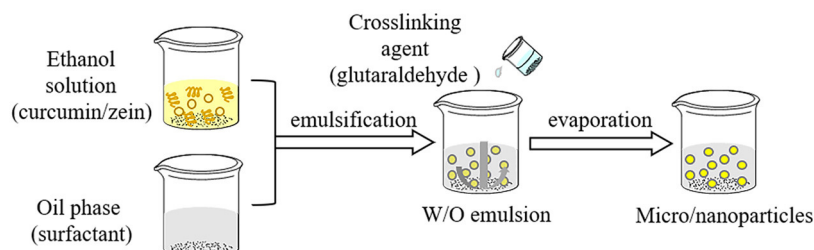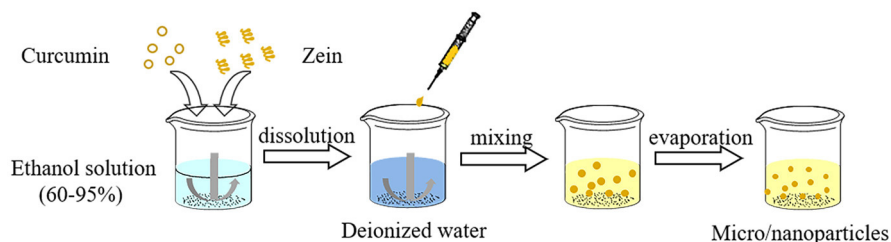
FIGURE 3
Preparation process of zein particles by chemical crosslinking **(A)**, emulsification/solvent evaporation **(B)** and antisolvent precipitation **(C)**.

generally believed that large size particles are easily formed at high polymer concentrations due to the high viscosity of the solution, which further complicates the solution atomization. Meanwhile, the growth rate of particles is accelerated at high polymer concentrations. The increase of CO_2 flow rate can promote the particle formation. In addition, the polarity of solvent affects the extraction efficiency of supercritical CO_2, thus affecting the formation of zein particles. As for higher-polarity alcohols (methanol>ethanol>isopropanol), the extraction efficiency of supercritical CO_2 (non-polar solvent) is lower, and the solidification rate of zein is slower. For example, zein dissolved in 90% methanol aqueous solution did not form particles by supercritical antisolvent technology, while zein dissolved in 90% isopropanol aqueous solution produced smaller particles than that dissolved in 90% ethanol aqueous solution. Reducing the water content of zein co-solvent is also helpful to supercritical CO_2 extraction (mass transfer process)

and speeds up the solidification of zein, thereby forming smaller and more uniform particles (31). It can be explained as follows: as the polarity of co-solvent increases (water or more polar alcohols are added), the mass transfer rate slows down due to the poor compatibility between CO_2 and co-solvent. Particles are formed when the polymer precipitation kinetics can overcome the mass transfer limitation. The particle size of zein can be adjusted from micron to nanometer by changing the type and concentration of alcohol.

Supercritical antisolvent technology with CO_2 has the advantages of mild operating temperature, friendly environment, simple operation and easy control. However, it is difficult to produce uniform zein nanoparticles unless 100% methanol is used as solvent and supercritical CO_2 is loaded at a high flow rate. In this case, it will increase production costs and may cause toxicity due to residual organic solvents.

FIGURE 4
Schematic representation of antisolvent dialysis method for the obtaining of zein micro- and nanoparticles. At time 0 h **(A)** and after 12 h of the process **(B)**.
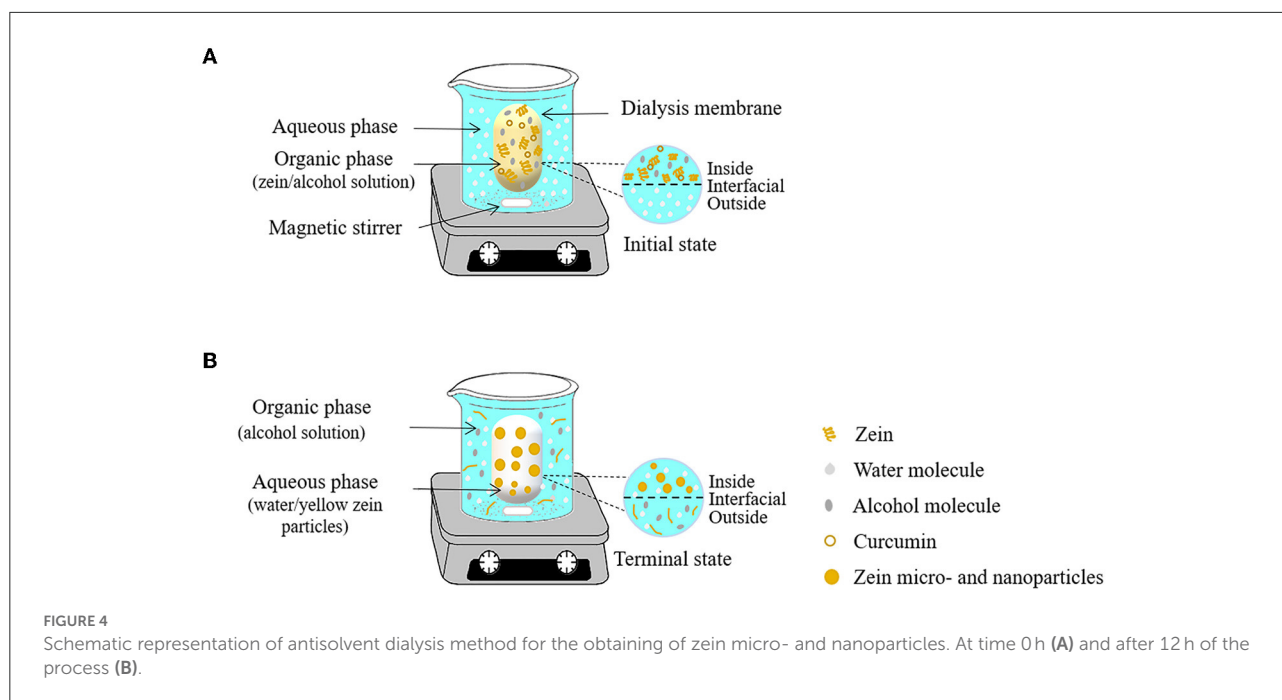
Antisolvent dialysis method

Antisolvent dialysis is a variant of antisolvent precipitation. Firstly, the biopolymer is miscible with the first solvent (organic phase) to form mother liquid. Then the first solvent is replaced by another solvent (aqueous phase) which is immiscible with the polymer to form a colloidal dispersion (35). The preparation of zein particles by antisolvent dialysis is mainly based on changes in polymer concentration gradient and solvent polarity. As shown in Figure 4, the dialysis bag containing an alcohol solution dissolving zein and curcumin is firstly placed in the aqueous phase, and then the organic solvent gradually diffused into the external aqueous phase through the semipermeable membrane. With this process, the change of the polar environment of zein induces the formation of zein particles. Compared with the antisolvent precipitation method, the advantage of the antisolvent dialysis method is that it only needs one-step to realize the formation of particles and solvent replacement simultaneously. Unlike antisolvent precipitation, additional operations (rotary evaporation) are required to remove organic solvents after particle formation.

pH-driven method

Although the preparation of zein nanoparticles by antisolvent methods is simple and efficient, the method involves a large number of organic solvents, which would bring certain safety risks (flammability) and increase the cost due to the removal of alcohols after the particle formation. To solve these problems, Pan and Zhong innovatively prepared zein nanoparticles based on the solubility of zein in alkaline environment (pH $\geq$ 11.5) and insolubility in neutral aqueous solution, namely pH driven method, also known as pH cycling or pH transition method (36). Briefly, zein is dissolved in deionized water at pH 7.0, then the pH is adjusted to 12 with NaOH, and then adjusted back to pH 7.0 by HCl. During the pH changing from alkalinity to neutrality, zein is protonated and its solubility decreases gradually and aggregates to form particles. In this process, hydrophobic ingredients are encapsulated inside the particles. In the past few years, the pH-driven method has been widely used to prepare zein composite nanoparticles, including zein-rhamnolipid (37), zein-NaCas (38) and zein-WPI (39) composite nanoparticles. Compounding with other hydrophilic or charged food-grade biopolymers can adjust the aggregation behavior of single zein nanoparticles, thereby improving the stability of zein nanoparticles.

Electrohydrodynamic atomization (EHDA)

EHDA, also known as electrospraying, has been used to prepare inorganic nanoparticles, drug nanoparticles and polymer drug delivery nanoparticles. The technique relies on the separation of liquids into tiny charged droplets under an electric field. The advantage of this technology is that it can produce spherical particles or fibrils with uniform morphology. The morphology and size of particles are seriously affected by processing parameters (e.g., polymer concentration, flow rate, voltage) (40). With the change of processing parameters, the particle size can change from hundreds of microns to several

nanometers. The particle size is gradually enlarged with the increase of zein concentration (2.5–15%) (40).

Among the above methods, antisolvent precipitation and supercritical antisolvent method have attracted the attention of researchers owing to their simple operation and large-scale production potential.

Zein-based nanoparticles as delivery system for hydrophobic bioactives

A variety of bioactive substances derived from plants, animals and microorganisms, such as the polyphenols (curcumin, resveratrol, and quercetin), and carotenoids (lycopene, lutein, astaxanthin), and vitamins A, D, E, K, have the wide range of health effects such as antioxidant, anti-inflammatory, anti-cancer and chronic disease prevention. However, these bioactive substances are susceptible to oxidation, crosslinking, or degradation in food processing, storage and digestion, and their absorption and utilization are limited because they are mostly insoluble in water. In order to improve the compatibility of these hydrophobic bioactives with food matrices and to ensure their stability during food processing and high bioavailability after digestion, it is necessary to add them to foods with the help of nano-sized delivery systems with good biocompatibility. Zein is an extremely promising carrier material for delivering hydrophobic bioactivity due to its excellent self-assembly characteristic, which makes it easy to form nanoparticles.

General properties of zein-based nanoparticles

As an amphiphilic prolamin, zein with distinct hydrophobic and hydrophilic domains can self-assemble into nanoparticles, which have been extensively exploited in encapsulation and delivery applications for hydrophobic bioactives. Here, curcumin is used as a model hydrophobic active ingredient to discuss the effect of different zein-based nanoparticles on physicochemical and functional properties of hydrophobic bioactives. Zein nanoparticles (ZNPs) can effectively improve the stability of bioactives and facilitate their targeted delivery. Through antisolvent precipitation, the stability of curcumin encapsulated in ZNPs was improved at all physiologically relevant pH and UV irradiation (30). Moreover, the system has good mucoadhesion property *in vitro*, and the retention rate of curcumin was more than 60% when it was retained in the gastrointestinal tract for 150 min. The size of curcumin-loaded ZNPs prepared by electrofluid-driven atomization was within 175 to 900 nm, and increased with the increase of zein concentration. After 3 months of storage (23 °C, 43% relative humidity in the dark), no significant changes in the morphology of the nanoparticles or curcumin content were found. These

nanoparticles showed good dispersion and coloring capacity in semi-skimmed milk compared to commercial curcumin (40). Furthermore, curcumin-loaded zein nanospheres formulated by antisolvent precipitation method improved liver targeting efficiency and antifibrotic activity of curcumin in a mouse model of carbon tetrachloride-induced liver fibrosis, compared with free curcumin (41).

Zein peptides nanoparticles

Due to the high surface hydrophobicity of zein and its isoelectric point of 6.2, ZNPs without any stabilizer tend to aggregate at neutral pH (42). Therefore, their dispersion stability should be optimized for the delivery application of ZNPs. Proline-rich zein contains a large number of amphiphilic peptides (43). Amphiphilic zein peptide is also a potential delivery system due to its small size and self-assembly property in water solution (43–45). Under chemical or enzymatic treatments, glutamine and asparagine residues of zein undergo a deamidation reaction, which can increase the hydrophilicity of zein (46). Enzymatic method is desirable to modify zein structure. Transglutaminase (TGase), protease, peptidoglutaminase (PGase), glutaminase, and protein glutaminase (PG) can be used for protein deamidation (46). Alcalase-degraded zein peptides tend to self-assemble into micelles, leading to strong hydrophobic complexation with curcumin (44). Without any stabilizer, curcumin-loaded zein peptide nanoparticles exhibited a monodisperse size distribution (<50 nm) and enhanced water solubility (above 8,200-fold vs. free curcumin in water). In addition, this system showed improved storage stability, and more than 60% of curcumin was retained after 72 h of storage at ambient conditions (46). The deamidated zein peptide, produced by alkaline hydrolysis for 36 h, was dissolved together with curcumin in an alkaline aqueous solution and then acidified to induce the co-assembly of the peptide and curcumin to form complex nanoparticles (47). The nanoparticles displayed a curcumin loading capacity of 31.9%, *in vitro* bioaccessibility of 75%, and a significant antioxidant effect after oral administration in mice.

Zein-based binary composite nanoparticles

The introduction of a biopolymer into the preparation process of ZNPs has been a prominent way to improve the stability and endue new functional properties. The resultant zein composite nanoparticles provide greater encapsulation efficiency (EE), better protection of the encapsulated bioactives from degradation and better controlled release during digestion than ZNPs alone. Zein-based binary composite nanoparticles fabricated with sodium caseinate (48, 49), WPI (6), chitosan (50, 51) and its derivative (52), pectin (53, 54), hyaluronan (55),

gum Arabic (56), and carrageenan (57) have been constructed to improve their physicochemical and functional properties.

The addition of amphiphilic protein can reduce the surface hydrophobicity of ZNPs, and enhance their electrostatic and steric repulsion. Zein-caseinate composite nanoparticles were fabricated by a low-energy liquid-liquid dispersion method (48). It was found that the solubility, thermal and UV irradiation stability of encapsulated curcumin were improved, which may be ascribed to the electrostatic and steric repulsion between the zein particles provided by anionic caseinate. Moreover, the cellular studies showed that zein-caseinate nanoparticles with the same level of curcumin exhibited enhanced bioavailability, compared with free curcumin. In another study, WPI-zein composite nanoparticles were fabricated using the pH-driven method (6). Compared with individual WPI nanoparticles or ZNPs, the WPI-zein composite nanoparticles showed improved physicochemical properties. ZNPs aggregated at pH 7.0 and WPI nanoparticles showed relatively poor resistance against high temperature (80 °C).

Many researches also focus on the effects of polysaccharide on the formation, properties and stability of ZNPs. For instance, water-soluble chitosan derivatives (N-(2-hydroxyl)propyl-3-trimethyl ammonium chitosan chloride, HTCC) with different molecular weight were synthesized and used to prepare zein-HTCC nanoparticles (52). HTCC coating was helpful to obtain high EE of curcumin, and EE was positively correlated with the molecular weight of HTCC due to the longer chain of the HTCC molecule could entrap more curcumin. In addition, zein composite nanoparticles with a unique structure were fabricated with chitosan in step-by-step to enhance the loading space of bioactives (51). Curcumin-zein-resveratrol-chitosan composite nanoparticles appeared as the three-dimensional network structure, which was proved to be an effective carrier for greatly improving the physical-, light-, thermal-, and storage stability of both curcumin and resveratrol. Shellac, a resin secreted by the female lac beetle, is insoluble in water but highly soluble in anhydrous ethanol. Zein-shellac binary nanoparticles provided a stronger encapsulation ability of curcumin. After combining shellac, the EE of curcumin increased from 82.7% to 93.2%. Moreover, zein-shellac nanoparticles exhibited improved photochemical, thermal stability and strong curcumin sustained-release ability (in both PBS and simulated gastrointestinal tract), which were ascribed to compact structure induced by binary complexation between zein and shellac (58).

Furthermore, some surfactants can stabilize ZNPs against aggregation by reducing hydrophobic attraction and increasing electrostatic and steric repulsion. Dai et al. (37) successfully prepared zein-rhamnolipid composite nanoparticles using a pH-driven method, which exhibited good stability from pH 3 to 8 and at low salt concentrations (0–100 mM NaCl, pH 7). Nevertheless, they were unstable under extremely acidic conditions or at high ionic strengths due to the suppression of these electrostatic forces. Interestingly, ZNPs stabilized by

different levels of surfactants may have different structures, which affect EE of curcumin and related physicochemical properties of nanoparticles. At a relatively low level of lecithin, the nanoparticles tended to aggregate due to embedded alkyl chains of lecithin in the hydrophobic region of zein. With the further increase in lecithin concentration, the strong hydrophobic interaction between the alkyl chain of lecithin with zein and curcumin led to compact structure and smaller size of zein-lecithin composite nanoparticles (59). There are two distinct binding behaviors of curcumin in ZNPs depending on the surfactant concentration (60). At Tween 20 concentration below 0.2 g/L, curcumin was bound in the hydrophobic cavities of the ZNPs; at Tween 20 concentration above 0.2 g/L, some curcumin was also bound in the micellar-like Tween 20 aggregates of the particles.

Cross-linking is another option that may improve the stability and delivery potentials of ZNPs. It is known that zein has some resistance to acid environment and pepsin digestion, but is susceptible to pancreatic enzymes. In terms of the stability under simulated gastric and intestinal conditions, tannic acid cross-linked ZNPs were more resistant against digestion by pancreatin (which was able to degrade α-zein dimers) than non-crosslinked ones (61).

Zein-based ternary composite nanoparticles

Although zein-based binary composite nanoparticles show desirable stability, many reports indicate that the development of ternary composite nanoparticles may be a more promising means of encapsulating, protecting and delivering bioactives. Zein/polysaccharide/surfactant ternary composite nanoparticles were prepared by antisolvent co-precipitation recently. The encapsulation efficiency of curcumin in zein-propylene glycol alginate-rhamnolipid (or lecithin) ternary composite nanoparticles was higher than that in pure zein or binary zein-propylene glycol alginate nanoparticles. Moreover, the presence of the surfactants significantly improved bioaccessibility of curcumin (62). In another study, ternary composite nanoparticles consisting of zein, chondroitin sulfate (CS) and sophorolipid enhanced EE, chemical stability, aqueous solubility and anticancer activity *in vitro* against HepG2, MCF-7 and HeLa cells of curcumin, compared with ZNPs and zein-CS nanoparticles (63), which were attributed to amphiphilic Spl. Its hydrophilic disaccharide sophorose could produce hydrogen bonding with –OH of CS, and its lipophilic long monounsaturated fatty acid chain could absorb on the hydrophobic region of zein by hydrophobic interaction. Zein/polysaccharide/protein ternary composite nanoparticles have also been extensively explored. The electrostatic biopolymer coatings consisting of a mixture of sodium alginate (70%) and fish gelatin (30%) improved the

pH, salt, and thermal stability of ZNPs, and produced a high bioaccessibility of curcumin *in vitro* and antioxidant capacity (64). The re-dispersibility of the freeze-dried nanoparticles was enhanced due to hydrophilic sodium caseinate and sodium alginate adsorbed sufficiently on the surface of the ZNPs, resulting in a decrease in zein surface hydrophobicity (65).

In the ternary composite nanoparticles, the type of polysaccharide critically influences the stability of the system. Partial replacement of the pectin (low charge density) with alginate (high charge density) to form the shell in the ternary composite nanoparticles improved aggregation stability at pH 5 to 7 and at high ionic strengths (2,000 mM NaCl), and the encapsulated curcumin exhibited better antioxidant activity (66). In another study, ternary composite nanoparticles composed of zein, hyaluronic acid and chitosan were prepared using the layer-by-layer technique to co-deliver curcumin and piperine, the nanoparticles were able to control the release of the bioactive ingredients in simulated gastrointestinal conditions and protected them from chemical degradation when exposed to UV light, high temperature, or long-term storage by manipulating the number of layers (67). Chitosan with lower molecular weight is a suitable outer coating to protect and control the release rate of both bioactive ingredients during simulated digestion than either medium- or high-molecular weight chitosan. In addition, crosslinking can significantly influence the release sustainability of active ingredients by modifying carrier microstructures (19). Caseinate-zein-pectin composite nanoparticles were prepared *via* a pH- and heating-induced electrostatic deposition, and 1-ethyl-3-(3-dimethyl aminopropyl) carbodiimide and N-hydroxysuccinimide (EDC/NHS) as chemical cross-linkers were used to covalently bridge the protein and polysaccharide layers. The obtained nanoparticles showed improved stability under simulated gastrointestinal conditions (68). Oxidized dextran as a macromolecular crosslinker and coating can also successfully apply to stabilize the zein-caseinate composite nanoparticles, which not only enhanced the colloidal stability of composite nanoparticles but also improved the controlled release rate of curcumin under simulated gastrointestinal conditions (69). We summarize the physicochemical properties of different zein nanoparticles loaded with hydrophobic bioactives consisting of zein with proteins, polysaccharides, polyphenols, and surfactants reported in recent years (Supplementary Table S1, Supporting Information).

Other Zein-based nanocarriers as delivery systems for hydrophobic bioactives

In addition to zein-based nanoparticles detailed above, nanofibers, nanomicelles, nanogels based on zein are excellent candidates as delivery systems for bioactives (Figure 5).

Zein-based nanofibers

Electrospinning is a unique and cost-effective route to prepare nanofibers, and large surface area-to-volume ratio nanofibers can be provided by adjusting the preparation parameters (electrostatic field strength, flow rate, solution concentration, etc.,). Ultrafine zein fluorescence nanofibers loaded with curcumin were developed by electrospinning (70). It was found the diameter of zein nanofibers increased slightly from 250 nm to 300 nm with the increase of the concentration of embedded curcumin (0–10%), the morphology and distribution of nanofibers did not change significantly, and curcumin aggregates were also not found in fibers surfaces, indicating curcumin was well-embedded within the fibers. It was also confirmed in the study of Deng et al. (71) that the embedded bioactive ingredient did not affect the appearance and morphology of nanofibers. However, pure zein nanofibers have poor mechanical properties and solvent resistance (72). Hybrid electrospinning of zein and other biopolymers has been considered as an effective mean to remedy these deficiencies. It has been reported that hybrid electrospinning of zein and gelatin enhanced the mechanical properties of pure zein nanofibers, elongation at break and elastic modulus were up to 87%, 72.1 MPa respectively (73). Additionally, both the glucose cross-linked gelatin/zein nanofibers and zein/tragacanth nanofibers with core-shell structure showed good sustained release properties (71, 74). Therefore, zein-based nanofibers prepared by electrospinning technology could be a potential candidate for delivering hydrophobic bioactives.

In addition, curcumin-loaded zein nanofibers exhibited excellent antibacterial activity, and the inhibition efficiency against food-borne pathogens increased with the increase of curcumin content (75–78). In addition, curcumin-loaded nanofibril films prepared by dispersing electrospun zein into konjac and glucomannan solution exhibited better hydrophobicity, water resistance property and excellent antibacterial activity, which can be used as food packaging materials (38).

Zein-based nanomicelles

Polymer micelles are also important nano-sized delivery systems, formed through spontaneous self-assembly of amphiphilic block copolymers into specific supramolecularly ordered aggregates for improving stability and bioavailability of active ingredients (79). In aqueous solution, polymer self-assembles into a core-shell architecture, in which the hydrophobic segment forms the core and the hydrophilic segment forms the external corona, when the copolymer concentration approaches the critical micelle concentration (80). The hydrophobic active ingredients can be located in the micelle core regardless of inclusion or bonding,
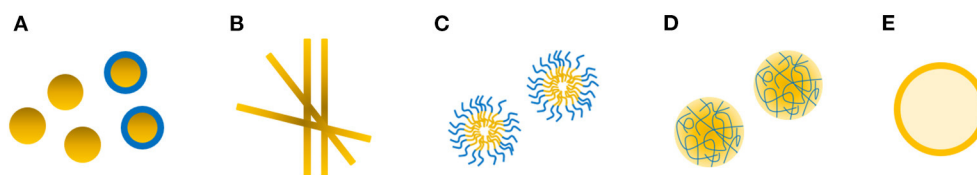
FIGURE 5
Schematic presentation of common zein-based nanosized delivery systems including nanoparticles **(A)**, nanofibers **(B)**, nanomicelles **(C)**, nanogels **(D)**, nanoemulsions **(E)**.

and the hydrophilic shell of the micelles increases the water solubility of the hydrophobic active ingredients. Many amphiphilic materials have been used to synthesize micelles, including synthetic polymers (81–83) and natural polymers (84–86).

Naturally accessible proteins and polysaccharides are attractive alternatives to synthetic polymers due to their good biocompatibility and low cost. Among them, zein with inherent hydrophobic regions have been widely discussed. In a previous study, methoxy polyethylene glycol grafted α-zein micelles (mPEG-g-α-zein) exhibited a sustained release effect of curcumin and low cytotoxicity (87). Although some PEG-modified products have been approved by FDA and other regulatory agencies and successfully used in the clinic, some researchers are still worried about whether it will cause subsequent toxicity and other side effects after long-term accumulation in the body (88). For this reason, zein-lactoferrin micelles were prepared *via* carbodiimide coupling reaction between the primary amine of zein and the carboxyl group of lactoferrin, which greatly enhanced the tumor targeting of the loaded drug (89). The effect could be attributed to: (i) the hydrophobic zein core in micelles had high drug loading; (ii) the hydrophilic lactoferrin shell enhanced the stability of micelles; (iii) lactoferrin provided the tumor targeting (90, 91). Similarly, the hydrophilic polysaccharide chondroitin sulfate (ChS) with the CD44-mediated tumor targeting effect was also used to prepared zein-ChS micelles (92). In addition, superhydrophilic zwitterionic polymer, poly(sulfobetaine methacrylate) (PSBMA) was also used to synthesize zein-PSBMA micelles. The micelles significantly improved the water solubility of curcumin, and curcumin loaded in micelles exhibited better stability, cellular uptake, cytotoxicity against cancer cells compared with native curcumin (93). Therefore, the amphiphilic zein-based micelles have great potential for delivering bioactives due to their outstanding stability and targeting capability.

Others

Nanogel is a nanosized hydrogel, and it possess the features of hydrogels and nanoparticles, which is an

TABLE 2 Advantages and disadvantages of different nano-sized delivery systems.

Systems	Advantages	Disadvantages
Nanoparticles	Good resistance to oxidation	Inability to limit oxygen permeation
	High encapsulation efficiency	Complex modifications
	Controlled release and targeting effect	Some methods are not suitable for large-scale production
Nanofibers	High loading capacity and sustainable release	Special equipment
		Strict processing parameters
	Easy to large-scale production	Solvent residue
Nanomicelles	Strong thermodynamic stability	Potential side effects from modifier involved
	High loading capacity and sustainable release	Instability in blood dream
	Long blood circulation time *in vivo*	
	Able to avoid phagocytosis by immune system cells without additional modifications	
Nanogels	High loading capacity and responsive release	Special equipment
		Potential side effects from the crosslinker involved
	Wide delivery route	
Nanoemulsions	Improved chemical stability and solubilization	Thermodynamically unstable
	High bioavailability	Inability to limit oxygen permeation

excellent active ingredient delivery system with high loading and controlled release performance (94, 95). Zein-hyaluronic acid nanogels loaded with curcumin exhibited high anticancer activity against the CT26 colorectal cancer cells due to the enhanced targetability to CD44 receptor by the presence of hyaluronic acid (96). On the other hand, all these nano-sized zein materials could be used as emulsifiers to construct stable nanoemulsions for delivering curcumin, either
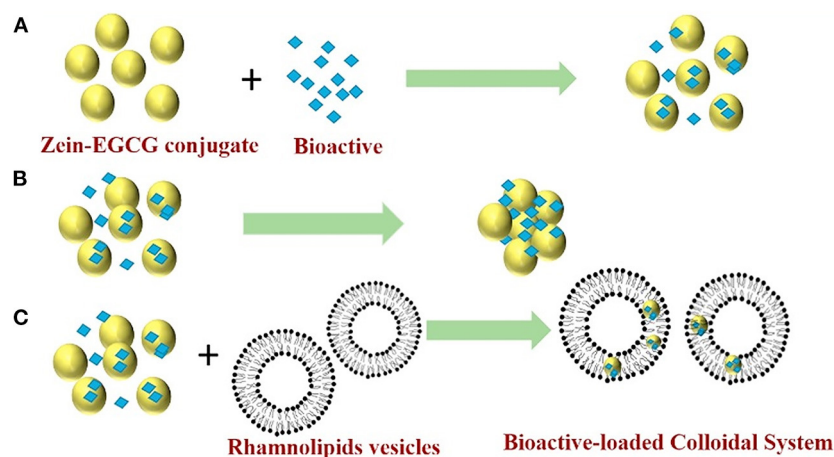
FIGURE 6
Proposed mechanisms for a mixed colloidal delivery system consisting of zein-EGCG conjugate nanoparticles and rhamnolipids vesicles. Zein-EGCG conjugate interacts with bioactive and self-assembles to form nanoparticles that embedded bioactive inside by antisolvent **(A)**; In the absence of surfactant, the nanoparticles aggregate due to hydrophobic interactions of zein in water solution **(B)**; In the presence of rhamnolipids vesicles, the nanoparticles do not aggregate because the coating of surfactant reduces hydrophobic interactions and increases the electrostatic and steric effects between nanoparticles **(C)**. Reprinted from (102) with permission from Elsevier.

oil-in-water single or multi-layer nanoemulsions (70, 97, 98).

Zein-based hybrid nano-delivery systems

Nano-sized delivery systems such as nanoparticles, nanofibers, nanomicelles, nanogels and nanoemulsions have been proved to possess several protective functional advantages for bioactives. Comparatively, zein-based nanoparticles have higher barrier properties than oil-in-water nanoemulsion in limiting peroxyl radical-induced oxidation processes of encapsulated curcumin (99). However, these two encapsulation systems were ineffectiveness in limiting oxygen permeation. In a comparative study of improving curcumin bioavailability by three potential delivery systems (ZNPs, nanoemulsions, and phospholipid nanoparticles), ZNPs were able to incorporate the highest level of curcumin per unit mass of particles. Nevertheless, nanoemulsions appeared to be the most effective at promoting both the chemical stability and solubilization of curcumin at an equal initial curcumin level, under simulated gastrointestinal conditions (100). Chuacharoen and Sabliov (101) also synthesized nanoemulsions and nanoparticles with entrapped curcumin at the same level of surfactant concentration. Compared with nanoemulsions, zein-based nanoparticles were found to be the better carriers based on their storage stability and sustained release profile.

To fully utilize the advantages of different systems, is it possible to achieve better encapsulation and delivery of hydrophobic bioactives if two or more systems are combined?

The advantages and disadvantages of different nano-sized delivery systems are summarized in Table 2. Reportedly, mixing curcumin-loaded ZNPs with lipid nanoparticles can increase the bioaccessibility and chemical stability of lipophilic bioactive agents (100). ZNPs can be designed to protect the curcumin from chemical degradation, whereas another type of nanoparticles (like lipid nanoparticles) can be designed to rapidly digest within the gastrointestinal tract and form mixed micelles that can solubilize and transport the hydrophobic curcumin. In a another study (102), zein-EGCG conjugate nanoparticles (Figure 6A) aggregated in water solution due to hydrophobic interaction of protein in the absence of surfactant (Figure 6B). However, mixing the nanoparticles with rhamnolipids vesicles formed uniform and stable bioactive-loaded colloids nanoparticles due to rhamnolipids adsorption and hydrophobic effect around the protein nanoparticles (Figure 6C). Furthermore, the mixed colloidal delivery system improved the digestibility of the nanoparticles and bioaccessibility of curcumin and resveratrol.

Conclusions and future trends for zein-based nano-sized carriers

Zein is considered as an ideal biopolymer for constructing nanoscale carriers owing to its intrinsic hydrophobic and self-assembly properties. Developing zein nanocarriers can provide controlled release possibilities and enhance the oral bioavailability of hydrophobic bioactives. The colloid stability of zein-based delivery system can be improved using chemical crosslinking, coating and complexation by

introducing other biopolymers (e.g., proteins, polysaccharide, phenols, surfactant). Most of these modification strategies can further enhance the encapsulation and delivery efficiency of bioactives.

Nevertheless, some issues remain to be considered for future study: (i) The appropriate loading level of nutrient and the actual sensory properties of these carriers for commercial foods should be determined; (ii) Various factors introduced in the process of carrier construction should be carefully considered, such as the involvement of toxic organic solvents; (iii) Whether the effects of the observations would also occur under more realistic physiological gastrointestinal conditions should be determined *via* using animal or human feeding models. In the future, zein based delivery systems will be designed to be functional and even more complex based on specific needs. More studies will focus on elucidating the efficacy and toxicity of these carriers as well as the biological fate of oral administration under physiological conditions. The preparation process requires more work based on a comprehensive analysis not only of their reproducibility, biocompatibility and immunogenicity, but also their scalability, storage stability and cost.

Author contributions

XY: writing—original draft preparation and revision. ML: writing—original draft preparation. XX and XL: project administration. FL: writing—review and editing, project administration, and funding acquisition. All authors contributed to the article and approved the submitted version.

Funding

Conflict of interest

The authors declare that the research was conducted in the absence of any commercial or financial relationships that could be construed as a potential conflict of interest.

Publisher's note

All claims expressed in this article are solely those of the authors and do not necessarily represent those of their affiliated organizations, or those of the publisher, the editors and the reviewers. Any product that may be evaluated in this article, or claim that may be made by its manufacturer, is not guaranteed or endorsed by the publisher.

Supplementary material

The Supplementary Material for this article can be found online at: https://www.frontiersin.org/articles/10.3389/fnut.2022.999373/full#supplementary-material

References

1. Hamaker B, Mohamed A, Habben J, Huang C, Larkins B. Efficient procedure for extracting maize and sorghum kernel proteins reveals higher prolamin contents than the conventional method. *Cereal Chem.* (1995) 72:583–8.

2. Patel AR. Functional and engineered colloids from edible materials for emerging applications in designing the food of the future. *Adv Funct Mater.* (2020) 30:1806809. doi: 10.1002/adfm.201806809

3. Wang T, Zhang D, Sun D, Gu J. Current status of in vivo bioanalysis of nano drug delivery systems. *J Pharm Sci.* (2020) 10:221–32. doi: 10.1016/j.jpha.2020.05.002

4. Yu X, Wu H, Hu H, Dong Z, Dang Y, Qi Q, et al. Zein nanoparticles as nontoxic delivery system for maytansine in the treatment of non-small cell lung cancer. *Drug Deliv.* (2020) 27:100–9. doi: 10.1080/10717544.2019.1704942

5. Wang H, Hao L, Wang P, Chen M, Jiang S, Jiang S. Release kinetics and antibacterial activity of curcumin loaded zein fibers. *Food Hydrocoll.* (2017) 63:437–46. doi: 10.1016/j.foodhyd.2016.09.028

6. Zhan X, Dai L, Zhang L, Gao Y. Entrapment of curcumin in whey protein isolate and zein composite nanoparticles using pH-driven method. *Food Hydrocoll.* (2020) 106:105839. doi: 10.1016/j.foodhyd.2020.105839

7. Chen S, Han Y, Huang J, Dai L, Du J, McClements DJ, et al. Fabrication and characterization of layer-by-layer composite nanoparticles based on zein and

hyaluronic acid for codelivery of curcumin and quercetagetin. *Appl Mater Inter.* (2019) 11:16922–33. doi: 10.1021/acsami.9b02529

8. Li H, Yuan Y, Zhu J, Wang T, Wang D, Xu Y. Zein/soluble soybean polysaccharide composite nanoparticles for encapsulation and oral delivery of lutein. *Food Hydrocoll.* (2020) 103:105715. doi: 10.1016/j.foodhyd.2020.105715

9. Rodríguez-Félix F, Del-Toro-Sánchez CL, Javier Cinco-Moroyoqui F, Juárez J, Ruiz-Cruz S, López-Ahumada GA, et al. Preparation and characterization of quercetin-loaded zein nanoparticles by electrospraying and study of *in vitro* bioavailability. *J Food Sci.* (2019) 84:2883–97. doi: 10.1111/1750-3841.14803

10. Ren X, Hou T, Liang Q, Zhang X, Hu D, Xu B, et al. Effects of frequency ultrasound on the properties of zein-chitosan complex coacervation for resveratrol encapsulation. *Food Chem.* (2019) 279:223–30. doi: 10.1016/j.foodchem.2018.11.025

11. Gali L, Bedjo F, Ferrari G, Donsì F. Formulation and characterization of zein/gum arabic nanoparticles for the encapsulation of a rutin-rich extract from Ruta chalepensis L. *Food Chem.* (2022) 367:129982. doi: 10.1016/j.foodchem.2021.129982

12. Wang M, Fu Y, Chen G, Shi Y, Li X, Zhang H, et al. Fabrication and characterization of carboxymethyl chitosan and tea polyphenols coating on zein

nanoparticles to encapsulate β-carotene by anti-solvent precipitation method. *Food Hydrocoll.* (2018) 77:577–87. doi: 10.1016/j.foodhyd.2017.10.036

13. Luo Y, Teng Z, Wang Q. Development of zein nanoparticles coated with carboxymethyl chitosan for encapsulation and controlled release of vitamin D3. *J Agri Food Chem.* (2012) 60:836–43. doi: 10.1021/jf204194z

14. Park CE, Park DJ, Kim BK. Effects of a chitosan coating on properties of retinol-encapsulated zein nanoparticles. *Food Sci Biotechnol.* (2015) 24:1725–33. doi: 10.1007/s10068-015-0224-7

15. Shukla R, Cheryan M. Zein: the industrial protein from corn. *Ind Crops Prod.* (2001) 13:171–92. doi: 10.1016/S0926-6690(00)00064-9

16. Sun C, Gao Y, Zhong Q. Effects of acidification by glucono-delta-lactone or hydrochloric acid on structures of zein-caseinate nanocomplexes self-assembled during a pH cycle. *Food Hydrocoll.* (2018) 82:173–85. doi: 10.1016/j.foodhyd.2018.04.007

17. Zhang H, Fu Y, Xu Y, Niu F, Li Z, Ba C, et al. One-step assembly of zein/caseinate/alginate nanoparticles for encapsulation and improved bioaccessibility of propolis. *Food Funct.* (2019) 10:635–45. doi: 10.1039/C8FO01614C

18. Kasaai MR. Zein and zein-based nano-materials for food and nutrition applications: a review. *Trends Food Sci Technol.* (2018) 79:184–97. doi: 10.1016/j.tifs.2018.07.015

19. Zhang Y, Cui L, Li F, Shi N, Li C, Chen Y, et al. Design, fabrication and biomedical applications of zein-based nano/micro-carrier systems. *Int J Pharm.* (2016) 513:191–210. doi: 10.1016/j.ijpharm.2016.09.023

20. Argos P, Pedersen K, Marks MD, Larkins BA, A. structural model for maize zein proteins. *J Biol Chem.* (1982) 257:9984–90. doi: 10.1016/S0021-9258(18)33974-7

21. Matsushima N, Danno GI, Takezawa H, Izumi Y. Three-dimensional structure of maize α-zein proteins studied by small-angle X-ray scattering. *BBA-Protein Struct M.* (1997) 1339:14–22. doi: 10.1016/S0167-4838(96)00212-9

22. Forato LA, Doriguetto AC, Fischer H, Mascarenhas YP, Craievich AF, Colnago LA. Conformation of the Z19 prolamin by FTIR, NMR, and SAXS. *J Agri Food Chem.* (2004) 52:2382–5. doi: 10.1021/jf035020+

23. Momany FA, Sessa DJ, Lawton JW, Selling GW, Hamaker SAH, Willett JL. Structural characterization of alpha-zein. *J Agri Food Chem.* (2006) 54:543–7. doi: 10.1021/jf058135h

24. Li Y, Li J, Xia Q, Zhang B, Wang Q, Huang Q. Understanding the dissolution of alpha-zein in aqueous ethanol and acetic acid solutions. *J Phys Chem B.* (2012) 116:12057–64. doi: 10.1021/jp305709y

25. Kyte J, Doolittle RF, A. simple method for displaying the hydropathic character of a protein. *J Mol Biol.* (1982) 157:105–32. doi: 10.1016/0022-2836(82)90515-0

26. Katayama H, Kanke M. Drug release from directly compressed tablets containing zein. *Drug Dev Ind Pharm.* (1992) 18:2173–84. doi: 10.3109/03639049209038755

27. Matsuda Y, Suzuki T, Sato E, Sato M, Koizumi S, Unno K, et al. Novel preparation of zein microspheres conjugated with PS-K available for cancer immunotherapy. *Chem Pharm Bull.* (1989) 37:757–9. doi: 10.1248/cpb.37.757

28. Suzuki T, Sato E, Matsuda Y, Tada H, Unno K, Kato T. Preparation of zein microspheres conjugated with antitumor drugs available for selective cancer chemotherapy and development of a simple colorimetric determination of drugs in microspheres. *Chem Pharm Bull.* (1989) 37:1051–4. doi: 10.1248/cpb.37.1051

29. Karthikeyan K, Lakra R, Rajaram R, Korrapati PS. Development and characterization of zein-based micro carrier system for sustained delivery of aceclofenac sodium. *AAPS PharmSciTech.* (2012) 13:143–9. doi: 10.1208/s12249-011-9731-x

30. Patel AR, Hu Y, Tiwari JK, Velikov KP. Synthesis and characterisation of zein-curcumin colloidal particles. *Soft Matter.* (2010) 6:6192–9. doi: 10.1039/c0sm00800a

31. Zhong Q, Jin M, Xiao D, Tian H, Zhang W. Application of supercritical anti-solvent technologies for the synthesis of delivery systems of bioactive food components. *Food Biophys.* (2008) 3:186–90. doi: 10.1007/s11483-008-9059-6

32. Jung J, Perrut M. Particle design using supercritical fluids: Literature and patent survey. *J Supercrit Fluid.* (2001) 20:179–219. doi: 10.1016/S0896-8446(01)00064-X

33. Zhong Q, Jin M, Davidson PM, Zivanovic S. Sustained release of lysozyme from zein microcapsules produced by a supercritical anti-solvent process. *Food Chem.* (2009) 115:697–700. doi: 10.1016/j.foodchem.2008.12.063

34. Hu D, Lin C, Liu L, Li S, Zhao Y. Preparation, characterization, and *in vitro* release investigation of lutein/zein nanoparticles via solution

enhanced dispersion by supercritical fluids. *J Food Eng.* (2012) 109:545–52. doi: 10.1016/j.jfoodeng.2011.10.025

35. Rodríguez-Félix F, Del-Toro-Sanchez CL, Tapia-Hernandez JA, A new design for obtaining of white zein micro- and nanoparticles powder: antisolvent-dialysis method. *Food Sci Biotechnol.* (2019) 29:619–29. doi: 10.1007/s10068-019-00702-9

36. Pan K. Zhong, Q. Low energy, organic solvent-free co-assembly of zein and caseinate to prepare stable dispersions. *Food Hydrocoll.* (2016) 52:600–6. doi: 10.1016/j.foodhyd.2015.08.014

37. Dai L, Zhou H, Wei Y, Gao Y, McClements DJ. Curcumin encapsulation in zein-rhamnolipid composite nanoparticles using a pH-driven method. *Food Hydrocoll.* (2019) 93:342–50. doi: 10.1016/j.foodhyd.2019.02.041

38. Wang L, Xue J, Zhang Y. Preparation and characterization of curcumin loaded caseinate/zein nanocomposite film using pH-driven method. *Ind Crops Prod.* (2019) 130:71–80. doi: 10.1016/j.indcrop.2018.12.072

39. Zhou D, Li S, Pei M, Yang H, Gu S, Tao Y, et al. Dopamine-modified hyaluronic acid hydrogel adhesives with fast-forming and high tissue adhesion. *ACS Appl Mater Inter.* (2020) 12:18225–34. doi: 10.1021/acsami.9b22120

40. Gomez-Estaca J, Balaguer MP, Gavara R, Hernandezmunoz P. Formation of zein nanoparticles by electrohydrodynamic atomization: effect of the main processing variables and suitability for encapsulating the food coloring and active ingredient curcumin. *Food Hydrocoll.* (2012) 28:82–91. doi: 10.1016/j.foodhyd.2011.11.013

41. Algandaby MM, Al-Sawahli MM, Ahmed OAA, Fahmy UA, Abdallah HM, Hattori M, et al. Curcumin-zein nanospheres improve liver targeting and antifibrotic activity of curcumin in carbon tetrachloride-induced mice liver fibrosis. *J Biomed Nanotechnol.* (2016) 12:1746–57. doi: 10.1166/jbn.2016.2270

42. Cheng CJ, Ferruzzi M, Jones OG. Fate of lutein-containing zein nanoparticles following simulated gastric and intestinal digestion. *Food Hydrocoll.* (2019) 87:229–36. doi: 10.1016/j.foodhyd.2018.08.013

43. Fernández-Carneado J, Kogan MJ, Castel S, Giralt E. Potential peptide carriers: Amphipathic proline-rich peptides derived from the N-terminal domain of γ-zein. *Angew Chem Int Ed.* (2004) 43:1811–4. doi: 10.1002/anie.200352540

44. Wang Y, Wang J, Yang X, Guo J, Lin Y. Amphiphilic zein hydrolysate as a novel nano-delivery vehicle for curcumin. *Food Funct.* (2015) 6:2636–45. doi: 10.1039/C5FO00422E

45. Pan R, Zou Y, Wang J, Wan Z, Guo J, Yang J, et al. Gamma/alpha-zein hydrolysates as oral delivery vehicles: enhanced physicochemical stability and *in vitro* bioaccessibility of curcumin. *Int J Food Sci Tech.* (2018) 53:1622–30. doi: 10.1111/ijfs.13744

46. Cabra V, Arreguin R, Vazquez-Duhalt R, Farres A. Effect of alkaline deamidation on the structure, surface hydrophobicity, and emulsifying properties of the Z19 α-zein. *J Agri Food Chem.* (2007) 55:439–45. doi: 10.1021/jf061002r

47. Li L, Yao P. High dispersity, stability and bioaccessibility of curcumin by assembling with deamidated zein peptide. *Food Chem.* (2020) 319:126577. doi: 10.1016/j.foodchem.2020.126577

48. Xue J, Zhang Y, Huang G, Liu J, Slavin M, Yu L. Zein-caseinate composite nanoparticles for bioactive delivery using curcumin as a probe compound. *Food Hydrocoll.* (2018) 83:25–35. doi: 10.1016/j.foodhyd.2018.04.037

49. Yan X, Zhang X, McClements DJ, Zou L, Liu X, Liu F. Co-encapsulation of epigallocatechin gallate (EGCG) and curcumin by two proteins-based nanoparticles: Role of EGCG. *J Agri Food Chem.* (2019) 67:13228–36. doi: 10.1021/acs.jafc.9b04415

50. Li M, Chen L, Xu M, Zhang J, Wang Q, Zeng Q, et al. The formation of zein-chitosan complex coacervated particles: Relationship to encapsulation and controlled release properties. *Int J Biol Macromol.* (2018) 116:1232–9. doi: 10.1016/j.ijbiomac.2018.05.107

51. Chen S, Han Y, Jian L, Liao W, Zhang Y, Gao Y. Fabrication, characterization, physicochemical stability of zein-chitosan nanocomplex for co-encapsulating curcumin and resveratrol. *Carbohyd Polym.* (2020) 236:116090. doi: 10.1016/j.carbpol.2020.116090

52. Liang H, Zhou B, He L, An Y, Lin L, Li Y, et al. Fabrication of zein/quaternized chitosan nanoparticles for the encapsulation and protection of curcumin. *RSC Adv.* (2015) 5:13891–900. doi: 10.1039/C4RA14270E

53. Hu K, Huang X, Gao Y, Huang X, Xiao H, McClements DJ. Core-shell biopolymer nanoparticle delivery systems: Synthesis and characterization of curcumin fortified zein-pectin nanoparticles. *Food Chem.* (2015) 182:275–81. doi: 10.1016/j.foodchem.2015.03.009

54. Cai T, Xiao P, Yu N, Zhou Y, Mao J, Peng H, et al. A novel pectin from Akebia trifoliata var. australis fruit peel and its use as a wall-material to coat curcumin-loaded zein nanoparticle. *Int J Biol Macromol.* (2020) 152:40–9. doi: 10.1016/j.ijbiomac.2020.02.234

55. Chen S, Han Y, Sun C, Dai L, Yang S, Wei Y, et al. Effect of molecular weight of hyaluronan on zein-based nanoparticles: Fabrication, structural characterization and delivery of curcumin. *Carbohyd Polym.* (2018) 201:599–607. doi: 10.1016/j.carbpol.2018.08.116

56. Chen G, Fu Y, Niu F, Zhang H, Li X, Li X. Evaluation of the colloidal/chemical performance of core-shell nanoparticle formed by zein and gum Arabic. *Colloid Surface A.* (2019) 560:130–5. doi: 10.1016/j.colsurfa.2018.10.006

57. Chen S, Li Q, Julian D, Han Y, Dai L, Mao L, et al. Co-delivery of curcumin and piperine in zein-carrageenan core-shell nanoparticles: Formation, structure, stability and *in vitro* gastrointestinal digestion. *Food Hydrocoll.* (2020) 99:105334. doi: 10.1016/j.foodhyd.2019.105334

58. Sun C, Xu C, Mao L, Wang D, Yang J, Gao Y. Preparation, characterization and stability of curcumin-loaded zein-shellac composite colloidal particles. *Food Chem.* (2017) 228:656–67. doi: 10.1016/j.foodchem.2017.02.001

59. Dai L, Sun C, Li R, Mao L, Liu F, Gao Y. Structural characterization, formation mechanism and stability of curcumin in zein-lecithin composite nanoparticles fabricated by antisolvent co-precipitation. *Food Chem.* (2017) 237:1163–71. doi: 10.1016/j.foodchem.2017.05.134

60. Wang X, Huang H, Chu X, Han Y, Li M, Li G, et al. Encapsulation and binding properties of curcumin in zein particles stabilized by Tween 20. *Colloid Surface A.* (2019) 577:274–80. doi: 10.1016/j.colsurfa.2019.05.094

61. Hu S, Wang T, Fernandez ML, Luo Y. Development of tannic acid cross-linked hollow zein nanoparticles as potential oral delivery vehicles for curcumin. *Food Hydrocoll.* (2016) 61:821–31. doi: 10.1016/j.foodhyd.2016.07.006

62. Dai L, Wei Y, Sun C, Mao L, McClements DJ, Gao Y. Development of protein-polysaccharide-surfactant ternary complex particles as delivery vehicles for curcumin. *Food Hydrocoll.* (2018) 85:75–85. doi: 10.1016/j.foodhyd.2018.06.052

63. Yuan Y, Ma M, Zhang S, Liu C, Chen P, Li H, et al. Effect of sophorolipid on the curcumin-loaded ternary composite nanoparticles self-assembled from zein and chondroitin sulfate. *Food Hydrocoll.* (2021) 113:106493. doi: 10.1016/j.foodhyd.2020.106493

64. Liu Q, Jing Y, Han C, Zhang H, Tian Y. Encapsulation of curcumin in zein/caseinate/sodium alginate nanoparticles with improved physicochemical and controlled release properties. *Food Hydrocoll.* (2019) 93:432–42. doi: 10.1016/j.foodhyd.2019.02.003

65. Yao K, Chen W, Song F, McClements DJ, Hu K. Tailoring zein nanoparticle functionality using biopolymer coatings: Impact on curcumin bioaccessibility and antioxidant capacity under simulated gastrointestinal conditions. *Food Hydrocoll.* (2018) 79:262–72. doi: 10.1016/j.foodhyd.2017.12.029

66. Huang X, Huang X, Gong Y, Xiao H, McClements DJ. Hu, K. Enhancement of curcumin water dispersibility and antioxidant activity using core-shell protein-polysaccharide nanoparticles. *Food Res Int.* (2016) 87:1–9. doi: 10.1016/j.foodres.2016.06.009

67. Chen S, McClements DJ, Jian L, Han Y, Dai L, Mao L, et al. Core-shell biopolymer nanoparticles for co-delivery of curcumin and piperine: sequential electrostatic deposition of hyaluronic acid and chitosan shells on the zein core. *ACS Appl Mater Inter.* (2019) 11:38103–15. doi: 10.1021/acsami.9b11782

68. Chang C, Wang T, Hu Q, Luo Y. Caseinate-zein-polysaccharide complex nanoparticles as potential oral delivery vehicles for curcumin: effect of polysaccharide type and chemical cross-linking. *Food Hydrocoll.* (2017) 72:254–62. doi: 10.1016/j.foodhyd.2017.05.039

69. Rodriguez NJ, Hu Q, Luo Y. Oxidized dextran as a macromolecular crosslinker stabilizes the zein/caseinate nanocomplex for the potential oral delivery of curcumin. *Molecules.* (2019) 24:4061. doi: 10.3390/molecules24224061

70. Brahatheeswaran D, Mathew A, Aswathy RG, Nagaoka Y, Venugopal K, Yoshida Y, et al. Hybrid fluorescent curcumin loaded zein electrospun nanofibrous scaffold for biomedical applications. *Biomed Mater.* (2012) 7:045001. doi: 10.1088/1748-6041/7/4/045001

71. Deng L, Li Y, Feng F, Wu D, Zhang H. Encapsulation of allopurinol by glucose cross-linked gelatin/zein nanofibers: Characterization and release behavior. *Food Hydrocoll.* (2019) 94:574–84. doi: 10.1016/j.foodhyd.2019.04.004

72. Zhang Y, Cui L, Chen Y, Zhang H, Zhong J, Sun Y, et al. Zein-based nanofibres for drug delivery: classes and current applications. *Curr Pharm Design.* (2015) 21:3199–207. doi: 10.2174/1381612821666150531170448

73. Deng L, Zhang X, Li Y, Que F, Kang X, Liu Y, et al. Characterization of gelatin/zein nanofibers by hybrid electrospinning. *Food Hydrocoll.* (2018) 75:72–80. doi: 10.1016/j.foodhyd.2017.09.011

74. Dehcheshmeh MA, Fathi M. Production of core-shell nanofibers from zein and tragacanth for encapsulation of saffron extract. *Int J Biol Macromol.* (2019) 122:272–9. doi: 10.1016/j.ijbiomac.2018.10.176

75. Bui HT, Chung OH, Park JS. Fabrication of electrospun antibacterial curcumin-loaded zein nanofibers. *Polym Korea.* (2014) 38:744–51. doi: 10.7317/pk.2014.38.6.744

76. Yilmaz A, Bozkurt F, Cicek PK, Dertli E, Durak MZ, Yilmaz MT, et al. novel antifungal surface-coating application to limit postharvest decay on coated apples: Molecular, thermal and morphological properties of electrospun zein-nanofiber mats loaded with curcumin. *Innov Food Sci Emerg.* (2016) 37:74–83. doi: 10.1016/j.ifset.2016.08.008

77. Wang L, Zhang Y. Eugenol nanoemulsion stabilized with zein and sodium caseinate by self-assembly. *J Agri Food Chem.* (2017) 65:2990–8. doi: 10.1021/acs.jafc.7b00194

78. Akrami-Hasan-Kohal M, Tayebi L, Ghorbani M. Curcumin-loaded naturally-based nanofibers as active wound dressing mats: Morphology, drug release, cell proliferation, and cell adhesion studies. *New J Chem.* (2020) 44:10343–51. doi: 10.1039/D0NJ01594F

79. Bu X, Ji N, Dai L, Dong X, Chen M, et al. Self-assembled micelles based on amphiphilic biopolymers for delivery of functional ingredients. *Trends Food Sci Technol.* (2021) 114:386–98. doi: 10.1016/j.tifs.2021.06.001

80. Sabra S, Abdelmoneem M, Abdelwakil M, Mabrouk MT, Anwar D, Mohamed R, et al. Self-assembled nanocarriers based on amphiphilic natural polymers for anti-cancer drug delivery applications. *Curr Pharm Design.* (2017) 23:5213–29. doi: 10.2174/1381612823666170526111029

81. Guan J, Zhou Z, Chen M, Li H, Tong D, Yang J, et al. Folate-conjugated and pH-responsive polymeric micelles for target-cell-specific anticancer drug delivery. *Acta Biomater.* (2017) 60:244–55. doi: 10.1016/j.actbio.2017.07.018

82. Li Q, Yao W, Yu X, Zhang B, Dong J, Jin Y. Drug-loaded pH-responsive polymeric micelles: Simulations and experiments of micelle formation, drug loading and drug release. *Colloid Surface B.* (2017) 158:709–16. doi: 10.1016/j.colsurfb.2017.07.063

83. Yotsumoto K, Ishii K, Kokubo M, Yasuoka S. Improvement of the skin penetration of hydrophobic drugs by polymeric micelles. *Int J Pharm.* (2018) 553:132–40. doi: 10.1016/j.ijpharm.2018.10.039

84. Di Prima G, Licciardi M, Bongiovì F, Pitarresi G, Giammona G. Inulin-based polymeric micelles functionalized with ocular permeation enhancers: improvement of dexamethasone permeation/penetration through bovine corneas. *Pharmaceutics.* (2021) 13:1431. doi: 10.3390/pharmaceutics 13091431

85. Ranadheera CS, Liyanaarachchi WS, Dissanayake M, Chandrapala J, Huppertz T, Vasiljevic T. Impact of shear and pH on properties of casein micelles in milk protein concentrate. *LWT-Food Sci Technol.* (2019) 108:370–6. doi: 10.1016/j.lwt.2019.03.090

86. Šmejkalová D, Muthný T, Nešporová K, Hermannová M, Achbergerová E, Huerta-Angeles G, et al. Hyaluronan polymeric micelles for topical drug delivery. *Carbohyd Polym.* (2017) 156:86–96. doi: 10.1016/j.carbpol.2016.09.013

87. Song R, Zhou Y, Li Y, Yang Z, Li F, Huang Q, et al. Preparation and characterization of mPEG-g-α-zein biohybrid micelles as a nano-carrier. *J Appl Polym Sci.* (2015) 132:42555. doi: 10.1002/app.42555

88. Schellekens H, Hennink WE, Brinks V. The immunogenicity of polyethylene glycol: Facts and fiction. *Pharmacol Res.* (2013) 30:1729–34. doi: 10.1007/s11095-013-1067-7

89. Sabra SA, Elzoghby AO, Sheweita SA, Haroun M, Helmy MW, Eldemellawy MA, et al. Self-assembled amphiphilic zein-lactoferrin micelles for tumor targeted co-delivery of rapamycin and wogonin to breast cancer. *Eur J Pharm Biopharm.* (2018) 128:156–69. doi: 10.1016/j.ejpb.2018.04.023

90. Abdelmoneem MA, Elnaggar MA, Hammady RS, Kamel SM, Helmy MW, Abdulkader MA, et al. Dual-targeted lactoferrin shell-oily core nanocapsules for synergistic targeted/herbal therapy of hepatocellular carcinoma. *ACS Appl Mater Inter.* (2019) 11:26731–44. doi: 10.1021/acsami.9b10164

91. Lin C, Lin I, Sung S, Su Y, Huang Y, Chiang CS, et al. Dual-targeted photopenetrative delivery of multiple micelles/hydrophobic drugs by a nanopea for enhanced tumor therapy. *Adv Funct Mater.* (2016) 26:4169–79. doi: 10.1002/adfm.201600498

92. Elhasany KA, Khattab SN, Bekhit AA, Ragab DM, Abdulkader MA, Zaky A, et al. Combination of magnetic targeting with synergistic inhibition of NF-κB and glutathione via micellar drug nanomedicine enhances its anti-tumor efficacy. *Eur J Pharm Biopharm.* (2020) 155:162–76. doi: 10.1016/j.ejpb.2020.08.004

93. Chen S, Li Q, Li H, Yang L, Yi J, Xie M, et al. Long-circulating zein-polysulfobetaine conjugate-based nanocarriers for enhancing the stability and pharmacokinetics of curcumin. *Mater Sci Eng C.* (2020) 109:110636. doi: 10.1016/j.msec.2020.110636

94. Ahmed S, Alhareth K, Mignet N. Advancement in nanogel formulations provides controlled drug release. *Int J Pharm.* (2020) 584:119435. doi: 10.1016/j.ijpharm.2020.119435

95. Cao Z, Zhou X, Wang G. Selective release of hydrophobic and hydrophilic cargos from multi-stimuli-responsive nanogels. *ACS Appl Mater Inter.* (2016) 8:28888–96. doi: 10.1021/acsami.6b10360

96. Seok HY, Rejinold NS, Lekshmi KM, Cherukula K, Park IK, Kim YC. CD44 targeting biocompatible and biodegradable hyaluronic acid cross-linked zein nanogels for curcumin delivery to cancer cells: *In vitro* and in vivo evaluation. *J Control Release.* (2018) 280:20–30. doi: 10.1016/j.jconrel.2018.04.050

97. Cui F, McClements DJ, Liu X, Liu F, Ngai T. Development of pH-responsive emulsions stabilized by whey protein fibrils. *Food Hydrocoll.* (2022) 122:107067. doi: 10.1016/j.foodhyd.2021.107067

98. Razavi R, Kenari RE, Farmani J, Jahanshahi M. Preparation of double-layer nanoemulsions with controlled release of glucose as prevention of hypoglycemia in diabetic patients. *Biomed Pharmacother.* (2021) 138:111464. doi: 10.1016/j.biopha.2021.111464

99. Pan Y, Tikekar RV, Wang MS, Avena-Bustillos RJ, Nitin N. Effect of barrier properties of zein colloidal particles and oil-in-water emulsions on oxidative stability of encapsulated bioactive compounds. *Food Hydrocoll.* (2015) 43:82–90. doi: 10.1016/j.foodhyd.2014.05.002

100. Zou L, Zheng B, Zhang R, Zhang Z, Liu W, Liu C, et al. Enhancing the bioaccessibility of hydrophobic bioactive agents using mixed colloidal dispersions: curcumin-loaded zein nanoparticles plus digestible lipid nanoparticles. *Food Res Int.* (2016) 81:74–82. doi: 10.1016/j.foodres.2015.12.035

101. Chuacharoen T, Sabliov CM. Comparative effects of curcumin when delivered in a nanoemulsion or nanoparticle form for food applications: study on stability and lipid oxidation inhibition. *LWT-Food Sci Technol.* (2019) 113:108319. doi: 10.1016/j.lwt.2019.108319

102. Liu F, Ma D, Luo X, Zhang Z, He L, Gao Y, et al. Fabrication and characterization of protein-phenolic conjugate nanoparticles for co-delivery of curcumin and resveratrol. *Food Hydrocoll.* (2018) 79:450–61. doi: 10.1016/j.foodhyd.2018.01.017

Formation and characterization of solid fat mimetic based on pea protein isolate/polysaccharide emulsion gels

Wenbo Hou[1,2,3], Jie Long[1,2,3], Yufei Hua[1,2,3], Yeming Chen[1,2,3], Xiangzhen Kong[1,2,3], Caimeng Zhang[1,2,3] and Xingfei Li[1,2,3]*

[1]State Key Laboratory of Food Science and Technology, Jiangnan University, Wuxi, Jiangsu, China, [2]School of Food Science and Technology, Jiangnan University, Wuxi, Jiangsu, China, [3]Collaborative Innovation Center of Food Safety and Quality Control in Jiangsu Province, Jiangnan University, Wuxi, Jiangsu, China

The emulsion gels that can be used as solid fat replacers were produced with different polysaccharides (κ-carrageenan, κC; high-acyl gellan, HA; konjac glucomannanon, and KGM), pea protein isolate (PPI) and sunflower seed oil. The effect of polysaccharide concentration on the texture, rheological property, microstructure, and water holding capacity of the mixed emulsion gels were investigated. Rheological results showed that the presence of polysaccharides enhanced the hardness, storage modulus and resistance against deformation of emulsion gel, where PPI/κC system exhibited superior hardness with a similar level of pig back fat, due to the self-gelation behavior of κC. CLSM and SEM results showed that the presence of κC, HA, and KGM broke the uniform structure of gel network and formed irregular, threadlike, and oval shaped inclusions respectively, resulting in the broken and coalescence of oil droplets. The α-helix content of emulsion gels decreased, while β-sheet, β-turn and random coils slightly increased due to the unfolding of protein during gel formation. This study may offer a valuable strategy for the development of solid fat mimetic with the characteristics closing to the pig back fat.

KEYWORDS

solid fat mimetic, pea protein isolate, polysaccharide, emulsion gels, gelation properties

Introduction

In recent years, there has been an increasing demand for diet for several reasons, such as health concerns, environmental issues, and sustainability (1, 2). To manufacture healthier and more environmentally friendly simulated meat products has become a focus in the field of meat and relative products development. For example, pea protein

isolates have been used as a substitute for meat protein due to their balanced amino acid composition, good nutritional value and functional properties (3–7). On the other hand, animal fat tissue contains a high amount of saturated fatty acids, which is linked with adverse impacts on human health (8). Therefore, various strategies to replace animal fats by healthier options have attracted people's attention gradually.

Oleogels and emulsion gels have been considered to be the two main technologies for replacing the fats in meat products. Oleogelation is defined as entrapping the liquid oil in a thermo-reversible and three-dimensional gel network using one or more oleogelator agents, and is characterized as semi-solid systems without changing its chemical composition (9, 10). Carnauba wax (CW) based oleogel was reinforced with adipic acid (AA) and it was applied to model cake and beef hamburger. The results showed that the texture and sensory properties of formulated cake and burgers prepared with CW2%/AA4% oleogel were reached the similar level of un-substituted products essentially (11). Moreover, the pork fat in more compact and lighter Bologna sausages was also replaced by monoglyceride oleogels made from traditional or high oleic sunflower oils. This study indicated that a reduction of 50% of pork fat back would not significantly change the hardness of sausages (12). However, it was worth noticing that, the stability of oleogels decreased over time, which was attributed to large crystals in oleogels and less contact points among them. Regarding emulsion gels, the emulsified fats were filled in to protein network, and then gelatinized emulsions to give them solid like mechanical properties (13). Using succinylated chicken liver protein and pre-emulsified sunflower oil to substitute back-fat in emulsified sausages obtained similar texture properties to high back-fat sausages, and also improved the quality and nutritional characteristic of sausages (14). However, replacing animal fats with inulin-based emulsion gels would result in a decrease in hardness of products (15, 16). In order to improve the texture characteristics of fat mimics, some studies had proposed to prepare substitution with fully hydrogenated canola oil and soy protein (17). Through this method, the texture of fat mimetic could be improved, but what was worth thinking was that hydrogenation forms trans-fatty acids had negative impact on human health by decreasing the proportion of "good cholesterol" and increasing the proportion of "bad cholesterol" (18).

Considering the instability of oleogel and the hazards of trans-fatty acids in hydrogenated oils, the objective of this research was to establish a method for preparing solid fat mimetic with higher-protein and lower-fat content by a healthier and environmentally friendly way. Three functional polysaccharides, κ-carrageenan, high-acyl gellan, and konjac glucomannanon have been commonly used as thickener in the food industry, especially for colloid snacks in China. The mixture of polysaccharides and pea protein

isolate (PPI) were crosslinked by transglutaminase (TG) to obtain a solid fat mimetic with excellent mechanical property similar to that of pig back fat. The possible influencing rule of solid fat mimetic was investigated from the rheological properties, microstructures, structure information, etc.

Materials and methods

Materials

κ-carrageenan (κC, MW~7313 kDa, detected by HPSEC-MALLS) was purchased from Aladdin Chemistry Co., Ltd., (Shanghai, China). High-acyl gellan (HA, MW~1435 kDa, detected by HPSEC-MALLS) and konjac glucomannan (KGM, MW~34 kDa, detected by HPSEC-MALLS) were purchased from Yuanye biological technology Co., Ltd., (Shanghai, China). Sunflower seed oil (SFO) and pig back fat were obtained from a local supermarket. Glutamine transaminases (TG, 100 U/g) were obtained from Beijing Solarbio Science and Technology Co., Ltd., (Beijing, China). Fluorescein isothiocyanate (FITC) and Nile red were obtained from Sigma-Aldrich (St. Louis, MO, USA). All other chemicals were analytical grade and did not require further purification.

Preparation of pea protein isolate

The PPI was prepared according to the method of Shen et al. (19). Briefly, the alcohol-washed pea meal was mixed with deionized water (1:10, w/v) and added 2.0 M NaOH to adjust the pH to 9.0. After centrifugation at 9,000 rpm, the supernatant was adjusted to pH 4.5 with 1.0 mol/L HCl and then centrifuged again to collect the protein curd. The protein curd was re-dissolved in water by adjusting pH to 7 using 1.0 mol/L NaOH, followed by centrifugation to remove insoluble residues. The above protein solution was freeze-dried and stored at −20°C before the further experiment.

Preparation of emulsion gels as solid fat mimetic

Polysaccharides (κC, HA, and KGM) were blended with the PPI dispersion to achieve a mixture solution containing 20% (w/w) of protein and 0.2, 0.6, 1.0% (w/w) of polysaccharide, separately. After adjusting to pH 7, the mixture solution was mixed with sunflower seed oil (30%, w/w) and homogenized with a Model V2700 homogenizer (Qingdao Huwazi Electric Appliance Co., Qingdao, China) for 4 min at 22,000 rpm to prepare emulsions. In order to induce gel formation by protein crosslinking, the TG (20 U/g protein) was added to

the emulsions. Samples were subsequently incubated at 37°C for 60 min, and then heated at 85°C for 15 min to inactivate the enzyme. Finally, the prepared emulsion gels were stored overnight at 4°C before analysis. The control group in this study was PPI emulsion crosslinked by TG without addition of polysaccharides under the same conditions.

Texture profile analysis

The textural parameters of emulsion gels and pure pork back fat were determined using TA-XT Plus texture analyzer (Stable Micro Systems Ltd., Godalming, UK) with a P36R probe, according to the method of Lu et al. (14) with some modification. Before experiment, the pre-cooling pig back fat was kept at 25°C for at least 2 h to recover the nature state. The cylinder samples (1.2 cm high, 1.2 cm diameter) were performed with a deformation level of 50% at 25°C using the following parameters: pretest speed, test speed and posttest speed were 2.0, 1.0, and 1.0 mm/s respectively, and contact force was 5 g. The four textural parameters hardness, springiness, cohesiveness, and chewiness were recorded in test.

Rheological measurements

Monitoring the rheological behavior of samples using an oscillatory rheometer (MCR 301, Anton Paar, Graz, Austria) with a parallel plate (PP50, diameter = 50 mm) and 1.0 mm gap. Low-density silicone oil was used to the edge of the parallel plate to prevent the evaporation of the liquid.

Temperature sweep and frequency sweep

The strain (0.1%) applied was within the linear viscoelastic region and the oscillation frequency was 0.1 Hz. The emulsions containing TG were heated from 25 to 37°C at a rate of 6°C /min and kept at 37°C for 60 min, then heated to 85°C at 6°C /min and kept at 85°C for 15 min to destroy the enzyme, finally, cooled to 25°C at a cooling rate of 6°C /min. After the temperature cycle, frequency sweeps of gelled simples were carried out in a range of angular frequencies between 6.28 and 126 rad/s with 0.1% strain at 25°C. The power law model was used to characterize the relationship between the G' and frequency (ω) as follows [Eq. (1)]:

$$G' = K'\omega^{n'} \tag{1}$$

where K' is the power law model constant and n' is the frequency exponent.

Creep and recovery tests

Creep-recovery test was executed by applying a constant shear stress, σ_0, of 50 Pa to the gelled simples for 300.1 s, after which the stress was released, a partial recovery was monitored for a further 600.3 s. Burger's model was used to interpret the creep data, which was used to characterize the viscoelastic properties. The model was expressed as Eq.(2) (20):

$$J(t) = \frac{1}{G_0} + \frac{1}{G_1}(1 - e^{-\frac{t}{\lambda}}) + \frac{t}{\mu_0} \tag{2}$$

where J is the creep compliance (1/Pa) which is the ratio of strain to stress; G_0 and G_1 respectively represent the instantaneous elastic modulus (Pa) and retarded elastic modulus (Pa); λ represents the retardation time of Kelvin component (s), and μ_0 is the viscous part (Pa s^{-1}) of Newtonian element.

Microstructure characterization

Confocal laser scanning microscopy

The protein phase was stained with fluorescein-5-isothiocyanate (0.1%, w/v) and the lipid phase was labeled by Nile Red (0.1%, w/v) prior to adding the TG dispersion. Afterward, the emulsion gels were prepared as described above, and imaged with a confocal laser scanning microscope (LSM710 Carl Zeiss AG Germany) objective. For locating the PPI and the oil droplets, FITC and Nile red were excited at 514 and 488 nm respectively.

Scanning electron microscopy

The liquid nitrogen pre-frozen samples were firstly freeze-dried to fix their structures, and then the oil phase was removed according to the method of Li et al. (21) with some alterations. Briefly, the cut sheet samples were soaked in petroleum ether for 24 h and this procedure was repeated three times, then the defatted samples were placed in a vacuum drying oven at 50°C for 4 h to evaporate the petroleum ether. A SEM QUANTA 200 (FEI Company, Hillsboro, OR, USA) was used to observe the microstructure of samples. The acceleration voltage was 10.0 kV, and the microtopography of the samples was observed at 100× and 1000×, respectively.

Low field nuclear magnetic resonance

Low field nuclear magnetic resonance (LF-NMR) relaxation tests were carried out with a LF-NMR analyzer (MesoMR23-060V-I, Niumag Analytical Instruments, Shanghai, China) to evaluate the state and distribution of water in samples. Approximately 3 g of gel was placed into a cylindrical glass tube and the T_2 relaxation time was measured using the CPMG sequence. The parameters were as follows: echo time, 0.3 ms; radio frequency delay time, 0.08 ms; waiting time, 3,500 ms and the number of scans, 8. A total of 15,000 echoes were acquired for analysis.

Determination of water holding capacity

The water holding capacity (WHC) was analyzed by a centrifugal procedure described by Qayum et al. (22) with some alterations. A certain amount of the sample was transferred to centrifuge tubes and centrifuged at 10,000 g at 4°C for 15 min, then refused the supernatant. WHC was defined as the percentage of sample weight after centrifugation (W_2) to its pre-centrifugation weight (W_1). The WHC was calculated using the following Eq. (3):

$$\text{WHC}\,(\%) \;=\; \frac{W_2}{W_1} \;\times\; 100 \tag{3}$$

FTIR spectroscopy

Infrared spectra were recorded using a Thermo Nicolet Nexus 470 FTIR spectrometer (Thermo Nicolet Analytical Instruments, MA, USA). The freeze-dried and crushed samples were mixed with potassium bromide and pressed into tablets for further FTIR measurement. The infrared spectrum had a scanning range of 4,000 to 400 cm^{-1}, a resolution of 4 cm^{-1} and 32 scanning times. The spectrum results were determined and computed by OMNIC (Ver.8.2) and Peakfit (Ver.4.12).

Statistical analysis

All tests were repeated at least triplicated. Statistical analysis was performed using SPSS 26.0 software (SPSS Inc., Chicago, IL, USA). In order to test the significant differences of results between different groups, Duncan test was used for one-way analysis of variance (ANOVA). Differences were considered significant at $p < 0.05$.

Results and discussion

Textural properties

Table 1 illustrates the hardness, springiness, cohesiveness and chewiness of the emulsion gels containing different concentration of κC, HA, and KGM. Hardness was one of the important texture parameters to evaluate the quality of gels and chewiness was the simulated energy when a sample was chewed to the point where it can be swallowed. The increase of hardness means more energy was demanded for chewing (23). Both the hardness and chewiness of the PPI/polysaccharide emulsion gels were higher than that of PPI emulsion gel (0% group). With the increase of polysaccharide concentration, the hardness and chewiness showed an increasing trend for all

three types of polysaccharides. At polysaccharide concentration of 1.0%, the maximum hardness of PPI/κC, PPI/HA, and PPI/KGM emulsion gels reached a level of 1951.49, 1792.91, and 1669.91 g respectively; and the hardness of PPI/κC emulsion gel showed the very similar level to that of pig back fat. A steric exclusion mechanism was reported to be related to the gel hardness and chewiness of protein/polysaccharide mixed gels containing no oil phase (24). In the mixed emulsion gel system, the increase of the polysaccharide concentration promoted the mutual attraction between protein molecules and reduced the contact area of the protein with the surrounding solution and the filled oil droplets might further enhanced the steric exclusion. In addition, protein and polysaccharide were thermodynamically incompatible at neutral pH (25, 26), which can result in microphase separation, and thus leading to an increase in regional effective protein concentration and protein–protein interactions during the gel formation. The gel hardness of PPI/κC emulsion gel was visibly higher than that of PPI/HA and PPI/KGM gels, which might be attributed to the synergistic interaction between κC self-gel and PPI (see section "Rheological behaviors"), because gelation behavior of HA and KGM was weak at the very low ionic strength and neutral pH (27, 28).

The springiness indicated how well samples could return to their original state after being compressed. On the other hand, cohesiveness was a standard to measure the deformation resistance of gel. The smaller the cohesiveness, the greater the damage to the irreversible structure after compression (17). The springiness and cohesiveness decreased with the increase in the content of polysaccharides, but still higher than that of pig back fat. The higher chewiness of the mixed gels also reflected an elastic dominated gel. This could be due to the limited content of polysaccharides that cannot affect protein dominated gelation behavior in mixed gels.

Rheological behaviors

The storage modulus (G') reflected the contribution of the elastic portion of gels and characterized the strength of gels. The changes of G' of the emulsion gels containing 0.2–1.0% (w/w) κC, HA and KGM subjected to the temperature cycling were shown in Figure 1. The G' of all emulsion gels exhibited a sharp increase in 30 min at the first insulation stage (37°C), leveled off gradually with the increase in insulation time. The G' values of emulsion gels for three κC, HA and KGM systems at this stage were higher than that of pure PPI emulsion gel, and gradually increased as the increase in polysaccharide concentration, which confirmed the enhanced hardness of PPI/polysaccharide emulsion gels. At the second insulation stage (85°C) and the followed cooling stage, the gelation curves of G' of the PPI/polysaccharide emulsion gels became different compared to pure PPI emulsion gel depending

TABLE 1 The texture profile analysis (TPA) data of emulsion gels containing different polysaccharides.

Sample	Hardness (g)	Springiness (%)	Cohesiveness	Chewiness
0%	1389.12 ± 39.98[d]	96.75 ± 2.35[a]	0.91 ± 0.01[a]	1224.24 ± 49.21[c]
0.2% κC	1569.69 ± 48.17[c]	95.19 ± 1.38[ab]	0.89 ± 0.01[b]	1337.42 ± 28.37[b]
0.6% κC	1790.86 ± 69.03[b]	93.45 ± 2.18[b]	0.88 ± 0.02[bc]	1478.53 ± 140.69[a]
1.0% κC	1951.49 ± 63.85[a]	93.47 ± 1.35[b]	0.87 ± 0.01[c]	1581.78 ± 88.22[a]
0%	1389.18 ± 39.98[d]	96.75 ± 2.35[a]	0.91 ± 0.01[a]	1224.24 ± 49.21[c]
0.2% HA	1471.84 ± 35.70[c]	95.39 ± 0.61[ab]	0.90 ± 0.00[b]	1356.05 ± 52.00[b]
0.6% HA	1581.40 ± 72.00[b]	95.04 ± 0.56[b]	0.89 ± 0.00[c]	1371.52 ± 36.19[b]
1.0% HA	1792.91 ± 75.20[a]	94.69 ± 0.66[b]	0.89 ± 0.01[d]	1506.44 ± 57.63[a]
0%	1389.18 ± 39.98[c]	96.75 ± 2.35[a]	0.91 ± 0.01[a]	1224.24 ± 49.21[c]
0.2% KGM	1431.51 ± 37.99[c]	96.71 ± 1.32[a]	0.91 ± 0.00[a]	1262.75 ± 30.71[c]
0.6% KGM	1545.30 ± 80.85[b]	95.97 ± 1.57[a]	0.91 ± 0.00[a]	1363.71 ± 77.67[b]
1.0% KGM	1669.91 ± 69.78[a]	95.77 ± 1.21[a]	0.90 ± 0.00[b]	1466.63 ± 66.60[a]
PBF	1971.56 ± 134.22	69.49 ± 1.65	0.69 ± 0.02	954.84 ± 89.54

Different letters represent significant differences between different samples ($P < 0.05$).
κC, κ-carrageenan; HA, high-acyl gellan; KGM, konjac glucomannanon; PBF, pig back fat.

FIGURE 1
Temperature cycling of the storage modulus (G') of emulsion gels containing different polysaccharides: **(A)** κC, **(B)** HA, and **(C)** KGM. κC, κ-carrageenan; HA, high-acyl gellan; KGM, konjac glucomannanon.
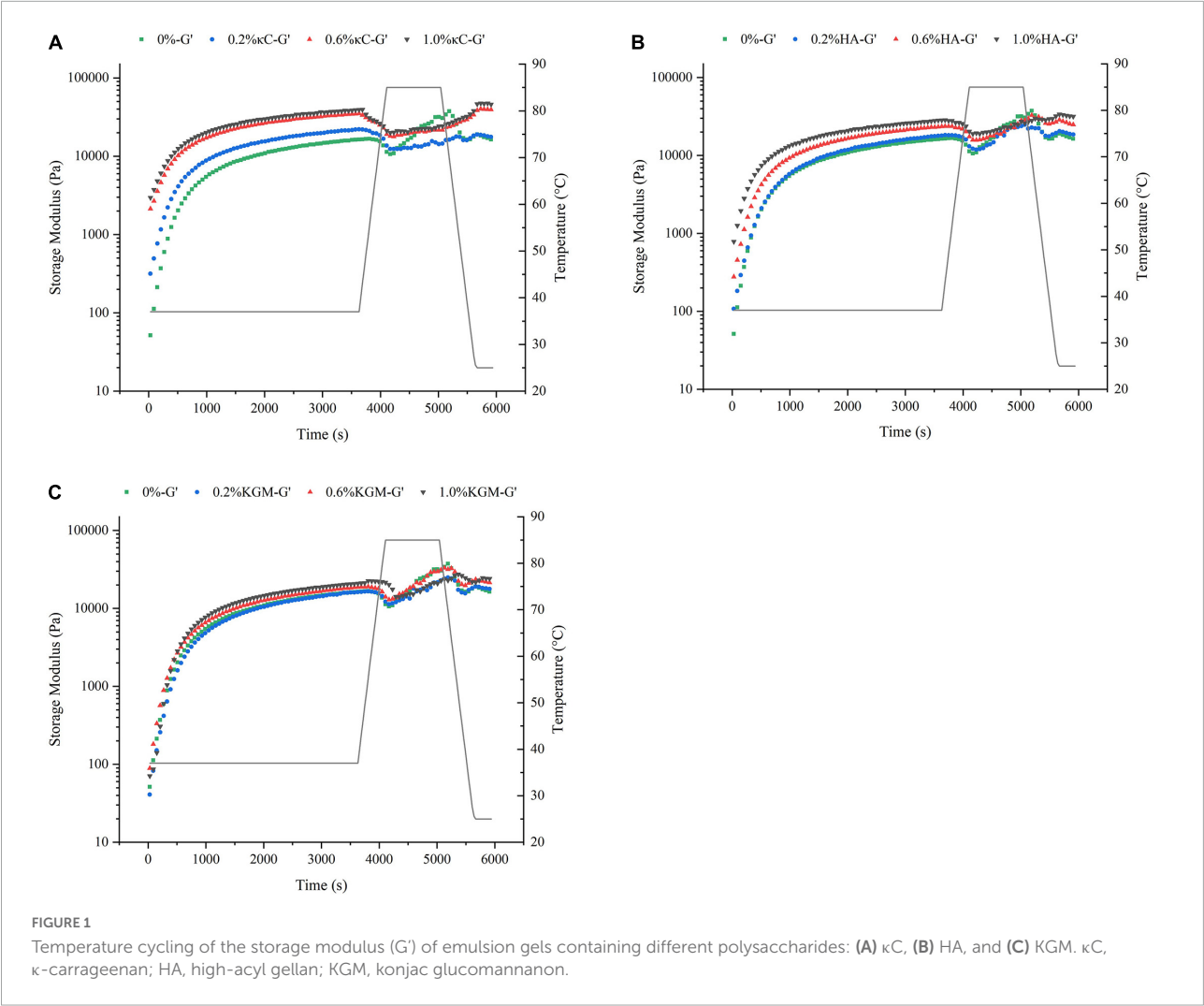
FIGURE 2
Final G' **(A)** and G" **(B)** of the emulsion gels containing different polysaccharides. κC, κ-carrageenan; HA, high-acyl gellan; KGM, konjac glucomannanon.

FIGURE 3
Frequency sweep of the storage modulus (G') of emulsion gels containing different polysaccharides (**A**, κC, **B**, HA, and **C**, KGM) at 25°C. κC, κ-carrageenan; HA, high-acyl gellan; KGM, konjac glucomannanon.

on the types and concentration of polysaccharide. For PPI/κC emulsion gels, the gel strength of G' increased more slowly than that of pure PPI emulsion gel and formed a "kink" in the curve of G'. This "kink" curve of G' has been reported in the BSA/carrageenan mixed gels, which was considered as the result of melting and gelation behavior of carrageenan (29). It can be inferred that the heat-induced melting and colling gelation behavior of κC helps to improve the final gel strength. The G' curves of PPI/KGM emulsion gel almost followed the very similar path of pure PPI emulsion gel at the second insulation stage (85°C) and the followed cooling stage. The reason is that KGM had little gelation behavior at low concentration, showing little impact on the protein gelation behavior (25). The G' curves of PPI/HA emulsion gel was similar to that of pure PPI emulsion gel at low concentration (0.2%), and showed slight kinks at 0.6 and 1.0%, suggesting that the gelation behavior of PPI became stronger at high HA content due to the non-Newtonian property of HA over 0.6% (30). Meanwhile, the incorporation of polysaccharides also improved the effective concentration of PPI by the steric exclusion (24), altering the gel formation process. The different rheological behavior of κC, HA and KGM in emulsion gels also affected the final values of G' and G" after the temperature cycling, as shown in **Figure 2**. It was found that the final G' and G" values of the emulsion gels varied in decreasing order of PPI/κC>PPI/HA>PPI/KGM at the same polysaccharide concentration, which were higher than that of pure protein emulsion gel, indicating a maximum synergistic effect of κC in enhancing protein gel strength.

To further examine the effect of κC, HA, and KGM on the rheological behaviors of emulsion gel system, frequency sweeps, and creep/recovery tests were carried out on the samples. Frequency sweeps provided the mechanical spectrum called the "fingerprint" of gels. Therefore, it was possible to determine the effect of the oscillatory stress rate on G' on the short time

scales of the linear viscoelastic region (LVER). The changes of G' of the emulsion gels containing κC, HA, and KGM over the frequency range of 6.28–128 rad/s were shown in **Figure 3**. The addition of different polysaccharides had different degrees of promotion effect on G'. Moreover, G' exhibited little dependence on the applied frequency suggesting that the network structure of gel was stable and not easy to destroy. The G' values of PPI/κC emulsion gel at 0.6 and 1.0% polysaccharide were significantly higher than that of HA and KGM systems over the whole frequency range. This phenomenon also corresponded well to the TPA test results in which the PPI/κC emulsion gel had the greatest hardness. **Table 2** showed the power law constant (K') and exponent (n') derived from the power law model. The values of K' and n' increased with the increase in the polysaccharide content, and reached the maximum at 1.0%. The increased K' of emulsion gels reflected a stronger gel network with higher rigidity (31). The values of n' of all emulsion gels were low, confirming that the time stability of the covalent bonds (TG induced) production in the gel network (32). Relevant researches showed that the n' of fully covalently crosslinked gels was 0, while the n' of physical gels was positive (33). The n' value increased with the increase of polysaccharide content, suggesting that the non-covalent interactions occurred between protein and polysaccharides.

The rheological properties of emulsion gels at 25°C were also characterized by transient tests, which made it possible to differentiate the structural characteristics of gels on a longer time scale (34). The changes in strain versus time (**Figure 4**) showed that the deformation degree of pure PPI emulsion gels was greatest, and it became smaller with the increase in the polysaccharide content, the emulsion gels containing 1.0% (w/w) of polysaccharide are least deformed, indicating the high resistance against external force. At 1.0% polysaccharide, the total strain of the emulsion gels increased in the order of PPI/κC<PPI/HA<PPI/KGM, suggesting the stronger gel network of PPI/κC emulsion gel. It was interesting that, the strains of recovery phase of PPI/κC, PPI/HA systems were obviously higher at 0.6 and 1.0% than at 0.2%, while PPI/KGM system showed the opposite trend, suggesting that the gelation of κC and HA reduced the anti-deformability of emulsion gels. Relationship between creep compliance and time could also reflect the rigidly of gels (35). A higher creep compliance (J) value signified a weaker structure, while a lower value indicated a stronger one (31). The creep behavior of emulsion gels was shown in **Figure 5**. The J of emulsion gels gradually decreased with the increase of polysaccharides content. In **Table 3**, values of parameters obtained from fitting creep data to Burger's model (Eq. 2) were listed. It can be seen that the addition of polysaccharides promoted the instantaneous elastic behavior (G_0) and delayed elastic behavior (G_1), and they reached the maximum at 1.0% κC, which demonstrated the incorporation of polysaccharides enhanced the structural strength of gels (31). The increase in the μ_0 value indicated an increase in the viscous

TABLE 2 The parameters of power law function model of emulsion gels containing different polysaccharides at 25°C.

Sample	K' (10^3Pa)	n'	r^2
0% κC	14.73 ± 2.85[d]	0.059 ± 0.001[d]	0.9989
0.2% κC	16.21 ± 1.96[c]	0.065 ± 0.000[c]	0.9997
0.6% κC	37.99 ± 3.19[b]	0.069 ± 0.000[a]	0.9999
1.0% κC	47.36 ± 6.78[a]	0.068 ± 0.000[b]	0.9996
0% HA	14.73 ± 2.85[d]	0.059 ± 0.001[d]	0.9989
0.2% HA	16.87 ± 4.83[c]	0.065 ± 0.001[c]	0.9980
0.6% HA	23.34 ± 2.69[b]	0.071 ± 0.000[b]	0.9997
1.0% HA	29.83 ± 2.8[a]	0.073 ± 0.000[a]	0.9998
0% KGM	14.73 ± 2.85[d]	0.059 ± 0.001[d]	0.9989
0.2% KGM	16.14 ± 2.21[c]	0.062 ± 0.000[c]	0.9995
0.6% KGM	19.87 ± 4.07[b]	0.066 ± 0.001[b]	0.9990
1.0% KGM	22.56 ± 2.41[a]	0.071 ± 0.000[a]	0.9998

Different letters represent significant differences between different samples ($P < 0.05$).
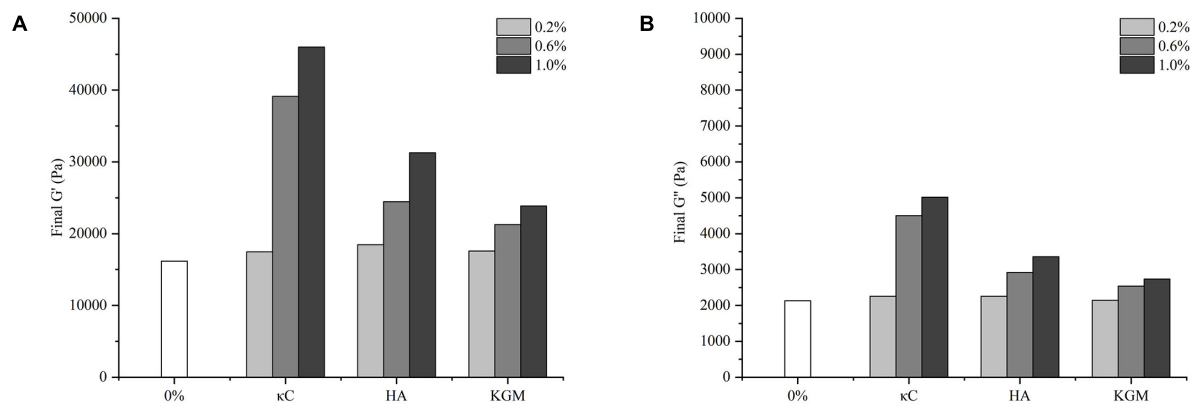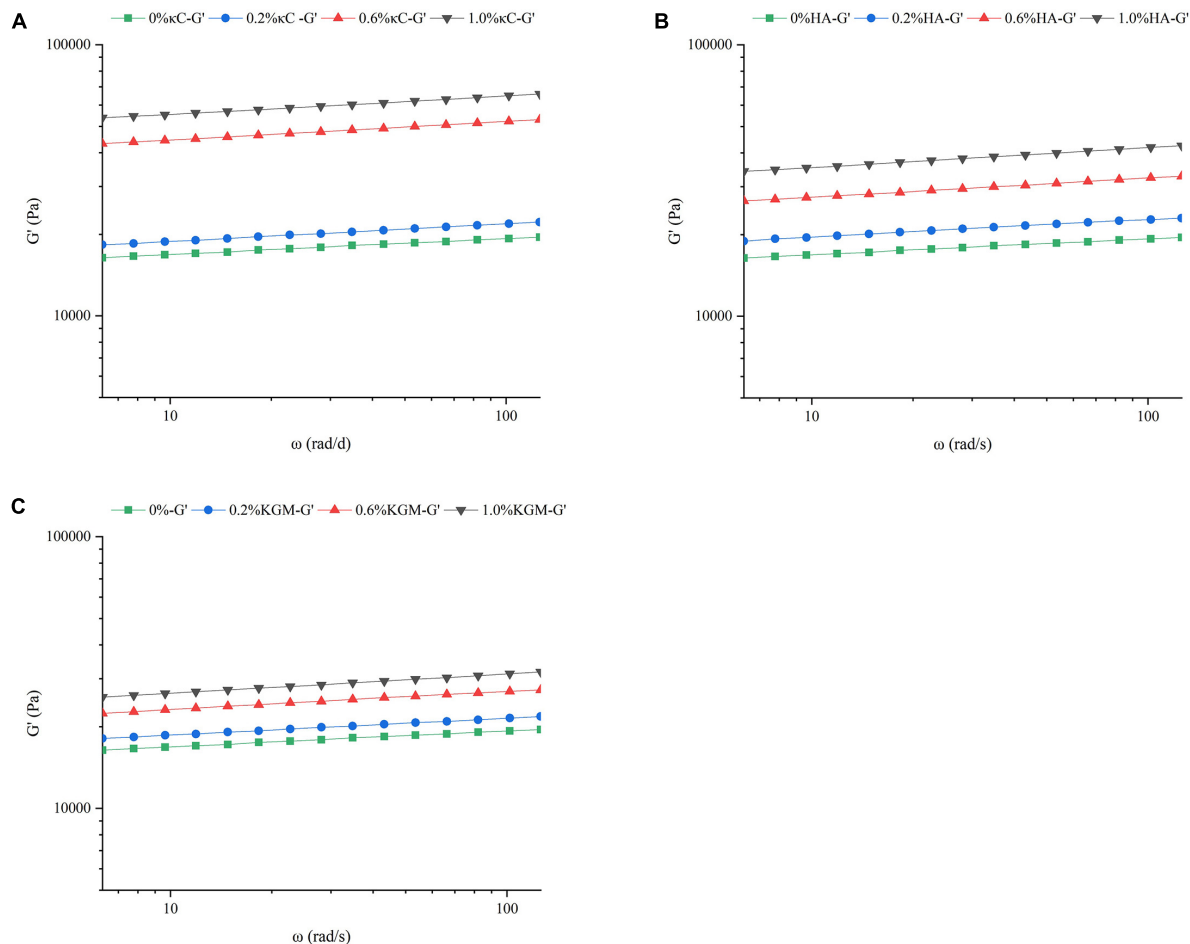κC, κ-carrageenan; HA, high-acyl gellan; KGM, konjac glucomannanon.

FIGURE 4

Creep-recovery behavior of emulsion gels containing different polysaccharides: **(A)** κC, **(B)** HA, and **(C)** KGM. κC, κ-carrageenan; HA, high-acyl gellan; KGM, konjac glucomannanon.

component of gels. The results showed that low content of polysaccharides had no noticeable effect on the viscosity, while polysaccharides at high concentrations had a promoting effect, especially κC. For the retardation time of Kelvin component (λ), PPI/κC emulsion gel with high λ values reached complete deformation more slowly than that of PPI/HA and PPI/KGM gels. The creep/recovery results reflected the enhancement of the gel structure in the presence of polysaccharide, and κC had the most significant promotion effect.

Microstructure analysis

The microscopic structures of the emulsion gels containing κC, HA, and KGM were characterized by CLSM and SEM. **Figure 6** showed the CLSM micrographs of the emulsion gels varied with polysaccharide proportion. The network structures of the emulsion gels without polysaccharide were continuous

uninterrupted and the oil droplets were distributed uniformly. Images of emulsion gels containing 0.2% (w/w) κC showed a distinct κC phase which appeared as melanocratic and small inclusions with irregular shapes (as indicated by the arrow in the figures), suggesting the formation of phase separation in PPI/κC emulsion gel. Increasing the concentration of κC to 0.6 or 1.0% further promoted the phase separation behavior with increased size of the κC inclusions. This phenomenon also occurred in PPI/HA and PPI/KGM emulsion gels where the HA-rich phase showed irregular threadlike inclusions and the KGM-rich phase appeared as oval inclusions (as indicated by arrows in the figures). Tobin et al. (25) showed a similar result for whey protein/KGM systems, finding a protein-enriched phase with entrapped KGM inclusions. The formation of this microstructure might be attributed to the polysaccharide-induced microphase separation during gel formation due to thermodynamically incompatibility between two biopolymers. The effective concentration of both polymers increased during
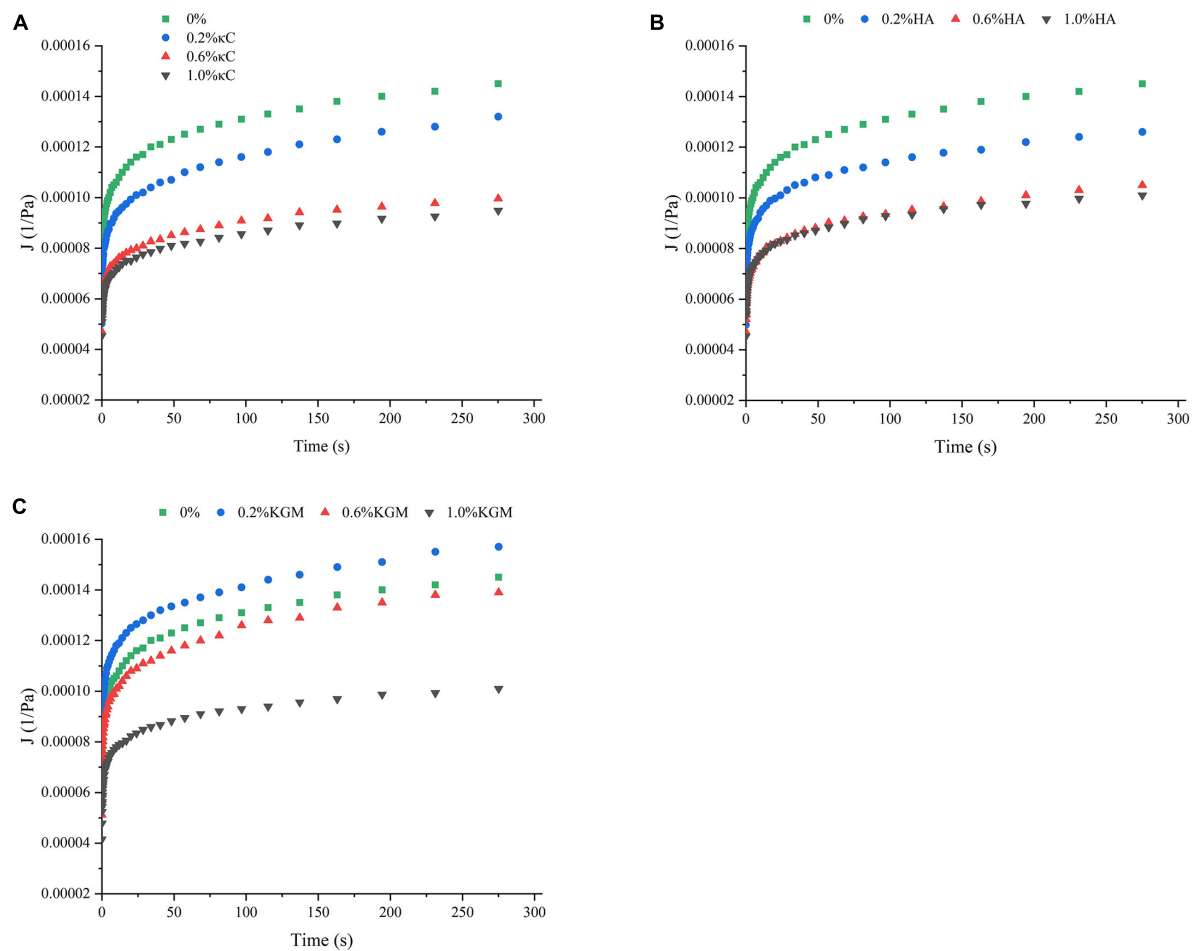
FIGURE 5

Compliance curve of emulsion gels containing different polysaccharides: **(A)** κC, **(B)** HA, and **(C)** KGM. κC, κ-carrageenan; HA, high-acyl gellan; KGM, konjac glucomannanon.

TABLE 3 The parameters of Burger's model of emulsion gels containing different polysaccharides.

Sample	G_0 (10^3 Pa)	G_1 (10^3 Pa)	λ (s)	μ_0 (10^6 Pas)	r^2
0% κC	13.67 ± 0.42^d	25.09 ± 0.70^d	3.56 ± 0.03^d	7.33 ± 0.01^c	0.9618
0.2% κC	15.2 ± 0.14^c	30.42 ± 0.84^c	3.93 ± 0.04^c	7.30 ± 0.01^c	0.9670
0.6% κC	17.57 ± 0.31^b	44.26 ± 0.92^b	4.71 ± 0.05^b	11.78 ± 0.02^b	0.9695
1.0% κC	18.42 ± 0.56^a	46.38 ± 1.04^a	4.86 ± 0.05^a	12.75 ± 0.02^a	0.9725
0% HA	13.67 ± 0.72^c	25.09 ± 0.7^d	3.56 ± 0.03^b	7.33 ± 0.01^d	0.9618
0.2% HA	15.40 ± 0.57^b	29.43 ± 0.82^c	3.39 ± 0.03^c	8.57 ± 0.01^c	0.9614
0.6% HA	17.80 ± 0.56^a	39.21 ± 0.42^b	3.99 ± 0.04^a	10.21 ± 0.02^b	0.9737
1.0% HA	17.66 ± 0.70^a	40.21 ± 0.56^a	3.99 ± 0.04^a	11.88 ± 0.02^a	0.9641
0% KGM	13.67 ± 0.42^c	25.09 ± 0.70^c	3.56 ± 0.03^a	7.33 ± 0.01^b	0.9618
0.2% KGM	12.04 ± 0.42^d	24.74 ± 0.70^c	3.51 ± 0.03^b	7.07 ± 0.01^c	0.9632
0.6% KGM	14.39 ± 0.24^b	27.62 ± 0.68^b	3.03 ± 0.03^d	6.80 ± 0.01^d	0.9550
1.0% KGM	18.40 ± 0.29^a	36.76 ± 0.61^a	3.20 ± 0.03^c	11.60 ± 0.02^a	0.9578

Different letters represent significant differences between different samples ($P < 0.05$). κC, κ-carrageenan; HA, high-acyl gellan; KGM, konjac glucomannanon.
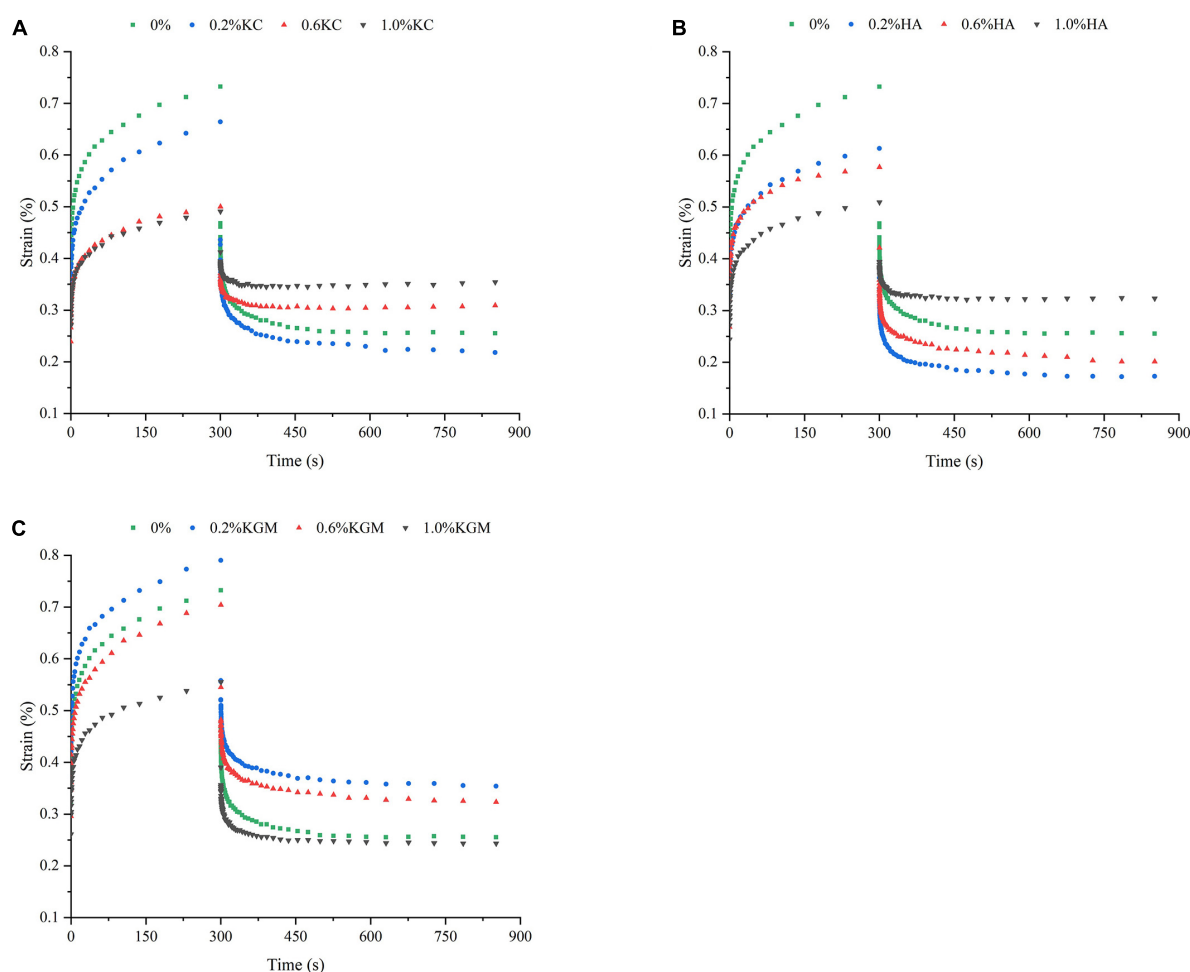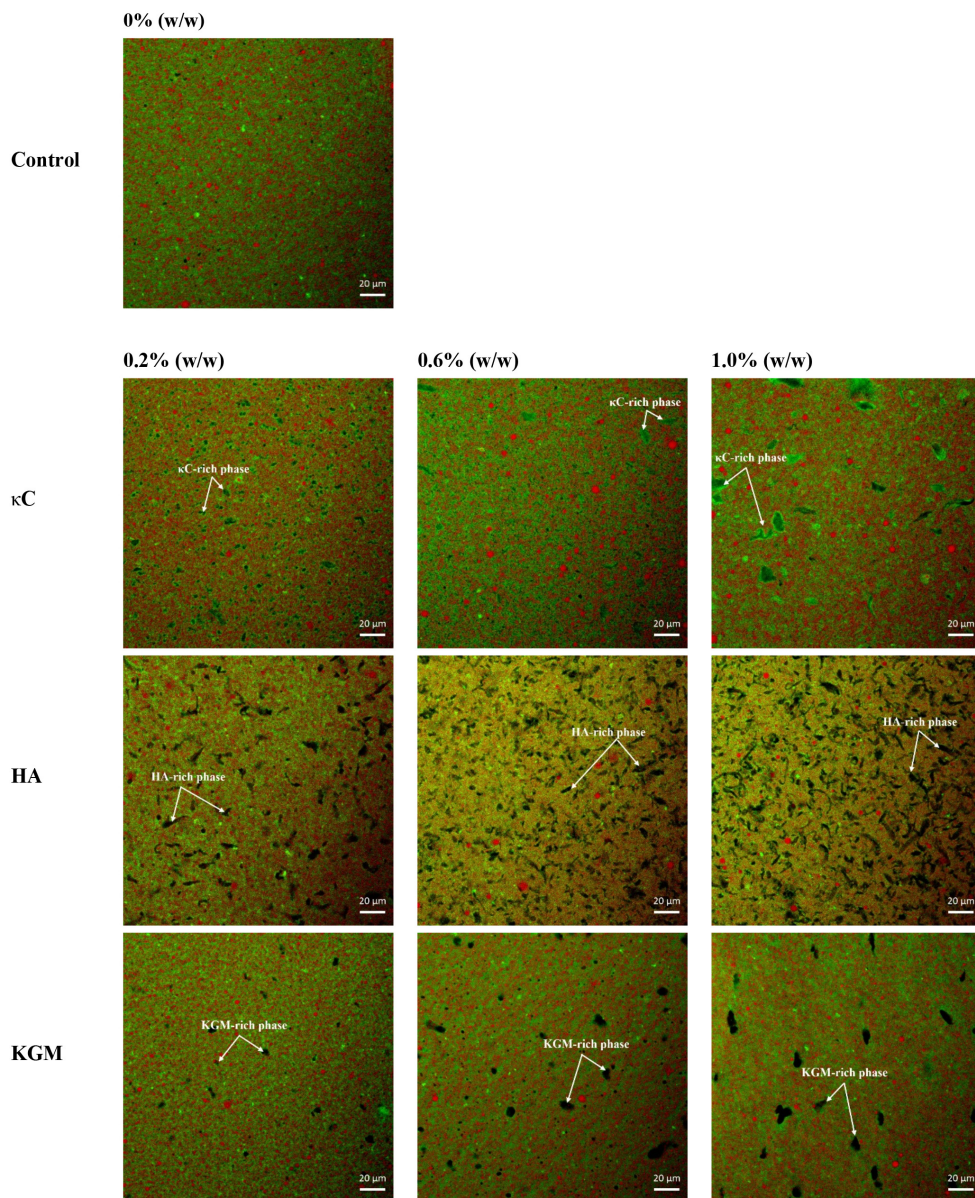
FIGURE 6

Confocal laser scanning microscopy (CLSM) images of emulsion gels containing different polysaccharides. Scale bar is 20 μm. κC, κ-carrageenan; HA, high-acyl gellan; KGM, konjac glucomannanon.

phase separation, confining them to a portion of the total volume, thus improving the gel strength of the integral system (25, 36). In addition, compared with homogeneous distribution of oil droplets of the pure protein emulsion gel, the oil droplets of all given mixed emulsion gels became unevenly distributed by forming large and small oil droplets, suggesting polysaccharide induced microphase separation also caused the broken and coalescence of oil droplets.

Further investigation of the evolution of emulsion gel microstructure was conducted using SEM. As shown in Figure 7, the coarser and less homogenous structures were

formed as the polysaccharide concentration increased. The 1000× pictures provided more details of the emulsion gels (inset). As shown in the images, a homogeneous structure that consisted of protein networks and oil droplets (circular shaped holes) with uniform size was observed in the PPI emulsion gels. As the concentration of polysaccharides increased, the structures of the PPI/polysaccharide emulsion gels became more heterogeneous with oil droplets of different sizes (see inset). Compared to PPI emulsion gels, the oil droplets in PPI/HA emulsion gels became larger in size, while the oil droplets for PPI/κC emulsion gels became smaller, due to the presence of
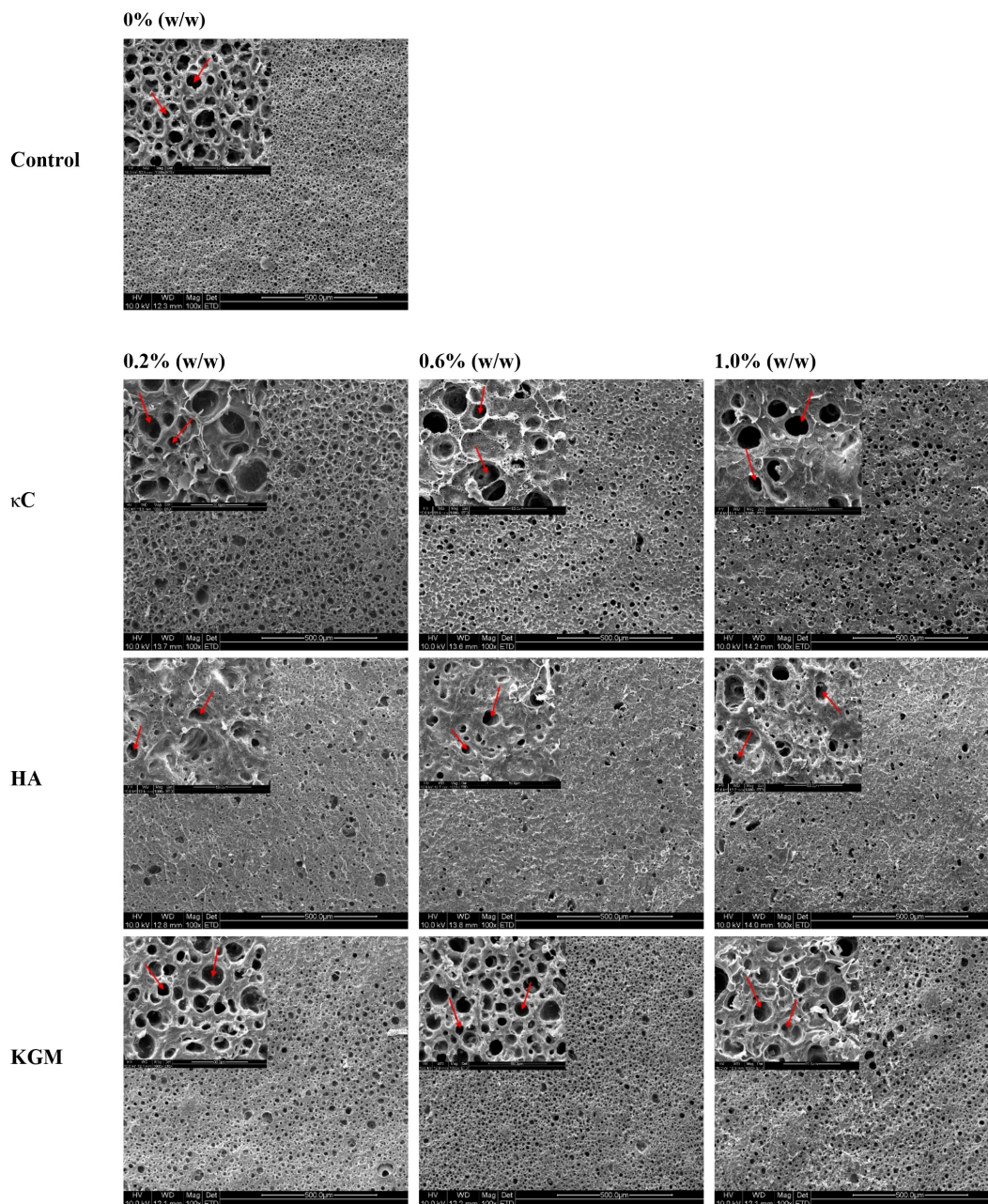
FIGURE 7
Scanning electron microscopy (SEM) images (100×) of emulsion gels containing different polysaccharides. The holes represent oil droplets; the insert figure represents the details of emulsion gel at (1000×). κC, κ-carrageenan; HA, high-acyl gellan; KGM, konjac glucomannanon.

a large amounts of irregular inclusions causing the broken of oil droplets (**Figure 6**, HA image). Combined with CLSM images, it seemed that HA-rich phase was disordered in the gels, while KGM-rich phase was evenly distributed in the gels. The difference in the gel microstructure among different polysaccharides further affected the textural and rheological properties of the three emulsion gel systems.

Water holding properties

Water molecules mobility and distribution in the gel systems were measured by LF-NMR. Water in gels can be divided into three types: T_{2b} was considered to be bound water, relaxation time mainly between 0 and 1 ms; T_{21} was considered to be immobilized water, which represented water trapped in the
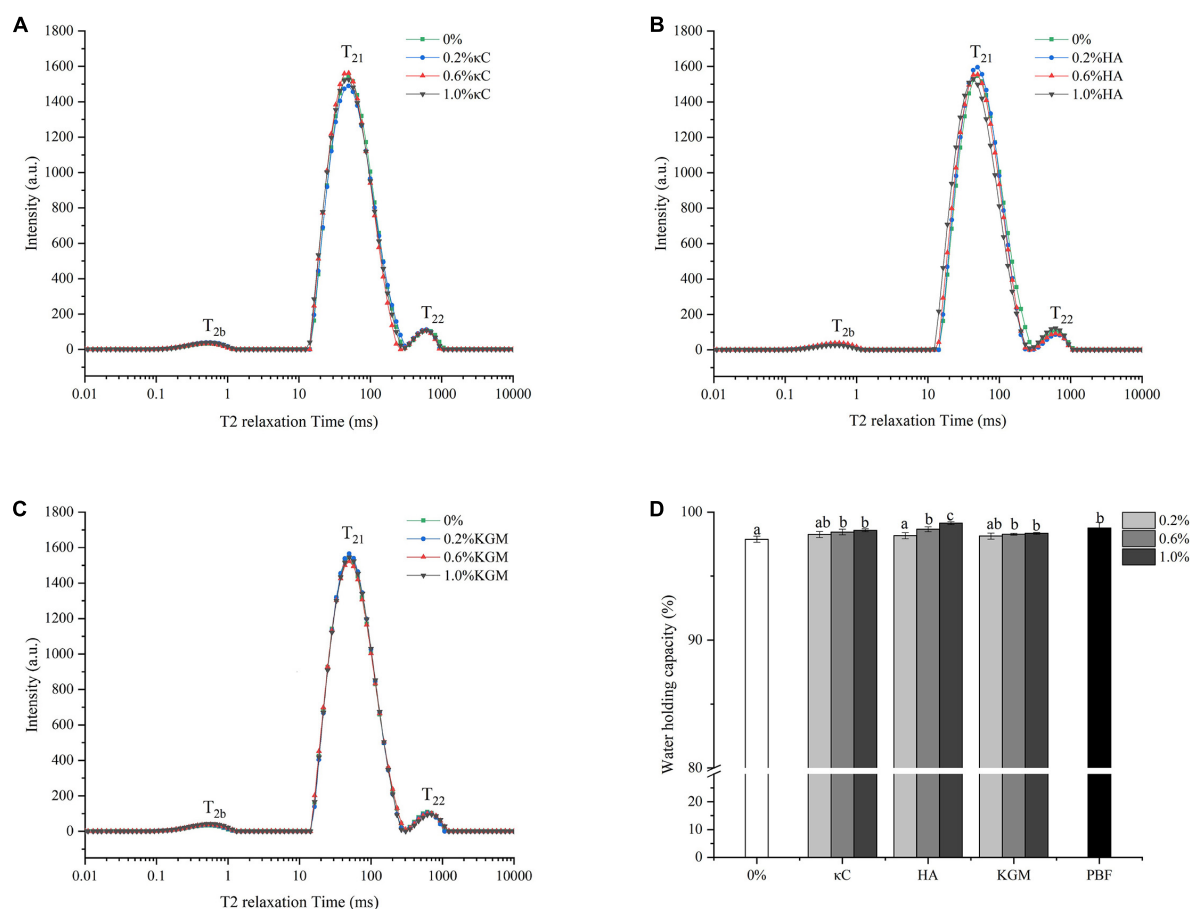
FIGURE 8

Water holding properties of emulsion gels containing different polysaccharides. **(A–C)** Transverse relaxation curves; **(D)** Water-holding capacity. Different letters indicate that the values are significantly different (*P* < 0.05). κC, κ-carrageenan; HA, high-acyl gellan; KGM, konjac glucomannanon; PBF, pig back fat.

three-dimension network, and the relaxation time was mainly between 40 and 60 ms; T_{22} was assigned to be free water, relaxation time mainly between 600 and 800 ms (37). As shown in **Figures 8A–C**, the T_{2b} and T_{21} fractions accounted for more than 96% in all emulsion gels. Here, the T_{21} relaxation peak held an overwhelmingly dominant position, suggesting the water mobility remained highly restricted. The WHC of emulsion gels was shown in **Figure 8D**, which was consistent with the results of LF-NMR. Within the treatment concentrations (0.2– 1.0% κC/HA/KGM), the WHC of PPI/polysaccharide emulsion gels slightly increased and reached a level comparable to pig back fat. It was reported that WHC was closely correlated with the density of the gel network structures (38, 39). In our work, the incorporation of polysaccharides formed a more heterogeneous microstructure (**Figures 6, 7**), suggesting that the WHC of the gel network structures was not be affected by the microphase separation of polysaccharide; while lower permeability of polysaccharides could allow water to be effectively "bound" in the emulsion gel matrices.

FTIR spectroscopy

The information of chemical interaction of the emulsion gels containing κC, HA, and KGM was further investigated by FTIR spectra. As shown in **Figure 9**, the broad absorption peak between 3,100 and 3,400 cm^{-1} was assigned to the response of hydrogen bond (O–H and N–H). With the addition of κC or HA or KGM, the peak of hydrogen bond moved to higher value, indicating the strength of hydrogen bonds was weakened in the emulsion gels during gel formation. It could be inferred that other forces were involved in the formation of PPI/polysaccharide emulsion gels. This observation agreed with the previous report of gelatin and κC/KGM composite gels (27). The strong absorption bands at 2,923, 2,853, 1,744, and 1,026 cm^{-1} belong to characteristic signals of sunflower seed oil. These results indicated that sunflower oil in the emulsion gels just as a filler, although the particle size of the oil droplets had changed.
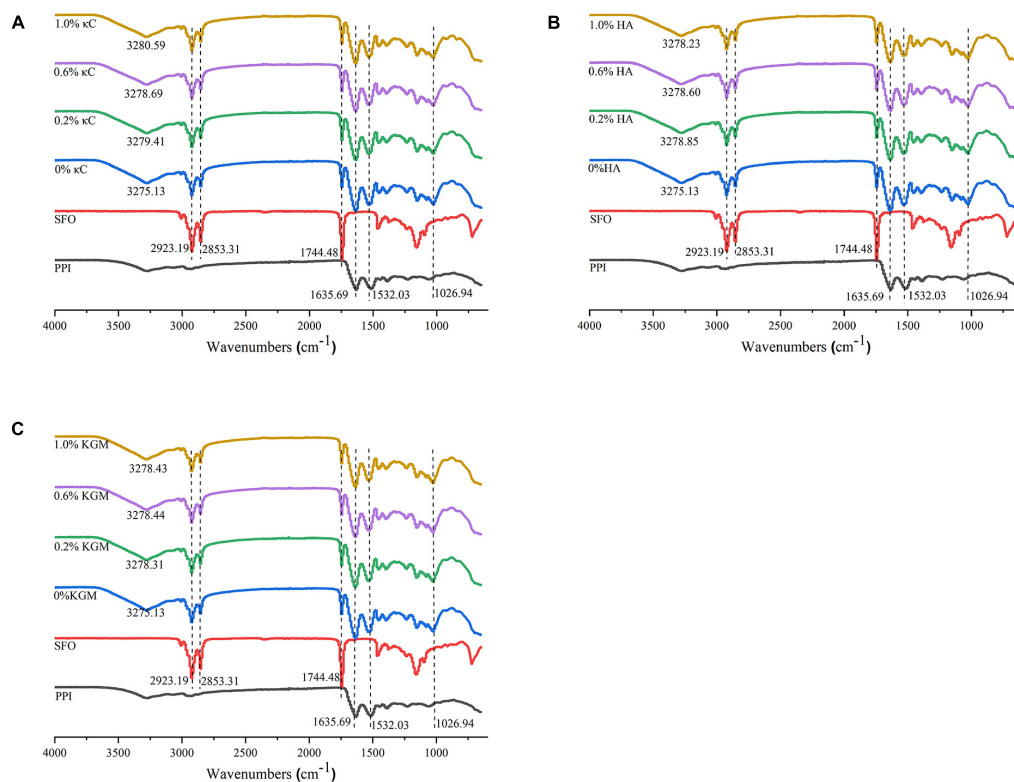
FIGURE 9
Infrared spectra of emulsion gels containing different polysaccharides: **(A)** κC, **(B)** HA, and **(C)** KGM. PPI, pea protein isolate; κC, κ-carrageenan; HA, high-acyl gellan; KGM, konjac glucomannanon; SFO, Sunflower seed oil.

TABLE 4 The composition of β-Sheet, random coils, α-Helix, β-Turns in secondary structure of emulsion gels containing different polysaccharides.

Sample	β -Sheet (%)	Random coils (%)	α -Helix (%)	β -Turns (%)
PPI	41.75 ± 0.57[a]	12.75 ± 0.06[b]	21.73 ± 0.20[a]	23.77 ± 0.25[c]
0% κC	42.44 ± 0.66[a]	13.94 ± 0.05[a]	14.18 ± 0.18[b]	29.40 ± 0.45[a]
0.2% κC	43.12 ± 0.27[a]	13.96 ± 0.09[a]	14.00 ± 0.10[b]	28.78 ± 0.22[ab]
0.6% κC	43.57 ± 0.18[a]	13.87 ± 0.03[a]	13.98 ± 0.02[b]	28.57 ± 0.18[b]
1.0% κC	43.13 ± 0.12[a]	13.91 ± 0.04[a]	14.05 ± 0.08[b]	28.93 ± 0.15[ab]
PPI	41.75 ± 0.57[a]	12.75 ± 0.06[b]	21.73 ± 0.20[a]	23.77 ± 0.25[c]
0% HA	42.44 ± 0.66[a]	13.94 ± 0.05[a]	14.18 ± 0.18[b]	29.40 ± 0.45[ab]
0.2% HA	43.18 ± 0.21[a]	13.96 ± 0.01[a]	14.05 ± 0.12[b]	28.81 ± 0.22[b]
0.6% HA	42.47 ± 0.29[a]	13.99 ± 0.05[a]	14.23 ± 0.15[b]	29.35 ± 0.19[ab]
1.0% HA	42.31 ± 0.05[a]	14.01 ± 0.06[a]	14.21 ± 0.11[b]	29.47 ± 0.08[a]
PPI	41.75 ± 0.57[a]	12.75 ± 0.06[b]	21.73 ± 0.20[a]	23.77 ± 0.25[c]
0% KGM	42.44 ± 0.66[a]	13.94 ± 0.05[a]	14.18 ± 0.18[b]	29.40 ± 0.45[ab]
0.2% KGM	43.08 ± 0.13[a]	13.92 ± 0.06[a]	14.10 ± 0.01[b]	28.93 ± 0.05[b]
0.6% KGM	42.30 ± 0.21[a]	13.94 ± 0.03[a]	14.21 ± 0.08[b]	29.52 ± 0.19[ab]
1.0% KGM	41.74 ± 0.14[a]	14.00 ± 0.05[a]	14.45 ± 0.09[b]	29.81 ± 0.07[a]

Different letters represent significant differences between different samples ($P < 0.05$).
PPI, pea protein isolate; κC, κ-carrageenan; HA, high-acyl gellan; KGM, konjac glucomannanon.

Proteins had characteristic absorption bonds in the infrared region (40). The amide I band (1635.69 cm^{-1}) was mainly caused by the C = O stretching vibration in the peptide bond.

The amide II band (1532.03 cm^{-1}) represented the bending vibration of the N-H group and the stretching vibration of the C-N group. For all PPI emulsion gels, increase in the

absorption peak intensity at amide I and II were observed compared to PPI samples, which might be attributable to the formation of hydrogen bonds and cross-linking induced isopeptide bonds during the gel formation (41). Changes in secondary structures of the protein calculate from amide I were listed in Table 4. Overall, the α-helix content of emulsion gels after TG crosslinking decreased significantly, while β-sheet, β-turn and random coils slightly increased compared to uncrosslinked PPI, which might be due to the unfolding of protein during TG crosslinking process. The presence of different polysaccharides had little influence on the secondary structures, which further suggested their filler role in the emulsion gels.

Conclusion

In this work, the effects of polysaccharide type and concentration on the texture, rheological, microstructure and other functional properties of PPI/polysaccharide emulsion gels were studied, in order to explore the similarity to functional properties of pig back fat. The presence of polysaccharide significantly enhanced the hardness of all three PPI/polysaccharide emulsion gel systems, and PPI/κC system at a high polysaccharide content reached a similar level in hardness with pig back fat. Rheological results indicated that κC underwent gelation during protein gelation, which exhibited synergistic effects with PPI in term of improving the storage modulus (G'). The frequency sweep, the creep and recovery test results confirmed that the increase in polysaccharide concentration especially for PPI/κC system, had an obvious promoting effect on G', instantaneous elastic behavior (G_0) and delayed elastic behavior (G_1), as well as the resistance against external forces. CLSM and SEM results indicated that the presence of polysaccharides destroyed the uniform distribution of protein network, resulted in the microphase separation (with different shapes of inclusions) as well as the broken and coalescence of oil droplets. However, the water holding capacity of PPI/polysaccharide emulsion gels was not affected by the microphase separation behavior. In the future, the plastic behavior and melting properties of PPI/polysaccharide emulsion gels will be further investigated to simulated more functional properties of pig back fat.

Data availability statement

The original contributions presented in this study are included in the article/supplementary material, further inquiries can be directed to the corresponding author.

Author contributions

WH: conceptualization, investigation, and writing – original draft. JL: data curation and investigation. YH: supervision and resources. YC: data curation and formal analysis. XK and CZ: writing – review and editing and validation. XL: methodology, conceptualization, and project administration. All authors contributed to the article and approved the submitted version.

Funding

Conflict of interest

The authors declare that the research was conducted in the absence of any commercial or financial relationships that could be construed as a potential conflict of interest.

Publisher's note

All claims expressed in this article are solely those of the authors and do not necessarily represent those of their affiliated organizations, or those of the publisher, the editors and the reviewers. Any product that may be evaluated in this article, or claim that may be made by its manufacturer, is not guaranteed or endorsed by the publisher.

References

1. Springmann M, Clark M, Mason-D'Croz D, Wiebe K, Bodirsky BL, Lassaletta L, et al. Options for keeping the food system within environmental limits. *Nature.* (2018) 562:519–25. doi: 10.1038/s41586-018-0594-0

2. Domingo JL, Nadal M. Carcinogenicity of consumption of red meat and processed meat: a review of scientific news since the IARC decision. *Food Chem Toxicol.* (2017) 105:256–61. doi: 10.1016/j.fct.2017.04.028

3. Saget S, Costa M, Santos CS, Vasconcelos MW, Gibbons J, Styles D, et al. Substitution of beef with pea protein reduces the environmental footprint of meat balls whilst supporting health and climate stabilisation goals. *J Cleaner Prod.* (2021) 297:126447. doi: 10.1016/j.jclepro.2021.126447

4. Godfray HCJ. *Meat: the Future Series-Alternative Proteins.* Cologny: World Economic Forum (2019).

5. Osen R, Toelstede S, Eisner P, Schweiggert-Weisz U. Effect of high moisture extrusion cooking on protein-protein interactions of pea (*Pisum sativum* L.) protein isolates. *Int J Food Sci Technol.* (2015) 50:1390–6. doi: 10.1111/ijfs.12783

6. Arshad M, Anwar S, Pasha I, Ahmed F, Aadil RM. Development of imitated meat product by utilizing pea and lentil protein isolates. *Int J Food Sci Technol.* (2022) 57:3031–7. doi: 10.1111/ijfs.15631

7. Huang ZG, Wang XY, Zhang JY, Liu Y, Zhou T, Chi SY, et al. Effect of heat treatment on the nonlinear rheological properties of acid-induced soy protein isolate gels modified by high-pressure homogenization. *LWT Food Sci Technol.* (2022) 157:113094. doi: 10.1016/j.lwt.2022.113094

8. Kang Z-L, Chen F-S, Ma H-J. Effect of pre-emulsified soy oil with soy protein isolate in frankfurters: a physical-chemical and Raman spectroscopy study. *LWT Food Sci Technol.* (2016) 74:465–71. doi: 10.1016/j.lwt.2016.08.011

9. Jeongtaek L, Sungmin J, Im Kyung O, Suyong L. Evaluation of soybean oil-carnauba wax oleogels as an alternative to high saturated fat frying media for instant fried noodles. *LWT Food Sci Technol.* (2017) 84:788–94. doi: 10.1016/j.lwt.2017.06.054

10. Puscas A, Muresan V, Socaciu C, Muste S. Oleogels in food: a review of current and potential applications. *Foods.* (2020) 9:E70. doi: 10.3390/foods9010070

11. Khiabani AA, Tabibiazar M, Roufegarinejad L, Hamishehkar H, Alizadeh A. Preparation and characterization of carnauba Wax/Adipic acid oleogel: a new reinforced oleogel for application in cake and beef burger. *Food Chem.* (2020) 333:127446. doi: 10.1016/j.foodchem.2020.127446

12. Ferro AC, Paglarini CD, Pollonio MAR, Cunha RL. Glyceryl monostearate-based oleogels as a new fat substitute in meat emulsion. *Meat Sci.* (2021) 174:108424. doi: 10.1016/j.meatsci.2020.108424

13. Dickinson E. Emulsion gels: the structuring of soft solids with protein-stabilized oil droplets. *Food Hydrocoll.* (2012) 28:224–41. doi: 10.1016/j.foodhyd.2011.12.017

14. Lu YY, Cao JX, Zhou CY, He J, Sun YY, Xia Q, et al. The technological and nutritional advantages of emulsified sausages with partial back-fat replacement by succinylated chicken liver protein and pre-emulsified sunflower oil. *LWT Food Sci Technol.* (2021) 149:111824. doi: 10.1016/j.lwt.2021.111824

15. Paglarini CD, Vidal VAS, Ribeiro W, Ribeiro APB, Bernardinelli OD, Herrero AM, et al. Using inulin-based emulsion gels as fat substitute in salt reduced bologna sausage. *J Sci Food Agric.* (2021) 101:505–17. doi: 10.1002/jsfa.10659

16. Serdaroglu M, Nacak B, Karabiyikoglu M. Effects of beef fat replacement with gelled emulsion prepared with olive oil on quality parameters of chicken patties. *Korean J Food Sci Anim Resour.* (2017) 37:376–84. doi: 10.5851/kosfa.2017.37.3.376

17. Dreher J, Blach C, Terjung N, Gibis M, Weiss J. Formation and characterization of plant-based emulsified and crosslinked fat crystal networks to mimic animal fat tissue. *J Food Sci.* (2020) 85:421–31. doi: 10.1111/1750-3841.14993

18. Edmund Daniel CO, Marangoni AG. Organogels: an alternative edible oil-structuring method. *J Am Oil Chem Soc.* (2012) 89:749–80. doi: 10.1007/s11746-012-2049-3

19. Shen KJ, Long J, Li XF, Hua YF, Chen YM, Kong XZ, et al. Complexation of pea protein isolate with dextran sulphate and interfacial adsorption behaviour and O/W emulsion stability at acidic conditions. *Int J Food Sci Technol.* (2022) 57:2333–45. doi: 10.1111/ijfs.15586

20. Steffe JF. *Rheological Methods in Food Process Engineering.* Dallas, TX: Freeman press (1996).

21. Xiaofei L, Chuo G, Peiyuan L, Jiaojiao S, Xi Y, Yurong G. Structural Characteristics of gluconic acid delta-lactone induced casein gels as regulated by Gellan gum incorporation. *Food Hydrocoll.* (2021) 120:106897. doi: 10.1016/j.foodhyd.2021.106897

22. Qayum A, Hussain M, Li M, Li J, Shi R, Li T, et al. Gelling, microstructure and water-holding properties of alpha-lactalbumin emulsion gel: impact of combined ultrasound pretreatment and laccase cross-linking. *Food Hydrocoll.* (2021) 110:106122. doi: 10.1016/j.foodhyd.2020.106122

23. Kwon HC, Shin DM, Yune JH, Jeong CH, Han SG. Evaluation of gels formulated with whey proteins and sodium dodecyl sulfate as a fat replacer in low-fat sausage. *Food Chem.* (2021) 337:127682. doi: 10.1016/j.foodchem.2020.127682

24. Zhao HB, Chen J, Hemar Y, Cui B. Improvement of the rheological and textural properties of calcium sulfate-induced soy protein isolate gels by the incorporation of different polysaccharides. *Food Chem.* (2020) 310:125983. doi: 10.1016/j.foodchem.2019.125983

25. Tobin JT, Fitzsimons SM, Chaurin V, Kelly AL, Fenelon MA. Thermodynamic incompatibility between denatured whey protein and konjac glucomannan. *Food Hydrocoll.* (2012) 27:201–7. doi: 10.1016/j.foodhyd.2011.07.004

26. Cakir E, Foegeding EA. Combining protein micro-phase separation and protein-polysaccharide segregative phase separation to produce gel structures. *Food Hydrocoll.* (2011) 25:1538–46. doi: 10.1016/j.foodhyd.2011.02.002

27. Cheng Z, Zhang B, Qiao D, Yan X, Zhao S, Jia C, et al. Addition of K-carrageenan increases the strength and chewiness of gelatin-based composite gel. *Food Hydrocoll.* (2022) 128:107565. doi: 10.1016/j.foodhyd.2022.107565

28. Pires Vilela JA, Cavallieri ÂLF, Lopes da Cunha R. The influence of gelation rate on the physical properties/structure of salt-induced gels of soy protein isolate–gellan gum. *Food Hydrocoll.* (2011) 25:1710–8.

29. Neiser S, Draget KI, Smidsrod O. Gel formation in heat-treated bovine serum albumin-kappa-carrageenan systems. *Food Hydrocoll.* (2000) 14:95–110. doi: 10.1016/s0268-005x(99)00052-1

30. Jampen S, Britt IJ, Tung MA. Gellan polymer solution properties: dilute and concentrated regimes. *Food Res Int.* (2000) 33:579–86.

31. Bi CH, Chi SY, Wang XY, Alkhatib A, Huang ZG, Liu Y. Effect of flax gum on the functional properties of soy protein isolate emulsion gel. *LWT Food Sci Technol.* (2021) 149:111846. doi: 10.1016/j.lwt.2021.111846

32. Moreno HM, Dominguez-Timon F, Diaz MT, Pedrosa MM, Borderias AJ, Tovar CA. Evaluation of gels made with different commercial pea protein isolate: rheological, structural and functional properties. *Food Hydrocoll.* (2020) 99:105375. doi: 10.1016/j.foodhyd.2019.105375

33. Zhang Q, Gu LP, Su YJ, Chang CH, Yang YJ, Li JH. Development of soy protein isolate/kappa-carrageenan composite hydrogels as a delivery system for hydrophilic compounds: *Monascus* yellow. *Int J Biol Macromol.* (2021) 172:281–8. doi: 10.1016/j.ijbiomac.2021.01.044

34. Herranz B, Tovar CA, Solo-de-Zaldivar B, Borderias AJ. Influence of alkali and temperature on glucomannan gels at high concentration. *LWT Food Sci Technol.* (2013) 51:500–6. doi: 10.1016/j.lwt.2012.11.023

35. Bi CH, Li D, Wang LJ, Gao F, Adhikari B. Effect of high shear homogenization on rheology, microstructure and fractal dimension of acid-induced spi gels. *J Food Eng.* (2014) 126:48–55. doi: 10.1016/j.jfoodeng.2013.10.040

36. Gilsenan PM, Richardson RK, Morris ER. Associative and segregative interactions between gelatin and low-methoxy pectin. Part 3. Quantitative analysis of co-gel moduli. *Food Hydrocoll.* (2003) 17:751–61.

37. Ma T, Xiong YL, Jiang J. Calcium-aided fabrication of pea protein hydrogels with filler emulsion particles coated by Ph12-Shifting and ultrasound treated protein. *Food Hydrocoll.* (2022) 125:107396. doi: 10.1016/j.foodhyd.2021.107396

38. Haibo Z, Weiwei L, Fang Q, Jie C. Calcium sulphate-induced soya bean protein tofu-type gels: influence of denaturation and particle size. *Int J Food Sci Technol.* (2016) 51:731–41. doi: 10.1111/ijfs.13010

39. Kuhn KR, Fazani Cavallieri AL, da Cunha RL. Cold-set whey protein gels induced by calcium or sodium salt addition. *Int J Food Sci Technol.* (2010) 45:348–57. doi: 10.1111/j.1365-2621.2009.02145.x

40. Liang XP, Ma CC, Yan XJ, Zeng HH, McClements DJ, Liu XB, et al. Structure, rheology and functionality of whey protein emulsion gels: effects of double cross-linking with transglutaminase and calcium ions. *Food Hydrocoll.* (2020) 102:105569. doi: 10.1016/j.foodhyd.2019.105569

41. Zhang X, Wang W, Wang Y, Wang Y, Wang X, Gao G, et al. Effects of nanofiber cellulose on functional properties of heat-induced chicken salt-soluble meat protein gel enhanced with microbial transglutaminase. *Food Hydrocoll.* (2018) 84:1–8. doi: 10.1016/j.foodhyd.2018.05.046

Recent advances in structural characterization of biomacromolecules in foods *via* small-angle X-ray scattering

Yang Sun[1]*[†], Xiujuan Li[2†], Ruixin Chen[1], Fei Liu[1] and Song Wei[3]*

[1]College of Vocational and Technical Education, Yunnan Normal University, Kunming, China, [2]Pharmaceutical Department, The Affiliated Taian City Central Hospital of Qingdao University, Taian, China, [3]Tumor Precise Intervention and Translational Medicine Laboratory, The Affiliated Taian City Central Hospital of Qingdao University, Taian, China

Small-angle X-ray scattering (SAXS) is a method for examining the solution structure, oligomeric state, conformational changes, and flexibility of biomacromolecules at a scale ranging from a few Angstroms to hundreds of nanometers. Wide time scales ranging from real time (milliseconds) to minutes can be also covered by SAXS. With many advantages, SAXS has been extensively used, it is widely used in the structural characterization of biomacromolecules in food science and technology. However, the application of SAXS in charactering the structure of food biomacromolecules has not been reviewed so far. In the current review, the principle, theoretical calculations and modeling programs are summarized, technical advances in the experimental setups and corresponding applications of *in situ* capabilities: combination of chromatography, time-resolved, temperature, pressure, flow-through are elaborated. Recent applications of SAXS for monitoring structural properties of biomacromolecules in food including protein, carbohydrate and lipid are also highlighted, and limitations and prospects for developing SAXS based on facility upgraded and artificial intelligence to study the structural properties of biomacromolecules are finally discussed. Future research should focus on extending machine time, simplifying SAXS data treatment, optimizing modeling methods in order to achieve an integrated structural biology based on SAXS as a practical tool for investigating the structure-function relationship of biomacromolecules in food industry.

Introduction

Bioactive macromolecules, including peptides, nuclear acids, proteins, carbohydrates, and lipids, are not only essential components of food but also are the dominant substances for food to realize its functions. Meantime, biomacromolecules are widely used as additives for beverages, yogurt, cereal products, nuts, snacks, etc. to improve the food nutrition (1). Besides, other functional properties, such as gelation, foamability, water retention and emulsification, typical functions induced by structural changes of biomacromolecules, play significant roles in food processing. Therefore, the structure-function relationship of biomacromolecules is one of the most important topics in food science and technology.

Several experimental techniques are available for the structural characterization of biomacromolecules. High-resolution structural techniques, including crystallography, electron microscopy (EM) and nuclear magnetic resonance (NMR) have yielded incredibly detailed structural information at the atomic level on highly populated static states (2–4). However, due to the requirement of good crystals for crystallography, requirement of solubilized and monodisperse sample, and the low molecular weight requirement of NMR, a significant fraction of food biomacromolecules cannot be analysed using these three high-resolution methods (5). Furthermore, because of the highly heterogeneous and polydisperse of most food biomacromolecules, it is also challenging for conventional techniques, Fourier Transform Infrared spectroscopy (FTIR), dynamic light scattering (DLS) to monitor the change in the structure of biomacromolecules, especially the dynamics of self-assemble and hydrolysis. Therefore, developing of alternative structural characterization techniques for biomacromolecules with rapid response, easy sample preparation, data collection under near-native conditions, and in situ capability, is needed in food science and technology.

Small-angle X-ray scattering (SAXS) is a powerful tool for structural characterization of samples under resolutions ranging from a few Angstroms to hundreds of nanometers. SAXS is sensitive to both ordered and not-ordered features in the sample and it has several advantages over direct characteristic techniques in that: a very small amount of sample for measurement, rapid data collection, no crystallization or fixation requirement, high-throughput screening model and multiple in situ capacities, etc. (6). These features make SAXS an interesting technique for academic and industrial applications of highly interdisciplinary field, including life science, biomedicine, and biomaterial engineering.

Since SAXS was first used to study the geometry of typical milk proteins β-lactoglobulin tetramer, there have been nearly 60 years of research on food biomacromolecules. Several studies have reviewed the advances and applications of SAXS in food

field (7–13). Gilbert summarized the principle and the latest activities in the application of SAXS to food colloids (14). This work provides information for the SAXS expert who is interested in applying this method to food colloids and the food scientist that wishes to gain knowledge of the former.

However, a work concluding the recent development and applications of modeling programs and in situ capabilities of SAXS for the structural characterization of food biomacromolecules is not available yet. Therefore, in the present review, the SAXS principle, theoretical calculations and modeling programs are summarized, technical advances in the experimental setups of in situ capabilities: coupled with chromatography, time-resolved, temperature, pressure, flow-through, are elaborated. Recent applications of SAXS for studying the structural properties of food biomacromolecules including proteins, carbohydrates and lipids are highlighted. Moreover, the limitations and prospects of SAXS are also discussed. We hope this review will provide reference information for food scientists who investigate the relationship between the structure and function of biomacromolecules using SAXS.

Principle, theoretical calculation, and programs

A typical bio-SAXS measurement is performed using a sample concentration at least $\sim$0.5–10 mg ml^{-1} with a $\sim$15–30 µl of volume, and generally takes less than a few minutes on a synchrotron beamline or dozens of minutes to hours using an in-house instrument (15). The principle of SAXS is that a collision between a monochromatic incident X-ray beam and a surface particle results in scattering of the beam in all directions. The one-dimensional (1D) scattered intensity $I(q)$ and the average of the various conformers present in the population of scattered particles are recorded using a two-dimensional (2D) detector. The magnitude of the scattering vector $q = 4\pi\sin\theta/\lambda$, where θ is the half of the angle between incident and scattered beams. At small angles (θ < 5°), the inhomogeneity in the electron clouds can be observed, which will provide information about the size and shape of biomacromolecules in the sample (16). The "background" scattering from the buffer is independently measured and subtracted from that of the solution (17).

The radius of gyration (R_g) of biomacromolecules can be estimated directly from small q values using Guinier approximation (18), $I\left(q\right) = I(0)\exp(\frac{-q^2 R_g^2}{3})$, where $I(q)$ is the scattering intensity and $I(0)$ is the forward scattering intensity. The pair-distance distribution function $p(r)$ (19), corresponding to the paired set of distances between all electrons within the scattered particle, can be generated via indirect Fourier transform by using the GNOM (20), PRIMUS

(21), BioXTAS RAW (22), and BIFT programs (23). By comparing with molecular weight determined from $I(0)$, the volume of the biomacromolecules can be calculated by the Porod approximation (24, 25). Moreover, the compactness or flexibility of biomacromolecules can be evaluated using the Kratky (26), dimensionless Kratky (27), and Porod-Debye plots (28). The principle, a typical SAXS measurement and derivative profiles can been seen from **Figure 1**.

The net scattering intensity is critically dependent on the scale factor, especially at high q regions (as shown in **Figure 2A**), and any minor deviation from the accurate value may have a significant impact on the final results (30). As seen from **Figures 2B–F**, a sharp decrease in the net scattering intensity at high q regions is observed due to a slight increase in scale factor (1.000–1.001) for background buffer subtraction. SAXS allows the determination of the structural properties under a broad range from a few Angstroms to hundreds of nanometers, which covers the size of biomacromolecules and their complex (**Figure 2G**). The maximum distance within a scattered particle (D_{max}) can be assessed by the distance r of the $p(r)$ distribution equals zero (**Figure 2H**). When the $p(r)$ curve with a maximum frequency at a distance less than half of the D_{max} (olive curve in **Figure 2H**), the scattered particle adopts rather extended and elongated conformation in solution. Therefore, the change in conformation and structure of biomacromolecules can be monitored by $p(r)$ profile. Moreover, an accurate determination of the scale factor for background subtraction has significant implications for obtaining the further reliable structural parameters of biomacromolecules (25).
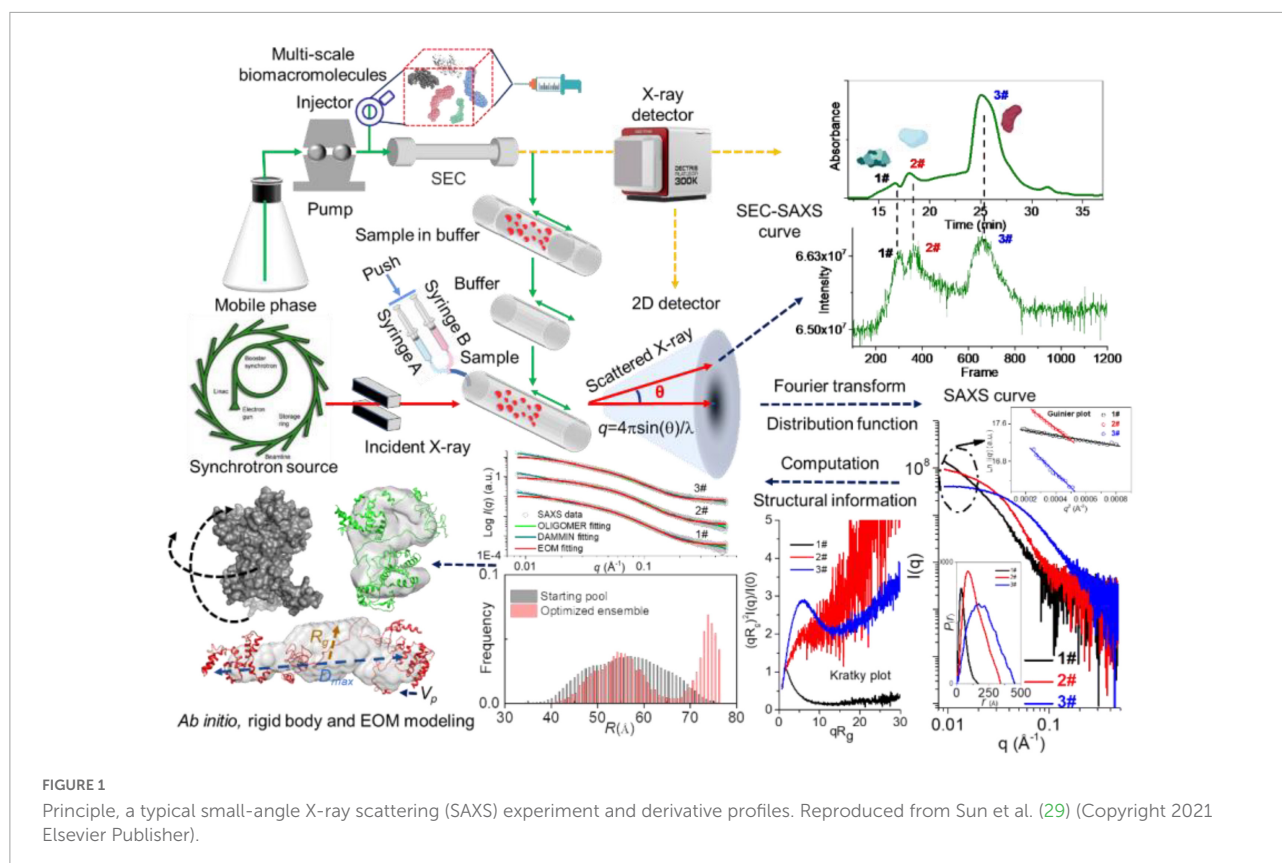
Small-angle X-ray scattering profile can then be used for a further series of theoretical calculations to obtain structural information, *ab initial* model and ensemble structures. By translating scattering curves into bead representations consisting of a set of dummy atoms, an *ab initio* model of biomacromolecule with a resolution of 10–30 Å can be obtained *via* DAMMIN (31) and GASBOR programs (32). It is noted that DAMMIN is the most used in the modeling programs for reconstructing low-resolution shape of biomacromolecule. An iterative phase retrieval method, density from solution scattering (DENSS), has been expanded to analyze SAXS data, which may avoid many of the assumptions limiting the resolution and accuracy of modeling algorithms by explicitly calculating electron density (33). Deep learning methods, such as DecodeSAXS, have been reported used to classify and reconstruct the shapes with model parameters (34, 35). Critical Assessment of Protein Structure Prediction (CASP), a machine learning program, utilizes SAXS data to build improved models simulating the global shape of the target (36). Google's AlphaFold 2 indisputably won the CASP14 competition. The results are so incredibly accurate that many have hailed this

code as the solution to the long-standing protein structure prediction problem.

MONSA program (31) can be used to treat biomacromolecules containing multiple phases (e.g., intensities from protein/nucleic acid complexes) (6). SREFLEX (37), SASREF (38), and CORAL (39) programs can be used for high-resolution modeling of rigid bodies. SAXSDom has been utilized to model stable multi-domain proteins with flexible linker regions (40). Moreover, CRYSOL is used to compare the SAXS data with a PDB file with an X-ray or NMR structure of a protein or a protein-DNA(RNA) complex (41). SUPCOMB is a tool for superimposing one 3D structure onto another (42). In the case of flexible and mixed biomacromolecule systems (protein, DNA, and RNA), the structural ensembles of the biomacromolecule can be acquired by the ensemble optimization method (EOM) (43). For the oligomeric and transient state system, the volume fraction of components can be calculated using OLIGOMER, and the *ab initio* model of intermediate may be acquired by DAMMIX (21, 44). A hybrid resolution molecular dynamic (MD) method (hySAXS) has been used to create an ensemble of structures for intrinsically disordered proteins (IDPs), which is comparable to the experimental SAXS data (45). The extended experimental inferential structure determination method (X-EISD) (46) and Bayesian/Maximum entropy (BME) method (47) can be also used to calculate the maximum log-likelihood of an IDPs ensemble derived from SAXS. LIPMIX (48) and BILMIX programs (49) enable polydispersity of the model in multilamellar and asymmetric lipid vesicles and simultaneously generate the corresponding size distribution, respectively. The program ELLLIP can reconstruct the quasi-atomistic models of ellipsoidal liposomes (50) as well as bi-micellar systems involving proteins (51).

Several integrated docking methods by fitting the theoretical scattering curve of possible models to the experimental SAXS data have been developed to estimate the structure of complexes. Examples of such docking methods include SASREF (38), FoXSDock (52), HADDOCK (53), ClusPro FMFT-SAXS (54), pyDockSAXS (55), RosettaDock$_{SAXS}$ (56), PatchDock (57), and ATTRACT-SAXS (58). It has shown that iSPOT can filter docked structure and characterize a native-like model combined SAXS with foot-printing data by generating theoretical scattering of crystal structure (59). Molodenskiy et al. presented a PyMOL plugin, MPBuilder, which provided a set of adaptable routines for modeling membrane proteins (MPs), protein-detergent complex, bicelles, and lipid scaffold (saponin nanoparticles, nanodiscs) validated with SEC-SAXS data (60).

A comprehensive list of programs to reconstruct the structure and model of biomacromolecules based on SAXS data is shown in **Table 1**, and many of the programs are publicly available to academic users and moderately easy to

FIGURE 1
Principle, a typical small-angle X-ray scattering (SAXS) experiment and derivative profiles. Reproduced from Sun et al. (29) (Copyright 2021 Elsevier Publisher).

operate. The details and applications of each program please see the corresponding reference. The popularity of SAXS has been propelled by novel data analysis and modeling algorithms. Developing user-friendly modeling programs will facilitate the utilization of SAXS for large-scale studies, which is also a major achievement in the community toward broader use of the method in combination with complementary techniques and enabling the cross-validation of structural data (61).

In situ capabilities of small-angle X-ray scattering

Size-exclusion chromatography-small-angle X-ray scattering

The online purification system coupled with SAXS, such as size-exclusion chromatography (SEC), gel filtration chromatography, and reversed-phase chromatography, is a standard approach for separating oligomeric species or components in a heterogeneous sample (62). The programs like CHROMIXS (63), DATASW (64), DELA (65), EFAMIX (66), and US-SOMO HPLC-SAXS module (67) have been developed to process chromatography-SAXS data. The

scheme for SEC-SAXS setup is shown in **Figures 1**, **6**, and applications of chromatography combined with SAXS for studying biomacromolecules are summarized in **Table 2**.

Although the nanocluster model for describing casein micelle structure is widely accepted, little direct evidence at the nanometer scale supported this model. Sun et al. (29) reported a method that can prove and quantify the conformation and the fine structure of the casein cluster based on SEC-SAXS. The SEC-SAXS results showed that casein cluster presented R_g values ranging from 39.45 to 40.77 Å with a D_{max} of 180 Å. The dimensionless Kratky plot suggested a rather extended and elongated conformation of casein cluster in solution. The experimental M_w according to the Bayesian Interference analysis was 50.3–64.7 kD with a probability of 91.54%, indicating the presence of 2–3 casein monomers in the cluster. Further, the DAMMIX and OLIGOMER results indicated that the cluster consisted of four species, α_{s1}-β-α_{s2}-casein, α_{s1}-casein, α_{s2}-casein and α_{s1}-α_{s2}-casein with a volume fraction of 64.3, 22.8, 8.5, and 4.4 %, respectively. The results of EOM indicated the presence of two conformers in α_{s1}-β-α_{s2}-casein, the elongated one (∼60 Å of R_g) with 64.7% of volume fraction and the compact one (∼35 Å of R_g) with 35.3% of volume fraction. It is the first time to reveal the structural properties of casein cluster based on SEC-SAXS, which may help understand better for internal structure of
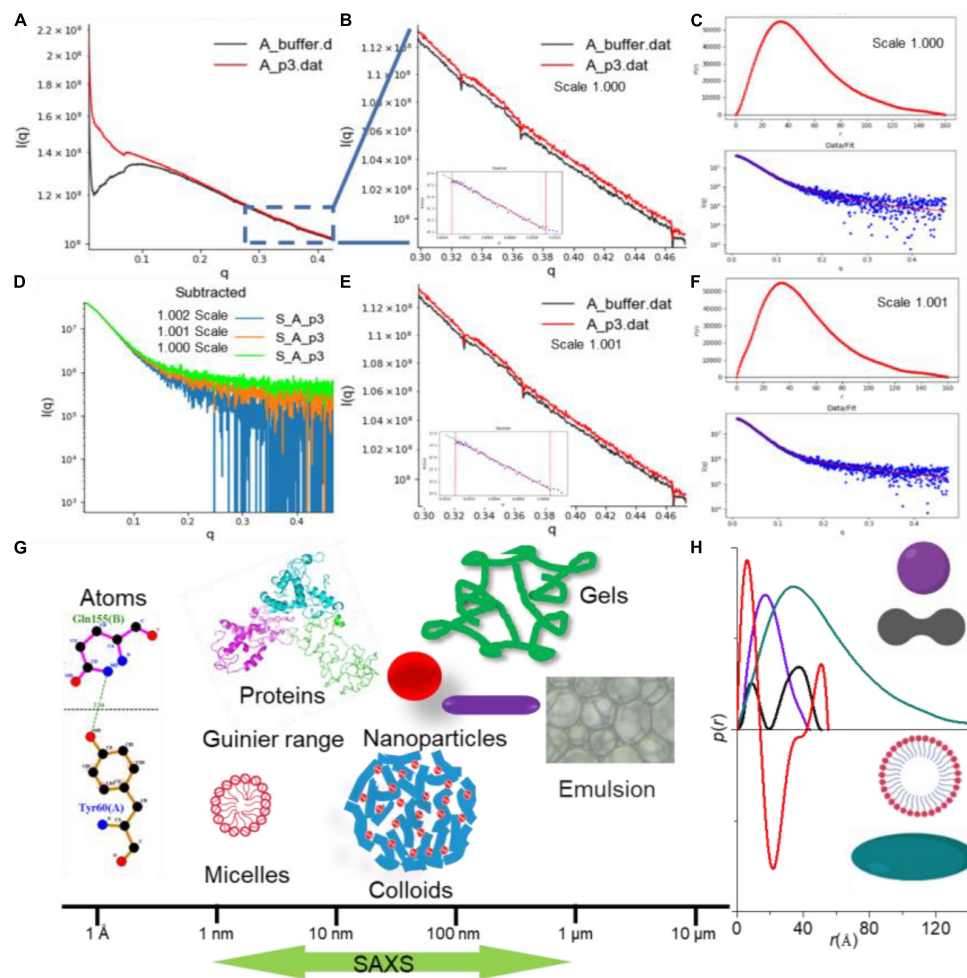
casein micelles regarding their primary casein cluster. Therefore, SAXS has been proved to be a powerful tool to study the structure and dynamics of the flexible, disordered and mixed biomacromolecules.

Time-resolved and time-dependent small-angle X-ray scattering

Small-angle X-ray scattering measurements are performed over a set time period ranging from microseconds to hours to assess the time-resolved (TR-SAXS) and time-dependent (*in situ* or real time) changes in structure and function for protein, carbohydrate, fat or non-nutritive compounds, such as gelatinization, assembly, micellization or colloid formation as well as in digestion and hydrolysis (68). This method is particularly suited to differentiate

triggers of structural changes, including optical excitation (69), electron transfer (70), temperature jump (T-jump) (71), pH-jump (72), photoreduction (73), and reactant concentration jump (74).

Kuang et al. investigated the lamellar structure change of waxy corn starch during gelatinization and reveal the gelatinization mechanism by TR-SAXS in the temperature range from 35 to 141.85 °C with a measurement of 60 s at each degree (75). Gilbert reviewed the latest activities in the application of time-dependent SAXS to food colloids (14). Hempt et al. reported a novel digestion model of milk using an integrated online flow-through TR-SAXS with an *in vitro* cell co-culture model (76). Krishnamoorthy et al. reported an approach based on the time-dependent SAXS from protein spherical nucleic acids to elucidate the enzymatic degradation of DNA, which should prove invaluable in probing other enzyme-catalyzed reactions on the nanoscale (77). The details of TR-SAXS

TABLE 1   List of some of the available software programs used in the analysis and reconstruction of models based on small-angle X-ray scattering (SAXS) data.

Program	Accepted experimental file	Functionality	Output	Web server	References
Membrane protein (MP) Builder	The plugin of both PyMOL and ATSAS, SAXS data	Generation and refinement of all-atom protein-detergent, bicelle, and lipid-scaffold (saponin nanoparticles, nano-discs) complexes	Models of protein-detergent assembles without minimized energy	https://github.com/emblsaxs/MPBuilder	(60)
Critical assessment of protein Structure prediction (CASP)	SAXS data	SAXS-assisted protein structure prediction	Predicted solution structure	https://predictioncenter.org/	(36)
CRYSOL in ATSAS	PDB, SAXS data	Evaluating atomic structure of biomacromolecules based on SAXS experimental data	Fitting with chi values	https://www.embl-hamburg.de/biosaxs/crysol.html	(51)
CORAL combines the algorithms of SASREF, BUNCH in ATSAS	PDB, SAXS data	Rigid body modeling of multidomain protein complexes against multiple SAXS data	PDB and fitting	https://www.embl-hamburg.de/biosaxs/manuals/coral.html	(39)
DAMMIN or MONSA in ATSAS	Output file of the program GNOM in ATSAS	Restoring *ab initio* shape of biomacromolecules	PDB and fitting	https://www.embl-hamburg.de/biosaxs/manuals/dammin.html	(31)
GASBOR in ATSAS	Output file of the program GNOM in ATSAS	Restoring *ab initio* of protein structure using a chain-like ensemble of *dummy residues*	PDB-alike file	https://www.embl-hamburg.de/biosaxs/manuals/gasbor.html	(32)
OLIGOMER in ATSAS	PDB, SAXS data	Computation of volume fractions of mixtures of protein with SAXS data from the components	Fitting and file containing volume fractions of components in mixture	https://www.embl-hamburg.de/biosaxs/manuals/oligomer.html	(21)
DAMMIX in ATSAS	PDB, SAXS data	Restoring *ab initio* shape of intermediate state component and its volume fraction	PDB and fitting	https://www.embl-hamburg.de/biosaxs/manuals/dammix.html	(44)
EOM in ATSAS	Amino acid sequence, PDB of domains/subunits, SAXS data	Fits an average theoretical scattering intensity derived from an ensemble of conformations to experimental SAXS data.	PDB and fitting	https://www.embl-hamburg.de/biosaxs/manuals/eom.html	(43)
FoXS	PDB, SAXS data	Computing a theoretical scattering profile of a structure and fitting of experimental profile	Fitting file of PDB with SAXS curve	https://modbase.compbio.ucsf.edu/foxs/	(52)
SAXSDom	Sequence of individual domain	Multidomain protein assembly modeling	PDB file of multidomain protein	https://github.com/jianlin-cheng/SAXSDom	(40)
FoXSDock	PDB files of receptor and ligand, SAXS data	Docking two rigid protein structures based on a SAXS profile of their complex	PDB file of complex	https://modbase.compbio.ucsf.edu/foxsdock	(52)
ATTRACT-SAXS	PDB files of receptor and ligand, SAXS data	Docking protein-protein benchmark with simulated SAXS data without a physiochemical force field	High-quality solution models of protein-protein complexes.	http://www.attract.ph.tum.de/services/ATTRACT/attract.htmltum.de	(58)
RosettaDockSAXS	SAXS data	Predicting unknown 3D atomic structures of protein-protein complexes	3D atomic structures	https://rosie.rosettacommons.org/docking/	(56)
DecodeSAXS	SAXS data	Machine learning methods to build 3D models	3D models	http://liulab.csrc.ac.cn:10005/submit/	(35)
pyDockSAXS	PDB files of receptor and ligand, SAXS data Complex type: enzyme inhibitor, antibody, or antigen	Structural models of protein–protein interactions at large scale.	Models of complex	life.bsc.es/pid/pydocksaxs	(114)

(Continued)

TABLE 1 (Continued)

Program	Accepted experimental file	Functionality	Output	Web server	References
ClusPro	PDB files of receptor and ligand	Protein–protein docking server based on fast Fourier transform (FFT) data	Models of complex	http://cluspro.org/ nousername.php	(115)
X-EISD	Sequence of protein, SAXS experimental data	Generating ensembles of IDPs	Ensembles	https://github.com/THGLab/ X-EISD	(46)
BME	Experimental data. Calculated data from simulation trajectory	Generating ensembles	Ensembles	https://github.com/KULL-Centre/BME	(47)
SAXScreen	SAXS data, ITC titration curve, ligand, and buffer SAXS data	Screening protocol utilizing SAXS to obtain structural information involving protein-RNA interactions.	Models of complex	https://github.com/zharmad/ SAXScreen	(116)

equipped with the laser pulse recording as a function of the time delay between laser pulse and incident X-ray are shown in **Figure 3**.

The SAXS beam equipped with the microfluidic device (continuous flow and stopped-flow) may not only reduce the sample damage by radiation (78), but also monitor the dynamic structural alternations during interactions in real-time (79). Hsu et al. characterized the transient partially folded state of bovine α-lactalbumin (BLA) coupled with TR-SAXS following a T-jump (74). The structural responses of BLA after an 11.5°C T-jump from the initial temperatures of 60, 65, and 70°C were individually recorded from 20 μs to 70 ms delay. Three states were molten globule state and two terminal unfolded states, U_1 and U_2. The application of TR-SAXS for structural characterization of biomacromolecules in foods is listed in **Table 3**.

Temperature

Temperature is one of the most important parameters controlling the formation, morphology, and structure of biomacromolecules, since much of biochemistry is thermally driven, functionally relevant conformational changes can also be triggered by changes in temperature. Generally, a trigger T-jump using a nanosecond laser pulse or an infrared (IR) light with a wavelength of 1450 nm (**Figure 3**, right upper) can be applied to most temperature-sensitive biomacromolecules to perturb the structural dynamics and reveal the changes in structural kinetics and association under various temperature conditions (80).

Berntsson et al. developed a CoSAXS beamline for millisecond T-jump experiments tracked by TR-SAXS with the Eiger2 and Mythen2 detectors and recorded the scattering of the solvent (80). A ~15°C T-jump can be triggered by a 2 ms infrared laser light and maintained for several seconds with additional laser pulses. The structural changes in lysozyme

induced by a T-jump were observed and the population of lysozyme structures differed at this temperature. Moreover, the data showed that IR radiation absorbed directly by the solvent did not show a significant effect compared with that induced by the thermal changes in the protein. Thus, the temperature induced change in structure of biomacromolecule and thermal dynamics of system can be monitored by SAXS effectively based on the scattering characteristic of sample in SAXS profile.

Pressure

High-pressure (HP) food treatment including pasteurization, sterilization, and shelf-life extension, has widely been used to ensure food safety and preserve various thermally sensitive nutrients and bioactive compounds (81). HP-SAXS can also be used to track a wide range of structural changes of food biomacromolecules under pressure in real time (82). Moreover, the experimental setup of TR-SAXS studies of kinetic events induced by sub-millisecond timescale hydrostatic pressure jumps (P-jump, 1–5,000 bar) is also available in several synchrotron SAXS beamlines (83). Typically, the diamond anvil cell (DAC) covers the measurement of milk, solid powders, crystals and crystalline liquids (84). Hydrostatic pressure cell (HPC) is widely used to study phase diagrams of lipid, nano-assemblies, or pressure-dependent structure-function of biomacromolecules (85, 86).

Lehmkühler et al. reported the pressure-induced formation of super crystals from high-quality PEGylated colloidal nanoparticles using 5 ms P-jump SAXS (87). They demonstrated the crystallization pressure (p_c) of the suspension by tracking SAXS patterns at pressures above 2 kbar in steps of 100 bar and verified p_c between 2.9 and 3 kbar. They observed that the pressure (p_f) jumped from 2.9 to 3.58 kbar averaging over 200 ms exposure time.

TABLE 2   Application of chromatography combined small-angle X-ray scattering (SAXS) for studying biomacromolecules.

Samples	X-ray source	Elution buffer column	Concentration/volume	Detector distance from sample	Flow	Exposure	References
BSA	EMBL P12 beamline	50 mM HEPES, 150 mM NaCl, 2% v/v glycerol, pH 7	Superdex 200 Increase 10/300	8.8 mg ml^{-1} 100 µl	Pilatus 6M, 3.3 m	0.5 mL min^{-1} + splitter	1 s	(117)
Glucose isomerase, *Streptomyces rubiginosus*	EMBL P12 beamline	50 mM Tris, 100 mM NaCl, 1 mM MgCl$_2$, 1% v/v glycerol, pH 7.5	Superdex 200 Increase 10/300	10.3 mg ml^{-1} 100 µl	Pilatus 6M, 1.5 m	0.5 ml min^{-1} + splitter	1 s	(117)
Class II pyruvate aldolase	EMBL P12 beamline	20 mM HEPES, pH 7.5	Superdex 200 Increase 10/300	8 mg ml^{-1} 80 µl	Pilatus 6M, 3.3 m	0.5 ml min^{-1} + splitter	1 s	SASDEX9
Ovalbumin + β Amylase mixture, Ovalbumin	EMBL P12 beamline	20 mM Tris, 150 mM NaCl, 5% glycerol	Superdex 200 Increase 10/300	15 mg ml^{-1} 100 µl	Pilatus 2M, 3.0 m	0.5 ml min^{-1} + splitter	1 s	(118)
Cycloamylose	SPring-8	Milli-Q water or 6% (v/v) methanol	30 × 1000 mm packed with TOSOH HW-55S	2.0 mg ml^{-1} 2.0 ml	Hamamatsu Photonics V5445P-MOD, 1.5 m	2 ml min^{-1}	2 s	(119)
Caseinate	SSRF BL19U2 beamline	10 mM Tris-HCl pH 6.7	Superdex 200 Increase 10/300	25 mg ml^{-1} 150 µl	Pilatus 1M, 3.0 m	0.5 ml min^{-1}	1 s	(29)
Ovalbumin Proteoglycans	KEK BL-10C station	10 mM PBS, pH 6.9 50 mM PBS, pH 6.9.	SB-806 M HQ, 300 × 8 mm, Shodex GF-7M HQ, Shodex	0.735 mg ml^{-1} 3% (w/v)	Pilatus3 2M, 1.98 m	0.3 ml min^{-1} 0.4 ml min^{-1}	3 min with intervals of 10 s	(120, 121)
Glucose isomerase	Australian Synchrotron coflow-SEC SAXS beamline	20 mM PBS with 128 mM NaCl, 22 mM KCl, 5% (v/v) glycerol, pH 7.5	Superdex S200 Increase 5/150	2.5 mg ml^{-1} 100 µl	Pilatus2 1M, 8 m	0.5 ml min^{-1}	2 s	(122)
Lysozyme	PLS II 4C SAXS beamline	10 mM PBS with 138 mM NaCl, pH 7.4	Agilent Bio SEC-5	20 mg ml^{-1} 100 µl	Rayonix 2D, no mention	0.06 ml min^{-1}	10 s	(123)
Immunoglobulin G	La-SSS adopts NANOPIX	100 mM Tris-HCl with 100 mM NaCl, pH 7.5	Superdex 200 Increase 10/300	5.0 mg ml^{-1} 500 µl	HyPix-6000, 0.35 m	0.02 ml min^{-1}	30 s	(124)
Apoferritin	BioXolver L, Xenonx	50 mM HEPES, pH 7.5	Superdex 200 Increase 10/300	0.5 mg mL^{-1} 500 µL	Single-photon-counting detector, 0.6 m	0.5 ml min^{-1}	30 s	(125)
Yeast alcohol dehydrogenase	EMBL P12 beamline	50 mM HEPES, 150 mM NaCl, 2% v/v glycerol, pH 7	Superdex 200 Increase 10/300	9.2 mg ml^{-1} 100 µl	Pilatus 6M, 3 m	0.5 ml min^{-1}	67 s	(117)

The characteristic time (tw) decreased from 6.1 to 0.07 s with a reduction in Bragg reflection width from 0.138 to 0.0458 Å^{-1}, suggesting the higher the p_f, the faster the formation of nanoparticle structure. The results showed that a larger P-jump induced attractive interactions and thereby accelerated the formation of colloidal nanocrystal superlattices with enhanced crystal quality. Therefore, HP-SAXS can be utilized to track the structural change during interactions of biomacromolecules as well as to monitor the preparation of various biobased nanostructures. Exploiting easy operation setup will broad the applications of SAXS for complex biomacromolecule system.

Applications of small-angle X-ray scattering in characterizing food biomacromolecules

Proteins

As one of the most significant biomacromolecules in food, protein plays an essentially nutritional role *in vivo*. Meanwhile, protein-based ingredients fulfill several technical functions in food formulations and contribute to texture, color, flavor, and other properties such as solubility, stability

FIGURE 3

In situ capabilities of small-angle X-ray scattering (SAXS).
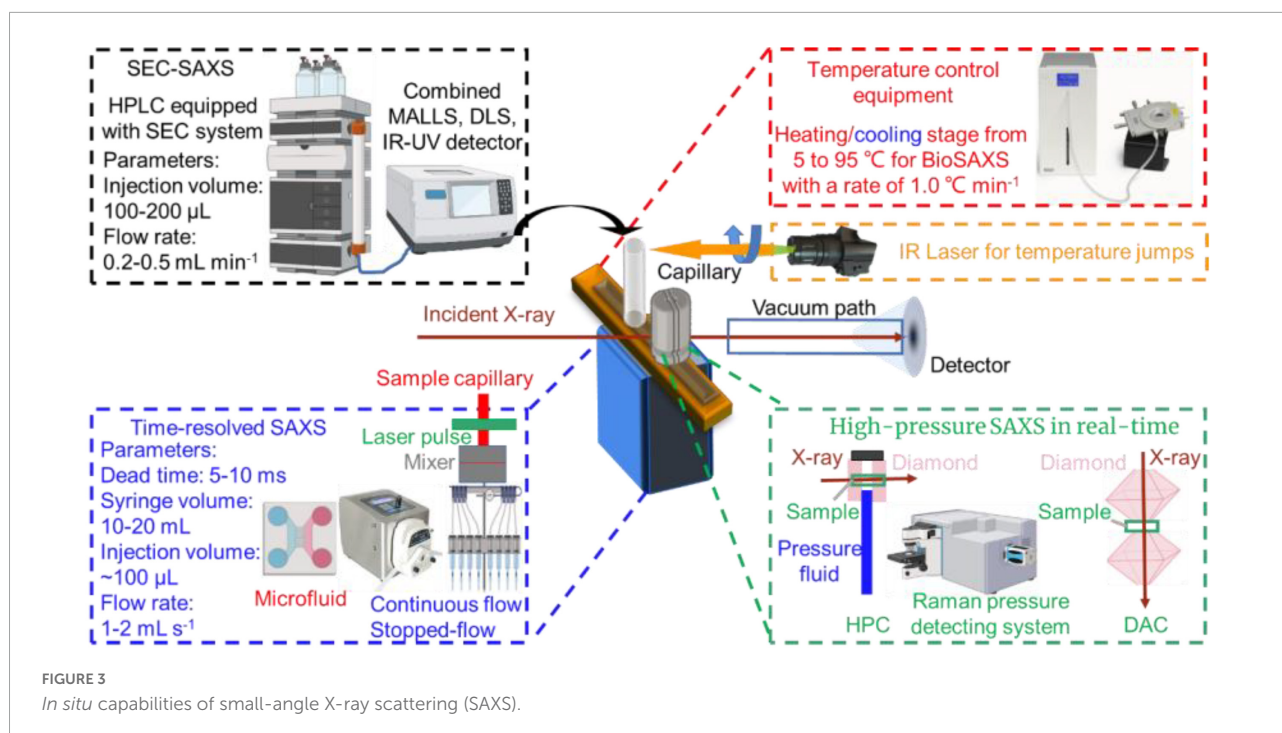
emulsification, gelation and foaming (88). These researches involve studying protein structure-function relationships, optimizing the utilization of the components of the product, improving the quality, reducing costs, and developing novel protein application (89). SAXS is one of the most suitable techniques for protein structure and function relations study.

According to Yang et al. SAXS was used to investigate the nanostructure of quinoa protein (*Chenopodium quinoa*) isolates (QPI), one of the emerging proteins native to South America with a well-balanced amino acid profile, and the effect of NaCl and CaCl$_2$ on the heat-induced gelation of QPI (90). Thermal treatment increased the sample $I(q)$ in low-q region and the scattering intensity remained almost the same in the high-q region, which suggested that heat-induced QPI aggregation and then gelation merely occurred on the micron scale, while the internal structure of QPI on the nanoscale changed little. A Guinier shoulder in the mid-q region (0.02 Å^{-1} < q < 0.08 Å^{-1}) of the Kratky plot suggested the existence of nanoscale protein particles or inhomogeneities in QPI gel containing 0–200 mM NaCl. By fitting with correlation length model ($I(q) = \frac{A}{Q^n} + \frac{C}{(Q\zeta)^m}$), the correlation length (ζ) or particle size of ∼32 Å was obtained for all the QPI gels containing 0–200 mM NaCl. Calcium binding or protein cross-linking induced minor protein inhomogeneities as indicated by substantial changes in the SAXS curve as well as a small peak at q∼0.2 Å^{-1} in SAXS patterns of QPI gel containing CaCl$_2$.

Pohl et al. (91) reported a high-throughput SAXS screening approach to assess the conformational stability and initial dispersion state of *Thermomyces lanuginosus* (TLL) and

Rhizomucor miehei (RML), important lipases used in the food industry. They found repulsion in nine different kinds of the buffer as indicated by the decreased intensity in the low q-region induced by interparticle diffraction, and a significantly reduced repulsion and reduced oligomerization in phosphate buffer. Salt (35, 70, 140 mM NaCl) had minimal impact on SAXS profiles of TLL in histidine buffer at pH 5.5 and pH 7.5. The major species in the solution in all conditions was found to be monomeric, which confirmed that the differences in SAXS data were related to protein-protein interaction, suggesting that SAXS is used more widely as a tool to gain in-depth knowledge especially for the later stages of protein formulation in the food industry (**Figure 4**).

The structure of casein micelles contributes to the primary physicochemical and organoleptic properties of milk. Yang et al. (92) analyzed the changes in the internal structure of CNs under HHP (up to ∼1,000 MPa) using *in situ* HP-SAXS equipped with DAC at room temperature. They found a decrease in both scattering intensities at low q (∼0.003 Å^{-1}) and high q (∼0.08 Å^{-1}), suggesting the disruption of CNs and solubilization of the colloidal calcium phosphate (CCP) nanoclusters under HP treatment. The SAXS profiles under pressures ranging from 270 to 960 MPa showed two isosbestic points at q values of ∼0.013 and 0.03 Å^{-1}, which confirmed the appearance of "sub-micelles" and dissociation of CCP. When the pressure returned to atmospheric pressure, the CNs structure reverted partially to the native one (**Figure 5A**). Similarly, Yang et al. (84) reported the hierarchical structure of milk at various lengths under a pressure of 200 or 400 MPa at

TABLE 3   Application of time-resolved small-angle X-ray scattering (TR-SAXS) at various synchrotron beamlines.

Samples	X-ray source	q-Range	Acquisition time	References
Gluten protein mixtures	ESRF beamline ID02	1.2×10^{-4}–6.0×10^{-3} Å^{-1}	5 ms	(126)
Gelation of pea and whey proteins	APS beamline 9-ID-C	1.0×10^{-4}–0.3 Å^{-1}	A 90 s measurement every 2–5 min	(127)
Polyphenol pea protein gel	APS beamline 9-ID-C	1.0×10^{-4}–1.0 Å^{-1}	20 s	(128)
Zein-based oleo gel	APS beamline 9-ID-C	1.0×10^{-4}–1.2 Å^{-1}	20 s	(129)
Liquid–liquid phase separation of BSA-YCl$_3$ system	ESRF beamline ID02	9.0×10^{-5}–7.0×10^{-3} Å^{-1}	5–50 ms	(130)
Cellulose nanofibers	NSLS beamline X9	1.0×10^{-3}–0.3 Å^{-1}	10 s	(131)
Gelation of amylose	SPring-8 BL-40B2	1.0×10^{-4}–0.8 Å^{-1}	1–62 min	(132)
Lipid/surfactant assemblies	ESRF beamline ID02	3.0×10^{-3}–0.19 Å^{-1}	20 ms	(133)
Waxy corn starch	SSRF BL16B1	0.025–0.15 Å^{-1}	60 s	(75)
Milk lipid crystallization during digestion	Australian Synchrotron SAXS beamline	$0.005 < q < 1.0$ Å^{-1}	5 s	(68)
Milk digestion in presence of a cell	Swiss Light Source SAXS beamline	$0.006 < q < 0.5$ Å^{-1}	70 min with an exposure time of 1 s and a 9 s delay	(76)
Krill oil-in-water emulsion	EMBL P12 beamline	$0.01 < q < 0.5$ Å^{-1}	3,500 s with a 1 s exposure and 9 s delay	(108)
Oleic acid (OA) and glycerol monooleate (GMO) self-assemblies	ELETTRA Austrian SAXS beamline	$0.018 < q < 0.5$ Å^{-1}	Five frames with an exposure time of 20 s	(134)
Liquid depot formulations	ELETTRA Austrian SAXS beamline	$0.02 < q < 0.5$ Å^{-1}	10 min with a 5 s exposure with 5 s delay	(135)
Lipid vesicles and Ca^{2+}	ESRF beamline ID02	$0.0067 < q < 0.5124$ Å^{-1}	35 frames, first frame 0.04 s after mixing, last frame 316.16 s with a 0.02 s exposure	(136)
Soy phosphatidylcholine-citrem nanoparticles	ELETTRA Austrian SAXS beamline	$0.01 < q < 0.4$ Å^{-1}	Four frames with a 0.25 s exposure	(137)

25, 40, or 60°C using HP-SAXS (Figure 5B). The changes in CNs nanostructures varied with pressure rather than time, and temperature played a central role during the HP process.

Consequently, SAXS can be used as an effective technique not only to track the dynamic properties of biomacromolecule interactions but also to monitor the internal structure of biomacromolecule assembles.

Carbohydrates

Carbohydrates contribute to the bulk of dietary energy and play a vital role due to their diverse biological properties and functionalities in the food industry, as a thickening, gelating, emulsifying, encapsulating, or bulking agent (93). Starch, as an important polysaccharide macronutrient, determines the processing and nutritional quality of starch-based foods (94). Increased attention is needed to identify significant opportunities for real-time monitoring of structural changes

during starch processing, such as swelling, gelatinization, retrogradation, and digestibility of starch.

Liu group reported dynamic changes in lamellar structure and gelatinization of cereal starches with different amylose contents in real time using *in situ* SAXS (Figure 6; 75, 95, 96). In the low-q region, the curves fitted with a simple power law equation, $I(q) \sim q^{-\alpha}$, where mass fractal dimension ($0 < \alpha < 3$) was an indication of compactness, whereas the surface fractal dimension ($3 < \alpha < 4$) was considered smooth. During gelatinization, all cereal starches showed a decreasing α value in the q-region between 0.01 and 0.02 Å^{-1}, with the corresponding size of ~30 to ~60 nm with the temperature increasing from ~70 to ~90°C, implying a mass fractal structure of the starch gel. Interestingly, an isosbestic point in the middle q-region was observed for all samples, which confirmed a two-step gelatinization of starches, namely, two-correlation length (ξ) of particles in the paste/gel system. The structural paraments of lamellae, the average thickness of amorphous layers (d_a), crystalline and amorphous layer thickness (d_c) and the long
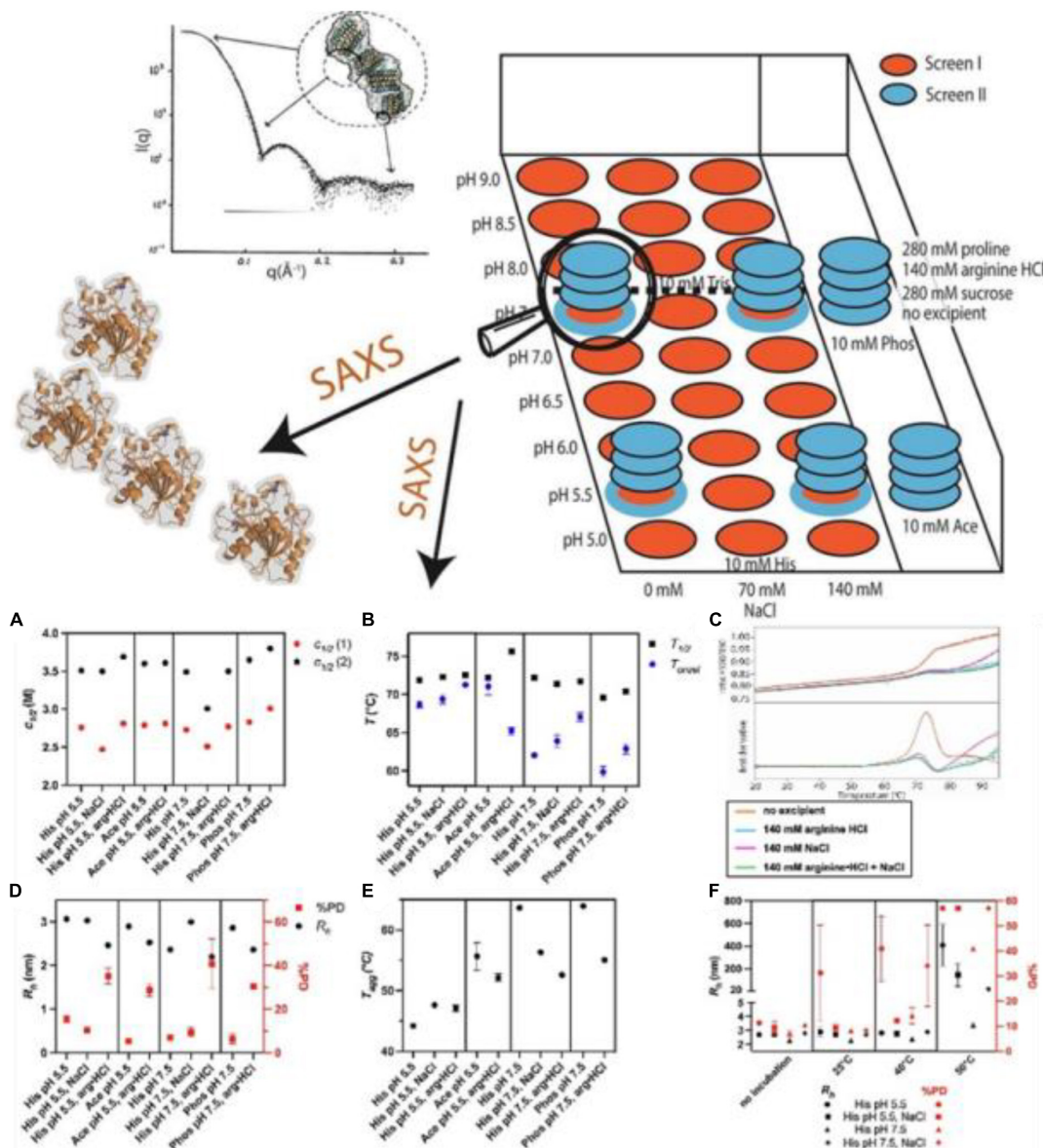
FIGURE 4

(Top) Combination of high throughput and structural screening to assess protein stability using small-angle X-ray scattering (SAXS). **(Bottom)** **(A−F)** High throughput stability screening of *Thermomyces lanuginosus* (TLL) (91) (Copyright 2022 Elsevier Publisher).

period distance (d_{ac}) parameters were calculated based on Lorentz-corrected SAXS profiles. For high-amylose maize starch (HAM), d_c increased from 65°C with a decreased d_a value, demonstrating swelling of the lamellae following water uptake. For normal maize starch (NMS) and mung bean starch (MBS), d_c increased from 60°C with a decreasing value of d_a. Both d_{ac} and d_c rapidly decreased at 72.2, 70.2, and 69.4°C for the high amylopectin (HAP), normal rice starch (NS) and HAM samples, respectively (96).

Starch has a strong tendency to retrograde and undergoes syneresis on cooling, namely, retrogradation.

The retrogradation starts with the self-assembly of amylose to form a double helix during the cooling and storage of starch gel, followed by the partial crystallization of branched polymers (amylopectin) after prolonged storage (97). Zeng et al. (94) reported the SAXS patterns of retrograde starch with α values of all samples ranging from 1.32 to 2.43, indicating the mass fractal structures of all retrograde starch samples. Compared with storage day 1, the fractal dimensions (D_m) on storage day 24 increased from 1.32 to 2.30, which was consistent with the formation of ordered crystalline structures in the long-range and an increase in the ordered structure of starch during storage.
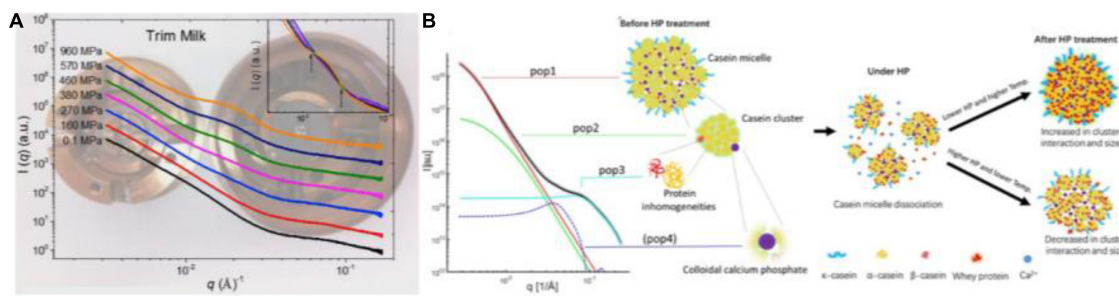
FIGURE 5
(A) *In situ* synchrotron small-angle X-ray scattering (SAXS) patterns of trim milk under different HHP using DAC (92) (Copyright 2018 Elsevier Publisher). **(B)** Graphic representation of the four contributions of CNs model at different length scales and structural dynamics during HHP from *in situ* SAXS, based on Yang et al. (84) (Copyright 2021 Elsevier Publisher).
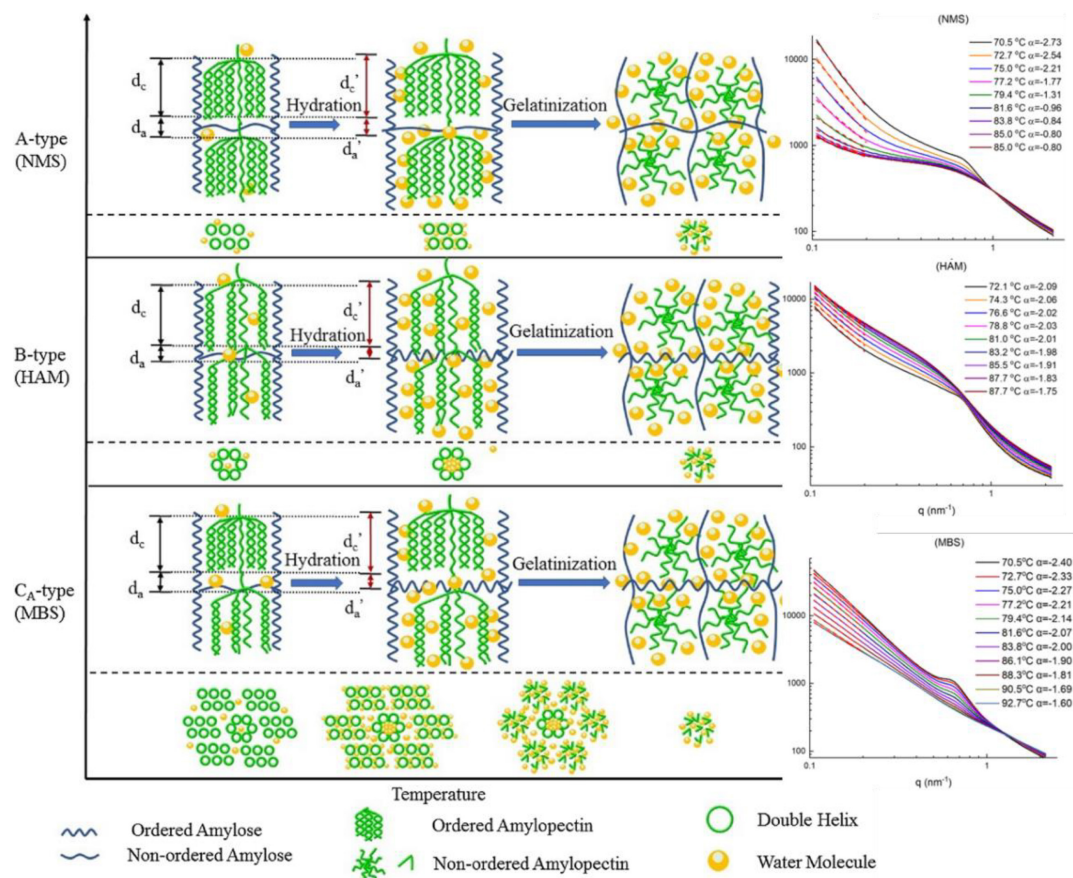
FIGURE 6
(Left) Schematic representation of lamellar and crystalline structural dynamics during heating. The two steps are shown: hydration, which is the uptake of water and swelling of starch granules; gelatinization, which is the disruption of starch crystal structure. **(Right)** Small-angle X-ray scattering (SAXS) profiles of HAM, NMS, MBS (95) (Copyright 2020 Elsevier Publisher).

Starch digestibility based on sustained dietary energy and low glycemic index (GI) of foods plays a vital role in public health (98). Yang et al. used SAXS to investigate thermally and enzymatically digested corn starches under various treatment times. The semi-crystalline lamellar structure of starch exhibited a scattering peak at a q-region of 0.06–0.07Å^{-1} with a size of 9-10 nm corresponding to the alternating crystalline and amorphous lamellar structure of amylopectin. The peak area of thermally treated and enzymatic digested starch was quantified by fitting SAXS data (0.02Å^{-1} < q < 0.2Å^{-1}) with a power-law

FIGURE 7
(Top) Setup of the microfluidic small-angle X-ray scattering (SAXS) device. **(Bottom left)** SAXS profiles of the w/o/w double emulsion interfaces obtained using the microfluidic device (RT; green), after storage at 50°C for 120 min (red) and for 240 min (blue), respectively. **(Bottom right)** Scheme of SAXS intensity at $q = 0.9$ nm^{-1} recorded along an axial line covering a whole double emulsion unit. Reproduced from Clemente et al. (102).

function combined with a Lorentzian peak with $I(q) = B + Cq^{-\alpha} - \frac{2A}{\pi}\left(\frac{W}{4(q-q_0)^2 + W^2}\right)$ (99). The thermal treatment induced water uptake in the amorphous regions of the granule during heating, leading to an increase in the intensity of the low q-region. In contrast, enzymatically treated samples showed changes in the crystalline and amorphous regions within the semi-crystalline lamellar structure and the amorphous growth rings. However, both treatments had little impact on the mass fractal structures of starch as the power law exponent (P) and long period distance (d) were around ∼2 and ∼10 nm for all samples.
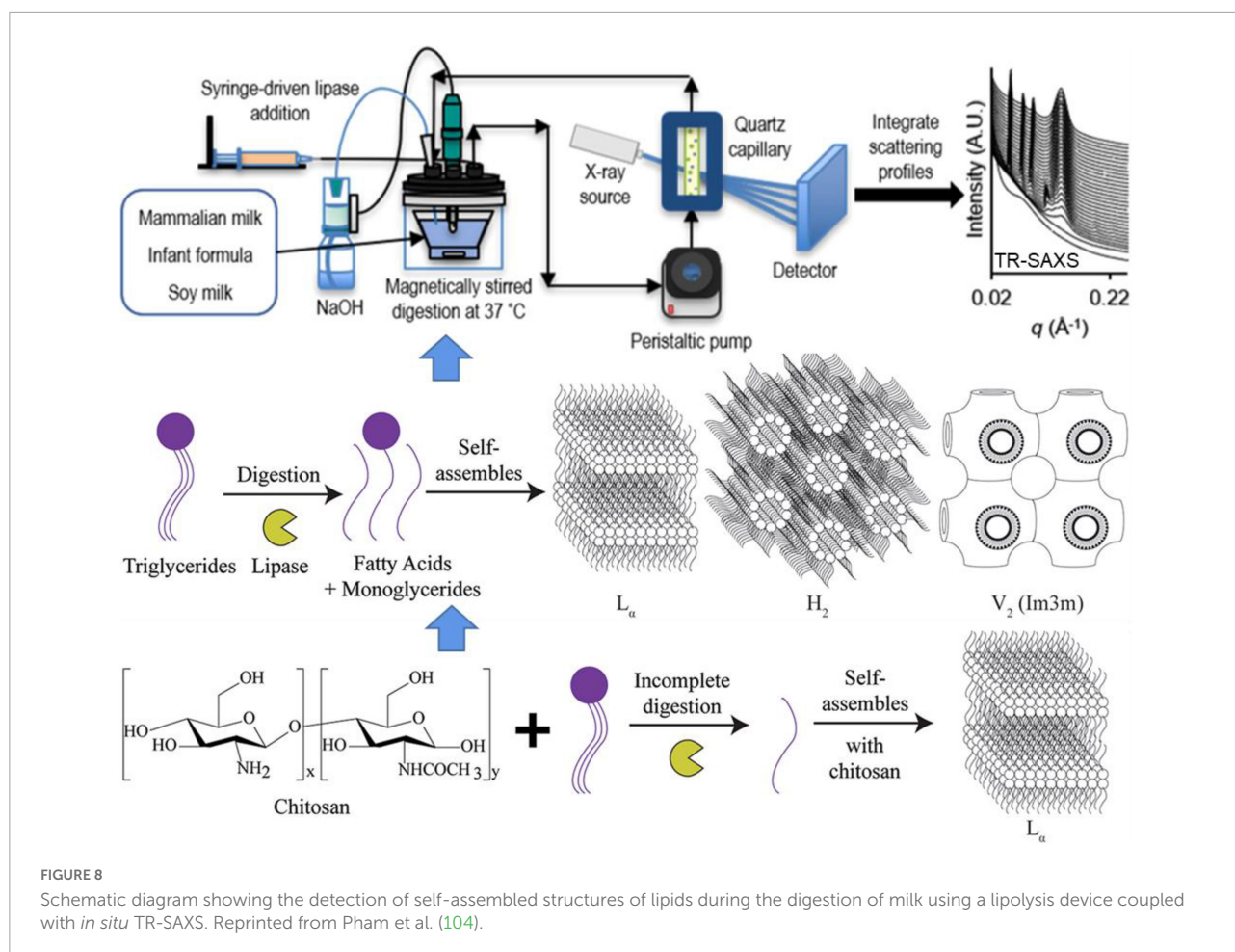
Overall, the structural parameters of biomacromolecules derived from SAXS data facilitated the determination of the structure-function relationship and the evolution of nanomaterials based on the role of carbohydrates in the food industry.

Lipids

Fats and oils are important sources of energy and nutrition, and contribute to the desirable functionality, texture and palatability of foods (100). Chemically, fats consist mainly of triglycerides (TAGs) combined with free fatty acid moieties. Besides nutritional properties, lipids facilitate the delivery of lipophilic nutraceuticals. Lipid-based colloid formation or

oleogelation is designed to simulate the structure and semi-solid rheological behavior, and is widely utilized in the food industry, including coating, bakery, dairy products, meat, plant-based and artificial meat products (101).

Clemente et al. (102) explored the water/oil/water interface of phospholipid 1,2-dimyristoyl-*sn-glycerol*-3-phosphocholine [DMPC; 1% (wt/wt)] dissolved in a mixture of volatile solvents such as cyclohexane/chloroform (volume ratio 2:1) using microfluidic devices and investigated the role of μ-SAXS (a sketch of the device provided in **Figure 7** Top). The structural characteristics of oil/DMPC bilayers were indicated by the decay in the intensity of the SAXS pattern with an inflection at $q = 0.074$ Å^{-1} corresponding to the first minimum value in the form factor of flat objects extending over large distances (**Figure 7** Bottom left), which was also reported in previous studies involving the liquid/liquid (L/L) interface of w/o emulsions generated by a microfluidic apparatus (103). The bilayer thickness was found to shrink under treatment at 50°C for 1 h, but not to increase the order of the lipid bilayers, as suggested by the minimum position ($q = 0.074$ Å^{-1}) shifting toward higher q-region ($q = 0.088$ Å^{-1}). The authors reported that the phase behavior and structural dynamics of phospholipids at the L/L interfaces can be detected well *via* micro-focusing SAXS (**Figure 7** Bottom right), which may provide deeper

FIGURE 8
Schematic diagram showing the detection of self-assembled structures of lipids during the digestion of milk using a lipolysis device coupled with *in situ* TR-SAXS. Reprinted from Pham et al. (104).

insight into the role of double lipid emulsions in the food industry.

Pham et al. (104) investigated the lipid self-assembly during *in vitro* digestion of bovine, human and goat milk using *in situ* TR-SAXS. The SAXS data revealed similar structural behavior during the early stages of the digestion of three types of milk, indicating lamellar (L_α), inverse hexagonal (H_2), and continuous cubic (V_2) phases (**Figure 8** Top and Middle). All the milk tested self-assembled into non-lamellar liquid crystalline structures, with coexisting lamellar phases associated with calcium soap formation. By tracking the changes in L_α, H_2, and V_2 phases, the investigators concluded that different structures were formed during the digestion of all three infant formulas tested. During the digestion, soy and human milk that released long-chain fatty acids showed an inverse micellar cubic I_2 phase at the oil–water interface, while bovine and goat milk yielded a greater proportion of medium-chain fatty acids tended to exhibit either the V_2 or a H_2 hexagonal phase. In addition, a TR-SAXS equipped with pH-stat or HHP system was used to monitor both the kinetics of lipolysis and structural behavior during the *in vitro* digestion of lipids in the presence of

carbohydrates, such as chitosan (105), amylose (106), and other commercial supplements (as shown in **Figure 8** Bottom).

Undoubtedly, the TR-SAXS (106–108) facilitates real-time monitoring of the crystallization of milk lipids under different treatments, but also assessment of the lipid self-assembly during *in vitro* digestion or under varying buffer conditions, which play a critical role in industrial applications involving the processing and storage of lipid-based foods.

Other biomacromolecules

Traditionally, natural sausage casings are made from collagen-rich intestinal submucosa derived from bovine, porcine and ovine sources. Collagen arrangement in the intestinal submucosa provides strength to animal tissues, although the relationship between structure and strength is not well-characterized. Gunn et al. (109) demonstrated collagen fibril orientation, orientation index (OI) and *d*-spacing of bovine, porcine and ovine sausage casings using SAXS. The *d*-spacing was calculated in the range of 64.8–65.2 nm, and the collagen

fibrils were arranged in planar layers with OI values of 0.86–0.91 based on the X-ray adsorption edge energies of all samples.

Pectin has been approved as Generally Recognized as Safe (GRAS) and as a food emulsifier, stabilizer, thickener, and gelling agent (110). Mendez et al. (111) elucidated the different emulsification mechanisms of three pectin sources (watermelon, citrus and apple) using SAXS. The two shoulder-like peaks in the low-q ($q < \sim0.03$ Å^{-1}) and high-q regions were as attributed to intermolecular interactions and chain clusters, and the scattering of rod-like pectin chains, respectively. The R_{g3} value of all samples with cross-sections of rod-like pectin chains ranged from 1.4 to 2.3 nm. The P_2 corresponding to the smallest structural level ranged from 1.8 to 2.8, suggesting the existence of flexible folded chains rather than ideal rigid rods. The R_{g2} values, referring to the size of the molecular clusters originating as a result of chain bending, determined for pectin solutions (20–38 nm) fall within the range previously determined by SAXS (6.3–42 nm) for pectin with different degrees of esterification.

Food-grade surfactants, like lauric arginate (LAE), have been used widely as a preservative against a wide range of food pathogens and spoilage organisms such as processed meats, dairy products and fruit juices (112). Nallamilli et al. (113) reported a coacervation complex of LAE with λ-carrageenan consisting of loosely packed and disordered LAE molecules with an internal bilayer-like structure indicated by a scattering intensity peak at $q \approx 0.161$ Å^{-1}, based on which, a periodicity value of $d = 2\pi/q \sim 3.9$ nm was calculated. This was consistent with the quantitative analysis involving fitting a Teubner-Strey structure factor yielding d-spacing of the lamellae from 3.75 to 4.01 nm. Formation of bilayer coacervates was observed at the LAE/carrageenan weight ratio of 2 and the maximum coacervation was detected at a ratio of 5.

Conclusion and outlook

In the current review, recent advances in the structural characterization of food biomacromolecules using SAXS are summarized, including the principle, theoretical calculation methods, *in situ* capabilities, and applications. The unique feature of SAXS not only provides direct and rapid structural information of biomolecules in their native state but also facilitates the elucidation of conformational dynamics in real-time. SAXS combined with online chromatography represents a fascinating tool for separating and detecting mixtures and flexible systems synchronously, such as disordered fragments in proteins, long-chain ribonucleic acid and IDPs, which significantly widens the range of SAXS applications. Microfluidics installed in SAXS facilitate the study of binding kinetics by reducing the required sample volume to the sub-microliter level. A combination of T-jump or P-jump pump coupled to TR-SAXS allows direct tracking of the structural dynamics triggered by changes in temperature or pressure over a set time period ranging from microseconds to hours. Based on the volume of studies reported, SAXS is becoming a promising tool for monitoring the structure, conformation, interaction, kinetics, and reaction of biomacromolecules to provide molecular insights into the structure-function relationship of biomolecules in different food processing applications.

In the next decade, the application of the fourth-generation of high-brilliance synchrotron facilities will provide insight into the biomacromolecules at the atomic and molecular levels, and promote cutting-edge research *via* high-resolution imaging, ultrafast process exploration and advanced structural analysis based on SAXS. Furthermore, with the development of artificial intelligence (AI), research that was previously inconceivable or wildly impractical, especially involving protein structure prediction, is now feasible. We have reason to anticipate potential future applications of AI coupled with high-brilliance SAXS in understanding not merely the individual biomacromolecules and complexes in the food industry, but entire cells or even tissues in life science.

Author contributions

YS: conceptualization, methodology, software, writing—review and editing, revise, and supervision. XL and RC: software and writing—review and editing. FL: writing and editing. SW: writing—review and editing, revise, and supervision.

Funding

Conflict of interest

The authors declare that the research was conducted in the absence of any commercial or financial relationships that could be construed as a potential conflict of interest.

Publisher's note

All claims expressed in this article are solely those of the authors and do not necessarily represent those of their affiliated organizations, or those of the publisher, the editors and the reviewers. Any product that may be evaluated in this article, or claim that may be made by its manufacturer, is not guaranteed or endorsed by the publisher.

References

1. Okolie CL, Akanbi TO, Mason B, Udenigwe CC, Aryee ANA. Influence of conventional and recent extraction technologies on physicochemical properties of bioactive macromolecules from natural sources: a review. *Food Res Int.* (2019) 116:827–39. doi: 10.1016/j.foodres.2018.09.018

2. Clore GM, Iwahara J. Theory, practice, and applications of paramagnetic relaxation enhancement for the characterization of transient low-population states of biological macromolecules and their complexes. *Chem Rev.* (2009) 109:4108–39. doi: 10.1021/cr900033p

3. Trampari S, Neumann C, Hjorth-Jensen SJ, Shahsavar A, Quistgaard EM, Nissen P. Insights into the mechanism of high lipid-detergent crystallization of membrane proteins. *J Appl Crystallogr.* (2021) 54:1775–83. doi: 10.1073/pnas.0606149103

4. Wehbie M, Onyia KK, Mahler F, Le Roy A, Deletraz A, Bouchemal I, et al. Maltose-based fluorinated surfactants for membrane-protein extraction and stabilization. *Langmuir.* (2021) 37:2111–22. doi: 10.1021/acs.langmuir.0c03214

5. Svergun DI, Koch MHJ. Small-angle scattering studies of biological macromolecules in solution. *Rep Prog Phys.* (2003) 66:1735–82.

6. Gräwert TW, Svergun DI. Structural modeling using solution small-angle X-ray scattering (SAXS). *J Mol Biol.* (2020) 432:3078–92. doi: 10.1016/j.jmb.2020.01.030

7. de Kruif CG. The structure of casein micelles: a review of small-angle scattering data. *J Appl Crystallogr.* (2014) 47:1479–89.

8. de Kruif CG, Huppertz T, Urban VS, Petukhov AV. Casein micelles and their internal structure. *Adv Colloid Interface Sci.* (2012) 171:36–52.

9. Huang J, Wang Z, Fan L, Ma S. A review of wheat starch analyses: methods, techniques, structure and function. *Int J Biol Macromol.* (2022) 203:130–42.

10. Lopez-Rubio A, Hernandez-Munoz P, Catala R, Gavara R, Lagaron JM. Improving packaged food quality and safety. Part 1: synchrotron X-ray analysis. *Food Addit Contam.* (2005) 22:988–93. doi: 10.1080/02652030500246370

11. Rostamabadi H, Falsafi SR, Assadpour E, Jafari SM. Evaluating the structural properties of bioactive-loaded nanocarriers with modern analytical tools. *Compr Rev Food Sci Food Saf.* (2020) 19:3266–322. doi: 10.1111/1541-4337.12653

12. Smith G, Brok E, Jensen GV, Midtgaard SR, Skar-Gislinge N, Arleth L. Casein studied by X-ray and neutron scattering. *Abstracts of Papers of the American Chemical Society.* Vol. 256. Washington, DC: American Chemical Society (2018).

13. Smith GN, Brok E, Christiansen MV, Ahrne L. Casein micelles in milk as sticky spheres. *Soft Matter.* (2020) 16:9955–63.

14. Gilbert EP. Small-angle X-Ray and neutron scattering in food colloids. *Curr Opin Colloid Interface Sci.* (2019) 42:55–72.

15. Schneidman-Duhovny D, Hammel M, Sali A. Macromolecular docking restrained by a small angle X-ray scattering profile. *J Struct Biol.* (2011) 173:461–71. doi: 10.1016/j.jsb.2010.09.023

16. Singh AK. Chapter 4 - Experimental methodologies for the characterization of nanoparticles. In: Singh AK editor. *Engineered Nanoparticles.* Boston, MA: Academic Press (2016). p. 125–70.

17. Molodenskiy DS, Svergun DI, Kikhney AG. Artificial neural networks for solution scattering data analysis. *Structure.* (2022) 30:900–8.e2.

18. Guinier A. La diffraction des rayons X aux très petits angles : application à l'étude de phénomènes ultramicroscopiques. *Ann Phys.* (1939) 11:161–237.

19. Glatter O. A new method for the evaluation of small-angle scattering data. *J. Appl Crystallogr.* (1977) 10:415–21.

20. Svergun DI. Determination of the regularization parameter in indirect-transform methods using perceptual criteria. *J Appl Crystallogr.* (1992) 25:495–503.

21. Konarev PV, Volkov VV, Sokolova AV, Koch MHJ, Svergun DI. PRIMUS: a windows PC-based system for small-angle scattering data analysis. *J Appl Crystallogr.* (2003) 36:1277–82.

22. Hopkins JB, Gillilan RE, Skou S. BioXTAS RAW: improvements to a free open-source program for small-angle X-ray scattering data reduction and analysis. *J Appl Crystallogr.* (2017) 50:1545–53. doi: 10.1107/S1600576717011438

23. Hansen S. Bayesian estimation of hyperparameters for indirect Fourier transformation in small-angle scattering. *J Appl Crystallogr.* (2000) 33:1415–21.

24. Porod G. Die Röntgenkleinwinkelstreuung von dichtgepackten kolloiden Systemen. *Kolloid Zeitschrift.* (1952) 125:51–7.

25. Trewhella J. Small angle scattering and structural biology: data quality and model validation. In: Nakamura H, Kleywegt G, Burley SK, Markley JL editors.

Integrative Structural Biology with Hybrid Methods. Berlin: Springer (2018). p. 77–100.

26. Pilz I, Glatter O, Kratky O. Small-angle X-ray scattering. *Methods Enzymol.* (1979) 61:148–249.

27. Bizien T, Durand D, Roblina P, Thureau A, Vachette P, Pérez J. A brief survey of state-of-the-art BioSAXS. *Protein Pept Lett.* (2016) 23:217–31. doi: 10.2174/0929866523666160106153655

28. Rambo RP, Tainer JA. Characterizing flexible and intrinsically unstructured biological macromolecules by SAS using the porod-debye law. *Biopolymers.* (2011) 95:559–71. doi: 10.1002/bip.21638

29. Sun Y, Tai Z, Yan T, Dai Y, Hemar Y, Li N. Unveiling the structure of the primary caseinate particle using small-angle X-ray scattering and simulation methodologies. *Food Res Int.* (2021) 149:110653. doi: 10.1016/j.foodres.2021.110653

30. Wang G, Xu L-F, Shen J-L, Yao G-B, Ge Z-L, Li W-Q, et al. Iterative and accurate determination of small angle X-ray scattering background. *Nucl Sci Tech.* (2016) 27:105.

31. Svergun DI. Restoring low resolution structure of biological macromolecules from solution scattering using simulated annealing. *Biophys J.* (1999) 76:2879–86. doi: 10.1016/S0006-3495(99)77443-6

32. Svergun DI, Petoukhov MV, Koch MHJ. Determination of domain structure of proteins from X-ray solution scattering. *Biophys J.* (2001) 80:2946–53. doi: 10.1016/S0006-3495(01)76260-1

33. Grant TD. Ab initio electron density determination directly from solution scattering data. *Nat Methods.* (2018) 15:191–3.

34. Franke D, Jeffries CM, Svergun DI. Machine learning methods for X-ray scattering data analysis from biomacromolecular solutions. *Biophys J.* (2018) 114:2485–92. doi: 10.1016/j.bpj.2018.04.018

35. He H, Liu C, Liu H. Model reconstruction from small-angle X-ray scattering data using deep learning methods. *iScience.* (2020) 23:100906. doi: 10.1016/j.isci.2020.100906

36. Hura GL, Hodge CD, Rosenberg D, Guzenko D, Duarte JM, Monastyrskyy B, et al. Small angle X-ray scattering-assisted protein structure prediction in CASP13 and emergence of solution structure differences. *Proteins.* (2019) 87:1298–314. doi: 10.1002/prot.25827

37. Panjkovich A, Svergun DI. Deciphering conformational transitions of proteins by small angle X-ray scattering and normal mode analysis. *Phys Chem Chem Phys.* (2016) 18:5707–19. doi: 10.1039/c5cp04540a

38. Petoukhov MV, Svergun DI. Global rigid body modeling of macromolecular complexes against small-angle scattering data. *Biophys J.* (2005) 89:1237–50. doi: 10.1529/biophysj.105.064154

39. Petoukhov MV, Franke D, Shkumatov AV, Tria G, Kikhney AG, Gajda M, et al. New developments in the ATSAS program package for small-angle scattering data analysis. *J Appl Crystallogr.* (2012) 45:342–50.

40. Hou J, Adhikari B, Tanner JJ, Cheng J. SAXSDom: modeling multidomain protein structures using small-angle X-ray scattering data. *Proteins.* (2020) 88:775–87. doi: 10.1002/prot.25865

41. Svergun D, Barberato C, Koch MHJ. CRYSOL– a program to evaluate X-ray solution scattering of biological macromolecules from atomic coordinates. *J Appl Crystallogr.* (1995) 28:768–73.

42. Kozin MB, Svergun DI. Automated matching of high- and low-resolution structural models. *J Appl Crystallogr.* (2001) 34:33–41.

43. Tria G, Mertens HDT, Kachala M, Svergun DI. Advanced ensemble modelling of flexible macromolecules using X-ray solution scattering. *IUCrJ.* (2015) 2:207–17. doi: 10.1107/S205225251500202X

44. Konarev PV, Svergun DI. Direct shape determination of intermediates in evolving macromolecular solutions from small-angle scattering data. *IUCrJ.* (2018) 5:402–9. doi: 10.1107/S2052252518005900

45. Hermann MR, Hub JS. SAXS-restrained ensemble simulations of intrinsically disordered proteins with commitment to the principle of maximum entropy. *J Chem Theory Comput.* (2019) 15:5103–15. doi: 10.1021/acs.jctc.9b00338

46. Lincoff J, Haghighatlari M, Krzeminski M, Teixeira JMC, Gomes G-NW, Gradinaru CC, et al. Extended experimental inferential structure determination method in determining the structural ensembles of disordered protein states. *Commun Chem.* (2020) 3:74. doi: 10.1038/s42004-020-0323-0

47. Bottaro S, Bengtsen T, Lindorff-Larsen K. Integrating molecular simulation and experimental data: a bayesian/maximum entropy reweighting approach. In:

Gáspári Z editor. *Structural Bioinformatics: Methods and Protocols*. New York, NY: Springer US (2020). p. 219–40. doi: 10.1007/978-1-0716-0270-6_15

48. Konarev PV, Gruzinov AY, Mertens HDT, Svergun DI. Restoring structural parameters of lipid mixtures from small-angle X-ray scattering data. *J Appl Crystallogr.* (2021) 54:169–79. doi: 10.1107/S16005767200115368

49. Konarev PV, Petoukhov MV, Dadinova LA, Fedorova NV, Volynsky PE, Svergun DI, et al. BILMIX: a new approach to restore the size polydispersity and electron density profiles of lipid bilayers from liposomes using small-angle X-ray scattering data. *J Appl Crystallogr.* (2020) 53:236–43.

50. Petukhov MV, Konarev PV, Dadinova LA, Fedorova NV, Volynsky PE, Svergun DI, et al. Quasi-atomistic approach to modeling of liposomes. *Crystallogr Rep.* (2020) 65:258–63.

51. Manalastas-Cantos K, Konarev PV, Hajizadeh NR, Kikhney AG, Petoukhov MV, Molodenskiy DS, et al. ATSAS 3.0: expanded functionality and new tools for small-angle scattering data analysis. *J Appl Crystallogr.* (2021) 54:343–55. doi: 10.1107/S1600576720013412

52. Schneidman-Duhovny D, Hammel M, Tainer JA, Sali A. FoXS, FoXSDock and MultiFoXS: single-state and multi-state structural modeling of proteins and their complexes based on SAXS profiles. *Nucleic Acids Res.* (2016) 44:W424–9. doi: 10.1093/nar/gkw389

53. Karaca E, Bonvin AMJJ. On the usefulness of ion-mobility mass spectrometry and SAXS data in scoring docking decoys. *Acta Crystallogr D Biol Crystallogr.* (2013) 69:683–94. doi: 10.1107/S0907444913007063

54. Ignatov M, Kazennov A, Kozakov D. ClusPro FMFT-SAXS: ultra-fast filtering using small-angle X-ray scattering data in protein docking. *J Mol Biol.* (2018) 430:2249–55. doi: 10.1016/j.jmb.2018.03.010

55. Jiménez-García B, Bernadó P, Fernández-Recio J. Structural characterization of protein–protein interactions with pyDockSAXS. In: Gáspári Z editor. *Structural Bioinformatics: Methods and Protocols*. New York, NY: Springer US (2020). p. 131–44.

56. Sønderby P, Rinnan Å, Madsen JJ, Harris P, Bukrinski JT, Peters GHJ. Small-angle X-ray scattering data in combination with Rosettadock improves the docking energy landscape. *J Chem Inf Model.* (2017) 57:2463–75. doi: 10.1021/acs.jcim.6b00789

57. Schneidman-Duhovny D, Hammel M. Modeling structure and dynamics of protein complexes with SAXS profiles. *Methods Mol Biol.* (2018) 1764:449–73.

58. Schindler, Christina EM, de Vries SJ, Sasse A, Zacharias M. SAXS data alone can generate high-quality models of protein-protein complexes. *Structure.* (2016) 24:1387–97. doi: 10.1016/j.str.2016.06.007

59. Huang W, Ravikumar KM, Parisien M, Yang S. Theoretical modeling of multiprotein complexes by iSPOT: integration of small-angle X-ray scattering, hydroxyl radical footprinting, and computational docking. *J Struct Biol.* (2016) 196:340–9. doi: 10.1016/j.jsb.2016.08.001

60. Molodenskiy DS, Svergun DI, Mertens HDT. MPBuilder: a PyMOL plugin for building and refinement of solubilized membrane proteins against small angle X-ray scattering data. *J Mol Biol.* (2021) 433:166888. doi: 10.1016/j.jmb.2021.166888

61. Mahieu E, Gabel F. Biological small-angle neutron scattering: recent results and development. *Acta Crystallogr D Struct Biol.* (2018) 74:715–26.

62. Brennich M, Hutin S, Weinhaupl K, Schanda P, Pernot P. Beyond size exclusion: online liquid chromatography for BioSAXS. *Acta Crystallogr A Found Adv.* (2017) 73:A83–83.

63. Panjkovich A, Svergun DI. CHROMIXS: automatic and interactive analysis of chromatography-coupled small-angle X-ray scattering data. *Bioinformatics.* (2018) 34:1944–6. doi: 10.1093/bioinformatics/btx846

64. Shkumatov AV, Strelkov SV. DATASW, a tool for HPLC–SAXS data analysis. *Acta Crystallogr D Biol Crystallogr.* (2015) 71:1347–50. doi: 10.1107/S1399004715007154

65. Malaby AW, Chakravarthy S, Irving TC, Kathuria SV, Bilsel O, Lambright DG. Methods for analysis of size-exclusion chromatography–small-angle X-ray scattering and reconstruction of protein scattering. *J Appl Crystallogr.* (2015) 48:1102–13. doi: 10.1107/S1600576715010420

66. Konarev PV, Graewert MA, Jeffries CM, Fukuda M, Cheremnykh TA, Volkov VV, et al. EFAMIX, a tool to decompose inline chromatography SAXS data from partially overlapping components. *Protein Sci.* (2022) 31:269–82. doi: 10.1002/pro.4237

67. Brookes E, Vachette P, Rocco M, Perez J. US-SOMO HPLC-SAXS module: dealing with capillary fouling and extraction of pure component patterns from poorly resolved SEC-SAXS data. *J Appl Crystallogr.* (2016) 49:1827–41. doi: 10.1107/S1600576716011201

68. Clulow AJ, Salim M, Hawley A, Boyd BJ. A closer look at the behaviour of milk lipids during digestion. *Chem Phys Lipids.* (2018) 211:107–16. doi: 10.1016/j.chemphyslip.2017.10.009

69. Ravishankar H, Nors Pedersen M, Sitsel A, Li C, Duelli A, Levantino M, et al. Tracking Ca2+ATPase intermediates in real-time by X-ray solution scattering. *Sci Adv.* (2020) 6:eaaz0981. doi: 10.1126/sciadv.aaz0981

70. Heyes DJ, Hardman SJO, Pedersen MN, Woodhouse J, De La Mora E, Wulff M, et al. Light-induced structural changes in a full-length cyanobacterial phytochrome probed by time-resolved X-ray scattering. *Commun Biol.* (2019) 2:1. doi: 10.1038/s42003-018-0242-0

71. Thompson MC, Barad BA, Wolff AM, Sun Cho H, Schotte F, Schwarz DMC, et al. Temperature-jump solution X-ray scattering reveals distinct motions in a dynamic enzyme. *Nat Chem.* (2019) 11:1058–66. doi: 10.1038/s41557-019-0329-3

72. Rimmerman D, Leshchev D, Hsu DJ, Hong J, Abraham B, Henning R, et al. Revealing fast structural dynamics in ph-responsive peptides with time-resolved X-ray scattering. *J Phys Chem B.* (2019) 123:2016–21. doi: 10.1021/acs.jpcb.9b00072

73. Kim TW, Lee SJ, Jo J, Kim JG, Ki H, Kim CW, et al. Protein folding from heterogeneous unfolded state revealed by time-resolved X-ray solution scattering. *Proc Natl Acad Sci USA.* (2020) 117:14996–5005. doi: 10.1073/pnas.1913442117

74. Hsu DJ, Leshchev D, Kosheleva I, Kohlstedt KL, Chen LX. Unfolding bovine α-lactalbumin with T-jump: characterizing disordered intermediates via time-resolved x-ray solution scattering and molecular dynamics simulations. *J Chem Phys.* (2021) 154:105101. doi: 10.1063/5.0039194

75. Kuang Q, Xu J, Liang Y, Xie F, Tian F, Zhou S, et al. Lamellar structure change of waxy corn starch during gelatinization by time-resolved synchrotron SAXS. *Food Hydrocoll.* (2017) 62:43–8.

76. Hempt C, Gontsarik M, Buerki-Thurnherr T, Hirsch C, Salentinig S. Nanostructure generation during milk digestion in presence of a cell culture model simulating the small intestine. *J Colloid Interface Sci.* (2020) 574:430–40. doi: 10.1016/j.jcis.2020.04.059

77. Krishnamoorthy K, Kewalramani S, Ehlen A, Moreau LM, Mirkin CA, de la Cruz MO, et al. Enzymatic degradation of DNA probed by in situ X-ray scattering. *ACS Nano.* (2019) 13:11382–91.

78. Narayanan T, Konovalov O. Synchrotron scattering methods for nanomaterials and soft matter research. *Materials.* (2020) 13:752.

79. Ilhan-Ayisigi E, Yaldiz B, Bor G, Yaghmur A, Yesil-Celiktas O. Advances in microfluidic synthesis and coupling with synchrotron SAXS for continuous production and real-time structural characterization of nano-self-assemblies. *Colloids Surf B Biointerfaces.* (2021) 201:111633. doi: 10.1016/j.colsurfb.2021.111633

80. Berntsson O, Terry AE, Plivelic TS. A setup for millisecond time-resolved X-ray solution scattering experiments at the CoSAXS beamline at the MAX IV Laboratory. *J Synchrotron Radiat.* (2022) 29:555–62. doi: 10.1107/S1600577522000996

81. Balasubramaniam VM. Process development of high pressure-based technologies for food: research advances and future perspectives. *Curr Opin Food Sci.* (2021) 42:270–277.

82. Ferreira Zielinski AA, Sanchez-Camargo ADP, Benvenutti L, Ferro DM, Dias JL, Salvador Ferreira SR. High-pressure fluid technologies: recent approaches to the production of natural pigments for food and pharmaceutical applications. *Trends Food Sci Technol.* (2021) 118:850–69.

83. Harish B, Gillilan RE, Zou J, Wang J, Raleigh DP, Royer CA. Protein unfolded states populated at high and ambient pressure are similarly compact. *Biophys J.* (2021) 120:2592–8. doi: 10.1016/j.bpj.2021.04.031

84. Yang S, Tyler AII, Ahrné L, Kirkensgaard JJK. Skimmed milk structural dynamics during high hydrostatic pressure processing from in situ SAXS. *Food Res Int.* (2021) 147:110527. doi: 10.1016/j.foodres.2021.110527

85. Rai DK, Gillilan RE, Huang Q, Miller R, Ting E, Lazarev A, et al. High-pressure small-angle X-ray scattering cell for biological solutions and soft materials. *J Appl Crystallogr.* (2021) 54:111–22. doi: 10.1107/S1600576720014752

86. Vella J, Hemar Y, Gu Q, Wu ZR, Li N, Söhnel T. In-situ SAXS investigation of high-pressure triglyceride polymorphism in milk cream and anhydrous milk fat. *LWT.* (2021) 135:110174.

87. Lehmkühler F, Schroer MA, Markmann V, Frenzel L, Möller J, Lange H, et al. Kinetics of pressure-induced nanocrystal superlattice formation. *Phys Chem Chem Phys.* (2019) 21:21349–54. doi: 10.1039/c9cp04658e

88. Loveday SM. Food proteins: technological, nutritional, and sustainability attributes of traditional and emerging proteins. *Annu Rev Food Sci Technol.* (2019) 10:311–39. doi: 10.1146/annurev-food-032818-121128

89. Alrosan M, Tan TC, Easa AM, Gammoh S, Alu'datt MH. Molecular forces governing protein-protein interaction: structure-function relationship of

complexes protein in the food industry. *Crit Rev Food Sci Nutr.* (2022) 62:4036–52. doi: 10.1080/10408398.2021.1871589

90. Yang Z, de Campo L, Gilbert EP, Knott R, Cheng L, Storer B, et al. Effect of NaCl and CaCl₂ concentration on the rheological and structural characteristics of thermally-induced quinoa protein gels. *Food Hydrocoll.* (2022) 124:107350.

91. Pohl C, Mahapatra S, Kulakova A, Streicher W, Peters GHJ, Nørgaard A, et al. Combination of high throughput and structural screening to assess protein stability – A screening perspective. *Eur J Pharm Biopharm.* (2022) 171:1–10. doi: 10.1016/j.ejpb.2021.08.018

92. Yang Z, Gu Q, Banjar W, Li N, Hemar Y. In situ study of skim milk structure changes under high hydrostatic pressure using synchrotron SAXS. *Food Hydrocoll.* (2018) 77:772–6.

93. Comerford KB, Papanikolaou Y, Jones JM, Rodriguez J, Slavin J, Angadi S, et al. Toward an evidence-based definition and classification of carbohydrate food quality: an expert panel report. *Nutrients.* (2021) 13:2667. doi: 10.3390/nu13082667

94. Zeng X, Zheng B, Li T, Chen L. How to synchronously slow down starch digestion and retrogradation: a structural analysis study. *Int J Biol Macromol.* (2022) 212:43–53. doi: 10.1016/j.ijbiomac.2022.05.099

95. Xu J, Blennow A, Li X, Chen L, Liu X. Gelatinization dynamics of starch in dependence of its lamellar structure, crystalline polymorphs and amylose content. *Carbohydr Polym.* (2020) 229:115481. doi: 10.1016/j.carbpol.2019.115481

96. Xu J, Li Z, Zhong Y, Zhou Q, Lv Q, Chen L, et al. The effects of molecular fine structure on rice starch granule gelatinization dynamics as investigated by in situ small-angle X-ray scattering. *Food Hydrocoll.* (2021) 121:107014.

97. Díaz-Calderón P, Simone E, Tyler AII, Enrione J, Foster T. A structural study of the self-association of different starches in presence of bacterial cellulose fibrils. *Carbohydr Polym.* (2022) 288:119361. doi: 10.1016/j.carbpol.2022.119361

98. Li C, Gong B, Hu Y, Liu X, Guan X, Zhang B. Combined crystalline, lamellar and granular structural insights into in vitro digestion rate of native starches. *Food Hydrocoll.* (2020) 105:105823.

99. Yang Z, Swedlund P, Hemar Y, Mo G, Wei Y, Li Z, et al. Effect of high hydrostatic pressure on the supramolecular structure of corn starch with different amylose contents. *Int J Biol Macromol.* (2016) 85:604–14.

100. Bascuas S, Morell P, Hernando I, Quiles A. Recent trends in oil structuring using hydrocolloids. *Food Hydrocoll.* (2021) 118:106612.

101. Wang G, Chen H, Wang L, Zou Y, Wan Z, Yang X. Formation of protein oleogels via capillary attraction of engineered protein particles. *Food Hydrocoll.* (2022) 133:107912.

102. Clemente I, Torbensen K, Di Cola E, Rossi F, Ristori S, Abou-Hassan A. Exploring the water/oil/water interface of phospholipid stabilized double emulsions by micro-focusing synchrotron SAXS. *RSC Adv.* (2019) 9:33429–35. doi: 10.1039/c9ra05894j

103. Di Cola E, Torbensen K, Clemente I, Rossi F, Ristori S, Abou-Hassan A. Lipid-stabilized water–oil interfaces studied by microfocusing small-angle X-ray scattering. *Langmuir.* (2017) 33:9100–5. doi: 10.1021/acs.langmuir.7b02076

104. Pham AC, Peng K-Y, Salim M, Ramirez G, Hawley A, Clulow AJ, et al. Correlating digestion-driven self-assembly in milk and infant formulas with changes in lipid composition. *ACS Appl Bio Mater.* (2020) 3:3087–98. doi: 10.1021/acsabm.0c00131

105. May KL, Tangso KJ, Hawley A, Boyd BJ, Clulow AJ. Interaction of chitosan-based dietary supplements with fats during lipid digestion. *Food Hydrocoll.* (2020) 108:105965.

106. Jia X, Sun S, Chen B, Zheng B, Guo Z. Understanding the crystal structure of lotus seed amylose–long-chain fatty acid complexes prepared by high hydrostatic pressure. *Food Res Int.* (2018) 111:334–41. doi: 10.1016/j.foodres.2018.05.053

107. Dyett B, Zychowski L, Bao L, Meikle TG, Peng S, Yu H, et al. Crystallization of Femtoliter Surface Droplet Arrays Revealed by Synchrotron Small-Angle X-ray Scattering. *Langmuir.* (2018) 34:9470–6. doi: 10.1021/acs.langmuir.8b01252

108. Yaghmur A, Lotfi S, Ariabod SA, Bor G, Gontsarik M, Salentinig S. Internal lamellar and inverse hexagonal liquid crystalline phases during the digestion of krill and astaxanthin oil-in-water emulsions. *Front Bioeng Biotechnol.* (2019) 7:384. doi: 10.3389/fbioe.2019.00384

109. Gunn S, Sizeland KH, Wells HC, Haverkamp RG. Collagen arrangement and strength in sausage casings produced from natural intestines. *Food Hydrocoll.* (2022) 129:107612.

110. Li Z, Xiong Y, Wang Y, Zhang Y, Luo Y. Low density lipoprotein-pectin complexes stabilized high internal phase pickering emulsions: the effects of pH conditions and mass ratios. *Food Hydrocoll.* (2023) 134:108004.

111. Mendez DA, Fabra MJ, Martínez-Abad A, Martínez-Sanz M, Gorria M, López-Rubio A. Understanding the different emulsification mechanisms of pectin: comparison between watermelon rind and two commercial pectin sources. *Food Hydrocoll.* (2021) 120:106957.

112. Hu X, Huang E, Barringer SA, Yousef AE. Factors affecting *Alicyclobacillus acidoterrestris* growth and guaiacol production and controlling apple juice spoilage by lauric arginate and ε-polylysine. *LWT.* (2020) 119:108883.

113. Nallamilli T, Ketomaeki M, Prozeller D, Mars J, Morsbach S, Mezger M, et al. Complex coacervation of food grade antimicrobial lauric arginate with lambda carrageenan. *Curr Res Food Sci.* (2021) 4:53–62. doi: 10.1016/j.crfs.2021.01.003

114. Jiménez-García B, Pons C, Svergun DI, Bernadó P, Fernández-Recio J. pyDockSAXS: protein–protein complex structure by SAXS and computational docking. *Nucleic Acids Res.* (2015) 43:W356–61.

115. Xia B, Vajda S, Kozakov D. Accounting for pairwise distance restraints in FFT-based protein–protein docking. *Bioinformatics.* (2016) 32:3342–4. doi: 10.1093/bioinformatics/btw306

116. Chen P-C, Masiewicz P, Rybin V, Svergun D, Hennig J. A General Small-Angle X-ray Scattering-Based Screening Protocol Validated for Protein–RNA Interactions. *ACS Comb Sci.* (2018) 20:197–202. doi: 10.1021/acscombsci.8b00007

117. Graewert M, Vela SD, Grwert TW, Molodenskiy DS, Jeffries CMJC. Adding size exclusion chromatography (SEC) and light scattering (LS) devices to obtain high-quality small angle X-ray scattering (SAXS) data. *Crystals.* (2020) 10:975.

118. Graewert MA, Franke D, Jeffries CM, Blanchet CE, Ruskule D, Kuhle K, et al. Automated pipeline for purification, biophysical and X-ray analysis of biomacromolecular solutions. *Sci Rep.* (2015) 5:10734. doi: 10.1038/srep10734

119. Takemasa M, Yuguchi Y, Kitamura S. Size and shape of cycloamylose estimated using column chromatography coupled with small-angle X-ray scattering. *Food Hydrocoll.* (2020) 108:105948.

120. Watanabe Y. Size-exclusion chromatography combined with solution X-ray scattering measurement of the heat-induced aggregates of water-soluble proteins at low ionic strength in a neutral solution. *J Chromatogr A.* (2019) 1603:190–8. doi: 10.1016/j.chroma.2019.06.042

121. Watanabe Y, Inoko Y. Characterization of a large glycoprotein proteoglycan by size-exclusion chromatography combined with light and X-ray scattering methods. *J Chromatogr A.* (2013) 1303:100–4. doi: 10.1016/j.chroma.2013.06.048

122. Ryan TM, Trewhella J, Murphy JM, Keown JR, Casey L, Pearce FG, et al. An optimized SEC-SAXS system enabling high X-ray dose for rapid SAXS assessment with correlated UV measurements for biomolecular structure analysis. *J Appl Crystallogr.* (2018) 51:97–111.

123. Kim JH, Min B, Yun YD, Choi HJ, Jin KS. Size-exclusion chromatography coupled with small-angle X-ray scattering on the 4C small-angle X-ray scattering beamline at pohang light source II. *Bull Korean Chem Soc.* (2020) 41:1052–5.

124. Inoue R, Nakagawa T, Morishima K, Sato N, Okuda A, Urade R, et al. Newly developed Laboratory-based Size exclusion chromatography Small-angle x-ray scattering System (La-SSS). *Sci Rep.* (2019) 9:12610. doi: 10.1038/s41598-019-48911-w

125. Bucciarelli S, Midtgaard SR, Nors Pedersen M, Skou S, Arleth L, Vestergaard B. Size-exclusion chromatography small-angle X-ray scattering of water soluble proteins on a laboratory instrument. *J Appl Crystallogr.* (2018) 51:1623–32. doi: 10.1107/S1600576718014462

126. Banc A, Pincemaille J, Costanzo S, Chauveau E, Appavou M-S, Morel M-H, et al. Phase separation dynamics of gluten protein mixtures. *Soft Matter.* (2019) 15:6160–70.

127. Chen D, Kuzmenko I, Ilavsky J, Pinho L, Campanella O. Structural evolution during gelation of pea and whey proteins envisaged by time-resolved ultra-small-angle x-ray scattering (USAXS). *Food Hydrocoll.* (2022) 126:107449.

128. Chen D, Zhu X, Ilavsky J, Whitmer T, Hatzakis E, Jones OG, et al. Polyphenols Weaken Pea Protein Gel by Formation of Large Aggregates with Diminished Noncovalent Interactions. *Biomacromolecules.* (2021) 22:1001–14. doi: 10.1021/acs.biomac.0c01753

129. Tsung K-L, Ilavsky J, Padua GW. Formation and characterization of zein-based oleogels. *J Agric Food Chem.* (2020) 68:13276–81. doi: 10.1021/acs.jafc.0c00184

130. Da Vela S, Braun MK, Dörr A, Greco A, Möller J, Fu Z, et al. Kinetics of liquid–liquid phase separation in protein solutions exhibiting LCST phase behavior studied by time-resolved USAXS and VSANS. *Soft Matter.* (2016) 12:9334–41. doi: 10.1039/c6sm01837h

131. Mao Y, Su Y, Hsiao BS. Probing structure and orientation in polymers using synchrotron small- and wide-angle X-ray scattering techniques. *Eur Polym J.* (2016) 81:433–46.

132. Yamamoto K, Suzuki S, Kitamura S, Yuguchi Y. Gelation and structural formation of amylose by in situ neutralization as observed by small-angle X-ray scattering. *Gels.* (2018) 4:57.

133. Royes J, Bjørnestad VA, Brun G, Narayanan T, Lund R, Tribet C. Transition kinetics of mixed lipid:photosurfactant assemblies studied by time-resolved small angle X-ray scattering. *J Colloid Interface Sci.* (2022) 610:830–41. doi: 10.1016/j.jcis.2021.11.133

134. Gontsarik M, Yaghmur A, Salentinig S. Dispersed liquid crystals as pH-adjustable antimicrobial peptide nanocarriers. *J Colloid Interface Sci.* (2021) 583:672–82. doi: 10.1016/j.jcis.2020.09.081

135. Yaghmur A, Rappolt M, Jonassen ALU, Schmitt M, Larsen SW. In situ monitoring of the formation of lipidic non-lamellar liquid crystalline depot formulations in synovial fluid. *J Colloid Interface Sci.* (2021) 582:773–81.

136. Komorowski K, Schaeper J, Sztucki M, Sharpnack L, Brehm G, Köster S, et al. Vesicle adhesion in the electrostatic strong-coupling regime studied by time-resolved small-angle X-ray scattering. *Soft Matter.* (2020) 16:4142–54.

137. Khaliqi K, Ghazal A, Azmi IDM, Amenitsch H, Mortensen K, Salentinig S, et al. Direct monitoring of lipid transfer on exposure of citrem nanoparticles to an ethanol solution containing soybean phospholipids by combining synchrotron SAXS with microfluidics. *Analyst.* (2017) 142:3118–26. doi: 10.1039/c7an00860k

Impacts of hesperidin on whey protein functionality: Interacting mechanism, antioxidant capacity, and emulsion stabilizing effects

Yin Wang[1], Yangkai Guo[1], Longtao Zhang[2], Meilan Yuan[1], Li Zhao[1], Chunqing Bai[1]* and David Julian McClements[3]*

[1]National R&D Branch Center for Freshwater Fish Processing, College of Life Science, Jiangxi Science and Technology Normal University, Nanchang, China, [2]College of Food Science, Fujian Agriculture and Forestry University, Fuzhou, Fujian, China, [3]Department of Food Science, University of Massachusetts, Amherst, MA, United States

The objective of this work was to explore the possibility of improving the antioxidant capacity and application of whey protein (WP) through non-covalent interactions with hesperidin (HES), a citrus polyphenol with nutraceutical activity. The interaction mechanism was elucidated using several spectroscopic methods and molecular docking analysis. The antioxidant capacity of the WP-HES complexes was analyzed and compared to that of the proteins alone. Moreover, the resistance of oil-in-water emulsions formulated using the WP-HES complexes as antioxidant emulsifiers to changes in environmental conditions (pH, ion strength, and oxidant) was evaluated. Our results showed that HES was incorporated into a single hydrophobic cavity in the WP molecule, where it was mainly held by hydrophobic attractive forces. As a result, the microenvironments of the non-polar tyrosine and tryptophan residues in the protein molecules were altered after complexation. Moreover, the α-helix and β-sheet regions in the protein decreased after complexation, while the β-turn and random regions increased. The antioxidant capacity of the WP-HES complexes was greater than that of the proteins alone. Non-radiative energy transfer from WP to HES was detected during complex formation. Compared to WP alone, the WP-HES complexes produced emulsions with smaller mean droplet diameters, exhibited higher pH and salt stability, and had better oxidative stability. The magnitude of these effects increased as the HES concentration was increased. This research would supply valuable information on the nature of the interactions between WP and HES. Moreover, it may lead to the creation of dual-function antioxidant emulsifiers for application in emulsified food products.

KEYWORDS

whey protein, hesperidin, interaction, molecular docking technology, emulsions

1. Introduction

Whey protein (WP), a co-product of cheese making, is widely used in the food industry as an emulsifying, foaming, thickening, film-forming, and encapsulating agent (1). The excellent nutritional profile and diverse functional attributes of WP have led to its widespread application a broad spectrum of food products (2–7). Like many other foods proteins, however, the application of WP is often limited because of its tendency to aggregate when exposed to certain types of environmental conditions, such as pH values around the isoelectric point, high salt levels, and heating above the thermal denaturation temperature. Moreover, WP only has a relatively low ability to retard lipid oxidation, which limits its application as a natural antioxidant in foods. The functional properties of proteins can often be improved by modifying their structures (8). Physical, chemical, and biological modification methods have been developed and employed for this purpose. Compared to other methods, physical modifications are often more affordable and environmentally friendly, and do not require regulatory approval (6, 8–12). Recently, improving the antioxidant activity of food proteins by physically attaching natural antioxidant molecules to their surfaces has gained increasing popularity.

Phenolic compounds are usually secondary metabolites produced by plants, which have at least one aromatic ring with one or more hydroxyl groups attached (5, 13). These molecules can scavenge free radicals and prevent oxidative damage, thereby acting as natural antioxidants. They have also been reported to exhibit various other health-promoting effects, including antitumor, anti-inflammatory, and antimicrobial activities (14). Phenolic compounds can be combined with proteins to create protein-phenolic complexes that can be used as multi-functional food ingredients, such as antioxidant emulsifiers. Numerous studies have reported that phenolic compounds can spontaneously bind to proteins *via* non-covalent interactions, and alter their structures and functionalities (8, 15).

Various kinds of proteins (e.g., whey protein, casein, and gelatin) and polyphenols (e.g., tannic acid, curcumin, and phenolic acids) have been shown to form protein-polyphenol complexes with different functional properties (15–18). For example, chlorogenic acid was reported to bind to casein and WP through non-covalent interactions, which altered the structure, solubility, and foaming capacity of the proteins (19). Proanthocyanidins have been reported to interact with rice proteins, which altered the secondary structure and surface hydrophobicity of the proteins (20). Other researchers reported that tyrosol and hydroxytyrosol in olive oil extracts showed no or weak binding to several food proteins (caseinate, bovine serum albumin, β-lactoglobulin, and gelatin), whereas other olive oil phenolics showed strong binding (21). Overall, these studies show that the strength of the binding interaction, the conformational changes of the proteins, and the functionality of

the complexes formed depend on polyphenol and protein type (5, 22).

In this study, we examined interactions between WP and hesperidin (HES). HES is a flavonoid glycoside phenolic compound, commonly found in citrus fruits such as oranges and lemons (23, 24). Because of its potential health benefits such as antihyperlipidemic, cardioprotective, antihypertensive, antidiabetic, and antioxidant activities, HES has attracted considerable attention for its potential application as a nutraceutical ingredient in foods (25, 26). Previous studies have reported the interaction of HES with various proteins, including glutenin (23), HMG-CoA reductase enzyme (27), SARS-CoV2 spike protein (28) and digestive enzyme (29). The results of these researches suggest that HES exerts strong binding affinity to these proteins. Jiang et al. (23) also reported that HES could improve the functional properties (thermal properties and emulsifying activity) of edible protein. It is known that the interacting mechanism varies greatly depending on protein and phenolic type (13, 14). For instance, previous studies suggest that the binding of HES to glutenin (23) was dominated by hydrogen bonding and hydrophobic forces, whereas the binding of HES to α-amylase was dominated by van der Waals forces and hydrogen bonding (29). Consequently, it is important to establish the binding mechanism for specific protein-phenolic pairs, as well as the impact of these interactions on the functionality of the complexes formed.

Whey proteins are commonly used as emulsifiers in the food industry to produce nutraceutical-loaded oil-in-water emulsions or nanoemulsions (30, 31). Typically, the WPs are dissolved in water and then homogenized with an oil phase containing the nutraceutical. The protein molecules adsorb to the oil-water interface and form a protective coating around the oil droplets, which can protect the nutraceuticals from chemical degradation, e.g., oxidation. However, WP only has limited potential to inhibit lipid oxidation in emulsions. We hypothesized that complexing WP with HES would improve its emulsifying and antioxidant properties, thereby leading to the formation of complexes that could be used as dual-purpose antioxidant emulsifiers in foods. Consequently, we used a combination experimental measurements and molecular dynamics simulations to understanding the interactions between WP and HES and their impact on protein functionality.

2. Materials and methods

2.1. Materials and reagents

WP (purity > 90%) was purchased from Shanghai Yuanye Biotech Co., Ltd., Diphenyl-2-picrylhydrazyl free radical (DPPH), HES, KBr (spectral purity), and 2,4,6-tris(2-pyridyl)-s-triazine (TPTZ) were purchased from Aladdin Industrial Company (Shanghai, China). All other chemical reagents were

of analytical grade. Double distilled water was used throughout the research. WP powder was dissolved in phosphate buffer (PB) solution (10 mM, pH 6.80) to obtain a stock WP solution of 0.5 mg/mL. This solution was diluted to 0.1 mg/mL with PB before use. An aqueous HES solution was prepared by weighing HES powder into water, adjusted the pH 12 using 0.1 mol/L NaOH for sufficiently soluble, and then made up to a constant volume using distilled water to obtain a stock solution containing 1×10^{-3} mol/L of HES.

2.2. Fluorescence spectra

A series of complex solutions with final HES concentrations from 0 to 26.7 μM was prepared according to Li et al. (32). Briefly, increasing aliquots of HES solution was dropped into 3.0 mL of 0.1 mg/mL WP. The mixture was adjusted to pH 6.80 with 0.01 M/L hydrochloric acid solution, equilibrated for 30 min, and then measured on a Model F-7000 fluorescence spectrofluorometer (Hitachi, Tokyo, Japan). The fluorescence emission spectra of the mixture samples kept at 298, 304, and 310 K, respectively, were recorded at an excitation wavelength of 280 nm.

2.3. Synchronous fluorescence spectrometry

Synchronous fluorescence spectrometry of the mixed samples was carried out using the same method described in section "2.2 Fluorescence spectra" but Δλ values of 15 and 60 nm were used to monitor the changes in the local environment of the tyrosine and tryptophan residues in the WP, respectively.

2.4. Ultraviolet- visible (UV-VIS) spectra measurements

Ultraviolet- visible (UV-VIS) spectra of samples placed in cuvettes were collected from 300 to 450 nm using a UV-visible spectrophotometer (UV-1800, Shanghai Meipuda Instrument Co., Ltd., Shanghai, China).

2.5. Fourier transform infrared spectroscopy (FTIR)

Fourier transform infrared spectroscopy (FTIR) spectra of freeze-dried samples mixed with potassium bromide (1:100 w/w) were recorded over the wavenumber range from 400 to 4,000 cm^{-1}. Amide I band (1,600–1,700 cm^{-1}) of the spectra was deconvoluted using Peak-Fit v4.12 software (SPSS

Inc., Chicago, IL). The secondary structures of the protein were then analyzed as the percentages of α-helixes, β-sheets, β-turns, and random coils.

2.6. Molecular docking simulation

The model structure of HES (ID: 10621) was downloaded from PubChem database.[1] The model structures of α-Lactalbumin (α-LA) and β-lactoglobulin (β-LG) named as PDB ID: 1F6S and 1BEB, respectively, were downloaded from the RCSB database[2] and then used to carry out the molecular docking simulations, since α-LA and β-LG are the most abundant constituents in WP. Before being imported into the AutoDock Vina Program (AutoDock 1.5.6), the original water molecules and ligands in the α-LA and β-LG 3D structure were deleted using PyMOL tools. In addition, hydrogen atoms and charges were added to the protein molecule structures prior to carrying out the simulations. HES and α-LA/β-LG were set as the ligand and receptor, respectively. The interaction between HES and α-LA/β-LG was then modeled using the AutoDock Vina Program. The docking was performed taking the center of the HES as the grid center (β-LG: −4.5, 4, 16. α-LA: 35, 50, 10) and docking boxes of size was 50Å × 40 Å × 55Å (β-LG) and 120Å × 160 Å × 72Å (α-LA), respectively. Top 10 poses of the docking results were saved, and the one that showed the lowest interaction energy was regarded as the optimized result. The interactions between HES and α-LA/β-LG were visualized using the Discovery Studio 2016 program.

2.7. Determination of antioxidant activity

The influence of HES binding on the antioxidant capacity of WP was evaluated by DPPH assay and ferric reducing power (FRAP assay).

2.7.1. DPPH assay

The DPPH radical scavenging capacity of the samples was determined using a method described previously (33), with some modifications. 1 mL of the test sample was mixed with 2 mL of DPPH reagent and then stored in the dark at room temperature for 30 min. The absorbance of the mixtures was then measured at 517 nm using a UV spectrophotometer (UV-1800, Shanghai Meipuda Instrument Co., Ltd., Shanghai, China). Results were expressed as the Trolox equivalent (TE) antioxidant capacity (mg of TE/L of sample).

---

1 http://PubChem.ncbi.nlm.nih.gov

2 http://www.rcsb.org

2.7.2. FRAP assay

The ferric reducing power of the samples was determined according to a method described previously (34), with slight modifications. Briefly, 1 mL of sample was added to 4.5 mL of FRAP working reagent, mixed thoroughly, and then placed in the dark at 37°C. After reaction for 10 min, the absorbance of the samples was measured at 593 nm using UV-1800 UV spectrophotometer. The ferric reducing power of HES-WP complexes, free HES, and free WP were measured and compared. Results are expressed in terms of the TE antioxidant capacity.

2.8. Stability WP-HES based emulsion

2.8.1. Nanoemulsion preparation

A 1.0 wt% WP solution was prepared by dispersing powdered WP (1.0 g) into 100 mL of 10 mM PB solution (PBS, pH 6.8) and stirring at ambient temperature for 5 h. The resulting solution was then stored overnight at 4°C and filtered (Fisher Scientific, PA) to remove any insoluble particles before further use. HES stock solutions were obtained by dispersing powdered HES powders in water as described in section "2.1 Materials and reagents" Different volumes of HES stock solution were added into the WP solution, sonicated for 15 min, and then stirred for 2 min to obtain HES-WP complexes with final HES concentrations of 1 or 2 mM. Coarse emulsions were formed by blending 90 wt% aqueous solutions containing WP or HED-WP complexes with 10 wt% coix seed oil at 12,000 rpm for 2 min by using a high-speed mixer. To fabricated fine emulsions, these coarse emulsions were then homogenized on a high-pressure homogenizer for 5 times at 110 MPa. Sodium azide (0.02 wt%) was added to prevent bacterial growth (please note, this is a non-food grade antimicrobial agent).

2.8.2. Particle size and zeta potential measurement

The particle size distribution and zeta potential of the emulsions were determined using a laser diffraction particle size analyzer (LS 12 320, Beckman Coulter, Inc., Brea, CA). To avoid multiple scattering, samples were diluted 100-fold by using PBS (pH 6.8, 10 mM) before measurement.

2.8.3. Morphological characterization

The microstructure of the emulsions was imaged using an inverted fluorescence microscope (ECLIPSE Ti-U, Nikon Co., Japan). Before analysis, 200 μL of emulsion was thoroughly mixed with an equal volume of PBS. Then, 20 μL of Nile red solution (1 mg/ml) were added into the mixture and the system was shaken to dye the oil phase. An aliquot of sample was then dropped on to a microscope slide, covered by a cover slip, and then imaged by using a 60 × oil objective lens.

2.8.4. The pH stability of emulsions

Emulsions made with WP or HED-WP complexes were adjusted to different pH values (pH 3.0–9.0) by adding a small amount of HCl (1 M) or NaOH (1 M) solutions. All samples were placed in 10 ml capped test tubes and stored at 4°C overnight. The particle size distribution, zeta potential, and microstructure of the emulsions were then determined.

2.8.5. Salt-stability

The salt-stability of emulsions prepared using either WP or HED-WP complexes as an emulsifier was determined by measuring their particle size distribution, zeta potential, and microstructure after they being exposed to a range of NaCl solutions (0–500 mM) overnight.

2.8.6. Oxidization stability

Freshly prepared coix oil loaded emulsions were placed in glass tubes with screwed caps, and then incubated in the dark for 15 days at 55°C. Samples were withdrawn periodically during storage for analysis of the extent of lipid oxidation. The primary reaction production (peroxide value, PV) and secondary reaction product (thiobarbituric acid reactive substances, TBARS) in the emulsions systems were determined according to the methods reported (35, 36). The content of lipid PV was calculated based on a standard curve of cumene hydroperoxide and expressed as mmol hydroperoxide per kg oil. The TBARS content was calculated from a standard curve prepared using 1, 1, 3, 3-tetramethoxypropane, and expressed as mmol malondialdehyde equivalent per kg oil.

2.9. Statistical analysis

All experiments were carried out at least three times and the data were expressed as the means ± standard deviation (SD). Significant differences were analyzed on "SPSS 19.0" statistical software using one-way ANOVA with Duncan's test, and $p < 0.05$ was considered as statistically significant.

3. Results and discussion

3.1. Fluorescence emission spectrum

Phenylalanine, tyrosine, and tryptophan are the main fluorescent amino acids in proteins. Of these, tryptophan is the dominant intrinsic fluorophore. It exhibits intrinsic protein fluorescence when excited at 280 nm and observed at around 350 nm (20). The intensity and wavelength of the resulting intrinsic protein fluorescence peak is highly sensitive to the local environment of the tryptophan residues (22). In our experiment, the fluorescence emission spectra of WP in the presence of various concentrations of HES were measured at
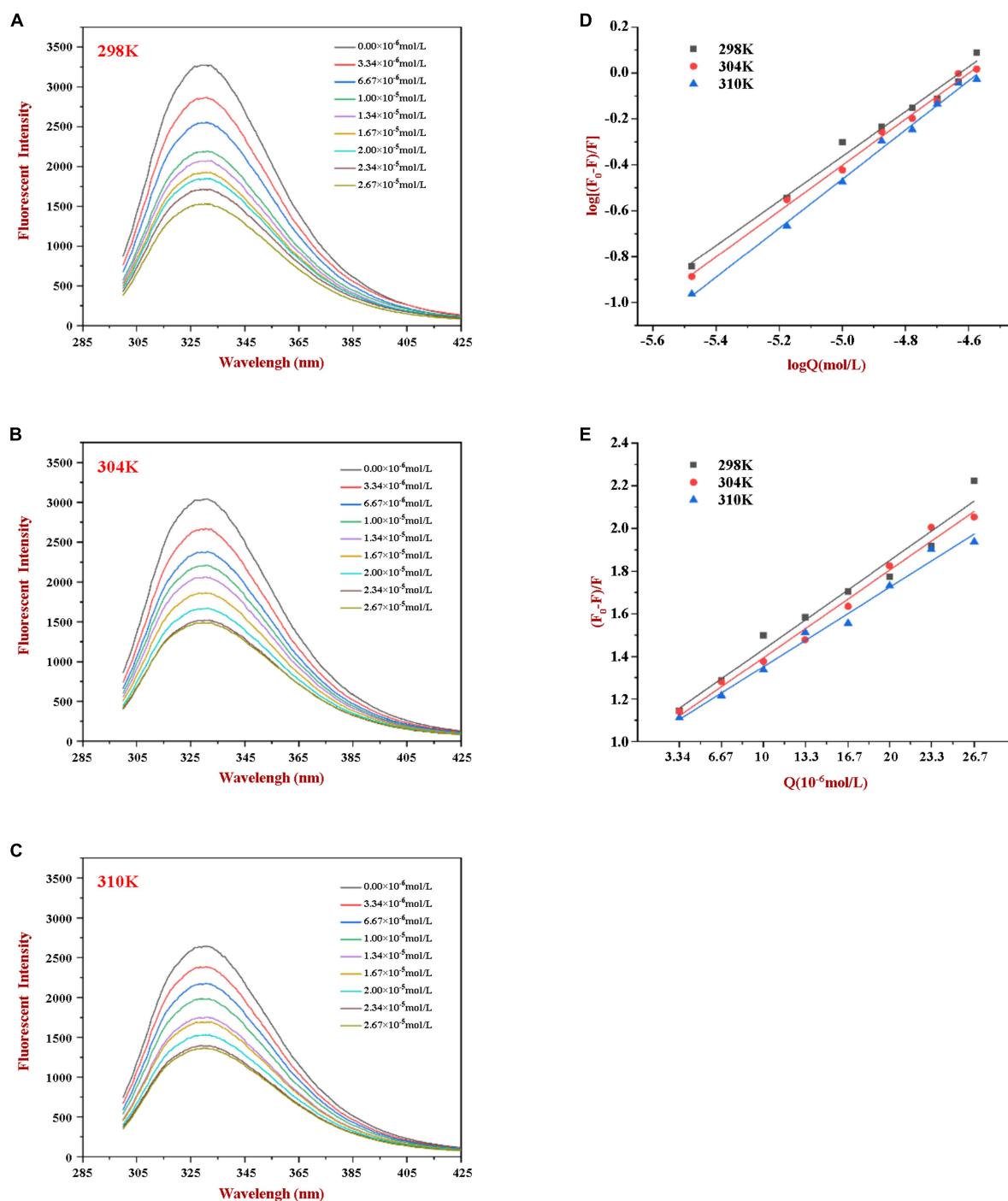
FIGURE 1

Fluorescence emission profiles of WP at various concentrations of HES (0−26.7 μM) at 298K **(A)**, 304K **(B)**, and 310K **(C)**. The Double-log plots **(D)** and Stern-Volmer plots **(E)** of the interaction between WP and HES at different temperatures.

different temperatures to explore the interactions between HES and WP. As shown in **Figure 1**, a strong fluorescence emission peak at approximately 345 nm was observed. The fluorescence intensity decreased gradually as the HES content was increased. Moreover, a slight red shift of about 2 nm occurred in the

wavelength where the peak maximum was observed when the HES levels were increased. The observed reduction in the fluorescence peak intensity, and shift in the peak position, of WP in the presence of HES is indicative of a binding interaction between the protein and polyphenol molecules (13, 22). The

red shift suggests that the microenvironment of the tryptophan residues was altered in a manner that was consistent with a decrease of hydrophobicity or increase in polarity in the binding sites in the protein molecules (5). Similar results have been reported by other researchers. Dai et al. found that resveratrol could quench rice glutelin's intrinsic fluorescence and alter its maximum peak of 2 nm (20) Kong et al. reported the ability of xylitol to quench the intrinsic fluorescence intensity of WP in a dose dependent-manner (5).

3.2. Fluorescence quenching mechanism

According to the literature, fluorescence quenching mechanisms can be categorized as either dynamic mechanism or static mechanism (8, 23). To establish the mechanism between WP and HES, the fluorescence quenching behavior of the protein and polyphenol was measured at three different temperatures (298, 304, and 310 K) and the data were then analyzed using a Stern-Volmer Eq. (1). As shown in **Figure 1**, the Stern-Volmer curves exhibited good linearity ($R > 0.99$) for all temperatures used (**Figure 1E**), indicating that quenching was either due to a collisional or a static mechanism. **Table 1** shows that the K_{SV} values decreased gradually as the temperature increased, being 4.44×10^4, 3.92×10^4, and 3.43×10^4 L·mol^{-1} for 298, 304, and 310 K, respectively. Moreover, the smallest K_Q value (343×10^{10} L·mol^{-1}·s^{-1}) was much higher than 2.0×10^{10} L·mol^{-1}·s^{-1} (the maximum diffusion collision quenching constant), indicating that HES could induce static quenching of WP. In addition, the decrease in K_{SV} values with increasing temperature suggests the interaction complex formed was less stable at higher temperatures (22).

For static quenching, Eq. (2) was used to calculate the binding constant (K_a) and the number (n) of binding site of the WP and HES interaction. As summarized in **Table 1**, the n values were all approximately equal to 1, suggesting that WP had one binding site for HES. The calculated K_a values of the WP-HES complexes decreased as the temperature increased, indicating that the binding force was diminished at higher temperatures, which is in consistence with K_{SV} (23). The weaker affinity of HES to WP may be due to the decrease in the strength of the hydrophobic interactions when the temperature was raised (5, 32).

$$\frac{F_0}{F} = 1 + K_Q\tau_0[Q] = 1 + K_{SV}[Q] \tag{1}$$

$$\log\frac{F_0 - F}{F} = \log K_a + n \log[Q] \tag{2}$$

Here, F_0 and F represent the fluorescent intensity of WP before and after HES was added, respectively. Also, τ_0 (10^{-8} s) is the fluorescence lifetime in the absence of quenchers, [Q] is the concentration of HES, K_{SV} is quenching constant for Stern-Volmer, K_Q is the quenching rate parameter, K_a is binding constant, and n is the number of binding sites.

3.3. Thermodynamic parameters

To better understand the main forces contributing to the formation of the WP-HES complexes, the enthalpy change (ΔH), entropy change (ΔS), and free energy change (ΔG) were calculated using the Van't Hoff equation Eq. (3) followed by the free energy Eq. (4)

$$\text{In}K_a = -\frac{\Delta H}{RT} + \frac{\Delta S}{R} \tag{3}$$

$$\Delta G = \Delta H - T\Delta S \tag{4}$$

Here, R is the gas constant (8.314 J·mol^{-1}K^{-1}), T is the absolute temperature (298, 304, or 310 K), and K_a is the binding constant, which is the same one shown in Eq. (2). The ΔH and ΔS values were obtained from the slope and intercept of the linear Van't Hoff curves based on ln K_a vs. 1/T, respectively, then ΔG was calculated using Eq. (4).

Four types of binding forces (hydrophobic, hydrogen bonding, van der Waals, and electrostatic forces) have been reported to play a role in the formation of non-covalent protein-polyphenol complexes (37). Insights into the relative importance of these forces can often be obtained by examining the relative signs of the free energy, enthalpy, and entropy changes. Negative ΔG values indicate spontaneous binding; positive ΔH and negative ΔS indicates electrostatic and hydrophobic interactions are the predominant force; negative ΔH and ΔS suggest van der Waals forces or hydrogen bonds play a major role in the interaction; positive ΔH and ΔS involve hydrophobic forces are the main force; negative ΔH and positive ΔS values indicate electrostatic forces are dominate (20). As shown in **Table 2**, ΔG was below zero, indicating that the binding of HES with WP was spontaneous. Meanwhile, the positive ΔS and ΔH (0.27 kJ·mol^{-1}·K^{-1} and 55.0 kJ·mol^{-1}) suggesting that hydrophobic forces are dominate driving forces for the WP and HES interaction. This result is consistent with previous studies, which also reported that hydrophobic interactions were the main driving force involved in formatting soy protein-resveratrol complexes (37, 38). WP-xylitol complex (5), and rice glutelin-procyanidin complex (37).

3.4. Non-radiative energy transfer

Based on Förster theory, non-radiative energy transfer usually occurs when there is sufficient overlap of the fluorescence emission spectrum of the donor molecule and the

TABLE 1 Quenching constants K_{SV}, binding constants Ka, and the number of binding sites n for the interaction between WP and HES at different temperatures.

T (K)	K_{SV} (× 10^4 L·mol^{-1})	K_a (× 10^5 L·mol^{-1})	n	K_Q (× 10^{11} L·mol^{-1}·s^{-1})	R
298	4.44 ± 0.25^a	7.54 ± 0.02^a	0.9791 ± 0.04^c	44.4 ± 0.25^a	0.993
304	3.92 ± 0.11^b	3.89 ± 0.11^b	0.9984 ± 0.03^b	39.2 ± 0.11^b	0.997
310	3.43 ± 0.18^c	3.14 ± 0.05^c	1.0745 ± 0.02^a	34.3 ± 0.18^c	0.998

R is the correlation coefficient for the K_{SV} values. Results are expressed as means $\pm$ SD ($n = 3$). Values with different uppercase letters in the same column are significantly different ($p < 0.05$).

ultraviolet absorption spectrum of the acceptor molecule, and the distance between the two molecules is below 7 nm (39). Energy transfer rate, spectral overlap, and distance between the donor and recipient can be calculated using the following equations:

$$E = 1 - \frac{F}{F_0} = \frac{R_0^6}{R_0^6 + r_6} \tag{5}$$

$$R_0^6 = 8.8 \times 10^{-25} K^2 n^{-4} \emptyset J \tag{6}$$

$$J = \frac{\sum F(\lambda)\, \varepsilon(\lambda)\, \lambda^4 \Delta\lambda}{\sum F(\lambda)\, \Delta\lambda} \tag{7}$$

Here, F_0 and F are the same values as in Eq. (1), E is the rate of energy transfer, r is the Förster distance between the WP and HES, R_0 is the critical energy transfer when 50% energy is transferred, K^2 is the dipole orientation factor, n is the refractive index of the medium, J is the spectral overlap integral, Ø is the fluorescence quantum yield of the WP in the absence of the HES, $F(\lambda)$ and $e(\lambda)$ are the WP's corrected fluorescence intensity and the HES's molar extinction coefficient at the wavelength of λ, respectively.

In our experiment, WP and HES are assumed to be the donor and acceptor, respectively, and the values of n, K^2, and Ø were taken to be 1.336, 2/3, and 0.12, respectively. The spectral overlap of the WP emission spectrum and the HES absorption spectrum is shown in **Figure 2**. Based on the above equations, E = 0.126, r = 2.896 nm, and R_0 = 2.097 nm. The value of distance "r" is smaller than 7 nm and within the range of 0.5 R_0 and 1.5 R_0, which suggests that the energy transfer occurs (from WP to HES), resulting in static quenching (29).

TABLE 2 Thermodynamic parameters for the interaction of WP with HES at different temperatures.

T (K)	ΔG (kJ·mol^{-1})	ΔS (kJ·kmol^{-1}·K^{-1})	ΔH (kJ·mol^{-1})
298	-25.43 ± 0.22^a	0.27 ± 0.55	55.03 ± 0.46
304	-27.05 ± 0.13^b		
310	-28.67 ± 0.09^c		

Results are expressed as means $\pm$ SD ($n = 3$). Values with different uppercase letters in the same column are significantly different ($p < 0.05$).

3.5. Synchronous fluorescence

Synchronous fluorescence spectroscopy is useful for providing information about changes in the local microenvironment of several amino acid residues in proteins, which can be used to analyze the influence of ligand binding on protein conformation (29, 32). When the Δλ values are set at 15 and 60 nm, this method can provide characteristic information about changes in the microenvironments of tyrosine and tryptophan residues, respectively (5). **Figure 3** shows the synchronous fluorescence spectra of WP in the presence of various concentrations of HES. Obviously, the fluorescence intensity of tryptophan (at maximum peak) was markedly higher than that of tyrosine (at maximum peak), indicating that tryptophan was the main contributor to the WP fluorescence signals. Moreover, the fluorescence intensity of the two residues decreased gradually with increasing HES concentration. When the HES concentration was 2.67×10^{-5} mm/ml, there was a decrease of 48.7 and 56.8% in the original fluorescence intensities of the tyrosine and tryptophan, respectively. The higher reduction in tryptophan fluorescence intensity may be because it was much closer to the binding sites than tyrosine, and therefore contributed more to the binding process (40). Taken together, the fluorescence and synchronous fluorescence spectroscopy measurements indicate that WP and HES formed non-fluorescent complexes (19). Meanwhile, both maximum peaks appeared to show slight shifts with increasing HES concentration. When Δλ was set at 60 nm, a blue shift from 275 to 270 nm occurred, which indicated that the hydrophobicity of the tryptophan microenvironment increased and/or its polarity decreased after HES bound to the WP (5, 38). This effect is consistent with the non-polar HES molecules binding to the hydrophobic pocket on the surface of the WP molecules where the tryptophan residues are located, thereby resulting in an increase in the hydrophobicity of their microenvironment (37). When Δλ was set at 15 nm, a small red shift from 290 to 292 nm was observed, suggesting only a slight decrease in hydrophobicity and/or increase in polarity around the tyrosine residues. These changes may be due to the fact that more tyrosine residues were exposed to an aqueous environment after binding, which may have been due to a change in protein conformation (19, 27). The observed microenvironment changes of the tyrosine and tryptophan residues therefore
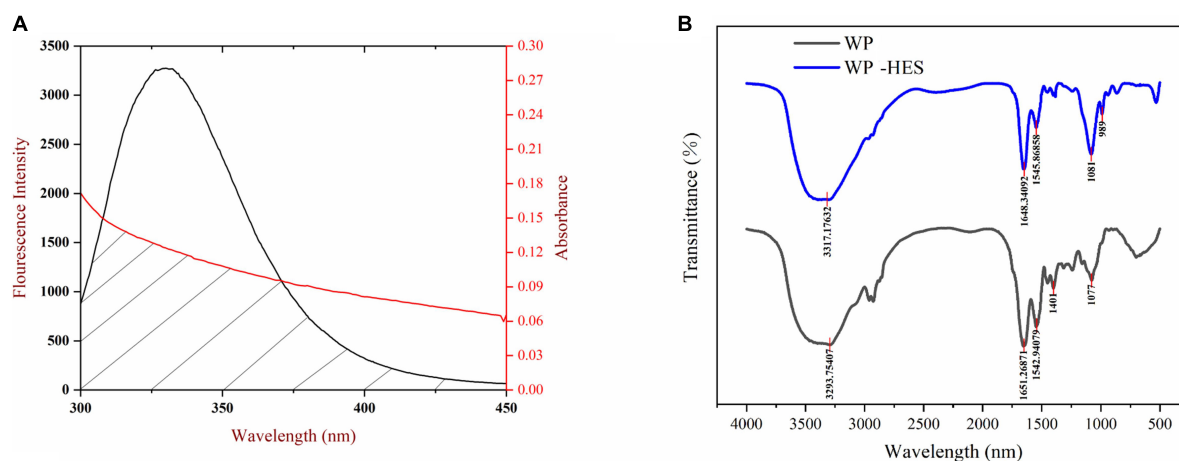
FIGURE 2
The overlapping area of the UV-VIS absorption spectrum of HES and the WP fluorescence spectrum **(A)**, the red line and black line represent UV-VIS absorption spectrum and fluorescence spectrum, respectively; FTIR spectrograms of WP and WP-HES **(B)**.
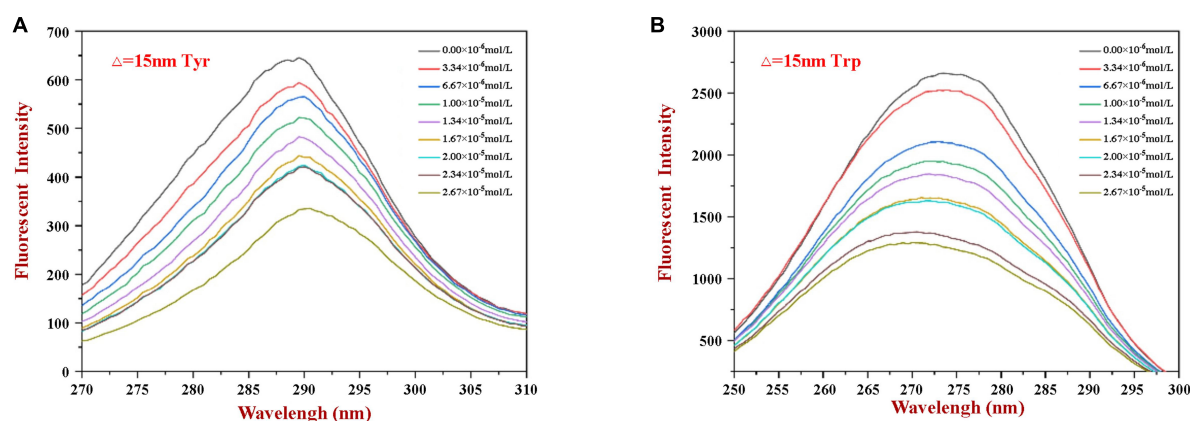

FIGURE 3
The synchronous fluorescence spectrum of WP in the absence and presence of HES at $\Delta\lambda$ = 15 nm **(A)** and $\Delta\lambda$ = 60 nm **(B)**.

TABLE 3 Secondary structure contents in WP and WP-HES.

Samples	α-helix	β-sheet	β-turn	Random coil
WP	22.08% ± 0.56[a]	32.35% ± 0.32[a]	26.71% ± 0.21[b]	18.86% ± 0.14[b]
WP-HES	19.55% ± 0.38[b]	27.16% ± 0.46[a]	32.05% ± 0.28[a]	21.24% ± 0.33[a]

Results are expressed as means ± SD (n = 3). Values with different uppercase letters in the same column are significantly different (p < 0.05).

suggest there was a change in the conformation of the WP molecule conformation after HES binding.

3.6. FTIR spectroscopy

Fourier transform infrared spectroscopy spectroscopy can be used to provide information about changes in the secondary structure of proteins (41). Several characteristic peaks were obtained for WP, which could be related to the presence of specific functional groups **Figure 2**: the broad band at 3,293 cm^{-1} (Amide A) is attributed to hydrogen bonding coupled with NH-stretching; the peak at 1,651 cm^{-1} (Amide I) is attributed to C-O stretching/hydrogen bonding coupled with COO-; the peak at 1542.94 cm^{-1} (Amide II) is attributed to NH bending coupled with CN stretching (42).

These peaks underwent various changes after binding of HES to WP: the amide A peak shifted to higher wavenumbers; the amide I peak moved to lower wavenumbers; and the amide
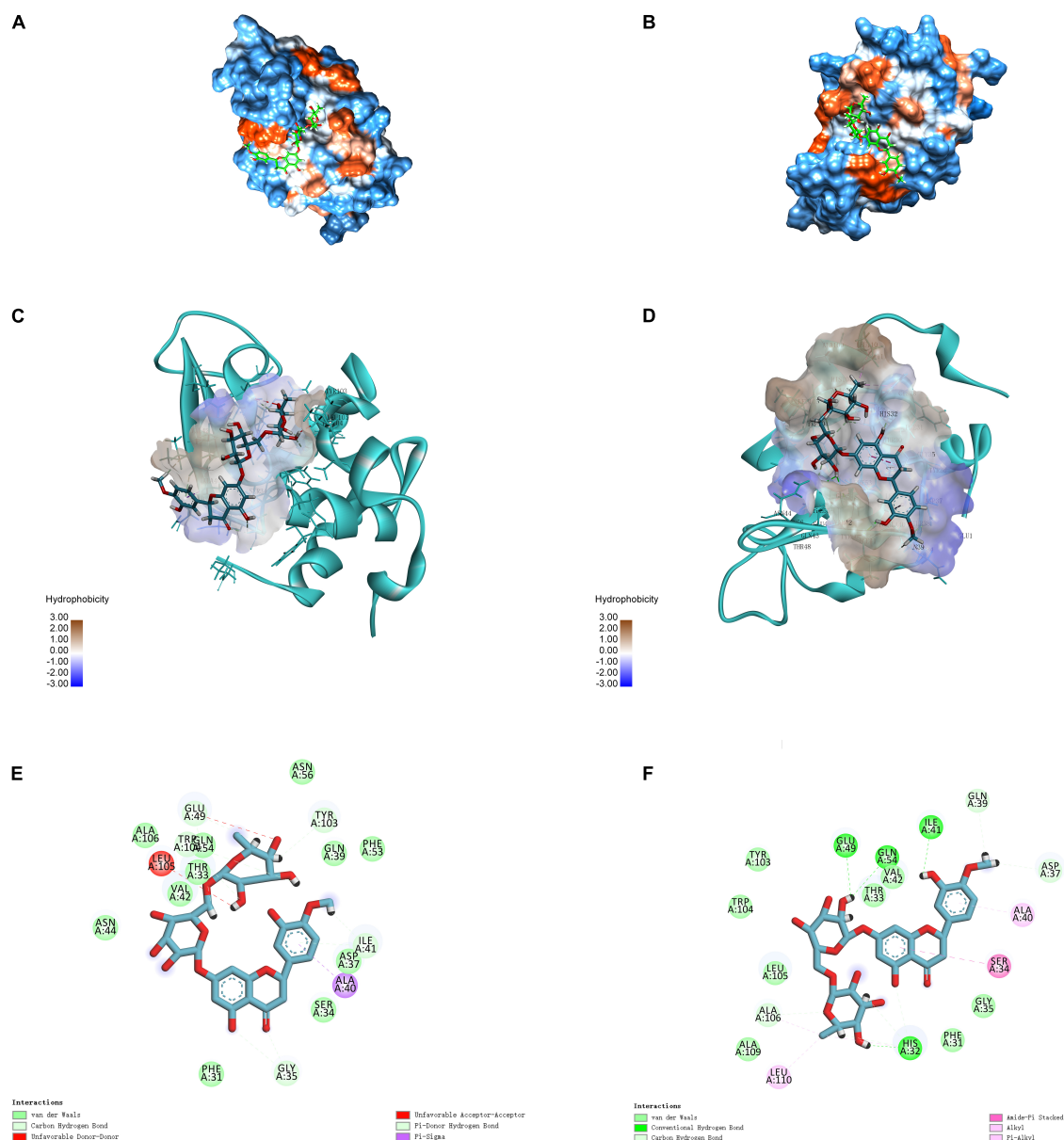
FIGURE 4
3D diagrams of α-LA-HES **(A)** and β-LG-HES **(B)**; the hydrophobicity surface of α-LA **(C)** and β-LG **(D)** interacted with HES, the red color and blue color represent hydrophobicity and hydrophilicity, respectively; 2D schematic interaction diagram α-LA-HES **(E)** and β-LG-HES **(F)**, the color of amino acid residue is drawn by interaction.

II shifted from 1542.94 to 1545.86 cm^{-1}. Moreover, there was a decrease in the intensities of all these peaks. These changes may be due to a hydrophobic interaction between the oxygen atom and hydroxyl group of HES and the C = O and C-N groups of the WP [43, 44]. Researchers reported a similar finding when using FTIR spectroscopy to study the interaction of gelatin with tannic acid and grape seed proanthocyanidins [17].

The amide I band is more sensitive to changes in the secondary structure of proteins than the amide H band [17]. Thus, the amide I spectra were deconvoluted to quantitatively analyze the secondary structure of the proteins before and after binding of the HES (Table 3). Before binding, the secondary structure of WP consisted of 32.4% of β-sheet, 26.7% of β-turn, 22.1% of a-helix, and 18.9% of random coil. After binding to HES, there was a major decrease in the α-helix (19.6%) and β-sheet (27.2%) content of the WP, and an increase in the β-turn and random coil structure. These changes suggest that binding of HES to the protein caused the ordered regions of the polypeptide chain to partially unfold. This result is consistent with previous studies, which reported a similar
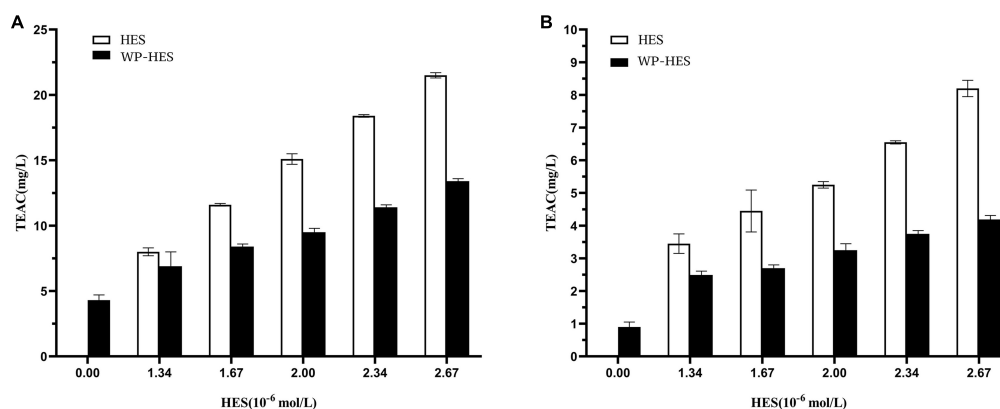
FIGURE 5

Diphenyl-2-picrylhydrazyl free radical scavenging activity **(A)** and ferric-reducing antioxidant power **(B)** of WP-HES complexes.
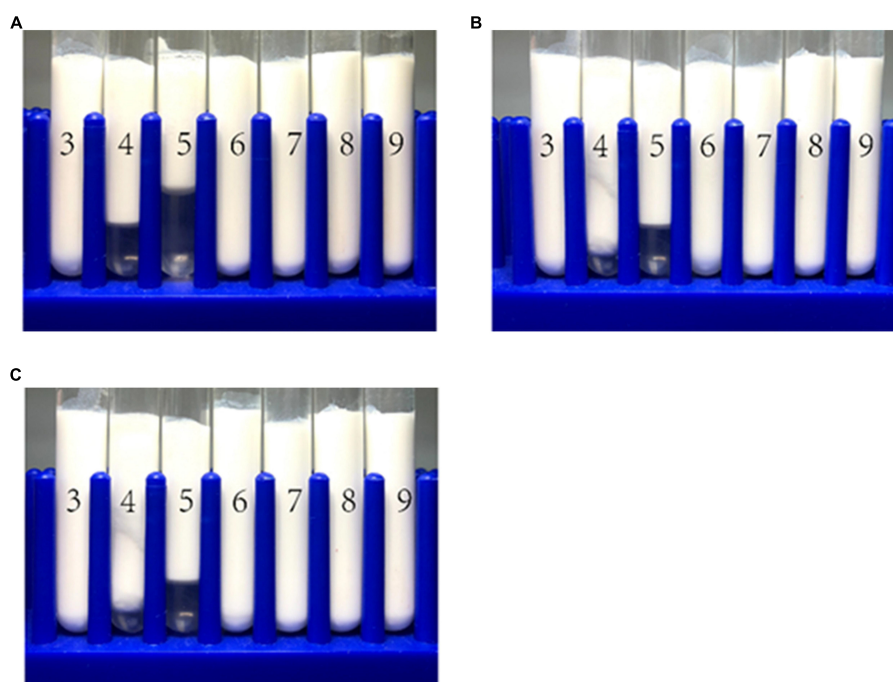

FIGURE 6

The visual appearance of WP-based emulsion **(A)**, WP-HES (1 mM) based emulsion **(B)**, and WP-HES (2 mM) based emulsion **(C)** under different pH values (numbers on the tubes).

change in secondary structure in casein after interacting with tea polyphenols (42).

3.7. Molecular docking simulation

Molecular docking simulation is a useful tool for providing insights into the interaction between receptor and ligand molecules (24, 42). In our simulations, HES was chosen as a ligand, whereas α-LA and β-LG, as the main components in WP,

were selected as receptors. The most likely molecular interaction conformations of α-LA/β-LG and HES, which were taken to be the ones with the lowest energy score, are shown in **Figure 4**. The 3D molecular docking mode (**Figure 4A**) and 2D interaction diagram (**Figure 4E**) suggest that HES inserted itself into a hydrophobic cavity in the β-LG. HES was mainly surrounded by 18 amino acid residues on the β-LG, including Gln 39, Asp 37, Ala 40, Ser 34, Gly 35, Phe 31, His 32, Leu 110, Ala 109, Ala 106, Leu 105, Trp 104, TYR 103, Glu 49, Gln 54, Val 42, Thr 33, Ile
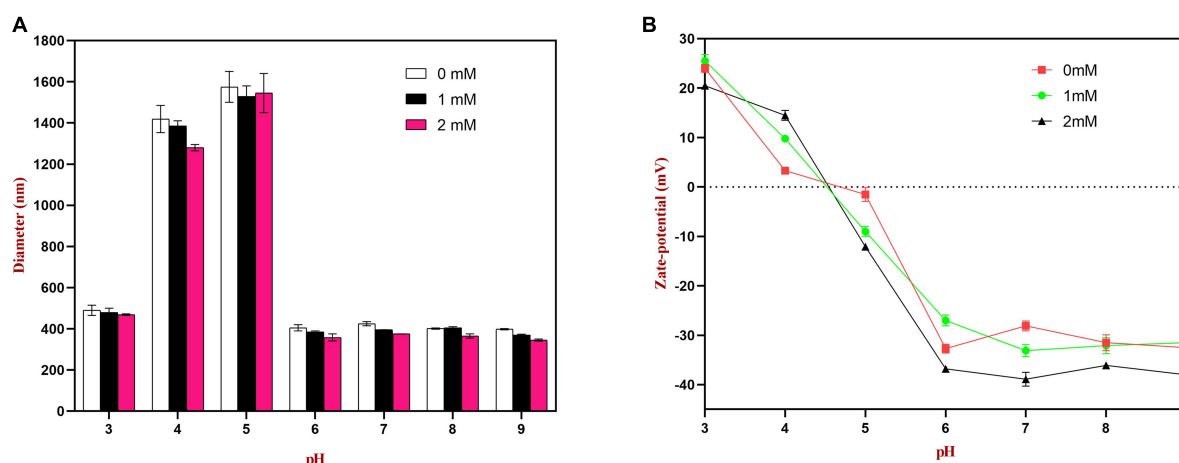
FIGURE 7

Effects of pH on the particle size **(A)** and zeta potential **(B)** of WP or WP-HES complex stabilized emulsions.

41. Among them, five hydrophobic interaction forces (four Pi-alkyl groups and one Amide-Pi Stacked) were found between the aromatic rings of HES and the alkyl groups of Ala 106, Leu 110, His 32, Ser 34, and Ala 40. Additionally, four hydrogen bonds were also observed between the H-acceptor sites of Glu 49, Gln 54, Ile 41, His 32 and the hydroxyl groups of HES. Similarly, HES entered into the hydrophobic inner cavity on α-LA surface and was surrounded by 18 amino acid residues. However, only one hydrophobic interaction (Pi-Sigma) was found between HES and Ala 40, and van der Waals forces and H-bonding drove the interaction. The different binding forces between α-LA/β-LG with HES could be assigned to their different structures. Obviously, the model of β-LG was more suitable to simulate the interaction between WP and HES, after comparing with the results of thermodynamic and FTIR analysis discussed earlier. The important role of hydrophobic interactions between proteins and phenolics were also reported by other researchers. For instance, WP-mulberry anthocyanin complexes were mainly held together by hydrophobic interactions, with van der Waals forces and H-bonding also making some contribution (43). Similarly, rice glutelin-procyanidin complexes were also found to be mainly held together by hydrophobic attractive forces (20).

3.8. Determination of antioxidant activity

The antioxidant capacities of the WP-HES complexes, WPs, and HES were compared using the FRAP reducing power and DPPH radical scavenging assays (34). Although these methods differ in reaction conditions and mechanisms, the antioxidant capacity of all the samples followed similar trends. Both FRAP (**Figure 5B**) and DPPH (**Figure 5A**) assays showed that the antioxidant activities of the WP-HES complexes and free HES

increased in a dose dependent manner with increasing HES concentration. However, the antioxidant capacity of the WP-HES complexes was significantly lower than that of free HES at the same HES concentration, and higher than that of the WP control (0 μM HES).

As shown in **Figure 5A**, the DPPH scavenging activity of the WP control was 1.09 mg TE/L solution. This value gradually increased to 4.2 mg TE/L when the HES concentration was raised to 26.7 μM. This result confirmed that the binding of HES to the WP increased the antioxidative activity of the protein. This result agrees with previous reports. For instance, the radical scavenging activity of β-lactoglobulin, α-lactalbumin, and BSA all increased after they bound epigallocatechin gallate (34) whereas the antioxidant activity of gelatin increased after it bound tannic acid (17). Mechanistically, the DPPH assay mainly depends on hydrogen atom donation by antioxidants, which neutralize the DPPH radicals (45, 46). Thus, the DPPH scavenging activity of an antioxidant is mainly due to its hydrogen-donating ability. It is possible that the binding of HES to WP resulted in the loss of phenolic hydroxyl groups in the HES, thereby decreasing its hydrogen donor ability (47). Furthermore, it is known that HES is an antioxidant that contains phenolic hydroxyl groups on its aromatic rings. After binding to the protein, there may still be some phenolic hydroxyl groups exposed in the WP-HES complex, which give it some antioxidant activity.

The principle of the FRAP assay is the reduction of the ferric complex in TPTZ (Fe^{3+}-TPTZ) to the ferrous form (Fe^{2+}-TPTZ) (20). Therefore, the FRAP assay is mainly measuring the ferric reducing potential of an antioxidant. **Figure 5B** shows that the FRAP activity of the WP increased from 4.12 to 13.48 mg TE/L after binding the HES. However, the FRAP activity values for all the WP-HES complexes were lower than those of the free HES at the same HES concentration. These results are therefore
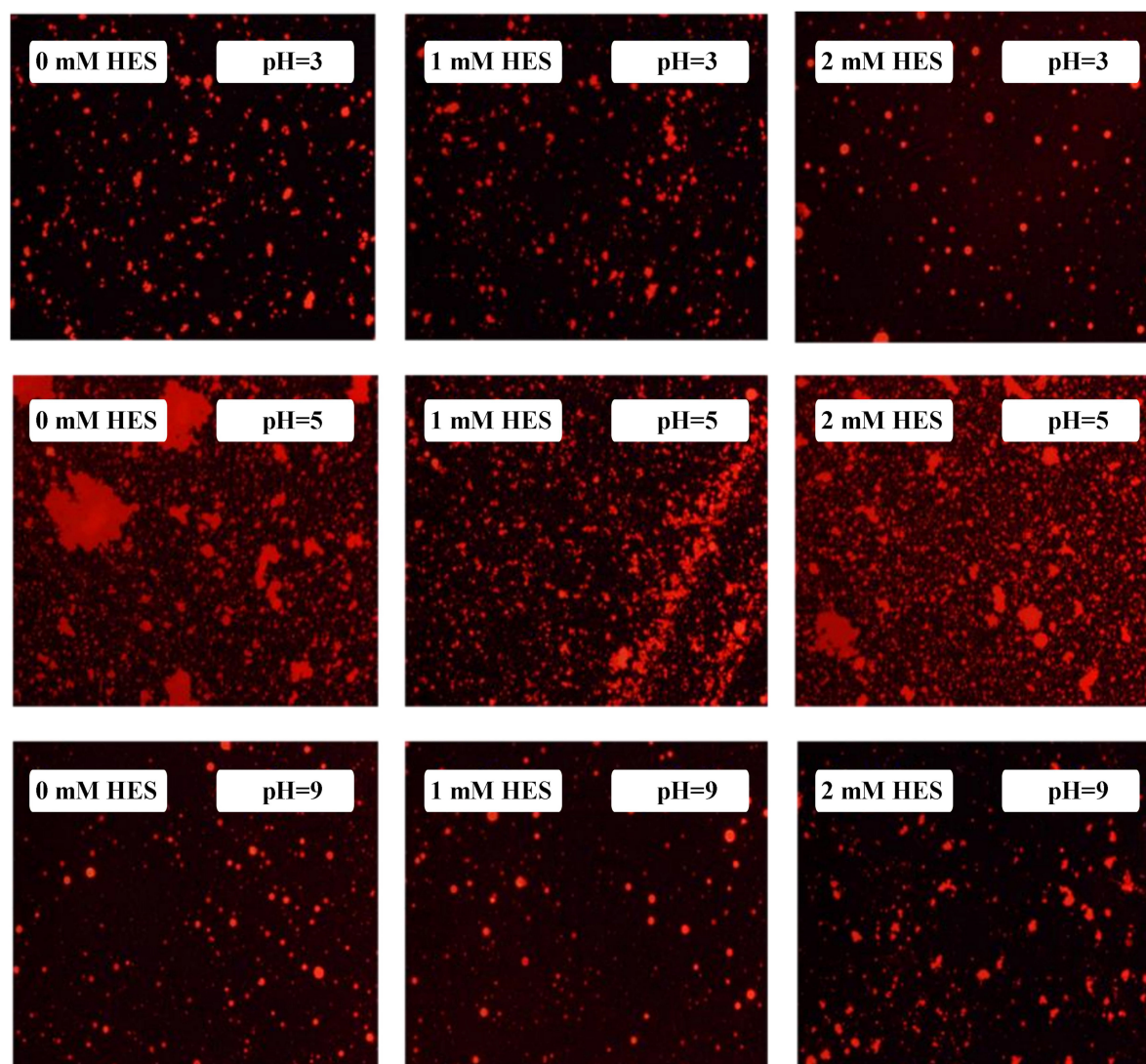
The microstructure of WP based emulsion or WP-HES based emulsions at different pH values.

in agreement with those of the DPPH radical scavenging activity assay. Thus, both methods confirm that binding of HES to WP improved the antioxidant capacity of the protein.

3.9. Stability study

In this section, we examined the impact of HES on the resistance of the whey-protein coated droplets in oil-in-water emulsions to changes in pH, salt, and lipid oxidation.

3.9.1. pH stability of emulsions

The emulsions used in different food and beverage products must function over a range of pH values, which may affect the stability and physicochemical properties of emulsions.

The influence of pH on the particle size, zeta-potential, and microstructure of emulsions stabilized by WPI-HES or WP was therefore measured. The emulsions had a uniform white appearance at pH 3 and from pH 6 to 9, but visibly separated at pH 4 and 5 (Figure 6). The mean particle diameters of the emulsions at pH 4 and 5 were significantly higher than those at other pH values, indicating appreciable droplet aggregation had occurred (Figure 7). Emulsions containing WP-coated oil droplets are predominantly stabilized by electrostatic repulsive interactions. The droplets aggregate at pH values near the isoelectric point of the adsorbed proteins (pH 5) because of the reduction in their electrical charge, which reduces the electrostatic repulsive forces. As a result, they tend to aggregate through van der Waals and hydrophobic attractive forces. Interestingly, the addition of HES reduced the amount
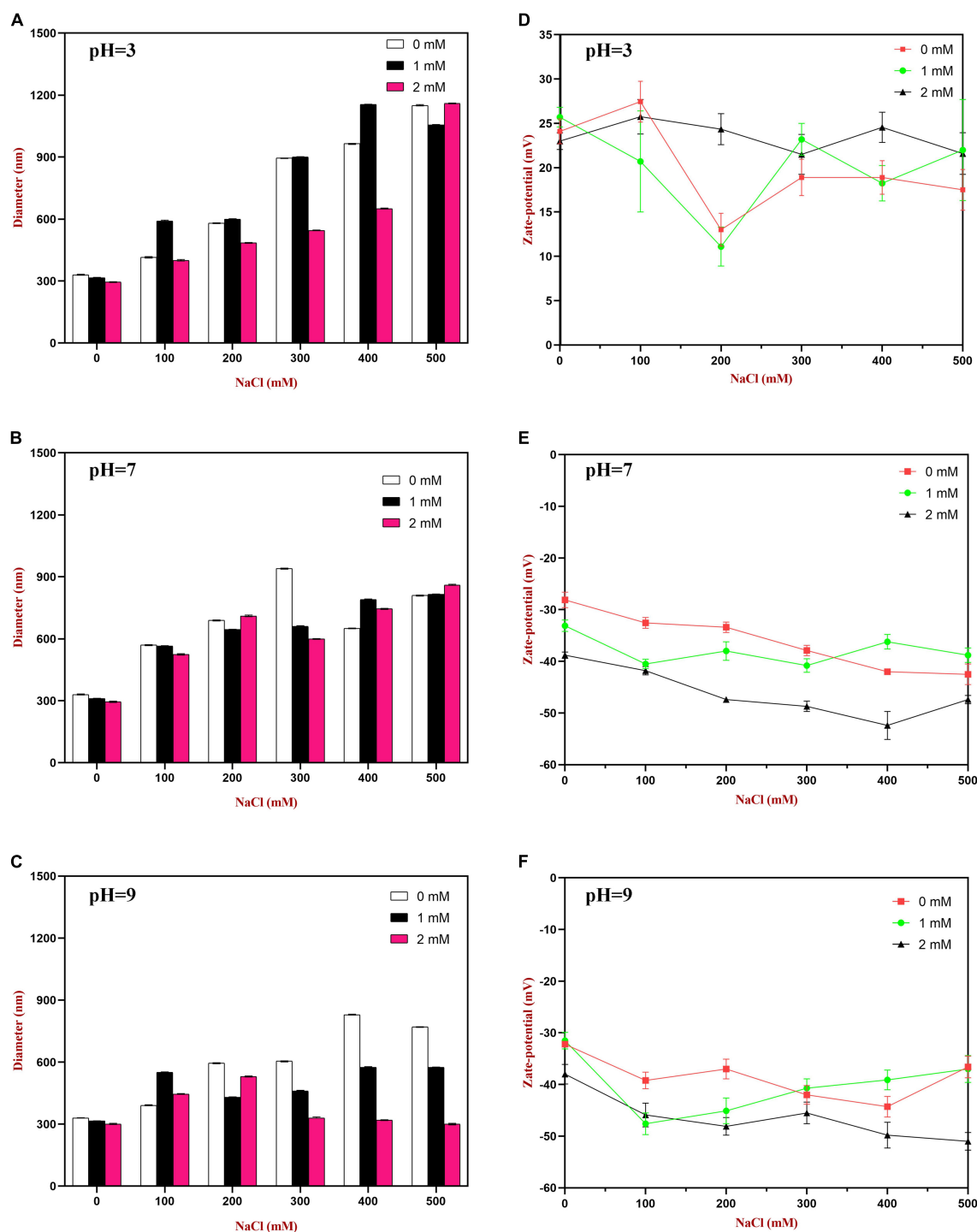
FIGURE 9

The particle size **(A–C)** and zeta-potential **(D–F)** changes of WP based emulsion or WP-HES based emulsions under different pH values and salt concentrations.

of creaming observed in the emulsions. Moreover, the mean particle diameters of the emulsion containing HES were smaller than the corresponding controls, with the particle size decreasing with rising HES concentration. This phenomenon

may be caused by non-covalent interactions between the protein and polyphenol molecules.

The spectroscopic analysis and molecular docking simulations discussed earlier showed that the binding
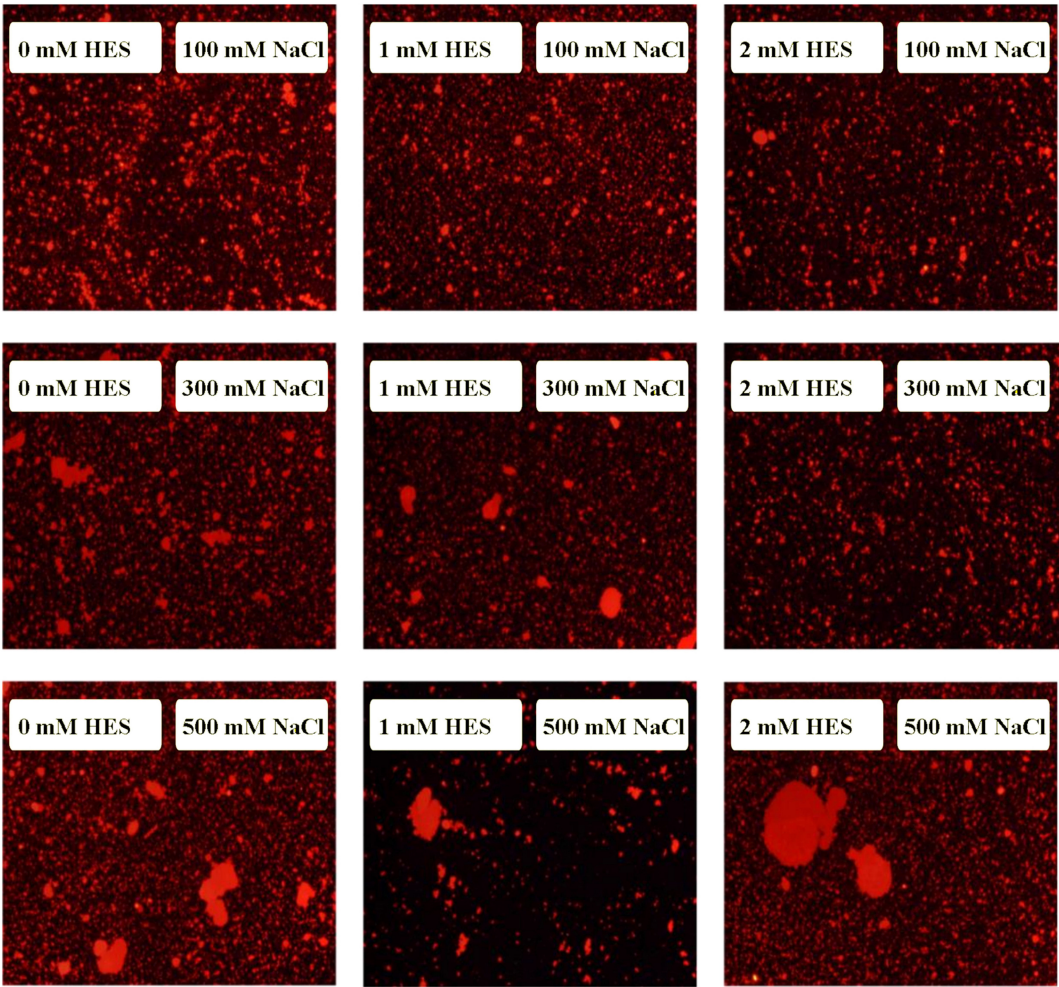
FIGURE 10
The microstructure of emulsions with different salt ion concentrations under acidic condition.
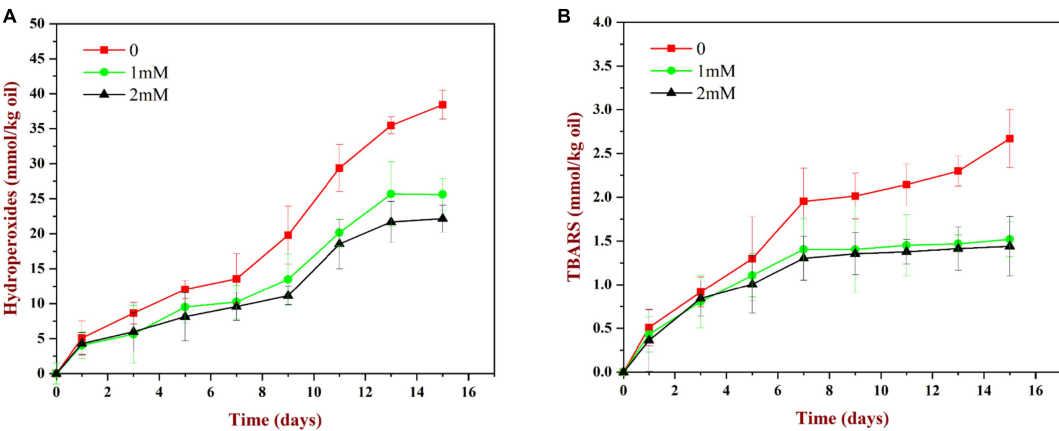

FIGURE 11
Change in PV **(A)** and TBARS **(B)** values for WP based emulsion or WP-HES based emulsions during storage at 55°C for 15 days.

interactions between the proteins and polyphenols were mainly a result of hydrophobic bonding, followed by some hydrogen bonding. The presence of the polyphenols may therefore have changed the surface chemistry of the protein-coated oil droplets, thereby altering the interactions between them. Moreover, the binding of the polyphenols caused some partial unfolding of the WP molecules, which may have improved their emulsifying characteristics, leading to the formation of small oil droplets during homogenization. Similar results were also reported by other researchers. Li et al. reported that rice bran protein-catechin complexes formed emulsions with smaller particle sizes than rice bran protein alone (48, 49) reported that soy protein-tea polyphenol complexes led to better emulsion formation and stability than using soy protein alone. It is known that there are many hydrophilic hydroxyl groups in HES. The binding of HES to WP would introduce some phenolic hydroxyl groups onto the surface of the protein molecules, thereby increasing their surface hydrophilicity, which may have reduced the tendency for droplets to aggregation through hydrophobic attraction.

The zeta potential values of the droplets were also measured to provide further insights into the pH sensitivity of the emulsions. According to DLVO theory, higher absolute zeta potential values lead to stronger electrostatic repulsion between droplets, thereby leading to greater resistance to aggregation (3). As shown in **Figure 7**, at pH 4.0 and 5.0, the surface charge of the emulsion without HES was close to neutral (ζ = + 2.9 and −1.5 mV, respectively). Thus, the zeta potential measurements provide strong support that the poor aggregation stability of the droplets at these pH values was due to a reduction in electrostatic repulsion. The absolute values of the zeta potential at pH 4.0 and 5.0 increased as the HES concentration was increased, indicating that the WP-HES complexes may have increased the resistance of the emulsions to aggregation by increasing the electrostatic repulsion between them. In addition, the binding of the polyphenols to the protein surfaces may have decreased the hydrophobic attraction between the droplets by covering exposed non-polar patches on the protein surfaces. Moreover, the presence of the polyphenols may have increased the steric repulsion between the droplets by increasing the thickness of the interfacial layer. Overall, the particle size and zeta-potential measurements are therefore consistent with the visual appearances and microstructures of the emulsions. Interestingly, the addition of HES caused a slight increase in the pH where zero charge was observed, as well as in the magnitude of the negative charge observed under alkaline conditions. This phenomenon suggests that the combination of HES with WP may have shifted the isoelectric point of the adsorbed proteins to a slightly higher value. Possibly, some of the free hydroxyl groups present in the WP-HES complexes became deprotonated

under alkaline conditions, which produced more negative charges (50).

The microstructures of the emulsions at pH 3, 5, and 9 were examined using an inverted fluorescence microscope (**Figure 8**). At pH 3, the microscopy images show that both emulsions contained well dispersed small particles. However, there were a few large particles in the emulsions containing WP-coated oil droplets, which were not seen in the ones containing WP-HES-coated droplets. At pH 5, both emulsions contained large aggregates, but the individual aggregates were much larger in the WP-emulsions than in the WP-HES ones. This result suggests that HES could partially inhibit the aggregation of the protein-coated droplets. At pH 9.0, uniformly distributed small particles were observed in both emulsions, with only a few small aggregates being seen, which can be attributed to the strong electrostatic repulsion between the highly negatively charged droplets under alkaline conditions. These results are therefore consistent with the appearance and particle size analysis of the emulsions.

3.9.2. Salt stability

Food emulsions may be used in food and beverage products with different ionic compositions, and so it is important to ascertain the resistance of droplets to increases in high ionic strength (51). The effect of salt concentration on the stability of WP- and WP-HES-emulsions after being stored at pH 3, 7, and 9 overnight was investigated.

At pH 3, the mean particle diameter of all the emulsions increased in a dose-dependent manner with increasing NaCl concentration (**Figure 9**). This increase in particle size can be attributed to electrostatic screening effects. Emulsions containing protein-coated oil droplets are mainly stabilized by electrostatic repulsion. The addition of mineral ions screened these electrostatic repulsive forces, which can promoted aggregation due to hydrophobic and van der Waals attractive forces (52). Compared to the control emulsions, the WP-HES-emulsions containing 2 mM HES had significantly smaller particle sizes (except at 500 mM NaCl). The electrophoresis measurements showed that all the emulsions contained positively charged droplets and that the magnitude of the zeta potential decreased with increasing salt concentration (**Figure 9D**), which can again be attributed to electrostatic screening effects. Microscopy analysis also confirmed that aggregation occurred as the NaCl concentration increased for both WP-HES- and WP-emulsions (**Figure 10**). The higher salt-stability of the emulsions containing the higher level of HES may be due to a reduction in hydrophobic attraction and increase in steric repulsion between the droplets (51, 53).

At pH 7, the particle size of all the emulsions increased with increasing NaCl concentration, which can again be attributed to screening of electrostatic repulsive forces. In this case, however, the presence of HES did not improve emulsion stability. Surprisingly, the magnitude of the zeta-potential

actually increased slightly with increasing salt concentration (**Figure 9E**). The addition of 2 mM HES led to a slight increase in the magnitude of the negative charge on the oil droplets, which may have been due to deprotonation of the polyphenol hydroxyl groups (17).

At pH 9, the addition of salt also promoted some droplet aggregation as seen in the particle size and microstructure images (**Figure 9**). This effect can again be attributed to screening of the electrostatic repulsion between the droplets by salt ions. In this case, the presence of HES improved the salt-stability of the emulsions, with a smaller rise in mean particle diameter and fewer larger particles in the microscopy images. This may have been at least partly because incorporating HES into the emulsions increased the magnitude of the negative zeta potential of the droplets, thereby increasing the electrostatic repulsion (54). The greater effect at pH 9 than at pH 7 may have been because a higher fraction of phenolic hydroxyl groups was deprotonated under stronger alkaline conditions.

3.9.3. Measurement of lipid oxidation

Oxidative degradation of lipids is one of most important factors limiting the shelf life and acceptability of many fatty foods (55). The secondary reaction products formed lead to rancidity and potential toxicity (17). In our experiments, the coix seed oil used to formulate the emulsions is rich in unsaturated fatty acids and is therefore highly susceptible to oxidation. The oil droplets in the emulsions prepared in our study were coated with WP molecules, which may offer some protection against oxidation. In this section, we examined the impact of HES on their antioxidant properties.

3.9.3.1. PV measurements

As shown in **Figure 11A**, the content of lipid hydroperoxides (primary reaction products) in all samples increased gradually during storage. The peroxide value increased relatively slowly during the first 7 days, but then increased rapidly. Compared to the WP-emulsions, the PV values of the WP-HES-emulsions were significantly reduced. Moreover, the extent of lipid oxidation decreased in a dose dependent manner as the HES concentration was increased. This effect may be because the binding of polyphenols to the WP molecules enhanced their antioxidant activity (**Figure 5**). Similar results have also been reported for other polyphenol-protein complex stabilized emulsions (17, 35).

3.9.3.2. TBARS measurements

As shown in **Figure 11B**, the TBARS values (secondary reaction products) increased during storage, which indicated that some of the primary oxidation products had broken down. The TBARS values increased steadily during the first 7 days of storage and then remained constant or only increased slowly. The addition of HES (1 or 2 mM) to the emulsions reduced the concentration of TBARS formed at longer storage times.

These results suggest that the polyphenols may have partially suppressed the formation of secondary reaction products, again possibly by binding to the adsorbed proteins and forming an interfacial layer with strong antioxidant properties.

4. Conclusion

In summary, this study has provided evidence for the hypothesis that non-covalent interactions are formed between HES and WP leading to the formation of WP-HES complexes. Molecular dynamic simulations and spectroscopy analysis suggested that hydrophobic interactions were the most important forces holding these complexes together, but that hydrogen bonding also played a role. Spectroscopy analysis also showed there was a change in the secondary structure of the WP molecules after binding the polyphenol, with decreases in α-helix and β-sheet structures and increases in β-turn and random coil structures. The binding of the HES to the WPs enhanced their antioxidant activity, as well as their ability to increase the resistance of emulsions to changes in pH and salt concentration. Overall, our results suggest that WP-HES complexes may be used in the food industry as antioxidant emulsifiers that have better performance than WP alone.

Data availability statement

The original contributions presented in this study are included in the article/supplementary material, further inquiries can be directed to the corresponding authors.

Author contributions

YW: conceptualization, software, formal analysis, investigation, and writing—review and editing. YG: conceptualization, methodology, formal analysis, and investigation. LTZ: resources and visualization. MY: investigation. LZ: software, resources, and funding acquisition. CB: supervision, funding acquisition, data curation, and project administration. DM: validation and supervision. All authors contributed to the article and approved the submitted version.

Funding

External Cooperation Program of Fujian Province (grant no. 2020/ 0011).

Publisher's note

All claims expressed in this article are solely those of the authors and do not necessarily represent those of their affiliated organizations, or those of the publisher, the editors and the reviewers. Any product that may be evaluated in this article, or claim that may be made by its manufacturer, is not guaranteed or endorsed by the publisher.

References

1. Foegeding E, Luck P, Vardhanabhuti B. *Milk protein products | whey protein products. Encyclopedia of dairy sciences (second edition).* San Diego: Academic Press (2011). doi: 10.1016/B978-0-12-374407-4.00350-2

2. Bhatt H, Cucheval A, Coker C, Patel H, Carr A, Bennett R. Effect of micellar structure of casein and its modification on plasmin-induced hydrolysis. *Int Dairy J.* (2017) 75:75–82. doi: 10.1016/j.idairyj.2017.07.009

3. Corfield R, Martínez K, Allievi M, Santagapita P, Mazzobre F, Schebor C, et al. Whey proteins-folic acid complexes: formation, isolation and bioavailability in a *Lactobacillus casei* model. *Food Struct.* (2020) 26:100162. doi: 10.1016/j.foostr.2020.100162

4. Jeong E, Park G, Kim J, Baek Y, Go G, Lee H. Whey proteins-fortified milk with adjusted casein to whey proteins ratio improved muscle strength and endurance exercise capacity without lean mass accretion in rats. *Foods.* (2022) 11:574. doi: 10.3390/foods11040574

5. Kong F, Kang S, An Y, Li W, Han H, Guan B, et al. The effect of non-covalent interactions of xylitol with whey protein and casein on structure and functionality of protein. *Int Dairy J.* (2020) 111:104841. doi: 10.1016/j.idairyj.2020.104841

6. Liu J, Ru Q, Ding Y. Glycation a promising method for food protein modification: physicochemical properties and structure, a review. *Food Res Int.* (2012) 49:170–83. doi: 10.1016/j.foodres.2012.07.034

7. Stender E, Koutina G, Almdal K, Hassenkam T, Mackie A, Ipsen R, et al. Isoenergic modification of whey protein structure by denaturation and crosslinking using transglutaminase. *Food Funct.* (2018) 9:797–805. doi: 10.1039/C7FO01451A

8. Liu J, Yong H, Yao X, Hu H, Yun D, Xiao L. Recent advances in phenolic–protein conjugates: synthesis, characterization, biological activities and potential applications. *RSC Adv.* (2019) 9:35825–40. doi: 10.1039/C9RA07808H

9. Gaspar A, de Góes-Favoni S. Action of microbial transglutaminase (MTGase) in the modification of food proteins: a review. *Food Chem.* (2015) 171:315–22. doi: 10.1016/j.foodchem.2014.09.019

10. Isaschar-Ovdat S, Fishman A. Crosslinking of food proteins mediated by oxidative enzymes–a review. *Trends Food Sci Technol.* (2018) 72:134–43. doi: 10.1016/j.tifs.2017.12.011

11. Li C, Enomoto H, Hayashi Y, Zhao H, Aoki T. Recent advances in phosphorylation of food proteins: a review. *LWT Food Sci Technol.* (2010) 43:1295–300. doi: 10.1016/j.lwt.2010.03.016

12. O'sullivan J, Park M, Beevers J, Greenwood R, Norton I. Applications of ultrasound for the functional modification of proteins and nanoemulsion formation: a review. *Food Hydrocoll.* (2017) 71:299–310. doi: 10.1016/j.foodhyd.2016.12.037

13. Kardum N, Glibetic M. Polyphenols and their interactions with other dietary compounds: implications for human health. *Adv Food Nutr Res.* (2018) 84:103–44. doi: 10.1016/bs.afnr.2017.12.001

14. Umar Lule S, Xia W. Food phenolics, pros and cons: a review. *Food Rev Int.* (2005) 21:367–88. doi: 10.1080/87559120500222862

15. Pham L, Wang B, Zisu B, Adhikari B. Complexation between flaxseed protein isolate and phenolic compounds: effects on interfacial, emulsifying and antioxidant properties of emulsions. *Food Hydrocoll.* (2019) 94:20–9. doi: 10.1016/j.foodhyd.2019.03.007

16. Guan H, Zhang W, Sun-Waterhouse D, Jiang Y, Li F, Waterhouse G, et al. Phenolic-protein interactions in foods and post ingestion: switches empowering health outcomes. *Trends Food Sci Technol.* (2021) 118:71–86. doi: 10.1016/j.tifs.2021.08.033

17. Huang Y, Li A, Qiu C, Teng Y, Wang Y. Self-assembled colloidal complexes of polyphenol–gelatin and their stabilizing effects on emulsions. *Food Funct.* (2017) 8:3145–54. doi: 10.1039/C7FO00705A

18. Jongberg S, Andersen M, Lund M. Characterisation of protein-polyphenol interactions in beer during forced aging. *J Inst Brew.* (2020) 126:371–81. doi: 10.1002/jib.623

19. Jiang J, Zhang Z, Zhao J, Liu Y. The effect of non-covalent interaction of chlorogenic acid with whey protein and casein on physicochemical and radical-scavenging activity of *in vitro* protein digests. *Food Chem.* (2018) 268:334–41. doi: 10.1016/j.foodchem.2018.06.015

20. Dai T, Li R, Liu C, Liu W, Li T, Chen J, et al. Effect of rice glutelin-resveratrol interactions on the formation and stability of emulsions: a multiphotonic spectroscopy and molecular docking study. *Food Hydrocoll.* (2019) 97:105234. doi: 10.1016/j.foodhyd.2019.105234

21. Pripp A, Vreeker R, van Duynhoven J. Binding of olive oil phenolics to food proteins. *J Sci Food Agric.* (2005) 85:354–62. doi: 10.1002/jsfa.1992

22. Sobhy R, Zhan F, Mekawi E, Khalifa I, Liang H, Li B. The noncovalent conjugations of bovine serum albumin with three structurally different phytosterols exerted antiglycation effects: a study with AGEs-inhibition, multispectral, and docking investigations. *Bioorg Chem.* (2020) 94:103478. doi: 10.1016/j.bioorg.2019.103478

23. Jiang H, Hu X, Pan J, Gong D, Zhang G. Effects of interaction between hesperetin/hesperidin and glutenin on the structure and functional properties of glutenin. *LWT.* (2022) 155:112983. doi: 10.1016/j.lwt.2021.112983

24. Xie M, Xu X, Wang Y. Interaction between hesperetin and human serum albumin revealed by spectroscopic methods. *Biochim Biophys Acta.* (2005) 1724:215–24. doi: 10.1016/j.bbagen.2005.04.009

25. Aranganathan S, Selvam J, Nalini N. Effect of hesperetin, a citrus flavonoid, on bacterial enzymes and carcinogen-induced aberrant crypt foci in colon cancer rats: a dose-dependent study. *J Pharm Pharmacol.* (2008) 60:1385–92. doi: 10.1211/jpp.60.10.0015

26. Khan A, Ikram M, Hahm J, Kim M. Antioxidant and anti-inflammatory effects of citrus flavonoid hesperetin: special focus on neurological disorders. *Antioxidants.* (2020) 9:609. doi: 10.3390/antiox9070609

27. Oktaviani A, Aprillia V, Suhartono E, Komari N. Hesperidin Interaction with HMG-CoA-reductase enzyme in hypercholesterolemia: a study in silico. *Berkala Kedokteran.* (2021) 17:173–8. doi: 10.20527/jbk.v17i2.11692

28. Basu A, Sarkar A, Maulik U. Molecular docking study of potential phytochemicals and their effects on the complex of SARS-CoV2 spike protein and human ACE2. *Sci Rep.* (2020) 10:17699. doi: 10.1038/s41598-020-74715-4

29. Khan M, Rehman M, Ismael M, AlAjmi M, Alruwaished G, Alokail M, et al. Bioflavonoid (hesperidin) restrains protein oxidation and advanced glycation end product formation by targeting ages and glycolytic enzymes. *Cell Biochem Biophys.* (2021) 79:833–44. doi: 10.1007/s12013-021-00997-8

30. Du Q, Tang J, Xu M, Lyu F, Zhang J, Qiu Y, et al. Whey protein and maltodextrin-stabilized oil-in-water emulsions: effects of dextrose equivalent. *Food Chem.* (2021) 339:128094. doi: 10.1016/j.foodchem.2020.128094

31. Smułek W, Siejak P, Fathordoobady F, Masewicz Ł, Guo Y, Jarzębska M, et al. Whey proteins as a potential co-surfactant with *Aesculus* hippocastanum L. as a stabilizer in nanoemulsions derived from hempseed oil. *Molecules.* (2021) 26:5856. doi: 10.3390/molecules26195856

32. Li T, Hu P, Dai T, Li P, Ye X, Chen J, et al. Comparing the binding interaction between β-lactoglobulin and flavonoids with different structure by

multi-spectroscopy analysis and molecular docking. *Spectrochim Acta A Mol Biomol Spectrosc.* (2018) 201:197–206. doi: 10.1016/j.saa.2018.05.011

33. Wu M, Zhou Z, Yang J, Zhang M, Cai F, Lu P. ZnO nanoparticles stabilized oregano essential oil Pickering emulsion for functional cellulose nanofibrils packaging films with antimicrobial and antioxidant activity. *Int J Biol Macromol.* (2021) 190:433–40. doi: 10.1016/j.ijbiomac.2021.08.210

34. Almajano M, Delgado M, Gordon M. Changes in the antioxidant properties of protein solutions in the presence of epigallocatechin gallate. *Food Chem.* (2007) 101:126–30. doi: 10.1016/j.foodchem.2006.01.009

35. Feng J, Cai H, Wang H, Li C, Liu S. Improved oxidative stability of fish oil emulsion by grafted ovalbumin-catechin conjugates. *Food Chem.* (2018) 241:60–9. doi: 10.1016/j.foodchem.2017.08.055

36. Walker R, McClements D, Decker E, Gumus C. Improvements in the formation and stability of fish oil-in-water nanoemulsions using carrier oils: MCT, thyme oil, & lemon oil. *J Food Eng.* (2017) 211:60–8. doi: 10.1016/j.jfoodeng.2017.05.004

37. Dai T, Yan X, Li Q, Li T, Liu C, McClements D, et al. Characterization of binding interaction between rice glutelin and gallic acid: multi-spectroscopic analyses and computational docking simulation. *Food Res Int.* (2017) 102:274–81. doi: 10.1016/j.foodres.2017.09.020

38. Wan Z, Wang J, Wang L, Yuan Y, Yang X. Complexation of resveratrol with soy protein and its improvement on oxidative stability of corn oil/water emulsions. *Food Chem.* (2014) 161:324–31. doi: 10.1016/j.foodchem.2014.04.028

39. Siddiqui G, Siddiqi M, Khan R, Naeem A. Probing the binding of phenolic aldehyde vanillin with bovine serum albumin: evidence from spectroscopic and docking approach. *Spectrochim Acta A Mol Biomol Spectrosc.* (2018) 203:40–7. doi: 10.1016/j.saa.2018.05.023

40. Xu X, Liu W, Zhong J, Luo L, Liu C, Luo S, et al. Binding interaction between rice glutelin and amylose: hydrophobic interaction and conformational changes. *Int J Biol Macromol.* (2015) 81:942–50. doi: 10.1016/j.ijbiomac.2015.09.041

41. Zhang T, Sun R, Ding M, Li L, Tao N, Wang X, et al. Commercial cold-water fish skin gelatin and bovine bone gelatin: structural, functional, and emulsion stability differences. *LWT.* (2020) 125:109207. doi: 10.1016/j.lwt.2020.109207

42. He Z, Xu M, Zeng M, Qin F, Chen J. Interactions of milk α-and β-casein with malvidin-3-O-glucoside and their effects on the stability of grape skin anthocyanin extracts. *Food Chem.* (2016) 199:314–22. doi: 10.1016/j.foodchem.2015.12.035

43. Khalifa I, Nie R, Ge Z, Li K, Li C. Understanding the shielding effects of whey protein on mulberry anthocyanins: insights from multispectral and molecular modelling investigations. *Int J Biol Macromol.* (2018) 119:116–24. doi: 10.1016/j.ijbiomac.2018.07.117

44. Rodríguez S, von Staszewski M, Pilosof A. Green tea polyphenols-whey proteins nanoparticles: bulk, interfacial and foaming behavior. *Food Hydrocoll.* (2015) 50:108–15. doi: 10.1016/j.foodhyd.2015.04.015

45. Calva-Estrada S, Jimenez-Fernandez M, Vallejo-Cardona A, Castillo-Herrera G, Lugo-Cervantes E. Cocoa nanoparticles to improve the physicochemical and functional properties of whey protein-based films to extend the shelf life of muffins. *Foods.* (2021) 10:2672. doi: 10.3390/foods10112672

46. Mezeiova E, Spilovska K, Nepovimova E, Gorecki L, Soukup O, Dolezal R, et al. Profiling donepezil template into multipotent hybrids with antioxidant properties. *J Enzyme Inhib Med Chem.* (2018) 33:583–606. doi: 10.1080/14756366.2018.1443326

47. Aewsiri T, Benjakul S, Visessanguan W, Wierenga P, Gruppen H. Antioxidative activity and emulsifying properties of cuttlefish skin gelatin–tannic acid complex as influenced by types of interaction. *Innov Food Sci Emerg Technol.* (2010) 11:712–20. doi: 10.1016/j.ifset.2010.04.001

48. Li D, Zhao Y, Wang X, Tang H, Wu N, Wu F, et al. Effects of (+)-catechin on a rice bran protein oil-in-water emulsion: droplet size, zeta-potential, emulsifying properties, and rheological behavior. *Food Hydrocoll.* (2020) 98:105306. doi: 10.1016/j.foodhyd.2019.105306

49. Tian B, Wang Y, Wang T, Mao L, Lu Y, Wang H, et al. Structure and functional properties of antioxidant nanoemulsions prepared with tea polyphenols and soybean protein isolate. *J Oleo Sci.* (2019) 68:689–97. doi: 10.5650/jos.ess19067

50. Katsuda M, McClements D, Miglioranza L, Decker E. Physical and oxidative stability of fish oil-in-water emulsions stabilized with β-lactoglobulin and pectin. *J Agric Food Chem.* (2008) 56:5926–31. doi: 10.1021/jf800574s

51. Wei Z, Gao Y. Physicochemical properties of β-carotene bilayer emulsions coated by milk proteins and chitosan–EGCG conjugates. *Food Hydrocoll.* (2016) 52:590–9. doi: 10.1016/j.foodhyd.2015.08.002

52. Helvaci S, Peker S, Ozdemir G. Effect of electrolytes on the surface behavior of rhamnolipids R1 and R2. *Colloids Surf.* (2004) 35:225–33. doi: 10.1016/j.colsurfb.2004.01.001

53. Aoki T, Decker E, McClements D. Influence of environmental stresses on stability of O/W emulsions containing droplets stabilized by multilayered membranes produced by a layer-by-layer electrostatic deposition technique. *Food Hydrocoll.* (2005) 19:209–20. doi: 10.1016/j.foodhyd.2004.05.006

54. Li M, Ritzoulis C, Du Q, Liu Y, Ding Y, Liu W, et al. Recent progress on protein-polyphenol complexes: effect on stability and nutrients delivery of oil-in-water emulsion system. *Front Nutr.* (2021) 8:765589. doi: 10.3389/fnut.2021.765589

55. Zhu Z, Zhao C, Yi J, Liu N, Cao Y, Decker E, et al. Impact of interfacial composition on lipid and protein co-oxidation in oil-in-water emulsions containing mixed emulsifers. *J Agric Food Chem.* (2018) 66:4458–68. doi: 10.1021/acs.jafc.8b00590

Check for updates

Antioxidant properties of fermented soymilk and its anti-inflammatory effect on DSS-induced colitis in mice

Yijiao Sun[1], Jingting Xu[1], Huiyan Zhao[1], Yue Li[1], Hui Zhang[1], Baichong Yang[2] and Shuntang Guo[1]*

[1]Beijing Key Laboratory of Plant Protein and Cereal Processing, College of Food Science and Nutritional Engineering, China Agricultural University, Beijing, China, [2]Pony Testing International Group Co., Ltd., Beijing, China

Lactic acid-fermented soymilk as a new plant-based food has aroused extensive attention because of its effects on nutrition and health. This study was conducted to delve into the antioxidative and anti-inflammatory activities of lactic acid-fermented soymilk. To elucidate the key factors that affect the antioxidant properties of fermented soymilk, the strains and preparation process were investigated. Findings show that the fermented soymilk prepared using hot-water blanching method (BT-80) demonstrated a better antioxidant activity than that using conventional method (CN-20). Besides, a huge difference was observed among the soymilks fermented with different strains. Among them, the YF-L903 fermented soymilk demonstrated the highest ABTS radical scavenging ability, which is about twofold of that of unfermented soymilk and 1.8-fold of that of L571 fermented soy milk. *In vitro* antioxidant experiments and the analysis of H_2O_2-induced oxidative damage model in Caco-2 cells showed that lactic acid-fermentation could improve the DPPH radical scavenging ability, ABTS radical scavenging ability, while reducing the content of reactive oxygen species (ROS) and malondialdehyde (MDA) in Caco-2 cells induced by H_2O_2, and increasing the content of superoxide dismutase (SOD). Consequently, cells are protected from the damage caused by active oxidation, and the repair ability of cells is enhanced. To identify the role of fermented soymilk in intestinal health, we investigate its preventive effect on dextran sodium sulfate-induced colitis mouse models. Results revealed that the fermented soymilk can significantly improve the health conditions of the mice, including alleviated of weight loss, relieved colonic injury, balanced the spleen-to-body weight ratio, reduced the disease index, and suppressed the inflammatory cytokines and oxidant indexes release. These results suggest that YF-L903 fermented soymilk is a promising natural antioxidant sources and anti-inflammatory agents for the food industry. We believe this work paves the way for elucidating the effect of lactic acid-fermented soymilk on intestinal health, and provides a reference for the preparation of fermented soymilk with higher nutritional and health value.

KEYWORDS

lactic acid bacteria, fermented soymilk, anti-inflammatory effect, antioxidant effect, physiologically active ingredients

1. Introduction

Soymilk, as a traditional plant protein beverage in China, is rich in soybean nutrients (e.g., protein and fat) and a variety of physiologically active substances (e.g., polyphenols, isoflavones, saponins, and phytosterols) (1, 2). Previous studies have found that these physiologically active ingredients play a significant role in the healthy functions of soymilk and other soy foods, and can prevent a variety of chronic diseases, including cardiovascular diseases, insulin resistance, breast cancer, and immune dysregulation (3). In recent years, with the rise of plant-based foods (4–6), fermented soymilk has attracted extensive attention because of its nutritionally and physiologically active components changes and its consequent enhanced health effects during fermentation (7–10). Fermented soymilk prepared using special *Lactobacillus fermentum* obtained from Xinjiang yak yogurt, Chongqing kimchi and Taiwan fermented cabbage, such as LP-HFY01, CQPC08, and TWK10, exhibited good free radical scavenging effect (11–14).

On the other hand, inflammatory bowel disease (IBD) refers to a chronic, progressive and recurrent intestinal disease characterized by chronic inflammation in the intestinal mucosa, and mainly includes ulcerative colitis (UC) and Crohn's disease (CD) (15–17). The current treatment of IBD mainly depends on long-term conventional anti-inflammatory treatment, which usually leads to drug intolerance or intolerance and limits the quality of life of patients (18). The pathogenesis of IBD is complex and diverse, resulting from the combined action of various factors, such as genetic factors, environmental factors, intestinal microbiota changes, and oxidative damage, immune dysfunction and psychological factors (19, 20). However, oxidative stress plays a key role in the development of intestinal injury in IBD, because it is primarily involved in the abnormal immune and inflammatory response (18). During the active disease phase, activated white blood cells will not only generate a wide spectrum of pro-inflammatory cytokines, but also excess oxidative reactions (18). It also has been proved that the improvement of antioxidant capacity by antioxidant active substances can effectively reduce the inflammatory damage caused by IBD (16).

Considering the antioxidative effect of fermented soymilk, we expect the fermented soymilk to has a preventive effect on UC. However, identifying whether the soymilk fermented by commercial *Lactobacillus plantarum* and other lactic acid bacteria (LAB) can suppress the oxidative stress, and maintain the redox homeostasis of the body, as well as confirming if we can improve the antioxidative effect by strain selection and changing preparation processing, still need further efforts. And very few studies have focused on the anti-inflammatory effect of soymilk *via* lactic acid bacteria fermentation.

Thus, this paper mainly discussed the effects of soymilk preparation process, different commercial LAB,

and fermentation time on the antioxidant activity of fermented soymilk, and studied the preventive effects of soymilk fermented by commercial LAB on dextran sodium sulfate (DSS)-induced colitis in mice. This work provides a theoretical basis for the therapeutic effect of fermented soymilk and a reference for the preparation of fermented soymilk with higher nutritional value.

2. Materials and methods

2.1. Experimental reagents and strains

Caco-2 cells were purchased from the Shanghai Cell Bank of Chinese Academy of Sciences. The strains, including L571 (*Lactobacillus plantarum*); YF-L904, YF-L903, and Mild1.0 (mixed strains of *Streptococcus thermophilus* and *Lactobacillus Bulgarian*); and ST-M5 (*Streptococcus thermophilus*), were obtained from Chr. Hansen (Hoersholm, Denmark). DMEM high glucose cell culture medium and fetal bovine serum (FBS) were purchased from Corning Technology Co., LTD. The iron reduction capacity test kit, ABTS free radical scavenging capacity test kit, and PBS buffer were purchased from Solarbio Technology Co., LTD. MTT was purchased from Sigma-Aldrich. The reactive oxygen species (ROS) detection kit, lipid oxidation (MDA) detection kit, total SOD activity detection kit (WST-8 method), ELISA kits of interleukin-6 (IL-6), interleukin-1β (IL-1β), and tumor necrosis factor-α (TNF-α) were purchased from Beyotime Biotechnology Co., LTD. T-AOC, T-SOD, and MDA commercial kits were purchased from Nanjing Jiancheng Bio-engineering Insititute.

2.2. Preparation of soymilk and fermented soymilk

2.2.1. Soymilk preparation using conventional method

Soymilk was prepared similarly to our previous reports (21, 22). Briefly, the selected soybeans (100 g) were washed and immersed in double-distilled water for 12 h at 4°C. Then the soaked soybeans were drained and ground in a soymilk machine with double-distilled water (700 mL) at room temperature. The obtained homogenate was filtered by a defatted cotton sheet to eliminate insoluble residues, and the filtrate was heated in boiling water bath for 5 min at 95°C. Subsequently, the soymilk was cooled to room temperature immediately by ice water bath. Soymilk prepared by this conventional method was coded as CN-20.

2.2.2. Soymilk preparation using hot-water blanching method

Another set of soymilk samples were prepared using a hot-water blanching approach as reported in our pervious works

(22, 23). Briefly, as shown in Scheme 1, a total of 100 g soybeans were washed and immersed in double-distilled water for 12 h at 4°C. The soaked soybeans were then drained and blanched using $NaHCO_3$ solution (0.04 mol/L, 300 mL) for 3 min at 80°C to deactivate lipoxygenases. Subsequently, the soybeans and blanching water were poured in a grinder contained with 400 mL of hot double-distilled water (80°C), and ground for 3 min. The obtained homogenate was filtered by a defatted cotton sheet to eliminate insoluble residues, and the obtained raw soymilk was heated in boiling water bath for 5 min at 95°C. After that, the soymilk was immediately cooled to room temperature by ice water bath. The corresponding soymilk prepared with the blanching treatment was coded as BT-80.

2.2.3. Preparation of fermented soymilk

Fermented soymilk was prepared according to pervious reports with some modifications (24). To obtain fermented soymilk, the lyophilized powders of L571, YF-L904, YF-L903, Mild1.0, and ST-M5 were added in 100 mL of soymilk at the ratio of 0.02% (w/v). The mixture was evenly stirred and then incubated at 42°C. In general, the fermentation was terminated when the titrated acidity reached 60 °T. Next, they were taken out and freeze dried into powder and stored in refrigerator at −18°C. The YF-L903 fermented soymilk powder was used for animal experiments. Considering that sucrose was generally added to improve the flavor and taste in actual factory fermentation, the sucrose (3%) here was also added during the preparation of fermented soymilk in animal experiments (fermented soymilk coded as FSM).

2.2.4. Preparation of the methanol extracts of soymilk (SE) and fermented soymilk (FSE)

To investigate the antioxidant effect, the soymilk powder and fermented soymilk powder were extracted with 0–100% methanol by stirring at 25°C for 12 h and filtered through filter paper. The methanol in the filtrate was removed by rotary evaporation, and the remaining part was freeze-dried into powder (soymilk extract coded as SE and fermented soymilk extract coded as FSE), which was collected and stored in the refrigerator at −18°C before using in antioxidative experiments.

2.3. Determination of nutritional contents

2.3.1. Determination of total phenolic content in methanol extracts of soymilk and fermented soymilk

The total phenolic content was determined by Folin-Ciocalteu method with minor modifications (14). In detail, 100 µL of the extracts was added in the mixture of 2.95 mL of distilled water, 250 µL of Folin-Ciocalteu phenol reagent

reagent, and 750 µL of $NaCO_3$ (7%). After 8 min reaction, 950 µL of distilled water was added. Then the reaction continued for 2 h, protected from light at room temperature. After that, the absorbance at 765 nm was measured. Standard curves were obtained using gallic acid as a standard sample. The measurement was repeated three times for each sample. The total phenolic content was expressed as gallic acid equivalents per gram of sample (mg GAE/g).

2.3.2. Determination of flavonoid content in methanol extracts of soymilk and fermented soymilk

The experiment was operated according to the instruction of plant flavonoid content detection kit (Beijing Solarbio Technology Co., LTD). In alkaline nitrite solution, flavonoids and aluminum ions form a red complex with characteristic absorption peak at 470 nm. The content of flavonoids in the extract can be calculated by measuring the absorbance at 470 nm. Standard curves were obtained using rutin as a standard sample. The measurement was repeated three times for each sample. The flavonoid content of the samples was expressed as rutin equivalents per gram of sample (mg GAE/g).

2.3.3. Determination of isoflavones content in soymilk and fermented soymilk by HPLC

The isoflavone content was determined by high-performance liquid chromatography (HPLC) in AOAC (25). Isoflavones in the samples were determined qualitatively and quantitatively using Shimadzu (Japan) HPLC system. The analytical conditions were adopted as follow, Column: 15 × 4.0 mm C18, mobile phase A: water + methanol + glacial acetic acid (88 + 10 + 2), mobile phase B: methanol + glacial acetic acid (98 + 2), flow rate: l mL/min. Detection wavelength: 260 nm. Column temperature: 50°C. Injection volume: 20 µL. The analysis time was 40 min/sample.

2.4. In vitro evaluation of the antioxidant capacity of fermented soymilk

2.4.1. DPPH radical scavenging ability

The 2,2-diphenyl-2-picrylhydrazyl (DPPH) radical scavenging activity was determined using the method of Yu et al. with some modifications (26). Briefly, a total of 0.1 mM DPPH solution was prepared with 95% ethanol and stored in the dark. Next, 0.2 mL of extract was mixed with 0.8 mL of DPPH solution, and the mixture was shaken vigorously to improve the uniformity. The obtained 1 mL samples were then incubated in the dark for 30 min, and the absorbance of the supernatant was measured at 517 nm (A_1). The absorbance of 0.2 mL DPPH solution prediluted with 0.8 mL ultrapure water

SCHEME 1
Fermented soymilk preparation process.
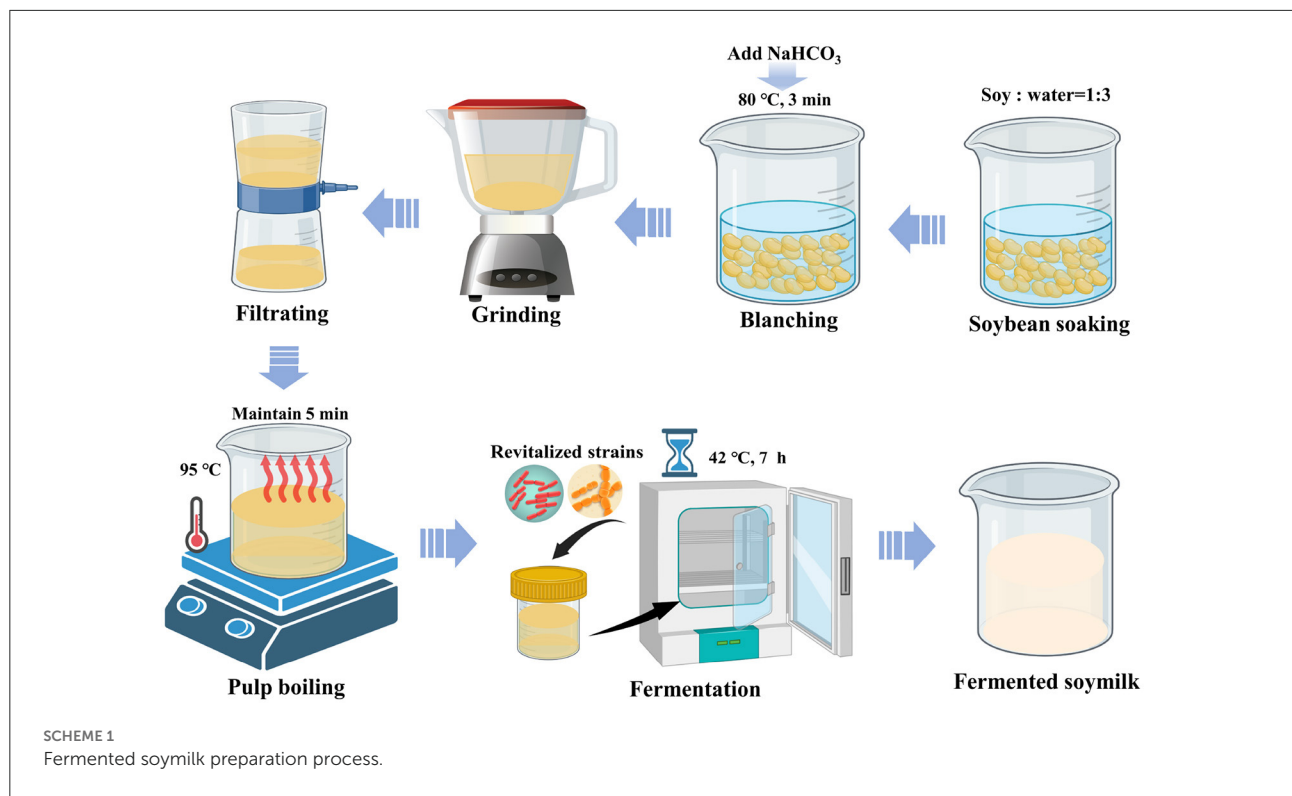
was measured as blank control (A_0). The absorbance of 0.2 mL test sample solution prediluted with 2 mL ethanol was used as standard control (A_2). The DPPH radical scavenging rate was calculated according to the Formula (1).

$$DPPH\ radical\ scavenging\ rate\% = 1 - \frac{(A_1 A_2)}{A_0} \times 100\% \quad (1)$$

2.4.2. Determination of ABTS radical scavenging ability

This experiment was operated according to the instructions of ABTS radical scavenging ability test kit. ABTS was oxidized to form stable blue-green cationic ABTS radicals with maximum absorption peaks at 405 nm or 734 nm. When ABTS radical solution was added with the sample, the antioxidant components could react with ABTS radical and make the reaction system fade, and the absorbance at 405 nm decreased. The change in absorbance at 405 nm was proportional to the degree of free radical removal in a certain range. The decrease in absorbance was measured to evaluate the ABTS free radical scavenging ability of the sample. A_1 denotes the absorbance of samples, A_0 denotes the absorbance of blank control, and A_2 denotes the absorbance of standard control. ABTS radical scavenging rate was calculated according to the Formula (2).

$$ABTS\ radical\ scavenging\ rate\% = 1 - \frac{(A_1 A_2)}{A_0} \times 100\% \quad (2)$$

2.4.3. Determination of metal ion-chelating ability

The metal ion-chelating activity was measured by following the previous report with minor modifications (27). A total of 2 mL of sample solution was obtained by mixing 0.1 mL of 2 mM $FeCl^2$ with 3.9 mL of distilled water in a reaction tube. Subsequently, ferrozine solution (0.1 mL of 5 mM) was then added and mixed vigorously. The mixture was set aside for 10 min at room temperature, and then photo-absorbance was detected at 562 nm. Distilled water without added sample was used as the blank. A_1 denotes the absorbance of samples, A_0 denotes the absorbance of blank control and A_2 denotes the absorbance of standard control. Metal ion-chelating rate was calculated according to the Formula (3).

$$Metal - ion\ chelating\ rate\% = 1 - \frac{(A_1 A_2)}{A_0} \times 100\% \quad (3)$$

2.4.4. Determination of total reduction capacity

The experiment was operated according to the instructions of the total antioxidant capacity assay kit (Beijing Solarbio Technology Co., LTD.). In acidic environment, the antioxidant components of the tested samples can reduce Fe^{3+}-tripyridinium triazine (Fe^{3+}-TPTZ) to produce blue Fe^{2+}-TPTZ, which has a maximum absorption at 593 nm. The enhanced degree of absorbance at 593 nm indicates the

antioxidant capacity of the sample. In our experiments, standard curve was collected from $FeSO_4 \bullet 7H_2O$, and the total reduction capacity was expressed as the content of Fe^{2+} in the solution.

2.5. Cell experiments

2.5.1. Caco-2 cell culture

The Caco-2 cells were cultured in 10 mL DMEM medium (containing 10% FBS, 100 U/mL penicillin, and 0.1 mg/mL streptomycin) at 37°C in a fully humidified atmosphere containing 5% CO_2. The medium was renewed every 48 h and cells were subcultured using 0.25% trypsin-EDTA when they reached 80–90% confluency.

2.5.2. H_2O_2-induced oxidative damage model in Caco-2 cells

First, the Caco-2 cells (100 μL, 5×10^4 cells/mL) were seeded in the wells of 96-well plate. After incubation for 18 h at 37°C, the grown medium was taken out, and the wells were washed with PBS twice. Then, the cells were treated with 100 μL of DMEM medium of H_2O_2 (0.25–8 mM), and the control group was added with 100 μL of DMEM medium without H_2O_2, and both incubated for 1–3 h. At last, the culture medium was removed by a pipette and the cells were washed twice with PBS. The cell viability was determined by MTT method same as described above.

2.5.3. Determination of cytotoxicity

The cytotoxicity of the samples was determined by MTT [3-(4, 5-dimethylthiazole-2-yl)-2, 5-diphenyltetrazolium bromide]. The Caco-2 cells (100 μL, 5×10^4 cells/mL) were seeded in the wells of 96-well plate. After incubating for 18 h at 37°C. Thereafter, the culture medium was changed to one that contained the sample to be tested, and the culture was continued for 24 h. 20 μL MTT (0.5 mg/mL) was added for further incubation for 4 h. Then, the culture medium was removed, 150 μL dimethyl sulfoxide (DMSO) was added, and the absorbance was measured at 490 nm after shaking slowly for 10 min to completely dissolve the purple color at the bottom completely. The results were expressed as the cell viability (%) of the experimental group compared with the control group.

2.5.4. Determination of the cell viability of H_2O_2-induced oxidative damage

Caco-2 cells (100μL, 5×10^4 cells/mL) were seeded in the wells of a 96-well plate. After incubating for 18 h at 37°C, the grown medium was taken out, and the wells were washed with PBS twice. Subsequently, the cells were treated with soymilk or fermented soymilk at the concentration of 125, 250, 500, and

1,000 μg/ml. After that, the culture medium was removed and washed with PBS for two to three times, the medium without H_2O_2 was added to the control group, whereas the medium containing H_2O_2 was added to the model and experimental groups to make the final H_2O_2 concentration reach 1 mM, and the incubation was continued for 1 h. After removing the culture medium, the cells were washed twice with PBS, and the cell viability was determined by MTT method.

### 2.5.5. Determination of ROS level in Caco-2 cells by H_2O_2-induced oxidative damage

Intracellular ROS levels were measured using reactive oxygen species assay kit. Caco-2 cells (100 μL, 5×10^4 cells/mL) were seeded in the wells of 96-well plate and incubation according to the method mentioned above. After the culture medium was removed and washed twice with PBS, 100 μL serum-free complete medium containing 10 μM DCFH-DA probe was added and cultured for 20 min. Cells were washed twice with serum-free complete medium, and their fluorescence intensity was measured using a microplate reader at 488 nm excitation wavelength and 525 nm emission wavelength.

2.5.6. Determination of MDA level in Caco-2 cells by H_2O_2-induced oxidative damage

The intracellular MDA levels were measured using lipid peroxidation MDA assay kit. First, the cells were treated according to the aforementioned method. Then the culture medium was removed and washed twice with PBS. RIPA cell lysate was added to lyse cells, and the protein concentration of samples in each group was determined by using the BCA protein concentration assay kit. A total of 0.37% TBA storage solution and MDA test solution were prepared. The samples/standards and MDA test solution were added and mixed according to the instructions, heated at 100°C for 15 min, cooled to room temperature, and centrifuged for 10 min (1,000×g). The absorbance of the supernatant was measured at 532 nm, and the molar concentration of MDA was calculated according to the standard curve. The results were expressed as the content of MDA per unit weight of protein (μmol/mg protein).

2.5.7. Determination of SOD activity in Caco-2 cells by H_2O_2-induced oxidative damage

Total SOD assay kit with WST-8 was used in this experiment. After following a commonly used incubation process mentioned above, the culture medium was removed and washed twice with PBS, and the SOD sample preparation solution was added to prepare the cell lysate. WST-8/enzyme working solution was prepared by mixing SOD detection buffer solution, WST-8 and enzyme solution in a proportion. The reaction starting solution (40×) was diluted to produce the reaction starting working

SCHEME 2
Diagram illustrating the protocol of mice model of colitis.
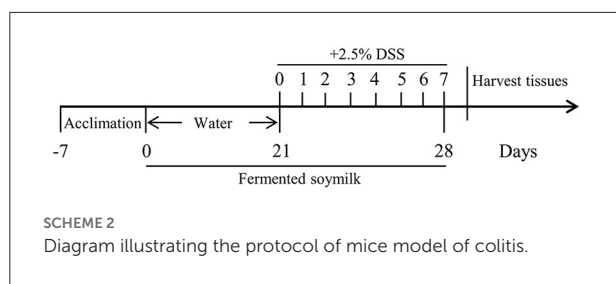
solution. In turn, the samples to be tested, SOD detection buffer solution, WST-8/enzyme working solution, and reaction starting solution were added according to the instructions, and the reaction was carried out at 37°C (30 min). The absorbance of the samples was measured at 450 nm, and SOD activity was expressed as U/mg protein.

2.6. Animal experiments

2.6.1. Animals and experimental design

C57BL/6JNifdc mice (male, 6–8 weeks old) were obtained from Vital River Laboratory Animal Technology Co., Ltd. (Beijing, China) and kept in polypropylene cages at 25 ± 2°C, under standard conditions of 12-h light/dark cycle with a relative humidity of 55 ± 5%. All experimental procedures were approved by the Animal Ethics Committee of Pony Testing International Group Co., Ltd (Approval No.: PONY-2022-FL-12). Mice had free access to basal diet (Vital River Laboratory Animal Technology Co., Ltd., Beijing, China) and water. After one-week adaption, mice were randomly divided into four groups ($n = 8$ in each group): (1) normal control group (Control), (2) DSS-induced colitis model group (DSS), (3) low-dose fermented soymilk group (DSS+L-FSM), and (4) high-dose fermented soymilk group (DSS+H-FSM).

The procedures were conducted as follows: During the whole experimental period, Group 1 (Control) and Group 2 (DSS) were given 0.2 mL of 0.9% normal saline every day by gavage. Meanwhile, mice in Group 3 (DSS+L-FSM) and Group 4 (DSS+H-FSM) were gavaged with 0.2 mL FSM (0.8 g/kg BW) and FSM (1.6 g/kg BW), respectively. From day 21 of the experimental period, nearly all mice, except normal control mice, were changed to free drinking deionized water containing 2.5% DSS (purchased from MP biomedicals, USA) as shown in Scheme 2.

2.6.2. Assessment of colitis

Body weight was measured daily for the entire duration of the study. Disease activity index (DAI) was evaluated to assess the severity of the colitis by combining scores of body weight loss, diarrhea of the stool, and the extent of the blood in the feces (28). From day 21 to day 28, body weight and DAI was measured daily. At day 28, all mice were sacrificed by cervical dislocation. The colon was collected and flushed by ice-cold PBS, and then the length was recorded. A section of the colon (about 1 cm) between the one third of the length to the midpoint was fixed in 10% formalin and embedded in paraffin. After being sectioned at about 5 μm, it was stained with hematoxylin and eosin (H&E). The histological analysis of stained colon section was conducted by optical microscopy and scored based on a scale that graded the extent of Mucous membrane (0–5), Destruction of epithelium and glands (0–3), Enlargement of gland recess (0–3), Reduction of goblet cells (0–3), Inflammatory cell infiltration (0–3), edema (0–3), Mucosal hemorrhage (0–3), Crypt abscess (0–3) and Dysplasia (0–3), respectively (29, 30).

2.6.3. Inflammatory cytokines and antioxidant indexes assay

At day 28, blood was obtained from the eyeballs of the mice, and centrifuged by a high-speed freezing centrifuge at 3,000 r/min for 10 min. The serum was then stored at an ultra-low temperature refrigerator (-80°C). ELISA kit (Beyotime Biotechnology Co., LTD.) was used to analyze the levels of TNF-α, IL-6, and IL-1β in the serum according to the instruction, while antioxidant indexes such as T-AOC, T-SOD, and MDA were quantified using commercial kits (Nanjing Jiancheng Bio-engineering Insititute, Nanjing, China).
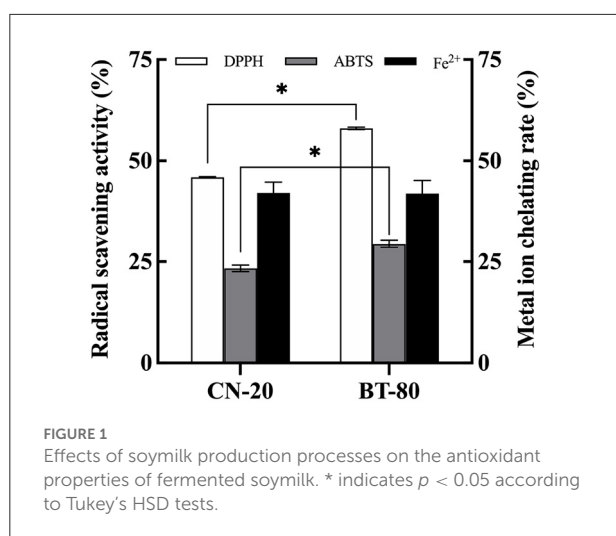
2.7. Statistical analysis

GraphPad Prism 9.0 and Spass 17.0 software were used to calculate and analyze the results, and which are presented as the mean±standard deviation ($X \pm SD$). The differences among the datasets were compared using one-way ANOVE followed by Tukey's HSD multiple comparison *post-hoc* tests. When $p < 0.05$ indicates statistical significance.

3. Results

3.1. Effect of fermentation conditions on antioxidant activity of soymilk *in vitro*

In order to obtain fermented soymilk with high antioxidative activity, the effect of soymilk preparation process on the *in vitro* antioxidant activity of fermented soymilk was investigated as shown in Figure 1. The BT-80 method is commonly used process in the preparation of soymilk drinks to remove the bean smell (24). While the CN-20 method is a traditional process for soymilk preparation. The DPPH and ABTS radical scavenging abilities of the BT-80 groups were 58.63, and 30.13%, respectively, which were significantly higher than those of the

FIGURE 1
Effects of soymilk production processes on the antioxidant properties of fermented soymilk. * indicates $p < 0.05$ according to Tukey's HSD tests.

CN-20 groups (45.81, and 23.94%, respectively). Meanwhile the Fe^{2+} chelation rates were all ∼41%. This result showed that the processing technology of fermented soymilk would influence its free radical scavenging capacity to some extent. The BT-80 method can improve the antioxidant capacity possibly due to the inactivation of enzymes, the existence of antioxidant physiological active substances and the accessibility of LAB fermentation. Consequently, the BT-80 method was chosen to prepare the soymilk in the following experiments.

To screen out an excellent commercial LAB product, the *in vitro* antioxidant activity of fermented soymilk prepared by five kinds of LAB (L571, Mild1.0, ST-M5, YF-L903, and YF-L904) were determined and compared as shown in Table 1, including the DPPH radical scavenging ability, ABTS radical scavenging ability, and Fe^{2+} chelation ability. The ABTS and DPPH radicals scavenging activity in the SM group (unfermented) were 14.96 and 39.37%, respectively, and the Fe^{2+} chelation rate was 50.36%. After fermentation, the ABTS and DPPH radicals scavenging ability were significantly enhanced regardless of the LAB strain used in fermentation. The Fe^{2+} chelation rate was also significantly increased, except for L571 fermented soymilk. This result further shows that lactic acid bacteria fermentation can improve the free radical scavenging and antioxidant activity of soybean milk. However, the extent of improving the free radical scavenging capacity differed among the LAB. The ABTS radical scavenging ability and the Fe^{2+} chelation rate of group YF-L903 was significantly higher than that of group L571. These results indicated that the free radical scavenging ability and Fe^{2+} chelation rate of fermented soymilk are closely related to the fermentation strain (31, 32). Take the three indicators into consideration, the YF-L903 would be the best choice for us.

It is well known that soybean isoflavones exhibit weak polarity, are soluble in 80% methanol or ethanol, and have various activities, such as preventing obesity, lowering blood sugar levels, reducing the risk of osteoporosis and breast cancer, and showing antioxidant and anti-inflammatory effects (33, 34). Soybean isoflavones are mainly composed of aglycone isoflavones (daidzein, genistein, glycitein) and glycoside isoflavones (daidzin, genistin, glycitin). In the fermentation process of soymilk, $β$-glucosidase in microorganisms can convert glycosidic flavonoid into aglycone flavonoid (35), so that the antioxidant and anti-inflammatory function of fermented soymilk is significantly improved (36).

Thus, we then investigated the effect of fermentation time on the antioxidation ability and the content of aglycone isoflavones in fermented soymilk. The DPPH and ABTS radical scavenging activity and metal ion chelating rate in soymilk and fermented soymilk were determined as shown in Figure 2A, in which the values for unfermented soymilk were 38, 26, and 55%, and they were increased to 44, 37, and 68% after 4 h of fermentation. However, the ABTS radical scavenging activity and metal ion chelating rate were decreased to 37, and 68% after 12 h of fermentation. These results showed that the antioxidant activity in soymilk increased first and then decreased with the prolongation of fermentation time. Besides, as shown in Figure 2B, the content of aglycone isoflavones in soymilk was 235 mg/kg, which increased to 257 mg/kg after 4 h of fermentation. However, this amount decreased slightly and finally became stable with continuous fermentation. Therefore, fermentation time has a significant influence on the content of active components in fermented soymilk and results in the difference in the antioxidative effects. The antioxidant activity of fermented soymilk is directly proportional to its content of aglycone isoflavones (36), and is significantly affected by the total isoflavone content of soybean and the fermentation time (37). Therefore, it is suggested to optimize the fermentation time of soy milk in practical application to maximize the antioxidant capacity of fermented soymilk. The above results showed that fermentation strain, fermentation time and soybean milk preparation technology are the key factors affecting the antioxidant activity of fermented soymilk. And the BT-80 method, LAB YF-L903 LAB and 8h was adopted to prepare the fermented soymilk for the subsequent experiments.

3.2. *In vitro* antioxidative effects of soymilk and fermented soymilk

Here, the antioxidant activities of solvent extracts with different polarity were analyzed. Figures 3A, B show that regardless of the polarity of the extractor, the free radical scavenging rate and total reducing capacity gradually increased with the increase of the extract concentration and decrease of the polarity of the extractor. The maximum free radical scavenging rate reached when the concentration of methanol was 80%. Therefore, 80% methanol extract can reflect the

TABLE 1 Antioxidant activity of soymilk fermented by different commercial lactic acid bacteria.

FSM with different lactic acid bacteria	ABTS scavenging activity (%)	DPPH scavenging activity (%)	Fe^{2+}chelation rate (%)
SM	14.96 ± 0.83[aA]	39.37 ± 0.04[a]	50.36 ± 0.03[b]
L571	16.76 ± 0.64[a]	42.32 ± 0.02[a]	32.10 ± 0.67[a]
Mild1.0	23.55 ± 2.38[b]	43.11 ± 1.43[a]	66.26 ± 0.27[d]
ST-M5	25.14 ± 0.41[bc]	44.09 ± 0.64[a]	68.10 ± 0.15[d]
YF-L904	28.37 ± 0.62[bc]	43.04 ± 2.23[a]	63.49 ± 0.29[c]
YF-L903	30.09 ± 0.51[c]	43.80 ± 0.14[a]	63.99 ± 0.23[c]

[A]Mean value ± standard deviation.
[a−d]Mean values with different letters in the same column are significantly different ($p < 0.05$), per Tukey's HSD test.
SM was the soymilk group without strain; L571, YF-L904, YF-L903, Mild1.0, and ST-M5 were the commercial fermentation strains, in which L571 was Lactobacillus plantarum, ST-M5 were Streptococcus thermophilus, YF-L904, YF-L903, and Mild1.0 were mixed strains of Streptococcus thermophilus and Lactobacillus germanicus.
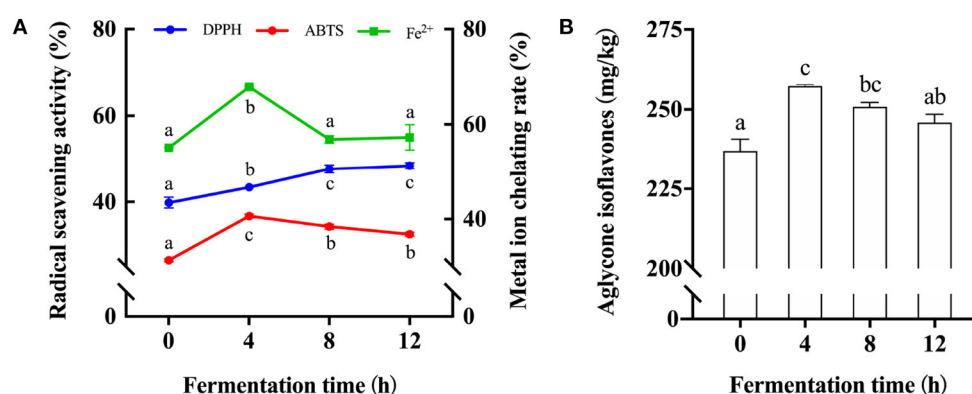
FIGURE 2
Changes of antioxidant activity and Aglycone isoflavone content in soymilk at different fermentation times. **(A)** Antioxidant activity of soymilk at different fermented times; **(B)** Aglycone isoflavone content in soymilk at different fermentation times; (a−c) Mean values with different letters in the same column are significantly different ($p < 0.05$), per Tukey's HSD test.

antioxidant activity of soymilk or fermented soymilk. Since isoflavones, saponins, and phenolic compounds in soybean have good antioxidant activities (9, 38), we also analyzed the flavonoid and total phenol contents in soymilk and fermented soymilk as shown in Figures 3C, D. The contents of flavonoids and total phenols in the 80% methanol extract were 6.96–8.53 mg/g and 9.01–10.08 mg/g, respectively, which were significantly higher than those in the water extract. In addition, the contents of flavonoids and phenolic compounds in the FSE were 8.53 and 10.08 mg/g, respectively, which were also significantly higher than those in the SE.

The antioxidative effects of the SE and FSE were further analyzed based on DPPH radical scavenging ability, ABTS radical scavenging ability, and iron reduction ability. As shown in Figure 4, the DPPH radical scavenging ability increased with the extract concentration and reached stability at 10 mg/mL. Noteworthy is that the DPPH radical scavenging ability of fermented soymilk was always 25% higher than that of soymilk

(Figure 4A). The ABTS radical scavenging ability exhibited a similar effect to that of DPPH, and the maximum value of fermented soymilk was 93.2% at 30 mg/mL, obvious higher than the 82% of soymilk (Figure 4B). The iron reducing ability of the extracts increased linearly with the increase of extract concentration, but there was no significant difference was observed between soymilk and fermented soymilk. A similar phenomenon was also reported by Lee and Chen et al., who showed that *Lactobacillus plantarum* P1201 or *Lactococcus acidophilus* MF204 fermented soymilk had stronger DPPH and ABTS radical scavenging ability than soymilk possibly due to the significant increase in conjugated linoleic acid (CLA) content and the conversion of glycosidic isoflavones to more physiologically active aglycone isoflavones during fermentation (39, 40).

The protective effects of soymilk and fermented soymilk against H$_2$O$_2$-induced oxidative stress in Caco-2 cells then were explored. As depicted in Figure 5, Firstly, the appropriate
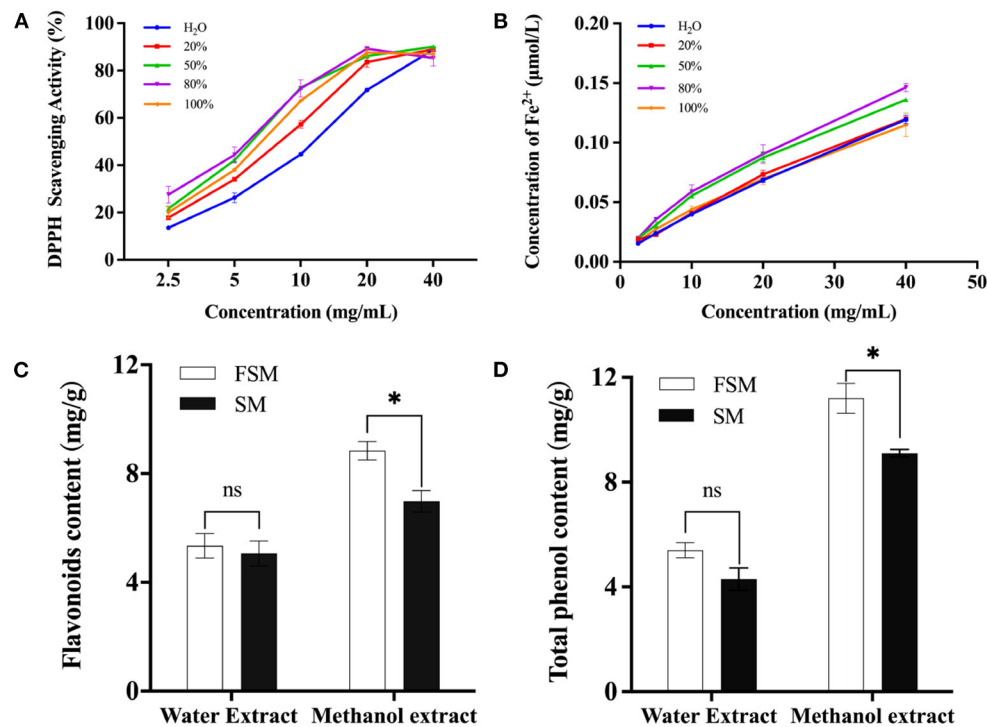
FIGURE 3
Effect of fermented soymilk active components extraction methods on antioxidant activity; **(A)** DPPH scavenging ability of fermented soymilk extract with different methanol concentrations; **(B)** Total reducing ability of the extract with different methanol concentrations; **(C)** Flavonoid content of the extract with water and 80% methanol; **(D)** Total phenolic content of the extract with water and 80% methanol. * indicates $p < 0.05$ according to Tukey's HSD tests.
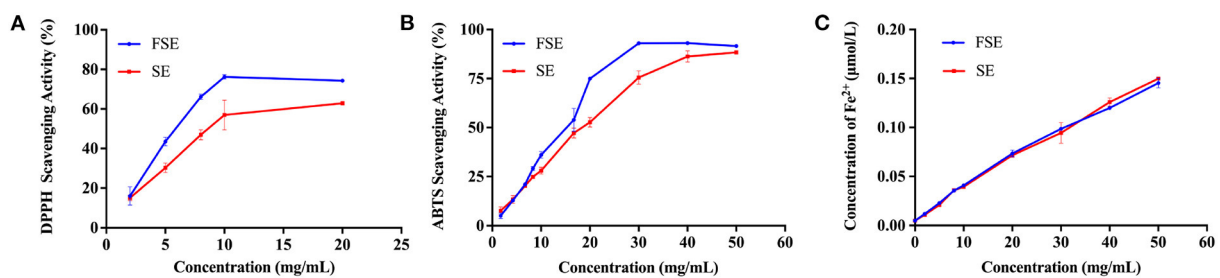

FIGURE 4
Antioxidant capacity of 80% methanol extracts of soymilk and fermented soymilk. **(A)** DPPH free radical scavenging ability; **(B)** Radical scavenging ability of ABTS; **(C)** Iron reduction capacity. FSE: 80% methanol extract of fermented soymilk, SE: 80% methanol extract of soymilk.

H_2O_2 concentration for induction was detected when the cells were in the half-life period. As shown in Figure 5A, the Caco-2 cell viability gradually decreased with the increase of H_2O_2 concentration. When the concentration of H_2O_2 reached 1 mM, the survival rate of Caco-2 cells decreased to about 50%. Thus, 1 mM H_2O_2-induced Caco-2 cells were chosen for the analysis of the protective effects of FSE and SE against oxidative stress.

Cell viability, ROS release, and malondialdehyde (MDA) and superoxide dismutase (SOD) activity were measured.

The cytotoxic effect of FSE and SE was tested as shown in Figure 5B. The cell viability of the control group was 100%. When the concentrations of FSE and SE were 0.125, 0.25, 0.5, and 1 mg/mL, there was no significant difference in cell viability compared with the control group, indicating that such
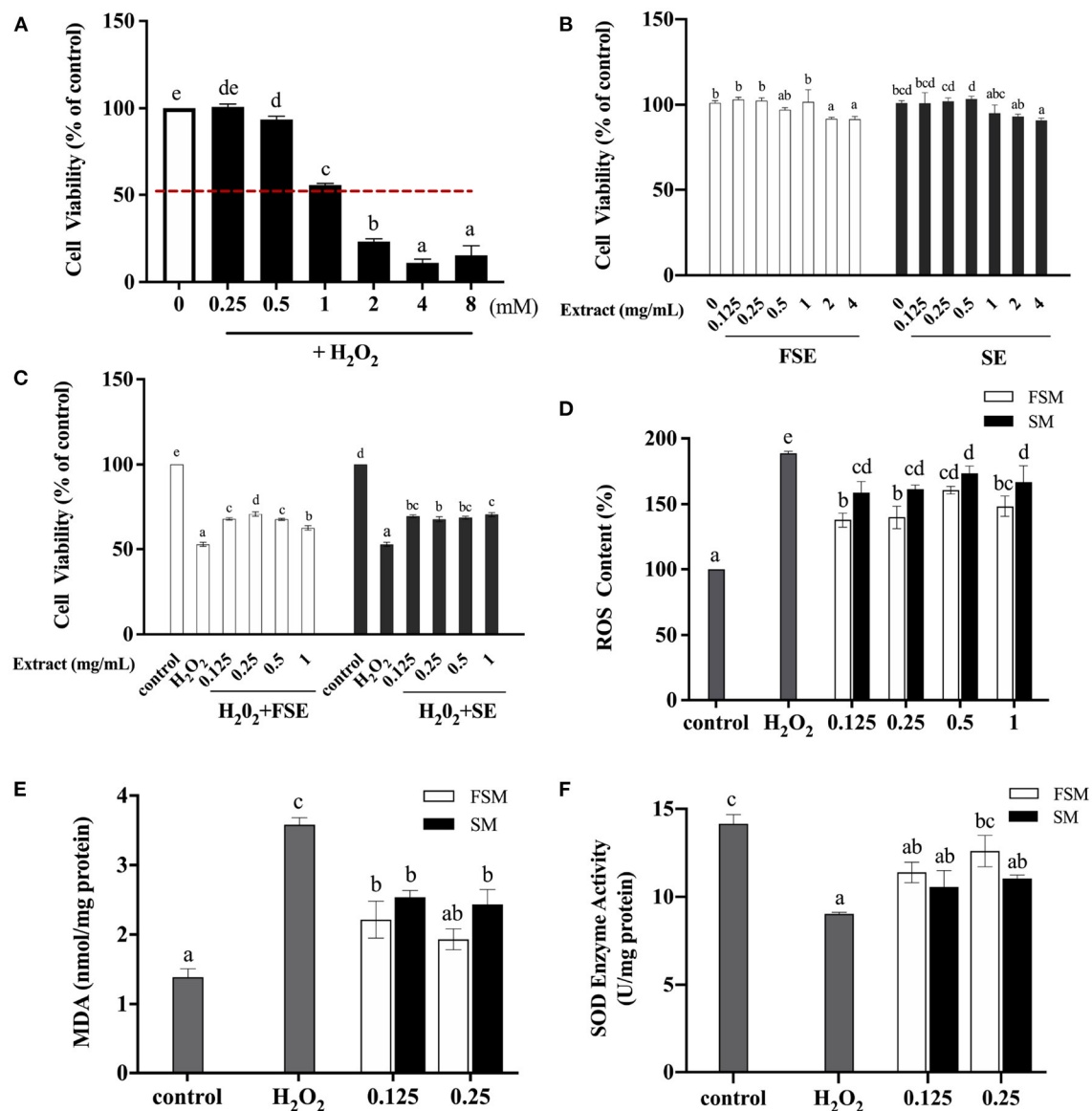
Protective effect of fermented soymilk on H_2O_2-induced oxidative damage in Caco-2 cells. **(A)** Effect of different concentrations of H_2O_2 on the activity of Caco-2 cells; **(B)** Effects of different concentrations of FSE and SE on the activity of Caco-2 cells; **(C)** Effects of different concentrations of FSE and SE on the activity of H_2O_2-induced Caco-2 cells; **(D)** Effects of FSE and SE on the content of reactive oxygen species (ROS) in H_2O_2-stimulated Caco-2 cells; **(E)** Effects of FSE and SE on the content of malondialdehyde (MDA) in H_2O_2-stimulated Caco-2 cells; **(F)** Effects of FSE and SE on the content of superoxide dismutase (SOD) in H_2O_2-stimulated Caco-2 cells. (a–d) Different letters indicate significant differences between groups according to Tukey's HSD test ($p < 0.05$).

concentrations had no toxic effect on these cells. However, when the concentration of FSE and SE reached 2 and 4 mg/mL, the cell viability was decreased to about 90%, indicating a significant inhibitory effect on cell viability. Therefore, in subsequent experiments, the maximum concentration of samples was selected as 1 mg/mL.

Figure 5C shows that compared with the control group, the cell viability of the injury model group (H_2O_2) was reduced

to 52.47%. When the concentration of SE and FSE was 0.125 mg/mL, the cell viability of the treatment group (SE+H_2O_2 and FSE+H_2O_2) was about 70%, which was significantly increased compared with that of the injury model group. This finding indicated that SE and FSE could help cells to resist the oxidative damage induced by H_2O_2. However, no significant increase in cell viability was observed with further increase of SE and FSE concentrations, indicating

that their protective effect on injured cells was not dose-dependent.

H_2O_2 induction leads to excessive ROS production, which can drive DNA damage and genetic instability and trigger oxidative stress-induced cell death (41). Figure 5D shows that compared with the injury model group (H_2O_2), the SE and FSE groups had significantly decreased ROS content, implying the ROS scavenging function of both extracts. The ROS scavenging ability of FSE was stronger than that of SE. Moreover, ROS can attack polyunsaturated fatty acids in biofilms, resulting in the peroxidation of lipids to form MDA. Figure 5E shows that compared with the control group, the injury model group had significantly increased MDA concentration. Meanwhile the SE and FSE significantly suppressed the increase of MDA content. Compared with SE, FSE demonstrated a stronger inhibiting ability for MDA, indicating its enhanced oxidative damage protection ability.

The effects of FSE and SE pretreatment on the SOD activity in oxidation-damaged cells were investigated as shown in Figure 5F. SOD is an important antioxidant enzyme in living organisms and can scavenge superoxide anion radical produced in the body, thus protecting cells from oxidative damage. It is also an important factor in maintaining the balance between oxidation and anti-oxidation, thus reflecting the antioxidant capacity of the body. Compared with that in the control group, the SOD activity in cells was significantly decreased in the H_2O_2 group. Compared with that in the H_2O_2 group, the SOD activity significantly increased in FSE and SE groups. These results indicated that FSE and SE could suppress the increase of intracellular ROS content induced by H_2O_2, reduce the oxidative damage, and restore cell viability by enhancing SOD activity. Furthermore, fermentation could improve the protective effect of soymilk against H_2O_2-induced oxidative damage in Caco-2 cells. Qian et al. (14) also found that *Lactobacillus casei* 16 fermented soymilk has a protective effect against the oxidative damage in HepG2 cells, which may be related to the increase in the content of total phenols and free amino acids. Fermented soymilk can also remarkably enhance the antioxidant capacity of prematurely aging mice and hyperlipidemic rats (11, 12, 40).

3.3. Preventive effect of fermented soymilk on DSS-induced colitis in mice

In IBD, oxidative stress refers to an imbalance between the production and elimination of ROS, not only occurs in the inflamed intestinal mucosa but also extends into the deeper layers of the intestinal wall and is mirrored within the systemic circulation (42, 43). Considering the ROS scavenging ability of fermented soymilk, as well as its effect of maintaining the redox homeostasis in the cells, we further explored the prevention

effect of fermented soymilk on colitis in mice. The experimental colitis was induced in mice by administering 2.5% DSS in water continuously for 7 days (Scheme 2). Physiological indices including fecal condition, weight changes, disease activity index (DAI), the length of colon and spleen-to-body weight ratio were recorded as shown in Figure 6 to investigate the prevention effect of fermented soymilk on DSS-induced colitis in mice. The mice in the control group had normal feces and colon length, no weight loss and DAI score, and a spleen-to-body weight ratio of 0.25%. After treatment with DSS, the mice showed loose stool. Compared with the DSS group, the group gavaged with fermented soymilk showed significantly improved fecal status and well-formed feces, regardless of low or high fermented soymilk dose (Figure 6A). In the DSS group, the body weight, and the colon length reduced significantly, DAI, and spleen-to-body weight ratio of mice increased visible. Compared with the DSS group, fermented soymilk intervention remarkably increased the body weight and colon length, and decreased the DAI in mice with colitis (Figures 6B–D). In particular, the spleen-to-body ratio was the same as that in the control group without significant difference (Figure 6E). The above experimental results directly demonstrated that lactic acid-fermented soymilk can enhance intestinal health and prevent colitis.

To further assess the impact of fermented soymilk on systemic response, pro-inflammatory cytokines in the serum was measured. TNF-α, IL-6, and IL-1β are inflammatory cytokines that reflect the level of immune response in the body. If a large number of inflammatory cytokines are released in the body, then the inflammatory response will be aggravated (44, 45). In this work, the release levels of inflammatory cytokines in mice with DSS-induced colitis were analyzed as shown in Figures 7A–C. After DSS treatment, the concentrations of TNF-α, IL-6, and IL-1β reached about 41, 350, and 50 pg/mL, drastically higher than those in the control group. Noteworthy is that the increase in inflammatory cytokine levels in the mice gavaged with fermented soymilk was significantly lower than that in the mice not treated with fermented soymilk, despite all groups receiving the same DSS treatment. The TNF-α level in the DSS + L – FSM and DSS + H – FSM groups was 21–28 pg/mL, which was close to 50% of that in the DSS treatment group. Meanwhile the level of IL-6 was 250–280 pg/mL, about 30% lower than that in the DSS group. Similarly, the concentrations of IL-1β was 25–35 pg/mL, about 50% lower than that in the DSS group. The above results indicated that the release of inflammatory factors in the serum of mice was significantly induced by the DSS treatment but was significantly inhibited by gavaging with fermented soymilk. Therefore, fermented soymilk could protect mice from colitis by inhibiting the release of inflammatory cytokines.

To elucidate the influence of fermented soymilk on oxidative stress, total antioxidant capacity (T-AOC), total superoxide dismutases (T-SOD), and glutathione peroxidase (MDA) in the
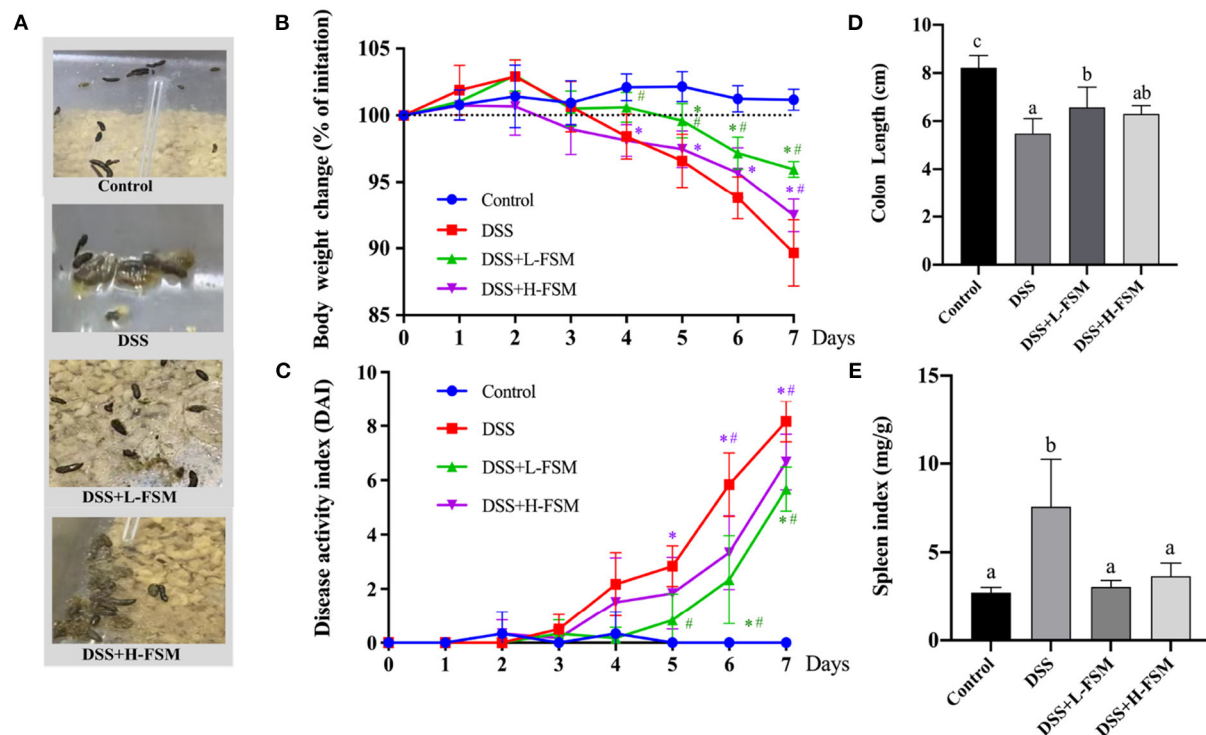
FIGURE 6
Effect of fermented soymilk on the health condition of DSS-induced colitis mice. **(A)** Fecal condition; **(B)** Daily body weight changes throughout the entire duration of the DSS treatment ($n = 6$ per group); **(C)** Disease activity index throughout the entire duration of the DSS treatment ($n = 6$ per group); **(D)** the lengths of colon ($n = 6$ per group); **(E)** Spleen-to-body weight ratio ($n = 6$ per group). Control, control group; DSS, colitis model group; DSS+L-FSM, low-dose fermented soymilk (0.8 g/kg BW) group; and DSS+H-FSM, high-dose fermented soymilk (1.6 g/kg BW) group. (a−d) Different letters indicate significant differences between groups according to Tukey's HSD test, *$p < 0.05$ relative to Control group, #$p < 0.05$ relative to DSS group.

serum was measured (Figures 7D–F). After DSS treatment, the concentrations of T-AOC and T-SOD were suppressed as shown in Figures 7D, E, and the level of MDA was increased in the mice with colitis compared with normal controls as shown in Figure 7F. However, the concentrations of T-AOC and T-SOD were substantially enhanced and the MDA were significantly attenuated by fermented soymilk compared with the DSS group. These results suggested that fermented soymilk can efficiently suppress the DSS-induced oxidative stress.

Histological analysis was conducted based on the H&E staining sections to further reveal the effect of fermented soymilk on the intestinal lesions in the mice with DSS-induced colitis. As depicted in Figure 8A, the complete mucosal surface, mucosal wrinkled wall, normal glands and crypts can be clearly observed in the control group. Although the mucosal wrinkled wall was visible after DSS treatment, the mucosal surface was incomplete, the glands were swollen and thickened, and the inflammatory cell infiltrated seriously, indicating that the animal model was successfully established. Compared with the DSS group, the mice gavaged with fermented soymilk and then treated with DSS demonstrated a better status, in which the mucosal wrinkled

wall was visible, part of glands swollen and thickened, and inflammatory cell infiltrated partially. Besides, the intestinal histological score of the DSS group increased significantly to 14 (Figure 8B), while the score of the groups treated with fermented soymilk was 30–50% of that in the DSS group. This result is consistent with the analysis of inflammatory cytokine release levels in the blood of mice (Figure 7), further demonstrating the protective effect of fermented soymilk against colitis in mice.

4. Discussion

Recently, the antioxidant and anti-inflammatory effects of the nutrients in plant-based food have attracted extensive attention (46, 47). Fermented soymilk prepared with *Lactobacillus plantarum* HFY01 and *Lactobacillus fermentum* CQPC04 exhibits good antioxidant activity, and can significantly improve D-galactose induced premature senescence in mice (11, 12). Yang et al. (40) also found that fermented soymilk could significantly improve the antioxidant capacity of hyperlipidemia rats, and reduce the arteriosclerosis index and coronary risk index. However, the preparation process of fermented
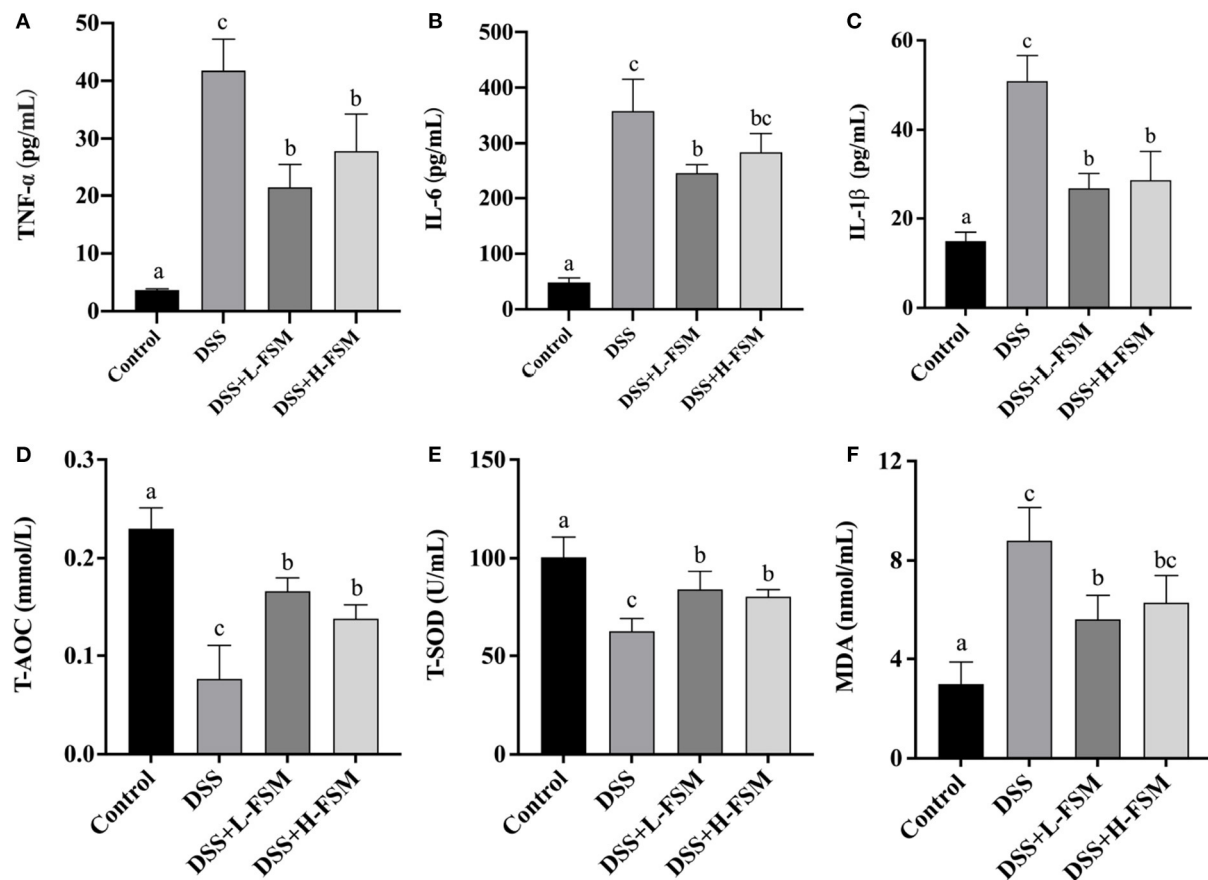
FIGURE 7

Effect of fermented soymilk on the release of blood inflammatory cytokines in mice with DSS-induced colitis. Concentrations of three pro-inflammatory cytokines, Tumor necrosis factor-α (TNF-α) **(A)**, interleukin-6 (IL-6) **(B)**, interleukin-1β (IL-1β) **(C)** in the serum ($n = 6$ per group). Concentrations of T-AOC **(D)**, T-SOD **(E)**, MDA **(F)** in the serum ($n = 6$ per group). (a–d) Different letters indicate significant differences between groups according to Tukey's HSD test ($p < 0.05$).

soymilk varies greatly for different production enterprises in raw materials, raw material treatment technology and strain selection. In this work, we investigated the effect of the raw material treatment, fermentation strain and fermentation time on the antioxidant activity of fermented soymilk. The results showed that all the three factors could influence the antioxidant activity of fermented soymilk, among which the hot blanching pretreatment of soybeans (BT-80 method) could improve the antioxidant activity significantly and removing the bean smell of soymilk. Furthermore, the antioxidant activity of fermented products could be improved regardless of which LAB strain was used for fermentation. Nevertheless, great differences in effect were observed between the strains. We optimized the processing conditions, including raw materials, fermentation strains and fermentation processes, and then developed fermented soymilk with high antioxidant activity for subsequent experiments.

We further studied the antioxidant effects of fermented soymilk extracts (FSE) by *in vitro* antioxidant test and using

H_2O_2-induced Caco-2 cell injury model. *In vitro* antioxidant experiments demonstrated that fermented soymilk has better antioxidant effect than that of soymilk possibly because the fermentation process increases the content of isoflavone aglycones and phenols (48), and hydrolyzes soy protein to produce active peptides, thus enhancing the antioxidant capacity of fermented soymilk (49, 50). In this work, the results of cell experiments also showed that fermented soymilk had significant protective effect on H_2O_2-induced injury of Caco-2 cells. In brief, when the concentration of fermented soymilk was >0.125 mg/mL, the levels of ROS, MDA and SOD in the cells were significantly decreased (Figures 5D–F). This result is consistent with the previous reports of using fermented soymilk to protect oxidative damage in HepG2 cells (14).

Meanwhile, IBD is a chronic, progressive, and recurrent bowel disease, and one of its main causative factors is the high levels of free radicals and low antioxidant capacity (51, 52). Inhibiting lipid peroxidation and scavenging of oxygen free
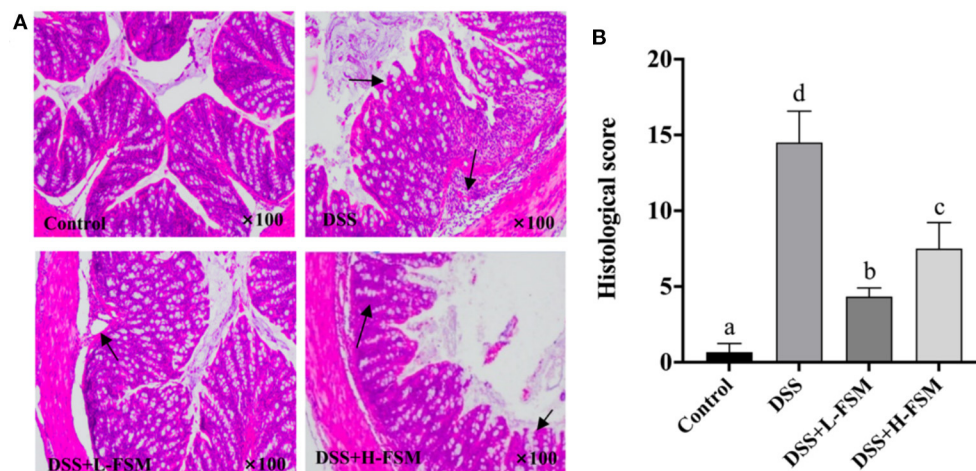
FIGURE 8
Effect of fermented soymilk on DSS-induced intestinal lesion in mice. **(A)** Histological analysis on the colonic section ($n = 6$ per group); The black arrows indicate inflammatory cell infiltration. **(B)** Histological score of the colonic section ($n = 6$ per group). (a−d) Different letters indicate significant differences between groups according to Tukey's HSD test ($p < 0.05$).

radicals can prevent and treat this disease (53, 54). Based on the pathogenesis of IBD, we investigated the preventive effect of fermented soymilk on DSS-induced colitis mice. Results showed that gavaged with fermented soymilk significantly improved the disease condition of DSS-induced colitis in mice. More precisely, the weight loss, the colon length, spleen-to-body ratio and disease index were improved; the release of TNF-α, IL-6, IL-8, and IL-1β was significantly inhibited; and the inflammation of colonic epithelial cells was relieved. This result further confirmed that fermented soymilk has an antioxidant and intestinal inflammation preventive effects. Considering the antioxidant effect of isoflavones, polyphenols, and active peptides in soybean and the ability of soy isoflavones and small molecule peptides to effectively relieve the symptoms of UC (55, 56), we speculated that the effect of fermented soymilk on preventing colitis in mice is closely related to the antioxidant activities of fermented soymilk. Besides, our previous work also showed that soybean β-conglycinin peptides (SGP) could promote the proliferation of Caco-2 cells, enhance the formation of intercellular tight junctions, and have a potential anti-infective ability (57). The animal experiments further revealed that the SGP could significantly reduce the histological injury, alleviate inflammatory symptoms and neutrophil infiltration in mice with DSS-induced colitis, and inhibit the expression of inflammatory regulator NF-κB/p65 (58). Moreover, LAB is a group of bacteria commonly used for the fermentation of various products, such as soymilk, milk, kimchi etc., (59, 60). LAB can regulate the balance of intestinal flora, prevent and reduce the occurrence of intestinal diseases, reduce oxidative stress damage in the intestine, and exhibit a good antioxidant activity (61, 62). The last activity can be attributed to the production of active

polysaccharides, SOD, catalase (CAT) and other antioxidant enzymes, as well as thioredoxin, glutathione and other reducing substances during the growth and metabolism of LAB (63). The level of active ingredients in fermented soybean products is significantly increases during the LAB fermentation (64).

5. Conclusion

In summary, the antioxidant activity of fermented soymilk is significantly affected by soymilk preparation processes and fermentation time. Fermentation strain is also a key factor affecting the antioxidant activity of fermented soymilk, and great variation in antioxidant activity is observed among the soymilk samples fermented with different LAB. By exploring the differences in antioxidation of fermented soymilk, we had obtained an optimal fermentation process and used in following experiments. Cell experiments also showed that fermented soymilk could reduce the ROS and MDA contents, and increase the SOD activity in H_2O_2-induced Caco-2 cells to protect them from the damage of ROS and enhance their repair ability. Meanwhile, Fermented soymilk can significantly improve the disease status of DSS-induced colitis in mice by reducing the rate of weight loss, balancing the spleen-to-body weight ratio, reducing the disease activity index, and inhibiting the release of inflammatory cytokines and antioxidant index. This study provides a novel insight into the production of fermented soymilk with excellent antioxidation activity, and will facilitate the formulation of treatment and prevention strategies for IBD and other inflammatory diseases.

Data availability statement

Ethics statement

Author contributions

Funding

Acknowledgments

Conflict of interest

Publisher's note

References

1. Bau TR, Ida EI. Soymilk processing with higher isoflavone aglycone content. *Food Chem.* (2015) 183:161–8. doi: 10.1016/j.foodchem.2015.03.026

2. Kietsiriroje N, Kanjanahirun K, Kwankaew J, Ponrak R, Soonthornpun S. Phytosterols and inulin-enriched soymilk increases glucagon-like peptide-1 secretion in healthy men: double-blind randomized controlled trial, subgroup study. *BMC Res Notes.* (2018) 11:844. doi: 10.1186/s13104-018-3958-5

3. Chatterjee C, Gleddie S, Xiao C-W. Soybean bioactive peptides and their functional properties. *Nutrients.* (2018) 10:1211. doi: 10.3390/nu10091211

4. Wang R, Guo S. Phytic acid and its interactions: contributions to protein functionality, food processing, and safety. *Compr Rev Food Sci F.* (2021) 20:2081–105. doi: 10.1111/1541-4337.12714

5. Zhang R, Han Y, McClements DJ, Xu D, Chen S. Production, characterization, delivery, and cholesterol-lowering mechanism of phytosterols: a review. *J Agr Food Chem.* (2022) 70:2483–94. doi: 10.1021/acs.jafc.1c07390

6. Liu J, Xu D, Chen S, Yuan F, Mao L, Gao Y. Superfruits in china: bioactive phytochemicals and their potential health benefits: a review. *Food Sci Nutr.* (2021) 9:6892–902. doi: 10.1002/fsn3.2614

7. Xiang H, Sun-Waterhouse D, Waterhouse GIN, et al. Fermentation-enabled wellness foods: a fresh perspective. *Food Sci Hum Well.* (2019) 8:203–43. doi: 10.1016/j.fshw.2019.08.003

8. Liu L, Chen X, Hao L, Zhang G, Jin Z, Li C, et al. Traditional fermented soybean products: processing, flavor formation, nutritional and biological activities. *Crit Rev Food Sci.* (2022) 62:1971–89. doi: 10.1080/10408398.2020.1848792

9. Sanlier N, Gokcen BB, Sezgin AC. Health benefits of fermented foods. *Crit Rev Food Sci.* (2019) 59:506–27. doi: 10.1080/10408398.2017.1383355

10. O'Leary K. Health benefits of fermented foods. *Nat Med.* (2021)

11. Li C, Fan Y, Li S, Zhou X, Park K-Y, Zhao X, et al. Antioxidant effect of soymilk fermented by *Lactobacillus plantarum* HFY01 on D-galactose-induced premature aging mouse model. *Front Nutr.* (2021) 8:667643. doi: 10.3389/fnut.2021.667643

12. Zhou X, Du H-H, Jiang M, Zhou C, Deng Y, Long X, et al. Antioxidant effect of *Lactobacillus fermentum* CQPC04-fermented soy milk on D-galactose-induced oxidative aging mice. *Front Nutr.* (2021) 8:727467. doi: 10.3389/fnut.2021.727467

13. Chuang Y-C, Cheng M-C, Lee C-C, Chiou T-Y, Tsai T-Y. Effect of ethanol extract from *Lactobacillus plantarum* TWK10-fermented soymilk on wound healing in streptozotocin-induced diabetic rat. *AMB Exp.* (2019) 9:163. doi: 10.1186/s13568-019-0886-2

14. Qian F, Zhang J, Hou K, Zhang Y, Wang Z, Luo P, et al. *In vitro* study of the antioxidative and antiproliferative capabilities of *Lactobacillus casei* 16-fermented soymilk. *Food Sci Nutr.* (2020) 8:48–57. doi: 10.1002/fsn3.1214

15. Yilmaz I, Dolar ME, Ozpinar H. Effect of administering kefir on the changes in fecal microbiota and symptoms of inflammatory bowel disease: a randomized controlled trial. *Turk J Gastroenterol.* (2019) 30:242–53. doi: 10.5152/tjg.2018.18227

16. Sakandar HA, Zhang H. Trends in probiotic(s)-fermented milks and their *in vivo* functionality: a review. *Trends Food Sci Tech.* (2021) 110:55–65. doi: 10.1016/j.tifs.2021.01.054

17. Yoon J-W, Ahn S-I, Jhoo J-W, Kim G-Y. Antioxidant activity of yogurt fermented at low temperature and its anti-inflammatory effect on DSS-induced colitis in mice. *Food Sci Anim Resour.* (2019) 39:162–76. doi: 10.5851/kosfa.2019.e13

18. Biasi F, Leonarduzzi G, Oteiza PI, Poli G. Inflammatory bowel disease: mechanisms, redox considerations, and therapeutic targets. *Antioxid Redox Sign.* (2013) 19:1711–47. doi: 10.1089/ars.2012.4530

19. Matsuoka K, Uemura Y, Kanai T, Kunisaki R, Suzuki Y, Yokoyama K, et al. Efficacy of bifidobacterium breve fermented milk in maintaining remission of ulcerative colitis. *Digest Dis Sci.* (2018) 63:1910–9. doi: 10.1007/s10620-018-4946-2

20. Kawahara M, Nemoto M, Nakata T, Kondo S, Takahashi H, Kimura B, et al. Anti-inflammatory properties of fermented soy milk with Lactococcus lactis subsp lactis S-SU2 in murine macrophage RAW2647 cells and DSS-induced IBD model mice. *Int Immunopharmacol.* (2015) 26:295–303. doi: 10.1016/j.intimp.2015.04.004

21. Wang R, Guo S. Effects of endogenous small molecular compounds on the rheological properties, texture and microstructure of soymilk coagulum: removal of phytate using ultrafiltration. *Food Chem.* (2016) 211:521–9. doi: 10.1016/j.foodchem.2016.05.086

22. Wang Y, Xing J, Wang R, Guo S. The analysis of the causes of protein precipitate formation in the blanched soymilk. *Food Chem.* (2017) 218:341–7. doi: 10.1016/j.foodchem.2016.09.084

23. Peng X, Wang Y, Xing J, Wang R, Shi X, Guo S. Characterization of particles in soymilks prepared by blanching soybeans and traditional method: a comparative study focusing on lipid-protein interaction. *Food Hydrocolloid.* (2017) 63:1–7. doi: 10.1016/j.foodhyd.2016.08.012

24. Shi X, Hao Z, Wang R, Chen Z, Zuo F, Wan Y, Guo S. Changes of hexanal content in fermented soymilk: Induced by lactic acid bacterial fermentation and thermal treatment. *J Food Process Pres.* (2022) 1:e16555. doi: 10.1111/jfpp.16555

25. Klump SP, Allred MC. MacDonald JL, Ballam JM. Determination of isoflavones in soy and selected foods containing soy by extraction, saponification, and liquid chromatography: collaborative study. *J AOAC Int.* (2001) 84:1865–83. doi: 10.1093/jaoac/84.6.1865

26. Han SS, Hur SJ, Lee SK, A. comparison of antioxidative and anti-inflammatory activities of sword beans and soybeans fermented with Bacillus subtilis. *Food Funct.* (2015) 6:2736–48. doi: 10.1039/C5FO00290G

27. Xie Z, Huang J, Xu X, Jin Z. Antioxidant activity of peptides isolated from alfalfa leaf protein hydrolysate. *Food Chem.* (2008) 111:370–6. doi: 10.1016/j.foodchem.2008.03.078

28. Lin Y, Yang X, Yue W, Xu X, Li B, Zou L, et al. Chemerin aggravates DSS-induced colitis by suppressing M2 macrophage polarization. *Cell Mol Immunol.* (2014) 11:355–66. doi: 10.1038/cmi.2014.15

29. Peng Y, Yan Y, Wan P, Chen D, Ding Y, Ran L, et al. Gut microbiota modulation and anti-inflammatory properties of anthocyanins from the fruits of Lycium ruthenicum Murray in dextran sodium sulfate-induced colitis in mice. *Free Radical Bio Med.* (2019) 136:96–108. doi: 10.1016/j.freeradbiomed.2019.04.005

30. Stillie R, Stadnyk AW. Role of TNF receptors, TNFR1 and TNFR2, in dextran sodium sulfate-induced colitis. *Inflamm Bowel Dis.* (2009) 15:1515–25. doi: 10.1002/ibd.20951

31. Yamamoto N, Shoji M, Hoshigami H, Watanabe K, Watanabe K, Takatsuzu T, et al. Antioxidant capacity of soymilk yogurt and exopolysaccharides produced by lactic acid bacteria. *Biosci Microbiota Food Health.* (2019) 38:97–104. doi: 10.12938/bmfh.18-017

32. Zhao D, Shah NP. Antiradical and tea polyphenol-stabilizing ability of functional fermented soymilk-tea beverage. *Food Chem.* (2014) 158:262–9. doi: 10.1016/j.foodchem.2014.02.119

33. Nakai S, Fujita M, Kamei Y. Health promotion effects of soy isoflavones. *J Nutr Sci Vitaminol.* (2020) 66:502–7. doi: 10.3177/jnsv.66.502

34. Cao Z-H, Green-Johnson JM, Buckley ND, Lin Q-Y. Bioactivity of soy-based fermented foods: a review. *Biotechnol Adv.* (2019) 37:223–38. doi: 10.1016/j.biotechadv.2018.12.001

35. Xu L, Du B, Xu B. A systematic, comparative study on the beneficial health components and antioxidant activities of commercially fermented soy products marketed in China. *Food Chem.* (2015) 174:202–13. doi: 10.1016/j.foodchem.2014.11.014

36. Chen Y, Wang Y, Chen J, Tang H, Wang C, Li Z, et al. Bioprocessing of soybeans (*Glycine max* L) by solid-state fermentation with *Eurotium cristatum* YL-1 improves total phenolic content, isoflavone aglycones, and antioxidant activity. *Rsc Adv.* (2020) 10:16928–41. doi: 10.1039/C9RA10344A

37. Nam DH, Kim HJ, Lim JS, Kim KH, Park C-S, Kim JH, et al. Simultaneous enhancement of free isoflavone content and antioxidant potential of soybean by fermentation with *Aspergillus oryzae*. *J Food Sci.* (2011) 76:H194–200. doi: 10.1111/j.1750-3841.2011.02350.x

38. Dimidi E, Cox SR, Rossi M, Whelan K. Fermented foods: definitions and characteristics, impact on the gut microbiota and effects on gastrointestinal health and disease. *Nutrients.* (2019) 11:1806. doi: 10.3390/nu11081806

39. Lee JH, Kim B, Hwang CE, Haque MA, Kim SC, Lee CS, et al. Changes in conjugated linoleic acid and isoflavone contents from fermented soymilks using *Lactobacillus plantarum* P1201 and screening for their digestive

enzyme inhibition and antioxidant properties. *J Funct Foods.* (2018) 43:17–28. doi: 10.1016/j.jff.2018.01.022

40. Chen J, Wu Y, Yang C, Xu X, Meng Y. Antioxidant and hypolipidemic effects of soymilk fermented *via Lactococcus acidophilus* MF204. *Food Funct.* (2017) 8:4414–20. doi: 10.1039/C7FO00701A

41. Moloney JN, Cotter TG. ROS signalling in the biology of cancer. *Semin Cell Dev Biol.* (2018) 80:50–64. doi: 10.1016/j.semcdb.2017.05.023

42. Bourgonje AR, von Martels JZH, Bulthuis MLC, van Londen M, Faber KN, Dijkstra G, et al. Crohn's disease in clinical remission is marked by systemic oxidative stress. *Front Physiol.* (2019) 10:499. doi: 10.3389/fphys.2019.00499

43. Moura FA, de Andrade KQ, Dos Santos JC, Araújo OR, Goulart MO. Antioxidant therapy for treatment of inflammatory bowel disease: does it work? *Redox Biol.* (2015) 6:617–39. doi: 10.1016/j.redox.2015.10.006

44. Wu SJ, Fang JY, Ng CC, Wang CY, Shyu YT. Anti-inflammatory activity of *Lactobacillus*-fermented adlay-soymilk in LPS-induced macrophages through suppression of NF-κB pathways. *Food Res Int.* (2013) 52:262–8. doi: 10.1016/j.foodres.2013.02.053

45. Liao CL, Huang HY, Sheen LY, Chou C-C. Anti-inflammatory activity of soymilk and fermented soymilk prepared with lactic acid bacterium and bifidobacterium. *J Food Drug Anal.* (2010) 18:202–10. doi: 10.38212/2224-6614.2268

46. Falcão HG, Silva MBR, de Camargo AC, Shahidi F, Franchin M, Rosalen PL, et al. Optimizing the potential bioactivity of isoflavones from soybeans *via* ultrasound pretreatment: antioxidant potential and NF-κB activation. *J Food Biochem.* (2019) 43:e13018. doi: 10.1111/jfbc.13018

47. Hiramatsu EY, de Ávila ARA, Gênova VM, de Queirós LD, Macedo GA, Martins IM, et al. Biotransformation processes in soymilk isoflavones to enhance anti-inflammatory potential in intestinal cellular model. *J Food Biochem.* (2020) 44:e13149. doi: 10.1111/jfbc.13149

48. da Silva Fernandes M, Lima FS, Rodrigues D, Handa C, Guelfi M, Garcia S. Evaluation of the isoflavone and total phenolic contents of kefir-fermented soymilk storage and after the *in vitro* digestive system simulation. *Food Chem.* (2017) 229:373–80. doi: 10.1016/j.foodchem.2017.02.095

49. Chourasia R, Phukon LC, Abedin MM, Sahoo D, Rai AK. Production and characterization of bioactive peptides in novel functional soybean chhurpi produced using *Lactobacillus delbrueckii* WS4. *Food Chem.* (2022) 387:132889. doi: 10.1016/j.foodchem.2022.132889

50. Singh BP, Vij S. *In vitro* stability of bioactive peptides derived from fermented soy milk against heat treatment, pH and gastrointestinal enzymes. *Lwt-Food Sci Technol.* (2018) 91:303–7. doi: 10.1016/j.lwt.2018.01.066

51. Lloyd-Price J, Arze C, Ananthakrishnan AN, Schirmer M, Avila-Pacheco J, Poon TW, et al. Multi-omics of the gut microbial ecosystem in inflammatory bowel diseases. *Nature.* (2019) 569:655. doi: 10.1038/s41586-019-1237-9

52. Liu P, Li Y, Wang R, Ren F, Wang X. Oxidative stress and antioxidant nanotherapeutic approaches for inflammatory bowel disease. *Biomedicines.* (2022) 10:85. doi: 10.3390/biomedicines10010085

53. Dziabowska-Grabias K, Sztanke M, Zajac P, Celejewski M, Kurek K, Szkutnicki S, et al. Antioxidant therapy in inflammatory bowel diseases. *Antioxidants.* (2021) 10:412. doi: 10.3390/antiox10030412

54. Zhang J, Li Q, Wei Y, Long X, Mu J, Pan Y, Zhao X. Process design of the antioxidant shuidouchi and its effect on preventing dextran sulfate sodium (DSS)-induced colitis in mice *via* antioxidant activity. *Appl Sci-Basel.* (2019) 9:5. doi: 10.3390/app9010005

55. Gao X, Fan W, Tan L, Shi Y, Ding C, Liu S, et al. Soy isoflavones ameliorate experimental colitis by targeting ERα/NLRP3 inflammasome pathways. *J Nutr Biochem.* (2020) 83:108438. doi: 10.1016/j.jnutbio.2020.108438

56. Al-Nakkash L, Kubinski A. Soy isoflavones and gastrointestinal health. *Curr Nutr Rep.* (2020) 9:193–201. doi: 10.1007/s13668-020-00314-4

57. Yang B, Lv Y, Chen Y, Wang J, Tang W, Guo S. Inhibitory action of soybean β-conglycinin hydrolysates on Salmonella typhimurium translocation in Caco-2 epithelial cell monolayers. *J Agr Food Chem.* (2008) 56:7522–7. doi: 10.1021/jf8012508

58. Ren J, Yang B, Lv Y, Guo S. Protective and reparative effects of peptides from soybean β-conglycinin on mice intestinal mucosa injury. *Int J Food Sci Nutr.* (2014) 65:345–50. doi: 10.3109/09637486.2013.854748

59. Jeong Y, Kim H, Lee JY, Won G, Choi SI, Kim GH, et al. The antioxidant, anti-diabetic, and anti-adipogenesis potential and probiotic properties of lactic acid bacteria isolated from human and fermented foods. *Fermentation.* (2021) 7:123. doi: 10.3390/fermentation7030123

60. Khubber S, Marti-Quijal FJ, Tomasevic I, Remize F, Barba FJ. Lactic acid fermentation as a useful strategy to recover antimicrobial and antioxidant

compounds from food and by-products. *Curr Opin Food Sci.* (2022) 43:189–98. doi: 10.1016/j.cofs.2021.11.013

61. Kumari M, Kokkiligadda A, Dasriya V, Naithani H. Functional relevance and health benefits of soymilk fermented by lactic acid bacteria. *J Appl Microbiol.* (2022) 133:104–19. doi: 10.1111/jam.15342

62. Oktaviani L, Astuti DI, Rosmiati M, Abduh MY. Fermentation of coffee pulp using indigenous lactic acid bacteria with simultaneousaeration to produce cascara with a high antioxidant activity. *Heliyon.* (2020) 6:e04462. doi: 10.1016/j.heliyon.2020.e04462

63. Bryukhanov A, Klimko A, Netrusov A. Antioxidant properties of lactic acid bacteria. *Microbiology.* (2022) 91:463–78. doi: 10.1134/S0026261722601439

64. Prado FG. Pereira GVd, Karp SG, Soccol CR. Fermented soy products and their potential health benefits: a review. *Microorganisms.* (2022) 10:1606. doi: 10.3390/microorganisms10081606

Check for updates

Effect of octenyl succinic anhydride modified starch on soy protein-polyphenol binary covalently linked complexes

Die Dong*, Tenglong Geng, Bo Cui*, Chao Yuan, Li Guo, Meng Zhao, Feixue Zou, Pengfei Liu and Hongxia Zhang

State Key Laboratory of Biobased Material and Green Papermaking, Department of Food Science and Engineering, Qilu University of Technology (Shandong Academy of Sciences), Jinan, Shandong, China

The present study aimed to investigate the effects of octenyl succinic anhydride modified starch (OSAS) on soy protein (SP)-(-)-epigallocatechin-3-gallate (EGCG) binary covalently linked complexes. Mean diameters of OSAS-SP-EGCG complexes decreased from 379.6 ± 54.9 nm to 272.7 ± 47.7 nm as the OSAS-to-SP-EGCG ratio changed from 1:2 to 4:1, while ζ-potential decreased from -19.1 ± 0.8 mV to -13.7 ± 1.2 mV. Fourier transform infrared spectroscopy results revealed that the characteristic peaks at 1725 cm^{-1} and 1569 cm^{-1} for OSAS disappeared in the OSAS-SP-EGCG complexes, indicating an interaction between OSAS and SP-EGCG complexes. X-ray diffraction analysis showed that with the increase of OSAS content, the diffraction peak at approximately 8.0° decreased from 8.22° to 7.74°, implying that the structures of OSAS and SP-EGCG complexes were rearranged after forming into OSAS-SP-EGCG complexes. The contact angle of the OSAS-SP-EGCG complexes significantly increased from 59.1° to 72.1° with the addition of OSAS increased, revealing that the addition of OSAS improved hydrophobicity of the SP-EGCG complexes. Transmission electron microscopy images revealed that the individual OSAS-SP-EGCG complexes became smaller but stuck together to form large fragments, which was different from the morphology of OSAS and SP-EGCG complexes. Thus, the OSAS-SP-EGCG complexes developed in this study may be effective emulsifiers for improving the stability of emulsion systems in the food industry.

KEYWORDS

octenyl succinic anhydride-modified starch, EGCG (—)-epigallocatechin-3-gallate, complexes, structure, soy proteins

1. Introduction

Proteins and polyphenols are widely found in various foods, playing important roles in food production and nutritional value (1). In food systems, the interactions between proteins and polyphenols during storage and processing cannot be avoided. Currently, protein-polyphenol complexes have received significant research interest. Proteins and polyphenols combine with phenolic hydroxyl groups and polar sites of the protein, such as hydrogen bonding and hydrophobic bonding, to form conjugates with specific functional properties (2, 3). In recent years, protein-polyphenol complexes have attracted increasing attention (4–6).

Soy protein (SP) is one of the most naturally widely used vegetable proteins and contains essential amino acids similar to those found in animal proteins (7). (-)-Epigallocatechin-3-gallate (EGCG), the major catechin in green tea, has high antioxidant activity attributed to the active phenolic hydroxyl groups and has been endowed with numerous health benefits (8). SP and EGCG can form non-covalent-linked and covalent-linked complexes via different types of interactions (9). In recent years, SP-EGCG complexes have been investigated in many studies, including their formation (9), functional properties (10, 11), antioxidant properties (12), and their use in emulsion stability and nutrient delivery (13, 14). However, it is difficult for SP-EGCG complexes to meet the different requirements of food systems. Thus, other food ingredients should be used to broaden the use of SP-EGCG complexes in the food industry. As reported previously, the addition of polysaccharides can influence the formation of SP-EGCG complexes and improve their physical and functional properties (12, 15).

Octenyl succinic anhydride-modified starch (OSAS) is produced using an esterification reaction between –OH groups on starch and the OSA reagent. OSAS has amphiphilic properties because it consists of a hydrophilic starch backbone with attached hydrophobic octenyl groups (16). The hydrophobic octenyl group impart an emulsifying capability to OSAS (17). Previous studies have shown that OSAS can be used as a food ingredient or emulsifier in food systems (18), as the OSAS molecule can form a thick coating around the oil droplets to increases the steric repulsion between the droplets (19). However, to our knowledge, there are no reports on the use of OSAS to improve the properties of SP-EGCG complexes.

The present study investigated the effects of OSAS on SP-EGCG complexes. The formation and structural properties of the OSAS-SP-EGCG complexes were characterized by mean diameter and ζ-potential measurements, Fourier transform infrared spectroscopy (FTIR), X-ray diffraction (XRD), contact angle analysis, and transmission electron microscopy (TEM). The results found here will help better understand the formation of OSAS-SP-EGCG complexes and aid in the design of new food materials for nutraceutical and biomaterial applications.

2. Materials and methods

2.1. Materials

SP were prepared as previously reported (20). The dried SP powder had 92.8% protein content, as determined by rapid N exceed (Elementar, Langenselbold, Germany), with a nitrogen conversion factor of 6.25. OSAS (CAS#66829-29-6) was purchased from Shanghai Yuanye Bio-Technology Co., Ltd. EGCG (purity ≥ 98%) was purchased from Shanghai Macklin Biochemical Co., Ltd. All chemicals used were of analytical grade and used without further purification. Distilled water from a Lichun water purification system (Lichun, Jinan, China) was used in all the experiments.

2.2. Preparation of SP-EGCG covalently linked complexes

SP-EGCG complexes formed by covalent interactions were prepared according to the procedures described by Ju et al. (21) with

some modifications. Briefly, 2.0 g SP was dissolved in 100 mL of distilled water at 25°C, and the pH of the dispersion was adjusted to 9.0 using 0.5 mol/L NaOH. SP-EGCG complexes were formed by mixing the SP solution with an EGCG concentration of 0.2% (w/v) for 12 h at 25°C. Dialysis was performed for 24 h using distilled water to remove free EGCG from the protein dispersion. Then, the pH of the dispersion was adjusted to 7.4 to stop the reaction. The dialysate was freeze-dried for further use.

2.3. Preparation of OSAS-SP-EGCG complexes

Octenyl succinic anhydride-modified starch dispersions (2%, w/v) were prepared by dispersing OSAS powder in distilled water, followed by gelatinization in a water bath at 95°C for 30 min to obtain a homogeneous solution. Fresh starch solution was prepared for each experiment.

Covalently linked SP-EGCG complexes were dispersed in distilled water at a concentration of 2% (w/v). The SP-EGCG complex dispersion was then mixed with OSA-modified starch dispersions (2%) in ratios of 1:4, 1:2, 1:1, and 2:1 (w/w). Each sample was adjusted to pH 7.0 and then freeze-dried. The resultant powders were incubated at 60°C and 79% relative humidity (RH) in the presence of saturated KBr solution for 24 h (22). The samples were pre-frozen and freeze-dried for further use.

2.4. Mean particle diameter and surface potential analysis

The mean particle diameter and surface potential of the OSAS-SP-EGCG complexes and covalently linked SP-EGCG complexes were measured at 25°C using dynamic light scattering and electrophoresis (Nano ZS, Malvern Instruments, Worcestershire, UK). Suspensions of the OSAS-SP-EGCG complexes were diluted 10-fold using a buffer solution to obtain an appropriate light intensity for reliable measurements. The mean and standard deviation were calculated from measurements of at least three samples.

2.5. FTIR

Freeze-dried OSAS, SP-EGCG, and OSAS-SP-EGCG complexes were combined with KBr and ground to form a mixture, which was then molded into a disk and analyzed using an FTIR spectrometer (Nicolet iS10, Thermo-Fisher, Waltham, MA, USA) at 25°C. The scanning range was set to 400–4000 cm^{-1} with a resolution of 4 cm^{-1} and 64 scans (23).

2.6. XRD

XRD (Ultima IV, Rigaku, Japan) was performed to determine whether OSAS, SP-EGCG, and OSAS-SP-EGCG complexes had crystalline structures or were amorphous, using a method similar to that used by Niu et al. (24). Briefly, freeze-dried OSAS, SP-EGCG, and OSAS-SP-EGCG complexes were analyzed using Cu Kα radiation, a scan angle of 2θ, a range of 5–60°, a scan rate of 2°/min, and working conditions of 40 kV and 40 mA.

2.7. Contact angle measurement

The contact angles of the OSAS, SP-EGCG, and OSAS-SP-EGCG complexes were determined using an OCA 40 (Dataphysics Instruments GmbH, Stuttgart, Germany) following the method described by Dai et al. (25). First, the dried sample powders were pressed to obtain particle-based tablets (13 mm diameter and 2 mm thickness). A drop of pure water (5 μL) was then lightly dripped onto the surface of the tablets. After equilibrium was reached, the droplet was photographed, and the profile of the droplet was automatically fitted to the Laplace-Young equation using software to acquire the contact angle. Measurements were performed at least three times.

2.8. Transmission electron microscopy

The morphology of the OSAS-SP-EGCG complexes was determined by transmission electron microscopy (TEM). Briefly, the samples were diluted 10-fold using double-distilled water and then placed onto a copper mesh grid for 4 min. The sample was then stained using a 1% uranyl acetate solution (1 min) and washed with double-distilled water three times. The sample-loaded grid
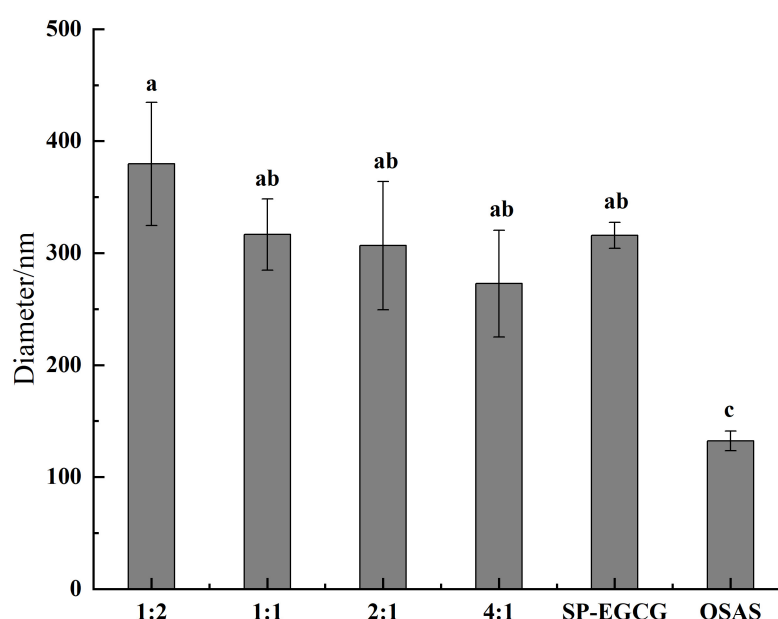

FIGURE 1
The average diameters for OSAS-SP-EGCG complexes, SP-EGCG complexes and OSAS.
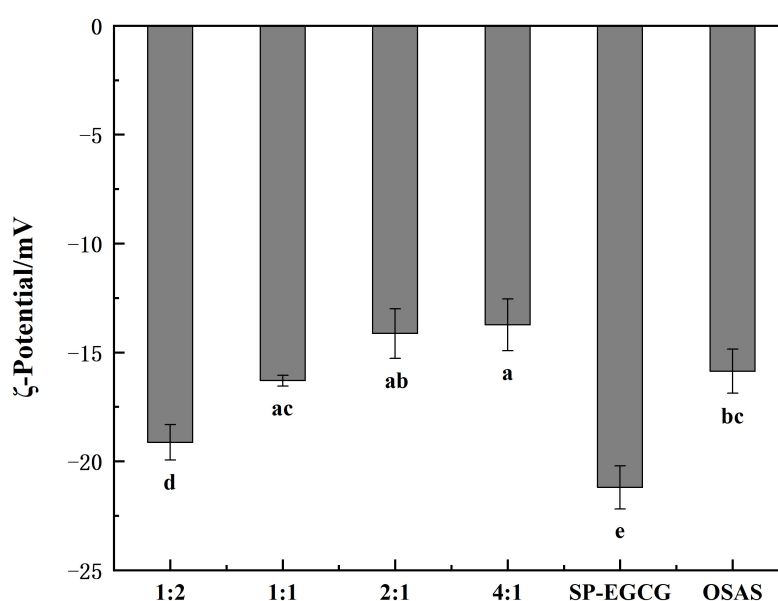

FIGURE 2
The ζ-potentials for OSAS-SP-EGCG complexes, SP-EGCG complexes and OSAS.

was air-dried at room temperature and imaged using a commercial TEM (JEM-2100F, JEOL, Ltd., Tokyo, Japan) operating at a voltage of 200 kV.

2.9. Statistical analysis

All measurements were performed in triplicate. Statistical significance ($p < 0.05$) was determined using SPSS statistical analysis program (SPSS Inc., Chicago, IL, USA). All data shown represent mean $\pm$ standard deviation (SD).

3. Results and discussion

3.1. Mean particle diameter and surface potential of OSAS-SP-EGCG complexes

The average sizes of the OSAS, SP-EGCG complexes, and OSAS-SP-EGCG complexes are shown in **Figure 1**. The OSAS and SP-EGCG complexes had an average particle size of 132.2 $\pm$ 8.8 nm and 315.8 $\pm$ 11.7 nm, respectively. Meanwhile, the average particle size noticeably changed to 379.6 $\pm$ 54.9 nm, 316.5 $\pm$ 31.8 nm,
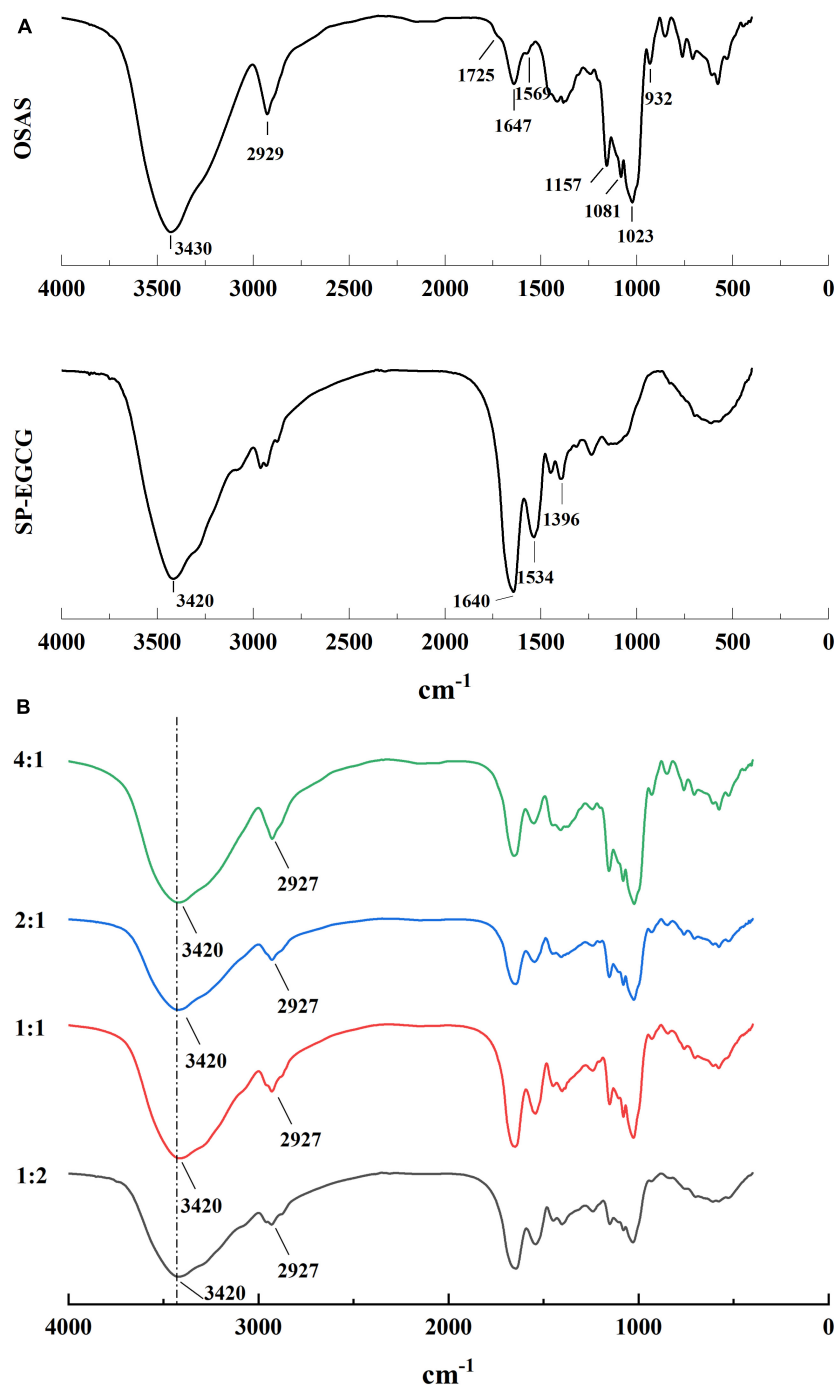

FIGURE 3
FTIR spectrum for OSAS, SP-EGCG complexes **(A)** and OSAS-SP-EGCG complexes **(B)**.

306.6 ± 57.2 nm and 272.7 ± 47.7 nm for OSAS-SP-EGCG complexes with mass ratios of OSAS to SP-EGCG at 1:2, 1:1, 2:1, and 4:1, respectively. With a lower addition of OSAS (i.e., the mass ratio of 1:2), the average size of the OSAS-SP-EGCG complexes increased significantly compared with that of the OSAS and SP-EGCG complexes. One speculative possibility is that SP-EGCG was excessive under these conditions. As a result, more SP-EGCG was bound to the surface of OSAS, resulting in micro-aggregation and the formation of large composites (26). It is also possible that the higher concentration of SP-EGCG resulted in a loose structure of the OSAS-SP-EGCG complexes, which may be due to the conformational changes induced by some other interactions between OSAS and SP-EGCG. By continuously increasing the concentration of OSAS (i.e., the OSAS-to-SP-EGCG mass ratio from 1:1 to 4:1), the average particle size significantly decreased ($p < 0.05$). This may be explained by the possibility that a relatively compact structure between OSAS

and SP-EGCG was formed with sufficient OSAS content under these conditions.

Figure 2 shows the surface charge densities of the OSAS, SP-EGCG complexes, and OSAS-SP-EGCG complexes. The results showed that the ξ-potentials of all samples examined were negative. The ξ-potentials for OSAS and SP-EGCG complexes were -15.9 ± 1.0mV and -21.2 ± 1.0 mV, respectively. The result corresponded to those of Zhao et al. (15) and Liu et al. (27), which were −16.8 mV and −18.0 mV for OSAS and SP-EGCG complexes, respectively. The OSAS-SP-EGCG complexes showed lower absolute ζ-potential values than that of the SP-EGCG complexes. This may be because the added OSAS interacted with the SP-EGCG complexes, causing a reduction in the net charge on the surface of OSAS-SP-EGCG, resulting in a reduction in ξ-potentials. With the mass ratio of OSAS to SP-EGCG complexes from 1:2 to 4:1, the absolute values of ξ-potentials for OSAS-SP-EGCG complexes continued to decrease
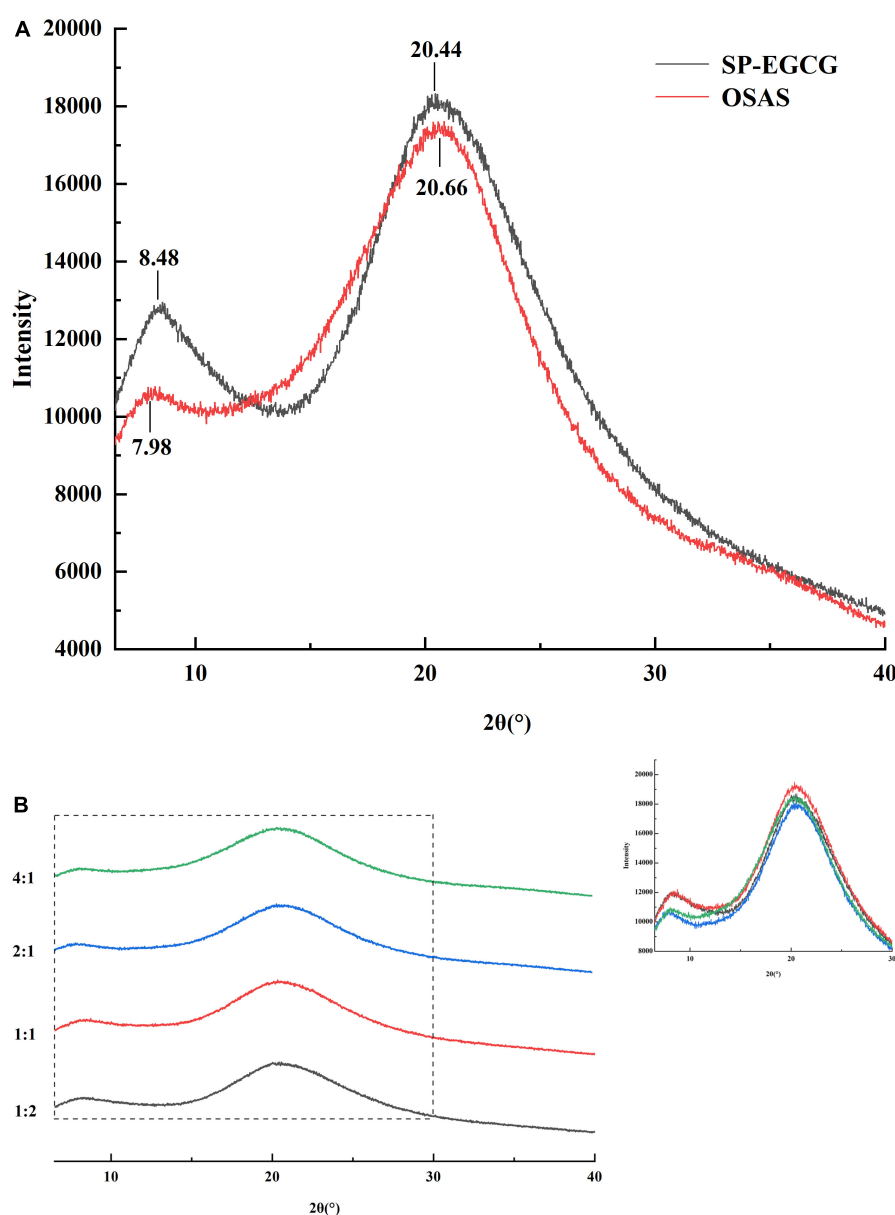

FIGURE 4
XRD spectrum for OSAS, SP-EGCG complexes (A) and OSAS-SP-EGCG complexes (B).

from -19.1 ± 0.8 mV to -13.7 ± 1.2 mV. This may be the reason for the interaction between the -COO$^-$ of OSAS and -NH$_3^+$ of SP-EGCG complexes. With the increase in OSAS content, more -NH$_3^+$ groups of SP-EGCG complexes reacted, resulting in a reduction in the absolute values of the ξ-potentials.

3.2. Structure of OSAS-SP-EGCG complexes revealed by FTIR analysis

The OSAS, SP-EGCG complexes, and OSAS-SP-EGCG complexes were freeze-dried, and the interaction between OSAS and SP-EGCG complexes was characterized by FTIR (**Figure 3**).

For both the OSAS and SP-EGCG complexes, there was a broad peak at approximately 3,400 cm^{-1}, which can be attributed to O–H stretching vibrations. For OSAS, characteristic peaks were also observed at 1,725 cm^{-1}, 1,569 cm^{-1}, 900–1,200 cm^{-1}, 2,929 cm^{-1}, and 1,647 cm^{-1}. The characteristic peak at 1,725 cm^{-1} was assigned to the C = O stretching vibration of the ester group, whereas the peak at 1,569 cm^{-1} was ascribed to the asymmetric stretching vibration of the carboxyl group (28, 29). The peaks at 900–1,200 cm^{-1} were characteristic of polysaccharide functional groups (27). The peak at 2,929 cm^{-1} was attributed to the C-H stretching vibration of the glucose unit (30). The peak at 1,647 cm^{-1} can be attributed to the bending vibration of water, presumably because some water molecules are associated with powdered starch (31). The FTIR spectrum of the SP-EGCG complexes showed absorption bands related to C = O stretching at 1,640 cm^{-1} (free carboxyl groups) and N–H bending at 1,534 cm^{-1} (amide II) (**Figure 3A**). These two peaks are primary characteristic peaks for SP, as reported by Chen et al. (32). The absorption band at 1396 cm^{-1} is attributed to C–N stretching and N–H bending (amide III) vibrations (33).
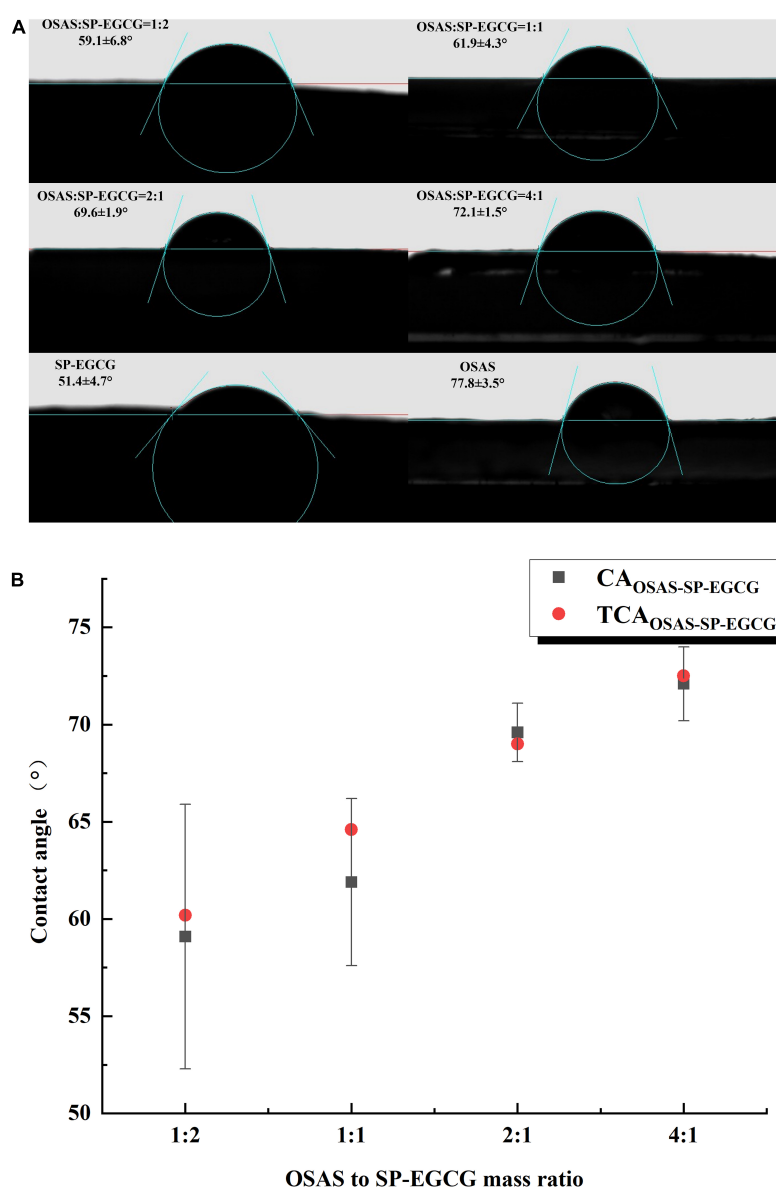

FIGURE 5
Contact angle for OSAS, SP-EGCG, and OSAS-SP-EGCG complexes **(A)** and the relationship between the measured and theoretical contact angle values for OSAS-SP-EGCG complexes **(B)**.

In the mixed OSAS-SP-EGCG systems, the broad peak at 3,420 cm^{-1} did not move toward lower wavenumbers (i.e., no red-shift) compared to the OSAS and SP-EGCG complexes. These results suggest that hydrogen bonding may not have occurred between the OSAS molecule and SP-EGCG complexes. It can also be seen from **Figure 3B** that the characteristic peaks at 1,725 cm^{-1} and 1,569 cm^{-1} for OSAS disappeared in the OSAS-SP-EGCG complexes, indicating an interaction between OSAS and SP-EGCG complexes. Meanwhile, as the OSAS-to-SP-EGCG ratio increased from 1:2 to 4:1, the peak at approximately 2,927 cm^{-1} became increasingly obvious, indicating an increase in the OSAS content of the OSAS-SP-EGCG complexes.

3.3. XRD analysis of OSA-SP-EGCG complexes

XRD data can provide direct structural information for the determination of amorphous or crystalline molecular characteristics. Thus, X-ray scattering techniques are commonly used to determine the crystal structures of starches, proteins, and other macromolecular biopolymers. The main diffraction peaks of SP-EGCG complexes were located at 8.48° and 20.44° in the 2θ region, which belonged to the α-helix and β-sheet molecular structures of soy proteins,

respectively (34, 35). This result agrees with the results reported by Tong et al. (6). For OSAS, the main diffraction peaks are located at 7.98° and 20.66° in the 2θ region. Previous studies found a characteristic peak at approximately 20° for V-type crystalline starch (36). As reported previously, the main diffraction peaks of OSA-modified starch are located at approximately 15°, 17°, 18°, and 23° in the 2θ region (37, 38). These differences may be due to gelatinization, after which the crystalline structures disappeared in OSAS (**Figure 4A**), and only two broad amorphous peaks appeared in the XRD spectra.

The OSAS-SP-EGCG complex also exhibited two peaks at approximately 8.0° and 20.5° (**Figure 4B**). The diffraction peak at approximately 8.0° decreased from 8.22° to 7.74° as the OSAS to SP-EGCG mixing ratio increased from 1:2 to 4:1, implying a rearrangement of the structures of the OSAS and SP-EGCG complexes after the formation of the OSAS-SP-EGCG complexes.

3.4. Contact angle measurement of OSAS-SP-EGCG complexes

Water contact angle measurements enable qualitative estimation of the changes in the hydrophobicity of the samples. The
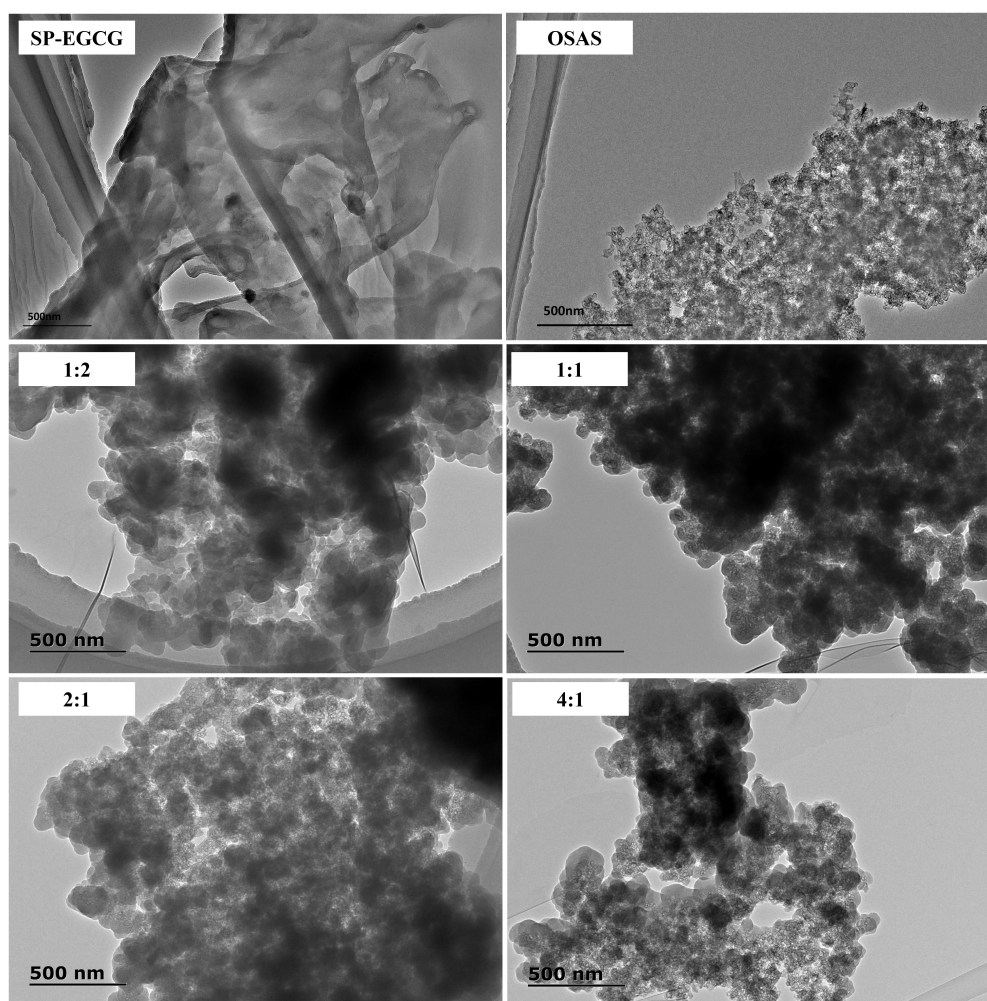

FIGURE 6
TEM images for OSAS, SP-EGCG complexes and OSAS-SP-EGCG complexes.

water contact angle values of the OSAS, SP-EGCG complexes, and OSAS-SP-EGCG complexes are shown in **Figure 5**. As illustrated in **Figure 5A**, the contact angle of SP-EGCG complexes was 51.4 ± 4.7°, suggesting that SP-EGCG complexes were predominantly hydrophilic. The contact angle of OSAS was 77.8 ± 3.5°, indicating higher hydrophobicity. As reported previously (39), the contact angle for OSAS is related to the degree of substitution (DS) of OSA and the starch source. After the addition of OSAS, the contact angle of the OSAS-SP-EGCG complexes significantly increased from 59.1° to 72.1° as the OSAS-to-SP-EGCG mixing ratio increased from 1:2 to 4:1. The results revealed that the hydrophobicity of SP-EGCG complexes was improved by the addition of OSAS, which was beneficial for the adsorption of OSAS-SP-EGCG complexes at the oil-water interface, thereby serving as a good emulsion stabilizer.

Furthermore, the regularity of the increase in the contact angle seemed to follow the OSAS-to-SP-EGCG complex mixing ratio. To determine whether the change in contact angle could be related to the mixing ratio of OSAS to SP-EGCG complex, the theoretical contact angle value was defined as follows:

$$TCA_{OSAS-SP-EGCG}$$
$$= CA_{SP-EGCG} \times R_{SP-EGCG} + CA_{OSAS} \times R_{OSAS}$$

where $CA_{SP-EGCG}$ and CA_{OSAS} are the contact angles for SP-EGCG complexes and OSAS, respectively. $R_{SP-EGCG}$ and R_{OSAS} are the ratio of SP-EGCG complexes and OSAS in the mixtures, respectively. As shown in **Figure 5B**, $TCA_{OSAS-SP-EGCG}$ for mixtures with different OSAS to SP-EGCG complex mixing ratios were in good agreement with the corresponding measured contact angles for the OSAS-SP-EGCG complexes. This indicated that the addition of OSAS greatly influenced the hydrophobicity of the SP-EGCG complexes. However, we could speculate that the actual ratio of OSAS to SP-EGCG complexes was approximately equal to the mixing ratio of OSAS to SP-EGCG complexes.

3.5. Morphology of the OSAS-SP-EGCG complexes

TEM was used to confirm the formation of OSAS-SP-EGCG complexes. **Figure 6** shows the TEM images of the OSAS, SP-EGCG complexes, and OSAS-SP-EGCG complexes.

It could be seen from **Figure 6** that the freeze-dried SP-EGCG complexes were distinct flaky particles with relatively larger fragments. The gelatinized OSAS were relatively smaller, and seemed to be stuck together with unsmooth surfaces. The morphologies of OSAS-SP-EGCG complexes with different OSAS to SP-EGCG mass ratios were all different from the morphology of SP-EGCG complexes. As shown in **Figure 6**, all the OSAS-SP-EGCG complexes were spherical with smooth surface and stuck together. This may be caused by interactions between OSAS and SP-EGCG to form tertiary complexes. With the increase in OSAS to SP-EGCG from 1:2 to 4:1, it appeared that the individual OSAS-SP-EGCG complexes became smaller but stuck together to form large fragments. This result agreed with the results showing that the mean diameter decreased as the OSAS to SP-EGCG ratio increased from 1:2 to 4:1 (**Figure 1**). Microscopy images indicated that the addition of OSAS had obvious effects on the microstructure of the SP-EGCG complexes.

4. Conclusion

In the present study, the effects of OSAS on SP-EGCG binary covalently linked complexes were investigated using diameter analysis, ζ-potential measurement, FTIR and XRD analyses, contact angle measurement, and TEM analysis. These results indicated the formation of OSAS-SP-EGCG complexes. In particular, the contact angle of the OSAS-SP-EGCG complexes prominently increased from 59.1° to 72.1° as the OSAS-to-SP-EGCG mixing ratio increased from 1:2 to 4:1. This revealed that the hydrophobicity of SP-EGCG complexes was improved by the addition of OSAS, which was beneficial for the adsorption of OSAS-SP-EGCG complexes at the oil-water interface, thereby serving as a good emulsion stabilizer. Consequently, the OSAS-SP-EGCG complexes developed here may be effective emulsifiers for improving the physical and chemical stability of emulsion systems in the food industry. In future studies, the use of OSAS-SP-EGCG complexes to stabilize oil-water emulsions should be investigated.

Data availability statement

The raw data supporting the conclusions of this article will be made available by the authors, without undue reservation.

Author contributions

DD and BC contributed to conception and design of the study. DD and TG organized the database. TG, CY, and LG performed the statistical analysis. DD wrote the first draft of the manuscript. MZ, FZ, PL, and HZ directed writing the manuscript. All authors contributed to manuscript revision, read, and approved the submitted version.

Funding

Conflict of interest

The authors declare that the research was conducted in the absence of any commercial or financial relationships that could be construed as a potential conflict of interest.

Publisher's note

All claims expressed in this article are solely those of the authors and do not necessarily represent those of their affiliated organizations, or those of the publisher, the editors and the reviewers. Any product that may be evaluated in this article, or claim that may be made by its manufacturer, is not guaranteed or endorsed by the publisher.

References

1. Quan TH, Benjakul S, Sae-leaw T, Balange AK, Maqsood S. Protein-polyphenol conjugates: antioxidant property, functionalities and their applications. *Trends Food Sci Technol.* (2019) 91:507–17. doi: 10.1016/j.tifs.2019.07.049

2. Hasni I, Bourassa P, Hamdani S, Samson G, Carpentier R, Tajmir-Riahi H-A. Interaction of milk α-and β-caseins with tea polyphenols. *Food Chem.* (2011) 126:630–9. doi: 10.1016/j.foodchem.2010.11.087

3. Wang W, Sun C, Mao L, Ma P, Liu F, Yang J, et al. The biological activities, chemical stability, metabolism and delivery systems of quercetin: a review. *Trends Food Sci Technol.* (2016) 56:21–38. doi: 10.1016/j.tifs.2016.07.004

4. Dumitrascu L, Stănciuc N, Grigore-Gurgu L, Aprodu I. Investigation on the interaction of heated soy proteins with anthocyanins from cornelian cherry fruits. *Spectrochim Acta A Mol Biomol Spectrosc.* (2020) 231:118114. doi: 10.1016/j.saa.2020.118114

5. Guo Y, Bao Y, Sun K, Chang C, Liu W. Effects of covalent interactions and gel characteristics on soy protein-tannic acid conjugates prepared under alkaline conditions. *Food Hydrocoll.* (2021) 112:106393. doi: 10.1016/j.foodhyd.2020.106293

6. Tong X, Cao J, Tian T, Lyu B, Miao L, Lian Z, et al. Changes in structure, rheological property and antioxidant activity of soy protein isolate fibrils by ultrasound pretreatment and EGCG. *Food Hydrocoll.* (2022) 122:107084. doi: 10.1016/j.foodhyd.2021.107084

7. Koshy RR, Mary SK, Thomas S, Pothan LA. Environment friendly green composites based on soy protein isolate-A review. *Food Hydrocoll.* (2015) 50:174–92.

8. Dai W, Ruan C, Zhang Y, Wang J, Liang J. Bioavailability enhancement of egcg by structural modification and nano-delivery: a review. *J Funct Foods.* (2020) 65:103732.

9. Zhou SD, Lin YF, Xu X, Meng L, Dong MS. Effect of non-covalent and covalent complexation of (-)-epigallocatechin gallate with soybean protein isolate on protein structure and in vitro digestion characteristics. *Food Chem.* (2020) 309:125718. doi: 10.1016/j.foodchem.2019.125718

10. Ge G, Guo W, Zheng J, Zhao M, Sun W. Effect of interaction between tea polyphenols with soymilk protein on inactivation of soybean trypsin inhibitor. *Food Hydrocoll.* (2021) 111:106177. doi: 10.1016/j.foodhyd.2020.106177

11. Xu J, Guo S, Li X, Jiang S, Zhong X, Zheng Z. Gel properties of transglutaminase-induced soy protein isolate–polyphenol complex: influence of epigallocatechin-3-gallate. *J Sci Food Agric.* (2021) 101:3870–9. doi: 10.1002/jsfa.11025

12. Yan S, Xie F, Zhang S, Jiang L, Qi B, Li Y. Effects of soybean protein isolate - polyphenol conjugate formation on the protein structure and emulsifying properties: protein - polyphenol emulsification performance in the presence of chitosan. *Colloids Surf A Phys Eng Asp.* (2021) 609:125641. doi: 10.1016/j.colsurfa.2020.125641

13. Djuardi AUP, Yuliana ND, Ogawa M, Akazawa T, Suhartono MT. Emulsifying properties and antioxidant activity of soy protein isolate conjugated with tea polyphenol extracts. *J Food Sci Technol.* (2020) 57:3591–600.

14. Shi A, Feng X, Wang Q, Adhikari B. Pickering and high internal phase Pickering emulsions stabilized by protein-based particles: a review of synthesis, application and prospective. *Food Hydrocoll.* (2020) 109:106117. doi: 10.1016/j.foodhyd.2020.106117

15. Zhao Y, Wang X, Li D, Tang H, Yu D, Wang L, et al. Effect of anionic polysaccharides on conformational changes and antioxidant properties of protein-polyphenol binary covalently-linked complexes. *Process Biochem.* (2020) 89:89–97. doi: 10.1016/j.procbio.2019.10.021

16. Tizzotti MJ, Sweedman MC, Schafer C, Gilbert RG. The influence of macromolecular architecture on the critical aggregation concentration of large amphiphilic starch derivatives. *Food Hydrocoll.* (2013) 31:365–74. doi: 10.1016/j.foodhyd.2012.11.023

17. Torres O, Tena NM, Murray B, Sarkar A. Novel starch based emulsion gels and emulsion microgel particles: design, structure and rheology. *Carbohydr Polym.* (2017) 178:86–94. doi: 10.1016/j.carbpol.2017.09.027

18. Tesch S, Gerhards C, Schubert H. Stabilization of emulsions by OSA starches. *J Food Eng.* (2002) 54:167–74. doi: 10.1016/S0260-8774(01)00206-0

19. Liu W, Li Y, Chen M, Xu F, Zhong F. Stabilizing oil-in-water emulsion with amorphous and granular octenyl succinic anhydride modified starches. *J Agric Food Chem.* (2018) 66:9301–8. doi: 10.1021/acs.jafc.8b02733

20. Dong D, Hua Y, Chen Y, Kong X, Zhang C, Wang Q. Charge compensation, phase diagram, and protein aggregation in soy protein-gum Arabic complex formation. *J Agric Food Chem.* (2013) 61:3934–40. doi: 10.1021/jf400305z

21. Ju M, Zhu G, Huang G, Shen X, Zhang Y, Jiang L, et al. A novel pickering emulsion produced using soy protein-anthocyanin complex nanoparticles. *Food Hydrocoll.* (2020) 99:105329. doi: 10.1016/j.foodhyd.2019.105329

22. Liu F, Ma C, McClements DJ, Gao Y. Development of polyphenol-protein-polysaccharide ternary complexes as emulsifiers for nutraceutical emulsions: impact on formation, stability, and bioaccessibility of β-carotene emulsions. *Food Hydrocoll.* (2016) 61:578–88. doi: 10.1016/j.foodhyd.2016.05.031

23. Dong D, Cui B. Fabrication, characterization and emulsifying properties of potato starch/soy protein complexes in acidic conditions. *Food Hydrocoll.* (2021) 115:106600. doi: 10.1016/j.foodhyd.2021.106600

24. Niu F, Kou M, Fan J, Pan W, Feng ZJ, Su Y, et al. Structural characteristics and rheological properties of ovalbumin-gum Arabic complex coacervates. *Food Chem.* (2018) 260:1–6. doi: 10.1016/j.foodchem.2018.03.141

25. Dai L, Sun C, Wei Y, Mao L, Gao Y. Characterization of Pickering emulsion gels stabilized by zein/gum arabic complex colloidal nanoparticles. *Food Hydrocoll.* (2018) 74:239–48. doi: 10.1016/j.foodhyd.2017.07.040

26. Le BC, Renard CM. Interactions between polyphenols and macromolecules: quantification methods and mechanisms. *Crit Rev Food Sci Nutr.* (2012) 52:213–48. doi: 10.1080/10408398.2010.499808

27. Liu Y, Yan C, Chen J, Wang Y, Liang R, Zou L, et al. Enhancement of beta-carotene stability by encapsulation in high internal phase emulsions stabilized by modified starch and tannic acid. *Food Hydrocoll.* (2020) 109:106083. doi: 10.1016/j.foodhyd.2020.106083

28. Thygesen LG, Løkke MM, Micklander E, Engelsen SB. Vibrational microspectroscopy of food. Raman vs. FT-IR. *Trends Food Sci Technol.* (2003) 14:50–7. doi: 10.1016/S0924-2244(02)00243-1

29. Nagaoka S, Tobata H, Takiguchi Y, Satoh T, Sakurai T, Takafuji M, et al. Characterization of cellulose microbeads prepared by a viscose-phase-separation method and their chemical modification with acid anhydride. *J Appl Polym Sci.* (2005) 97:149–57. doi: 10.1002/app.21539

30. Lin Q, Liang R, Zhong F, Ye AM, Hemar Y, Yang Z, et al. Selfassembled micelles based on OSA-modified starches for enhancing solubility of β-carotene: effect of starch macromolecular architecture. *J Agric Food Chem.* (2019) 67: 6614–24.

31. He H, Hong Y, Gu Z, Liu G, Cheng L, Li Z. Improved stability and controlled release of CLA with spray-dried microcapsules of OSA-modified starch and xanthan gum. *Carbohydr Polym.* (2016) 147:243–50. doi: 10.1016/j.carbpol.2016.03.078

32. Chen F, Ou S, Tang C. Core-shell soy protein-soy polysaccharide complex (nano)particles as carriers for improved stability and sustained release of curcumin. *J Agric Food Chem.* (2016) 64:5053–9. doi: 10.1021/acs.jafc.6b01176

33. Muhoza B, Xia SQ, Zhang XM. Gelatin and high methyl pectin coacervates crosslinked with tannic acid: the characterization, rheological properties, and application for peppermint oil microencapsulation. *Food Hydrocoll.* (2019) 97:105174. doi: 10.1016/j.foodhyd.2019.105174

34. Gu W, Liu X, Ye Q, Gao Q, Shi SQ. Bio-inspired co-deposition strategy of aramid fibers to improve performance of soy protein isolate-based adhesive. *Ind Crops Prod.* (2020) 150:112424. doi: 10.1016/j.indcrop.2020.112424

35. Li H, Li C, Gao Q, Zhang S, Li J. Properties of soybean-flour-based adhesives enhanced by attapulgite and glycerol polyglycidyl ether. *Ind Crops Prod.* (2014) 59:35–40. doi: 10.1016/j.indcrop.2014.04.041

36. Deng N, Deng Z, Tang C, Liu C, Luo S, Chen T, et al. Formation, structure and properties of the starch-polyphenol inclusion complex: a review. *Trends Food Sci Technol.* (2021) 112:667–75. doi: 10.1016/j.tifs.2021.04.032

37. Wang W, Liu C, Zhang H, Zhu X, Wang L, Zhang N, et al. Properties of OSA-modified starch and emulsion prepared with different materials: glutinous rice starch, japonica rice starch, and Indica rice starch. *Food Res Int.* (2022) 161:111845. doi: 10.1016/j.foodres.2022.111845

38. Guo J, Tang W, Lu S, Fang Z, Tu K, Zheng M. Solubility improvement of hesperetin by using different octenyl succinic anhydride modified starches. *LWT Food Sci Technol.* (2018) 95:255–61. doi: 10.1016/j.lwt.2018.04.056

39. Zhu J, Li L, Chen L, Li X. Nano-structure of octenyl succinic anhydride modified starch micelle. *Food Hydrocoll.* (2013) 32:1–8.

Improvement of functional characteristics of *Hypophthalmichthys molitrix* protein by modification with chitosan oligosaccharide

Haihua Cong[1]*[†], Qiming Wu[2†], Zhuoran Zhang[1] and Juntao Kan[2]*

[1]School of Food and Drug, Shanghai Zhongqiao University of Vocational Technology, Shanghai, China,
[2]Nutrilite Health Institute, Shanghai, China

In the food processing field, it is very often that fish proteins are denatured affecting the nutritional value of the product which is vital to be solved. By using appropriate sugar donors for glycosylation with protein, improving the stability and emulsification properties of fish proteins can be achieved. This research looks into the impacts of enzymatic chitosan oligosaccharide (CO) at various concentration (0.15%, 0.30%, 0.45%, 0.60%, w/v) upon the molecular makeup and function of silver carp myofibrillar protein (MP) in an attempt to comprehend the impact of electrostatic binding among MP as well as CO on protein conformation. Analysis was done on the impact of various CO concentrations upon MP's secondary structure, conformational changes, and functional characteristics. Twelve sodium dodecyl sulfate polyacrylamide gel electrophoresis (SDS-PAGE) assays were implemented to monitor MP; Fourier transform infrared spectroscopy, endogenous fluorescence spectroscopy, and UV absorption spectra were carried out to investigate the influence of CO on MP; Particle size distribution, emulsifying activity index (EAI), solubility, turbidity, sulfhydryl content, carbonyl content, foaming capacity, surface hydrophobicity, emulsifying stability index (ESI), and foam persistence were all investigated. In addition, we used dynamic light scattering, scanning electron microscope, and atomic force microscope to analyze myosin (MO) and 0.60% CO-MO complex. The results demonstrated that CO and MP form complexes through hydrogen bonding and electrostatic interactions. CO modification not only delayed the oxidation of MP but also promoted MP to show better solubility, foaming, and foaming stability. In addition, CO modified myosin particle size decreased, reducing myosin's roughness and making myosin's structure more compact. To sum up, molecular interaction could change functional characteristics, and products with special properties could be developed after modification with chitosan oligosaccharide.

KEYWORDS

chitosan oligosaccharide, myofibrillar protein, myosin, functional, silver carp

1. Introduction

Fish protein is one of the important protein sources in the diet and is abundant in amino acids. The principle element from fish protein contain myofibrillar proteins (MP), which have great functional qualities like that of the ability to create gels and retain water (1). However, throughout preparation, treatment, and preservation, certain chemical qualities and low thermal

stability of fish myofibrillar proteins result in decreased MP solubility and emulsifying properties. To enhance fish protein's functional characteristics and yield better food, it is therefore crucial to prevent or minimize denaturation during both food preservation and preparation (2). The most recent techniques for strengthening the functional characteristics of proteins include: enzymatic modification; chemical techniques like the use of sodium alginate (SA) and L-histidine, acid, small-molecule compounds or proteases; and physical techniques like high-intensity ultrasound (HIU), high pressure processing (HPP), high pressure homogenization (HPH), superfine grinding (SG), washing, and dilution (1).

It is feasible to add new activities to fish proteins and enhance their essential features through glycosylation (3). The emulsifying characteristics and dietary proteins' thermal stableness could be gotten better through glycosylation as well as alginic acid oligosaccharide or glucan, for example, which also increased the solubility for carp MP when joined in ribose (4). Glycosylation is its bond attachment of carbohydrates to amino groups that are accessible in proteins, and it is used in the Amadori rearrangement step of the Maillard process to produce new glycoproteins. In contrast to different types of alteration, the glycosylation reaction takes place in fairly secure conditions. Because glycosylation process does not require extra compounds, it is preferable to use it in manufacturing of food and beverages (5).

The selection of the proper glycosyl donor to engage with the protein is a crucial stage in the glycosylation process. Studies have shown that the solubility of MP is significantly improved by glycosylation, such as ribose or glucose. The protein's thermal stability and emulsifying properties were greatly improved when dextran was used as the sugar donor. Choosing small molecule sugar donors with the appropriate molecular mass, polymerization level, and structural characteristics is considered important (4). Chitosan oligosaccharide (CO) is manufactured by depolymerization of chitosan (e.g., acid hydrolysis, redox hydrolysis, enzymolysis, or high-energy cleavage). CO promoted the water solubility of protein and decreased the solution viscosity of protein. CO modified by the Maillard reaction has a variety of biological and pharmaceutical applications. CO and β-lactoglobulin can effectively enhance the antioxidant activity of the complex. Whey protein isolate's solubility, thermal conductivity, and emulsification qualities were all increased by CO, and tropomyosin's allergenicity was diminished (6–8).

Currently, many reports have focused on the fundamental research and applications of using the electrostatic interactions among polysaccharides and proteins from numerous sources to enable the building into complex condensates at different scales (9). However, the strength of the interface performance of protein polysaccharide complex condensate depends not only on the scale effect and physicochemical properties of the complex but also on the degree of conformational transformation of protein in the process of electrostatic binding (4, 10–12). Consequently, the crucial thing turns out to be to look into the effect of electrostatic binding with polysaccharides upon that configuration of protein molecules as well as to further understand the properties of interfaces and the process of complex condensates.

Whereas, the effect of electrostatic binding between MP and CO on protein conformation has not yet been revealed, which is vital in further to understand the mechanism of the MP/CO complex stabilizing the lotion and proposing relevant regulatory strategies (13, 14). Throughout this research, UV scanning spectroscopy, internal fluorescence spectroscopy, as well as Fourier transform infrared spectroscopy were performed to look into potential effects of oligosaccharides on myofibrillar proteins. Moreover, 12 sodium dodecyl sulfate polyacrylamide gel electrophoresis (SDS-PAGE), sulfhydryl content, carbonyl content, surface hydrophobicity, solubility, turbidity, foaming capacity, foam stability, emulsifying activity index (EAI), emulsion stability index (ESI) and arrangement of particle sizes had been undertaken, and such impact of distinct densities of chitosan oligosaccharide on the secondary structure, conformational changes, and function of myofibrillar protein were also analyzed. In addition, we also analyze the effect of 0.60% chitosan oligosaccharide on myosin by using dynamic light scattering, atomic force microscope, and scanning electron microscopy (Figure 1). This study can further analyze the interface mechanism of CO-MP complexes, and offer fresh perspectives for enhancing proteins' functional characteristics after electrostatic binding to functional oligosaccharides with proteins in the process of glycosylation, which is convenient for future researchers to conduct further exploration in this field.
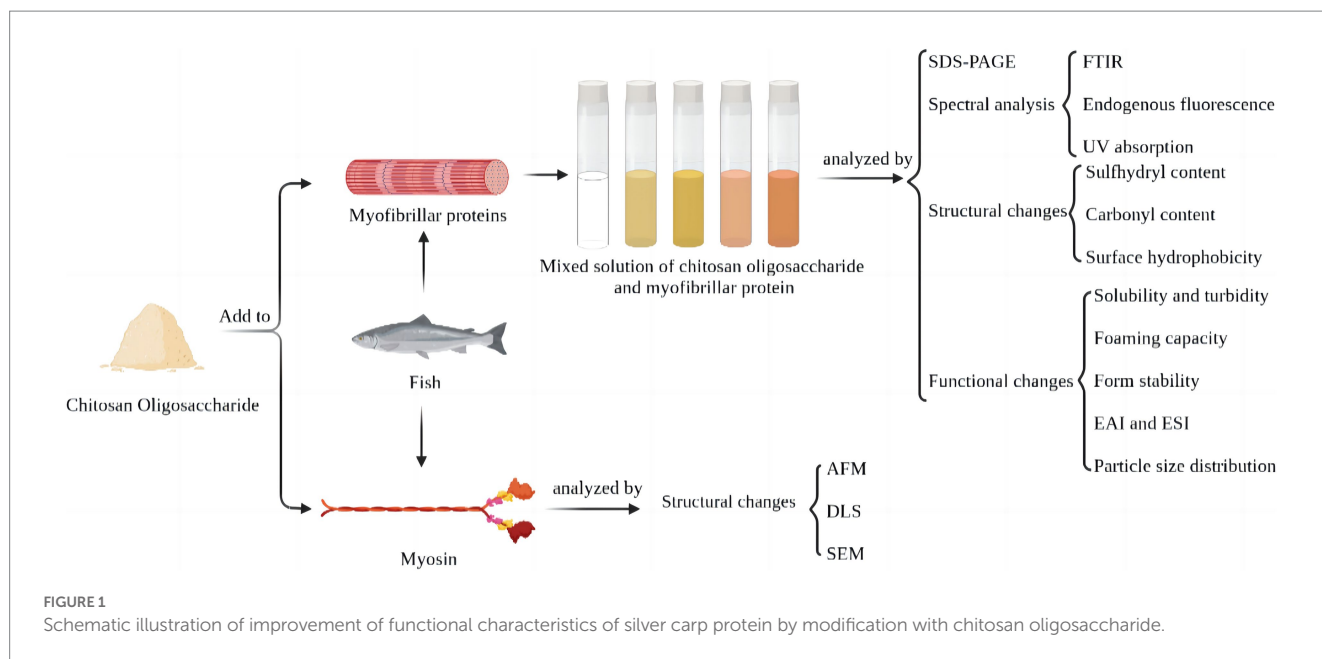
2. Materials and methods

2.1. Materials and reagents

Enzymatic chitosan oligosaccharide was given access through the Institute of process engineering, Chinese Academy of Sciences; the fresh silver carp was purchased from the Dalian food and cooked food trading center and transported to the laboratory within 40 min. After slaughter, the head and viscera were removed and washed for standby.

Sodium dodecyl sulfate (SDS) was provided by Tianjin Damao Chemical Reagent Factory (Tianjin, China); DTNB, DNPH, TCA and ANS were provided by Shanghai Macklin Biochemical Co., Ltd. (Shanghai, China); EDTA was provided by Tianjin Zhiyuan Chemical Reagent Co., Ltd. (Tianjin, China); β-mercaptoethanol was provided by Shanghai Yaji Biotechnology Co., Ltd. (Shanghai, China). Potassium bromid was spectrally pure, all other chemicals were analytical grade and provided by Sigma-Aldrich (St. Louis, MO, USA) Sigma-Aldrich (St. Louis, MO, USA) or Sinopharm Chemical Reagent Co., Ltd. (Shanghai, China).

2.2. Instruments and equipment

DS-1 high speed tissue crusher, Shanghai specimen model factory; HR/T 20 mm vertical high-speed freezing centrifuge, Hunan Hexi Instrument Equipment Co., Ltd.; Synergy h1 / h1m microplate reader, American Berton Instrument Co., Ltd.; F-2700 fluorescence spectrophotometer, Hitachi, Japan; Nexus670 infrared spectrometer, PerkinElmer, USA; UV-9000 double beam UV–Vis spectrophotometer, Shanghai yuanxi Instrument Co., Ltd.; Scientz-30D vacuum freeze dryer, Ningbo Scientz Biotechnology Co., Ltd., China; HH-6 Digital display thermostatic water bath, Guohua Electric Appliances Co., Ltd., China; FJ300-SH Digital display high-speed dispersion homogenizer, Shanghai Biaoben Mould Factory, China; Tescan Vega3 Scanning Electron Microscope, Hitachi Ltd., Japan; Mastersizer 2000 Particle size analyzer, Malvern Instruments UK Co., Ltd., UK; Atomic force microscopy, Bruker Co., Ltd., German.

FIGURE 1
Schematic illustration of improvement of functional characteristics of silver carp protein by modification with chitosan oligosaccharide.

2.3. Methods

2.3.1. Extraction of myofibrillar protein

Remove silver carp's back tenderloin by hand, cut it into minced meat, add 5 times the volume of $10\,mmol\,L^{-1}$ Tris–HCl (pH 7.2) buffer, homogenize it at $4{,}000\,r\,min^{-1}$ for 2 min, after that centrifuge it at $5{,}000\,r\,min^{-1}$ at 4°C until 15 min; Precipitate in 5 times volume of $10\,mmol\,L^{-1}$ Tris–HCl (containing $0.6\,mol\,L^{-1}$ NaCl, pH 7.2) buffer, homogenize at $4{,}000\,r\,min^{-1}$ for 30 s, centrifuge at $4{,}500\,r\,min^{-1}$ at 4°C for 20 min, after that take supernatant, which is myofibrillar protein. A biuret reagent has been utilized to measure the concentration (15).

2.3.2. Preparation of composite

The approach was founded on Yang et al. (16). Dilute the extracted myofibrillar protein with $10\,mmol\,L^{-1}$ Tris–HCl (containing $0.6\,mol\,L^{-1}$ NaCl, pH 7.2) buffer to 10 mg mL^{-1}, and put it into a centrifuge tube for standby. Add CO of different concentrations (0.00%, w/v, 0.15%, w/v, 0.30%, w/v, 0.45%, w/v, 0.60%, w/v), stand at 4°C, and measure after CO is fully swollen.

2.3.3. Sodium dodecyl sulfate polyacrylamide gel electrophoresis (SDS-PAGE)

The crosslinking of CO-MP was judged using a transitory buffered system SDS-PAGE that comprised 5% stacking as well as 12% detaching gels (17). The loading capacity of each lane is 10 μL. The gel was stained with 0.1% (w/v). Gels were stained for 1 h with 0.1% (w/v) Coomassie Brilliant Blue R-250 in an 80% methanol and 20% acetic acid solution, and then destained for 2 h in a solution of 50% methanol and 10% acetic acid. By contrasting the band with the standard protein solution, the relative molecular weight standard of the band was identified.

2.3.4. Fourier transform infrared spectroscopy

With a few change, the technique was altered according to Xu et al. (17) and Hu et al. (18). After freeze-drying, the dried sample powder was fully mixed with anhydrous potassium bromide in

1:50, pressurized for 2 min under the pressure of about 18 MPa, and the scanning range was $450 \sim 4{,}000\ cm^{-1}$. Based on second derivative spectrum, gauss peak fitting is adopted, the integral area is used to estimate the protein secondary structure %. $1{,}651 \sim 1{,}600\ cm^{-1}$ is considered as α-helix structure band, $1{,}600 \sim 1{,}639\ cm^{-1}$ is regarded as β-sheet band, $1{,}661 \sim 1{,}700\ cm^{-1}$ is considered as β-turn structure band, $1{,}640 \sim 1{,}650\ cm^{-1}$ is considered as random coil band (12).

2.3.5. Endogenous fluorescence spectrum

A fluorescence spectrophotometer was employed in order to analyze the solution's fluorescence spectrum. Proteins' fluorescence spectra of the were then examined at emission wavelengths of 300 to 450 nm and excitation wavelengths of 280 nm for different C3G concentration gradients. Measure the fluorescence intensity (19). Using stern Volmer equation:

$$\frac{F_0}{F} = 1 + K_{SV}\left[Q\right]$$

where: F_0 and F are the highest fluorescence intensity of oligosaccharide free and oligosaccharide protein solution respectively; [Q] is the concentration of oligosaccharide (mg mL^{-1}); K_{SV} is the quenching constant (20).

2.3.6. UV absorption spectrum

Dilute the myofibrillar protein sample to 1 mg mL^{-1}, take Tris–HCl (containing $0.6\,mol\,L^{-1}$ NaCl, pH 7.2) buffer as blank, and obtain the ultraviolet absorption spectrum in the range of $230 \sim 600$ nm. Use Originpro 2017 software to obtain the second derivative spectrum of UV absorption spectrum data (20).

2.3.7. Active sulfhydryl

The method of active sulfhydryl content was determined according to Yildiz et al. (21) and slightly modified. Dilute the sample protein concentration to 4 mg mL^{-1}: 0.5 mL of the sample and 4.5 mL

of the reaction buffer ($0.2\ mol\ L^{-1}$ Tris–HCl, $10\ mmol\ L^{-1}$ EDTA, pH 6.8) was mixed, add 0.5 mL of DTNB ($10\ mmol\ L^{-1}$) solution, react at 4°C for 1 h, and then measure the absorbance at 412 nm.

$$\text{Sulfhydryl concentration}\left(mol\ 10^{-5}\ g\right) = \frac{\left(A - A_0\right) \times D \times 10^5}{13600 \times C}$$

where: *A*: sample absorbance; *A*₀: absorbance of blank sample; *D*: Protein dilution ratio: Molar extinction coefficient 13,600 $(mol\ L^{-1})^{-1}\ cm^{-1}$; *C*: Protein concentration.

2.3.8. Carbonyl content

The method is slightly modified according to Bin Zhang et al. (22) research. The prepared myofibrillar protein sample was diluted to $2.0–2.5\ mg\ mL^{-1}$, 0.5 mL of the sample was mixed with 1 mL of $10\ mmol\ L^{-1}$ DNPH ($2\ mol\ L^{-1}$ HCl), and then reacted in darkness at room temperature for 1 h with vortexing every 10 min. Blank was prepared by adding an equal volume of $2\ mol\ L^{-1}$ HCl as the replacement of DNPH solution. The mixture was precipitated with 20% (w/v; final concentration) TCA solution and centrifuged at $2,000 \times g$ for 10 min at 4°C. The precipitate obtained by centrifugation ($5,000\ r·min^{-1}$, 4°C for 10 min) was washed thrice with 1 mL of ethanol: ethyl acetate (1:1, v/v). The ethanol/ethyl acetate extract was nearly discolored on the third wash, which indicated excess dinitrophenol was removed. The protein precipitate was then dissolved in 4 mL of $6\ mol\ L^{-1}$ guanidine hydrochloride (dissolved in $20\ mmol\ L^{-1}$ phosphate buffer) and incubated at 37°C for 20 min in a water bath. The supernatant was taken to measure the absorbance of the sample at 370 nm after centrifugation ($10,000\ r\ min^{-1}$, 5 min). The calculation formula of the carbonyl group is:

$$\text{Carbonyl content}\left(mol\ mg^{-1}\right) = \frac{\left(A - A_0\right) \times D}{\varepsilon \times C} \times 10^6$$

where: *A*: absorbance of DNPH added; *A*₀: absorbance of blank (DNPH not added); *D*: Protein dilution ratio: Molar extinction coefficient 22,000 $(mol\ L^{-1})^{-1}\ cm^{-1}$; *C*: Protein concentration.

2.3.9. Surface hydrophobicity

The surface hydrophobicity of the sample was determined referring to Li et al. (23) with slight modification. The samples were adjusted to different concentrations ($0.1–0.5\ mg\ mL^{-1}$) with $10\ mmol\ L^{-1}$ Tris–HCl ($0.6\ mol\ L^{-1}$ NaCl, pH 7.2), and 2 mL of the adjusted samples were mixed with 10 μL ANS (8-anilino) -1-Naphthalenesulfonic acid (10 mM, pH 7.5) solution in a chromatographic cabinet. After incubating in darkness at 4°C for 20 min, the fluorescence value was taken (SynergyH1/H1M microplate reader), using an excitation wavelength at 375 nm, emission wavelength at 485 nm, and a gain of 50. Fluorescence intensity was plotted against protein concentration, and the slope of this line was designated as protein surface hydrophobicity (*S*₀).

2.3.10. Solubility

The MP solution was diluted with buffer to $5\ mg\ mL^{-1}$, left standing at 4°C for 1 h, and centrifuged ($5,500\ r\ min^{-1}$, 4°C, 15 min). The protein concentration in the supernatant was measured with a biuret using bovine serum albumin as a standard protein (24).

2.3.11. Turbidity

Samples were diluted to $1\ mg\ mL^{-1}$ with $10\ mmol\ L^{-1}$ Tris–HCl (containing $0.6\ mol\ L^{-1}$ NaCl, pH 7.2) buffer. The turbidity of diluted samples was measured at a wavelength of 340 nm using the microplate reader (25).

2.3.12. Foaming capacity and foam stability

The foaming capacity and stability were identified by referring to Ping-Ping et al. (9). Phosphate buffer (0.1 M, pH 7.4) was used to prepare sample solution. An FJ-180 high-speed homogenizer is used to homogenize ($10,000 \times g$) for 5 min at room temperature, then the foaming capacity was expressed in terms of volume change rate. Foaming stability was expressed as the rate of change in foam volume after 20 min.

2.3.13. Emulsifying activity index (EAI) and emulsion stability index (ESI)

The emulsifying activity and emulsifying stability were determined as reported by Yildiz et al. (21). Soy oil (1 mL) and 3 mL of CO-MP composite sample were homogenized ($10,000\ r\ min^{-1}$) to prepare oil-in-water (O-W) emulsions for 5 min and sonicated immediately for 5 min. The test oil concentration is 0.25% (w/w). Ultrasound is used to generate complex emulsions. After the emulsion was formed, the absorbance was measured at 500 nm at 0 min (A_0) and 10 min (A_{10}), respectively. The calculation formulas of emulsifying activity index (EAI) and emulsion stability index (ESI) are as follows:

$$\text{EAI}\left(m^2\ g^{-1}\right) = \frac{2 \times T \times A_0 \times D}{C \times \varphi \times L \times 10000}$$

$$\text{ESI}\left(min\right) = A_0 \times 10 / \left(A_0 - A_{10}\right)$$

where: *T*: 2.303; *D*: Dilution factor; *C*: Weight of protein per unit volume ($mg\ mL^{-1}$); 50: Optical path width (0.01 M); *φ*: Oil volume fraction (0.25); Where A_0 and A_{10} were the absorbance measured at 0 and 10 min, respectively.

2.3.14. Particle size distribution

By using the laser light scattering method and Mastersizer 2000 instrument (Malvern Instruments Ltd., Worcestershire, UK), the volume-weighted mean particle diameter ($d_{4,3}$) and surface-weighted mean particle diameter ($d_{3,2}$) of the emulsions were measured. After storing the samples at room temperature (approximately 22°C) for 10 days (26). Emulsions containing different SE concentrations were diluted 100-fold with 0.01 M phosphate buffer (pH 7.0) to avoid multiple scattering effects. The $d_{4,3}$ and $d_{3,2}$ were calculated using the following equations:

$$d_{4,3} = \left(\Sigma n_i\ d_i^4 / \Sigma n_i\ d_i^3\right)$$

$$d_{3,2} = \left(\Sigma n_i\ d_i^3 / \Sigma n_i\ d_i^2\right)$$

where d_i is the droplet diameter and n_i is the number of droplets of diameter d_i. The refractive indexes of the continuous and dispersed phases were set at 1.33 and 1.48, respectively.

2.3.15. Myosin extraction

The method of myosin extraction process using these two references Cao et al. (27) and (28). The concentrations of myosin were diluted to 10.0 mg/mL using 0.5 mol/l KCl (20 mmol/l Tris–HCl, pH 7.5) buffer for storage and use, all analytical representations must be tested within 3 days.

2.3.16. Atomic force microscope

The concentration of the myosin sample was adjusted to 1 mg mL^{-1}, and an appropriate solution was applied in drops on the surface of the freshly peeled mica sheet and dried naturally at room temperature to form a myosin adsorption layer (29). Atomic force microscopy measurements were performed using the TAP 150 probe model (MPP-1210010) and the molecular force operating mode. The thickness of the microcantilever is $T = 1.5$–$2.5 \mu m$, $L = 115$–$135 \mu m$, $W = 25$–$35 \mu m$; the resonance frequency f0 is 150–200 kHz; the elastic coefficient k is 5 N m^{-1}, and the resolution is 256*256.

2.3.17. Dynamic light scattering

The particle size distribution of the protein was determined by dynamic light scattering using a ZS90 equipped with a 4 mw He-Ne ion laser ($l = 633$ nm) (29). The 1 mg mL^{-1} protein solution was placed in a 1 cm diameter quartz test tube at $25 \pm 0.1°C$ with a detection angle of 90°.

2.3.18. Scanning electron microscopy

A Tescan Vega3 SEM was used to observe the surface morphology of complex powder (200× magnification). Complex powder was evenly mounted on an aluminum stub, coated with a thin layer of gold, and observed using a cabin voltage of 20.0 kV (30).

2.4. Statistical analysis

All the samples were measured in triplicate and results were expressed as mean ± standard deviation (SD). Differences between mean values were conducted using the one-way analysis of variance (ANOVA) by SPSS 17.0 software. Significant differences were determined at $p < 0.05$.

3. Results and analysis

3.1. SDS–PAGE

As shown in Figure 2A, (Note: m is Markers; 1 is MP, 2 is 0.15% CO-MP, 3 is 0.30% CO-MP, 4 is 0.45% CO-MP, and 5 is 0.60% CO-MP), troponin T (about 34 kDa), actin (about 45 kDa), myosin heavy chain (MHC, about 200 kDa), paramyosin (about 100 kDa), as well as tropomyosin (about 38 kDa) make up the majority of MP, which is corroborated by additional studies somewhat on typical MP protein spectrum (22). The intensity of all bands identified in MP decreased with increasing CO content, suggesting that these subunits are involved in Maillard reactions with CO and MP. After CO modification, the molecular weight of MHC decreases, which may be since insoluble aggregates or cross-linked compounds induced by CO cannot enter the stacked gel (9, 23). While actin, tropomyosin, and troponin T bands migrate upward, indicating that a large

molecular weight product was formed. The mobility of electrophoretic bands only depends on the molecular weight of protein subunits. Similar discoveries demonstrated that the CO addition postponed MP's aggregation (12, 17).

3.2. Spectral analysis

3.2.1. Fourier transform infrared spectroscopy analysis

FTIR was incorporated to examine water-soluble MP's, CO's, microstructures, and also their compounds, at the same time, we tried to discuss more and potential intermolecular interactions' features (i.e., electrostatic interactions and hydrogen bonds). Because of stretching bands of -NH's overlapping, a broad absorption peak of CO appeared near 3,435 cm^{-1} of the -OH group, and the absorption bands of the C-H bond at position 2,885 cm^{-1} manifested in a mild maximum. As shown in Figure 2B, amide I, II as well as III all have had the primary absorbing reaching a maximum of MP at 1655 cm^{-1} (amide I) for C=O stretching, 1,544 cm^{-1} for N–H bending, also 1,397 cm^{-1} for C–N stretching and N–H bending, respectively. O-H and N-H organizations, both released and attached, were capable of establishing hydrogen bonds including the carbonyl group of such peptide interconnection in proteins, which resulted in the broad band noticed in the 3,500–3,000 cm^{-1} zone. The 3,500–3,000 cm^{-1} range broad band was attributable to free and bound O–H and N–H groups, which were able to form hydrogen bonding with the carbonyl group of the peptide linkage in proteins (17). The amide II and III bands of the CO-MP complexes were shifted toward higher wavenumbers than MP, amide II moved from 1,544 to 1,586 cm^{-1}, amide III moved from 1,397 to around 1,411 cm^{-1}, indicating that the carboxylic acid group of MP (-COO) was closely related to CO. There are electrostatic interactions between (-NH$_3^+$)'s amino units (31, 32). Additionally, MP demonstrated broadband at about 3,000–3,600 cm^{-1}, and the broadband was more obvious with the increase of CO addition, indicating the enhancement of the hydrogen bonds. The results showed that hydrogen bonds and electrostatic interaction participated in MP with CO directly, also MP's secondary structure has been altered through CO (33).

A recognized characteristic absorption peak of the secondary structure is the amide I. Protein's secondary structure has mostly been upheld by noncovalent interactions forcing. When the environment changes, protein molecules rearranges to capture the smallest power and preserve a largely equilibrium point (32). It had been protein secondary structure's recognized characteristic peak that is the amide I range (1,600 ~ 1700 cm^{-1}), primarily closely linked towards C=O's stretching vibration according to Figure 2C.

After CO modification, except 0.60% group α-helix content increased slightly, indicating that 0.60% CO effectively maintained the stability of MP structure, which inhibited the exposure of water-soluble proteins and hydrophobic reissued by interacting with protein molecules (34); Except for 0.15 and 0.60% CO-MP, in every group β-turn's quantity increased; while β-sheet's percentage in 0.15% also in 0.30% CO-MP was lower than that in the MP group. Similar results has shown in the study of Zhang et al. (35), the formation of the α-helix and β-turn structures is not beneficial for the formation of β-sheet nor structures which is random coil. Above changes tendency in secondary structure content indicated that the modification of
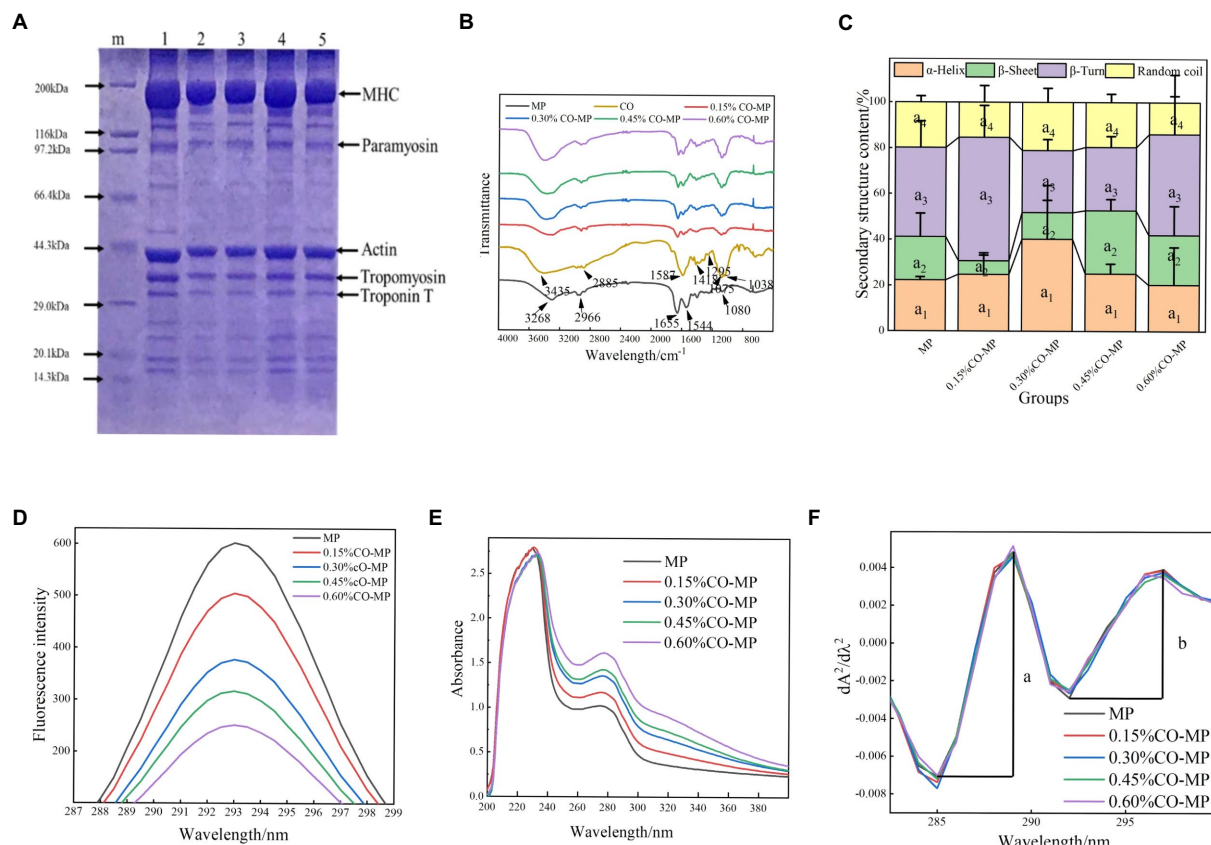
FIGURE 2
(A) SDS-PAGE patterns of a mixture of chitosan oligosaccharide (CO) and myofibrillar protein (MP) (Note: m is Markers; 1 is MP, 2 is 0.15% CO-MP, 3 is 0.30% CO-MP, 4 is 0.45% CO-MP, and 5 is 0.60% CO-MP) **(B)** Effect of CO on the Fourier transform infrared spectroscopy of MP **(C)** Effect of CO on the secondary structure content of MP **(D)** Effect of CO on the endogenous fluorescence spectra of MP **(E)** Effect of CO on the ultraviolet absorption spectrum of MP **(F)** Effect of CO on the ultraviolet second-derivative spectrum of MP.

TABLE 1 Effect of chitosan oligosaccharide (CO) on the related parameters of myofibrillar protein (MP) fluorescence quenching.

Groups	Peak	KSV	KS
MP	585	-	-
0.15% CO-MP	505.76	128.39	1.04×10^{10}
0.30% CO-MP	371.57	198.42	1.91×10^{10}
0.45% CO-MP	341.2	200.25	1.59×10^{10}
0.60% CO-MP	262.27	232.37	2.05×10^{10}

chitosan oligosaccharide made the protein molecular structure more stable.

3.2.2. Endogenous fluorescence spectrum analysis

As fluorescent compounds are generated, the Maillard process takes place as well, and these compounds could be the antecedents to brown colors (17). According to Figure 2D, native MP did not undergo fluorescence quenching, but after CO modification, with the increase of CO addition, the protein fluorescence intensity decreased significantly ($p < 0.05$), resulting in its fluorescence quenching, while its maximum the absorption peak (λ_{max}) and peak shape remained

unchanged. The fluorescence intensity varied as the Maillard reaction proceeded. After CO modification, the quenching constant (K_{SV}) increased with the increase of CO addition, and the quenching of 0.60% CO-MP sample was the highest (Table 1). The fluorescence quenching process is generally divided into dynamic quenching and static quenching. At room temperature 25°C, when $KS > 2.0 \times 10^{10} l \cdot mol^{-1} \cdot s^{-1}$, static quenching happens, by contrast, it could turn out to be dynamic quenching (36). The contribution about CO on MP fluorescence quenching belongs to dynamic fluorescence quenching was illustrated by $KS < 2.0 \times 10^{10} l \cdot mol^{-1} \cdot s^{-1}$. Following above consequence, it could be concluded that the binding force between oligosaccharide molecules and MP surface groups was not strong, and stable ground-state complexes were not formed, which could only be formed through source of low bonding involving hydrogen bonds as well as hydrophobic interactions.

3.2.3. UV absorption spectrum analysis

Protein's UV absorption spectrum is mostly caused due to the reason that tryptophan and tyrosine's side chain units being exposed to UV light. The difference in the UV absorption spectra of the protein can be used to extrapolate the shape change of the protein. One or much aromatic amino acid residues may experience alterations in their surroundings as a result of conformational and dissociative changes as well as protein degradation (37). According to Figure 2E,

the maximum UV absorption peak increased with the addition of CO, but the peak did not shift obviously, indicating that CO modification did not change the micro-environment around Tyr. The addition of CO led to the enhancement of the maximum UV absorption value, indicating that CO changed the molecular structure of MP, exposing more Trp and Tyr residues, and this trend grew stronger with the content of oligosaccharides (38).

With the increase of CO addition, the maximum absorption peak in the UV absorption spectrum increased, which proved that CO could make protein tertiary structure alter as a result. The resulting UV second derivative allowed for the identification of alterations in MP's tertiary structure. This method is widely used for the conformational identification of protein molecules. As shown in Figure 2F, there were two positive absorption peaks near 289 nm and 296 nm (Trp and Tyr act together), and two peaks of negative absorption at 285 nm and 292 nm (Trp act). The value of r depends on the relative amount of Trp and Tyr and the amount exposed to the aqueous phase, i.e., $r = A / B$ (39). The value of r for MP increased with increasing CO addition, while 0.6% CO-MP showed a decreasing trend, but numerical value was also significantly higher than MP (Table 2).

It has been shown that: for Tyr, the value of "r" increases with increasing solvent polarity, while for Trp, the value of "r" is almost independent of solvent polarity; furthermore, the value of "r" and the positions of the peaks and troughs are functions of the relative amounts of Tyr and Trp and the average polarity of the two amino acids in the environment (40). "R" values for any sample were higher than those for native protein, which suggested that Tyr and Trp residues had been exposed toward a hydrophobic milieu, possibly as a result of the protein depolymerization (40). The higher r value indicated that during the depolymerization and unfolding of such molecular structure, MP's latent tyrosine residues eventually appeared on the surface and move to the hydrophobic region and change their three-dimensional position (41).

3.3. Structural changes at the molecular scale

3.3.1. Sulfhydryl content

The presence of sulfhydryl (SH) is an sign of how oxidized a protein is. The abundant SH units found in myofibrillar proteins are quickly converted to disulfide sites, resulting in reduced surface or total SH content. MPs are vulnerable to physical and chemical modifications and can be used to evaluate their exposure to protein surfaces (33). According to Figure 3A, the MP's active SH group content dropped significantly with the increase of CO addition

($p < 0.05$). These results showed that after CO modification, the exposure of MP SH units was delayed, and MP's oxidation was delayed to enhance protein's identity (22). This matched with the carbonyl study results.

3.3.2. Carbonyl content

Notably major changes to oxidized muscle protein is protein carbonylation, and oxidation's rate is usually measured in the number of carbonyl compounds. MP goes through a variety of modifications during storage, involving conformational changes and accumulation, especially myofibrillar oxidation, which results in significant alterations, particularly the creation of carbonyl compounds (42). According to Figure 3B, after CO modification, the carbonyl quantity of myofibrillar protein was considerably reduced ($p < 0.05$), and 0.60% CO-MP's carbonyl quantity was lower.

MP's carbonyls, which were produced by certain amino acid side chains, were linked to structural modifications that lead to disintegration, accumulation, solubility, and functional loss. Hydrogen bonds occur between cationic amino acids' polarity residues, oligosaccharides could take place in some of the water molecules that were present at the protein surface. This was in accordance with studies by Zhang et al. (22), which discovered that a particular pathway of interaction among oligosaccharide and shrimp MP. This supposed that in charge of the amount of oligosaccharide could control protein carbonyl during frozen storage (or processing), and oligosaccharide inactivated oxidation, acted as a scavenger of free radicals, and inhibited the formation of specific protein carbonyl as a metal chelating agent. It needed to be further verified and analyzed by experiments.

3.3.3. Surface hydrophobicity

Analyzing hydrophobic residues' dispersion which is disclosed over protein's exterior, something that is strongly attributable to the usable characteristics, is an excellent approach for assessing the protein's surface hydrophobicity (43). From Figure 3C, the surface hydrophobicity gradually decreased with the increase of CO addition, which indicated that the hydrophobic portion of the molecule was exposed and conformation changed. Protein gather might result from hydrophobic interactions among uncovered hydrophobic residues. Therefore, the addition of CO directly affected the conformational changes of protein molecules. It has been demonstrated that the addition of carrageenan oligosaccharides could postpone the rise in surface hydrophobicity and limit overall oxidation of MP, bind to functional groups in MP with the ionic or hydrogen bonds, forming a protective barrier and inhibiting the oxidative denaturation of proteins (22). Both oligosaccharides and MP were hydrophilical, overall findings from this investigation revealed that chitosan oligosaccharide may form protection of MP and retard oxidative protein denaturation.

3.4. Changes in functional characteristics

3.4.1. Solubility and turbidity

From Figure 4A, the MP's solubility greatly rised following CO modification ($p < 0.05$), but the solubility of MP was not severely affected by the amount of CO. CO is attached to the surface of MP, which makes the system have more hydrophilic groups, which can

TABLE 2 Effect of chitosan oligosaccharide (CO) on the second derivative *r* value of myofibrillar protein (MP).

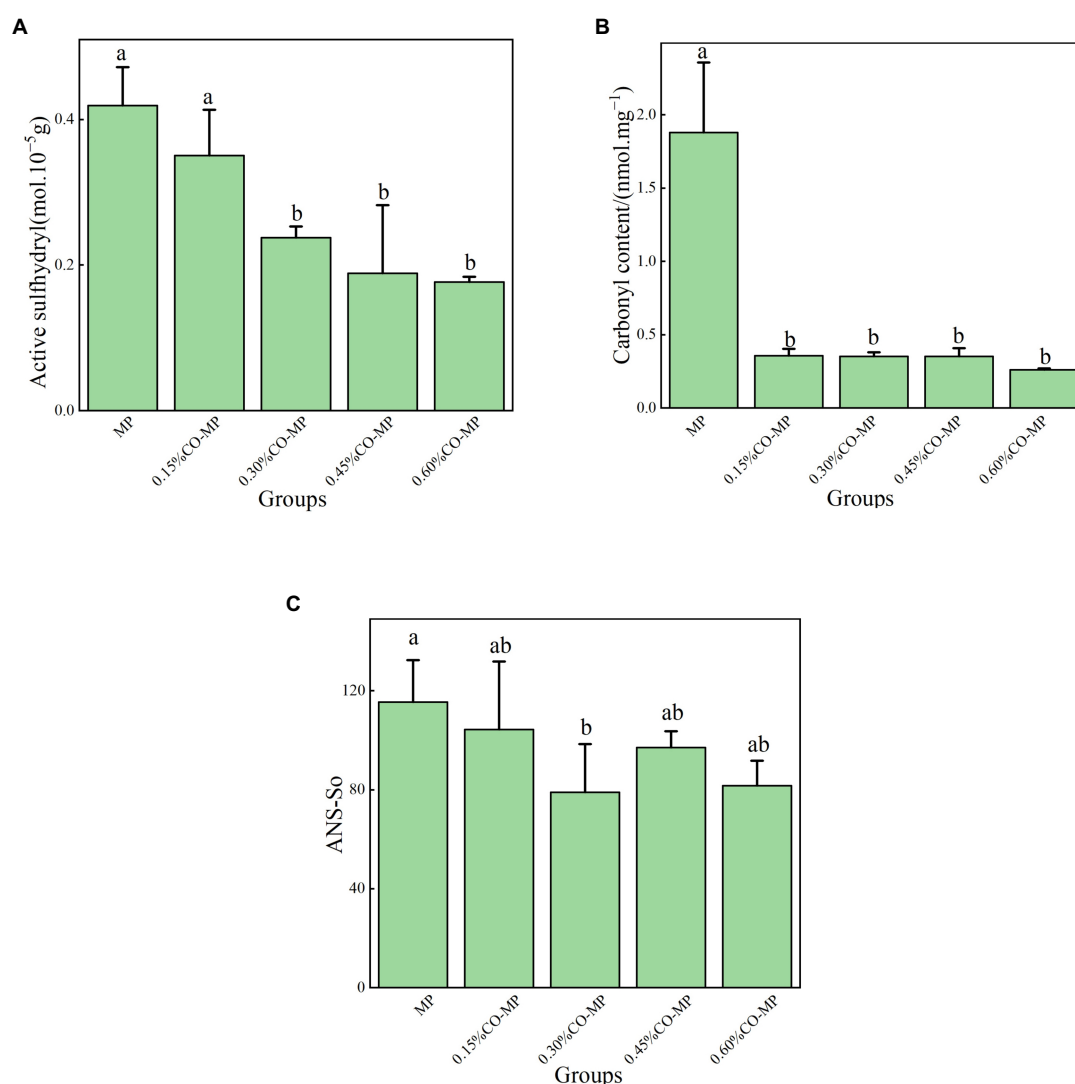| Groups	*r* value
MP	1.62 ± 0.09^a
0.15% CO-MP	1.84 ± 0.05^{ab}
0.30% CO-MP	1.91 ± 0.04^a
0.45% CO-MP	1.98 ± 0.12^a
0.60% CO-MP	1.96 ± 0.12^a

FIGURE 3
(A) Effect of chitosan oligosaccharide (CO) on the active sulfhydryl content of myofibrillar protein (MP) **(B)** Effect of CO on the carbonyl content of MP
(C) Effect of CO on the surface hydrophobicity of MP.

enhance MP's affinity with water molecules and inhibit the connection within MP molecules, boosting the solubility (43).

Alteration in hue is a prime determinant of how much the Maillard reaction happens (44). As shown in Figure 4B, after CO modification, the turbidity of myofibrillar protein increased considerably which is following adding more and more CO ($p < 0.05$). MP solution's color was deepened, on the one hand, because CO itself was pale yellow, and on the other hand, some chemical changes occurred in CO and MP in the solution. This was in accordance with the finding that carbonyl and sulfhydryl groups were significantly reduced in MP and also suggested that a Maillard reaction might occur between MP and CO (17).

3.4.2. Foaming capacity and foam stability

Foam is a colloidal framework of gas in a solution that has a tendency to suddenly split and is trapped by the composition layers that rises to the top due to density variations. Foam is an important indicator of emulsion performance (45). Figure 4C, the better foaming

ability and stability were partly a result of the higher solubility brought on by the addition of CO ($p < 0.05$), and the performance was better at 0.15%–0.30%.

The foaming properties of emulsifiers are related to their spreading and absorption capacity at the air-water edge. Hence it could possibly be concluded which the saccharification of MP with CO encouraged the development of a film around the bubbles in the aqueous dispersion phase and inhibited melding (9, 46). What's more, since protein's solubility had a significant impact on the dielectric behavior, the increased solubility by the application of CO brought and contributed to the better foaming ability and stability.

3.4.3. Emulsifying activity index and emulsion stability index

A protein's capacity to lower the interfacial stress between two normally incompatible liquids is what gives its emulsifying properties. As shown in Figures 4D,E, the emulsification of MP climbed dramatically, well with application of more CO amount ($p < 0.05$), and
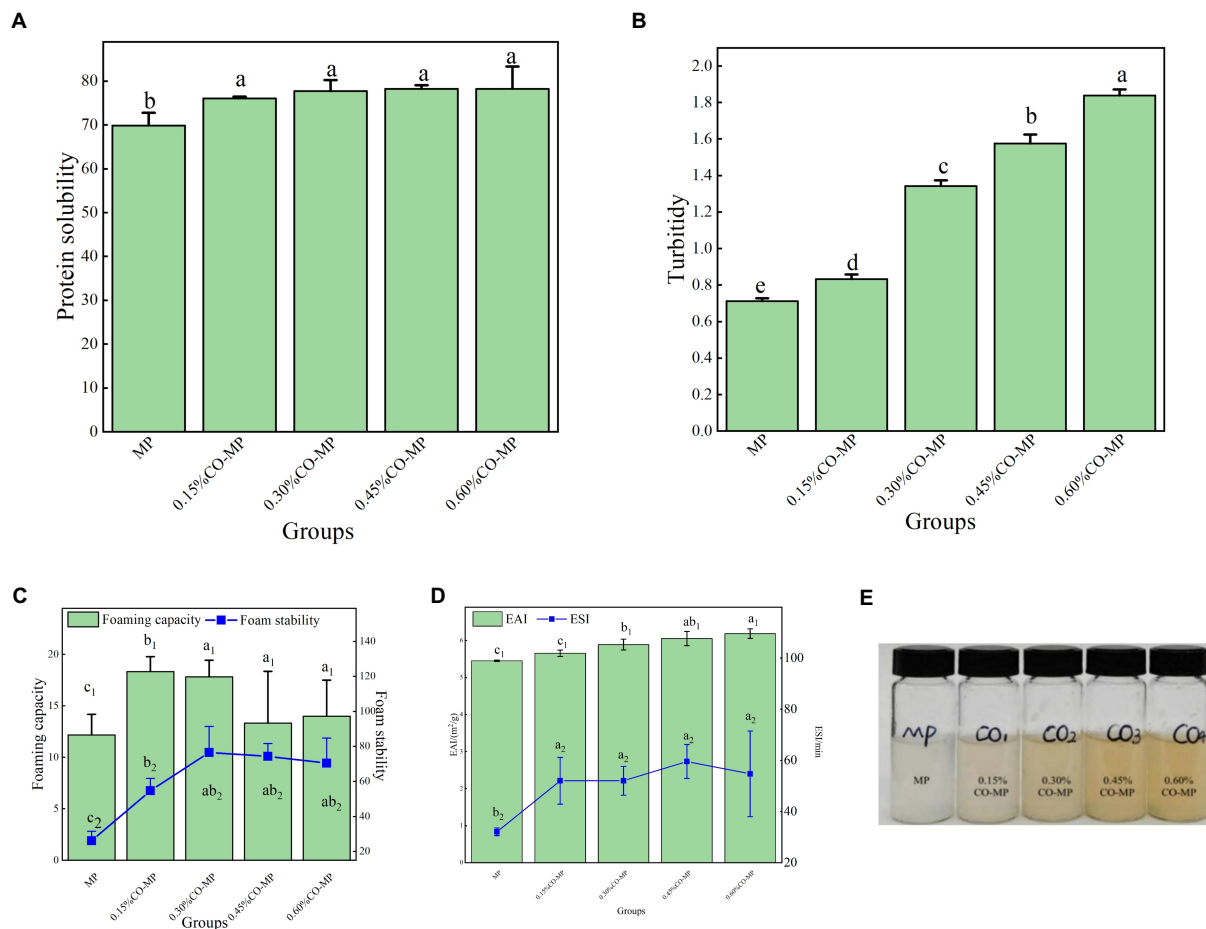
FIGURE 4
(A) The influence of chitosan oligosaccharide (CO) on the solubility of myofibrillar protein (MP) **(B)** The influence of CO on the turbidity of MP **(C)** The influence of CO on the influence of foaming capacity and foam stability of MP **(D,E)** The influence of CO on the emulsifying activity index (EAI) and emulsion stability index (ESI) of MP.

0.60% CO-MP showed higher emulsification ability. Most of the time, the reduction of the emulsifier interfacial tension was created by aiming the emulsifier's hydrophobic and hydrophilic components at the polar element and non-polar part (oil phase) (water phase). Given the greater solubility that resulted from the addition of CO, CO-MP demonstrated a greater ability to emulsify in this investigation, which made it easier to use at the oil–water interface. What's more, because of steric hindrance of CO, it was feasible to avert the emulsion's spread phase droplets coalescing, thus maintaining the durability of the emulsion (9).

3.5. Particle size distribution

The results of droplet diameter reveal that interface area is one of the important factors affecting particle size (26), and The interaction among proteins and small molecules within lotion has been confirmed by numerous investigations using droplet diameter (46). To learn more regarding the protein's microstructure, using the laser particle size scanner. From Figure 5A, there was a particle size peak at 92.01 μm, MP was at 92.01 μm. After CO modification, with the increase of CO addition, the peak value at MP decreased, and the size

was smaller gradually, which decreased significantly in every CO group. As shown in Table 3, after CO modification, the volume average diameter $d_{4,3}$ of MP samples drastically dropped with the growth in CO, while 0.60% CO-MP samples were significantly different from 0.15% CO-MP and 0.30% CO-MP samples ($p < 0.05$), and there wasn't a great deal of a distinction here from 0.45% CO-MP samples ($p > 0.05$).

After CO modification, the average diameter $d_{3,2}$ of MP area drastically shrank with an upsurge in CO supply ($p < 0.05$), and $d_{3,2}$ of 0.60% CO-MP sample was massively reduced which is the totally different with the remaining ($p < 0.05$), but still no statistically noteworthy distinction was identified among 0.15% CO-MP, 0.30% CO-MP and 0.45% CO-MP ($p > 0.05$).

After CO modification, the interfacial activity of MP was significantly increased, the interfacial adsorption speed was accelerated, and the droplet size of the lotion was significantly reduced. MP could be more effectively and easily located on the oxygen/water interface (26). The results demonstrated that the mixture's particle size gradually decreased with the increase of CO addition, inhibiting protein aggregation (12), and MP has higher stability (47). The reduction in particle size suggested that CO and MP particles had generated a soluble combination that resisted protein
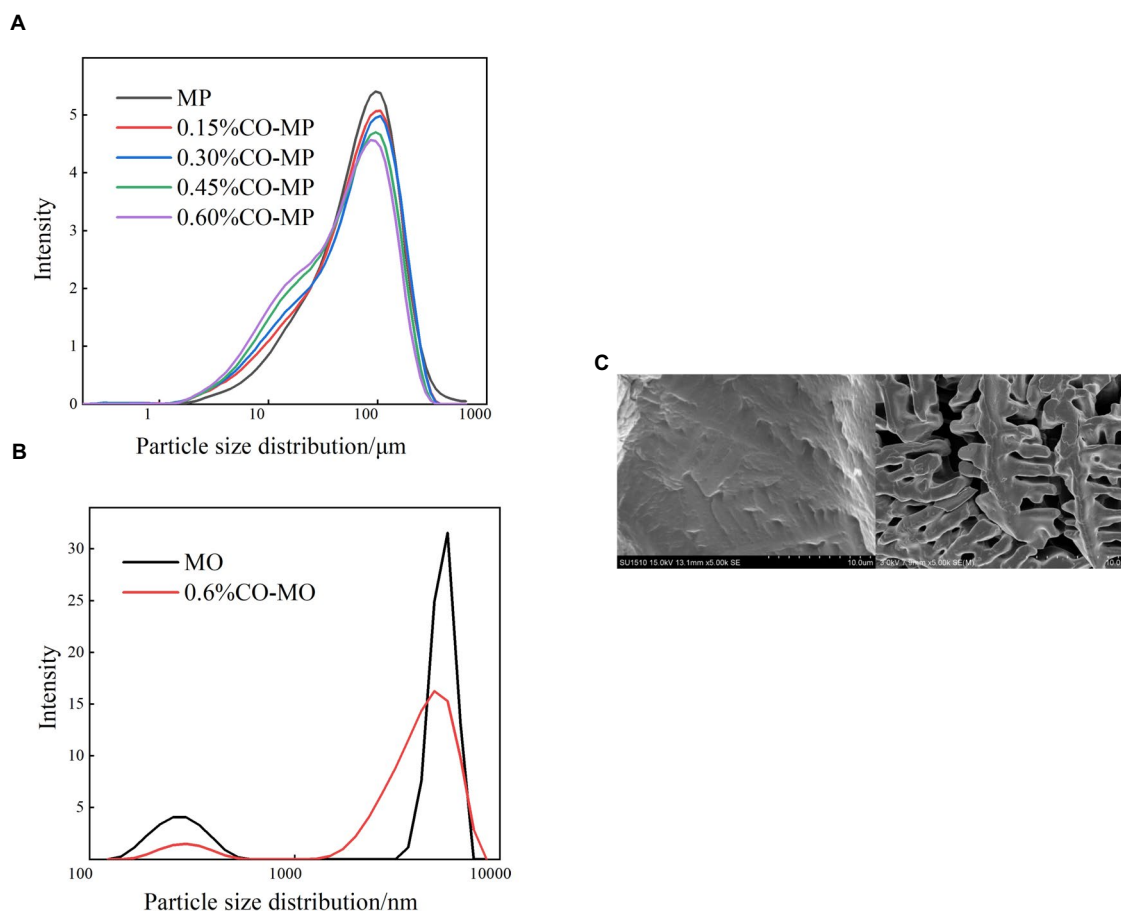
FIGURE 5
(A) The influence of chitosan oligosaccharide (CO) on the particle size of myofibrillar protein (MP) **(B)** The effect of 0.60% CO on the particle size of myosin (MP) **(C)** SEM of myosin.

denaturation. This behavior could be due to the strengthening of electrostatic repulsion following CO alteration. Moreover, the presence of CO might make the mixture viscous, lower the collision frequency of particles and potentially hinder the development of large protein–protein clumps.

3.6. Structural changes at the microscopic scale

3.6.1. AFM changes of myosin after CO modification

The study of dietary proteins has made excellent and widespread by utilizing atomic force microscopy. The most common atomic force microscope application approach for studying dietary proteins is nanoimaging. The morphological and structural characteristics of meat protein have been extensively studied to determine the composition, tenderness, and toughness of the tissue (48).
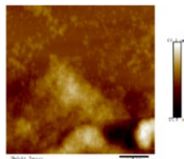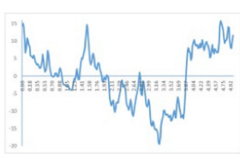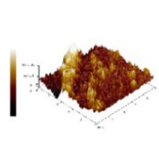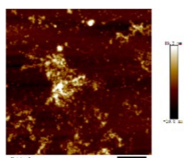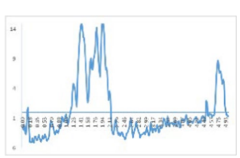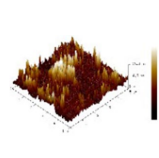
We observed morphological changes with AFM and evaluated the effect of CO on myosin in macromolecular crowding environment. The difference in mean roughness could be used to measure the amount of protein gather. Table 4 revealed that the layer of untreated myosin was rough, 0.60% CO reduced the surface roughness and

TABLE 3 The effect of chitosan oligosaccharide (CO) on the average diameter $d_{4,3}$ and $d_{3,2}$ of myofibrillar protein (MP) droplets.

Groups	$d_{4,3}$ (μm)	$d_{3,2}$ (μm)
MP	92.01 ± 2.09^a	37.13 ± 1.19^a
0.15% CO-MP	80.72 ± 0.91^b	30.38 ± 1.70^b
0.30% CO-MP	77.03 ± 0.04^c	28.37 ± 0.38^b
0.45% CO-MP	73.98 ± 0.25^{cd}	27.31 ± 1.82^b
0.60% CO-MP	71.38 ± 0.97^d	21.88 ± 3.59^c

height of myosin. The morphological structures of MO and 0.6% CO-MO mixtures were shown in Table 4. It could be seen from the 3D and 2D images that the surface of untreated MO had a rough surface; the morphology of MO aggregates was quite different from that of 0.6% CO-MO, which indicated that CO affected the surface morphology of MO, made the MO surface smoother and delaying the aggregation of MO. The results showed that myosin's morphology was impacted by CO, which also smoothed out its exterior as well as slowed down myosin's tendency to aggregate. This outcome might be the result of CO-MO being assembled into base pairs or multimers, leading to a consequence which shows poor unfolding of MOs, worse grouping of MOs, and inferior clustering heights of MOs (49).

TABLE 4　Atomic force microscope images of chitosan oligosaccharide (CO) and myosin (MO).

	2D	Height	3D	Roughness
CO				4.91 ± 0.77
0.60% CO-MO				3.72 ± 0.40

3.6.2. DLS changes of myosin after CO modification

MO sample demonstrated the same trend as the MP sample. The particle size distribution of 0.60% CO-MO complex moved to smaller particles, as shown in Figure 5B: MO sample showed double peaks in the figure. After CO modification, both peaks decreased. The peak at MO shifted, revealing that the CO-MO complex's size was distributed to small particles. The DLS results showed the obvious unfolding of myosin, and the CO-MO complex had higher stability (50). This further proved and demonstrated that the particle size's became smaller and inhibited protein aggregation because of a formation of CO-MO complex (12).

3.6.3. SEM changes of myosin after CO modification

The SEM microstructure of CO-treated MO was compared with that of MO as shown in Figure 5C. The MO structure closely resembled a thin cloth with particles of different sizes on it, while in the CO-MO coacervate, vacuoles of various sizes were spaced apart in a permeable system structure. Changes could result from the MO losing its internal structure and suffering bodily harm from the ice crystals that are being produced. A sophisticated compressed system was formed through the collision of two macromolecules with antagonistic energies, trapping water droplets in the condensed phase and boosting the intricacy of such organization (33).

4. Discussion

The effect of chitosan oligosaccharide on myofibrillar protein denaturation of silver carp during cold storage was studied. Chitosan oligosaccharide's addition could greatly decrease capacity average diameter of MP ($d_{4,3}$) and space average diameter of MP ($d_{3,2}$) with increment of CO concentration; chitosan oligosaccharide and myofibrillar protein formed CO-MP complex through electrostatic interaction, which had better stability. This denser structure could make the exterior of myosin smoother as well as reduce the roughness of myosin. The complex's fluorescence intensity dropped as the CO concentration increasing, but its higher absorption apex (λ_{max}) and peak shape essentially stayed unaltered. The addition of CO enhanced the accessibility of tryptophan residues, but did not affect the tryptophan's milieu. The CO-MP complex had good antioxidant properties, the addition of chitosan oligosaccharide could reduce the content of carbonyl, sulfhydryl oxidation, 0.60% group seemed to have a better effect, and the disulfide covalent bond is formed. The complex's interfacial hydrophobicity diminished as CO concentration increase. The solubility and turbidity increased significantly. CO-MP had better foaming and foam stability, but the emulsifying performance was not obvious. It was speculated that the reason for this was that chitosan oligosaccharide has a substantial molecular mass.

The binding force between oligosaccharide molecules and MP surface groups was not strong, and stable ground state complexes cannot be formed, which only feeble non-covalent bonds, including hydrogen bonds and hydrophobic interactions could create. The relationship between MP and CO involved both electrostatic interaction and hydrogen bonds. CO's addition could change molecular structure of MP, expose more Trp and Tyr residues. The exposure of MP sulfhydryl also delayed and the oxidation of MP, thus the quality of protein was improved.

Through establishing hydrogen bonds with charged amino acids' polarity residues, CO could replace some of the liquid molecules and coat the exterior of proteins. The attachment of CO to the surface of MP caused more hydrophilic groups in the complex, which could inhibit the association of MP molecules, enhance their propensity for molecules of water and solubility. In addition, the higher solubility brought by the addition of CO also helped to strengthen MP's foaming capabilities and stability. Because protein's solubility had a positive correlation with the interface capability, the emulsification of MP increased significantly with the increase of the amount of CO, and 0.60% CO-MP had a higher emulsifying ability. The particle size's dropping further indicated the creation of a protein-aggregation-inhibiting solvent complicated of CO and MP particles. This behavior could be due to the augmentation of electrostatic interactions following CO modification.

Microscopic studies of CO and myosin further verified that complexation blocked proteins against accumulating. CO-MO condensates showed a porous network structure with different sizes of vacuolar intervals. As well as 0.60% group working with MO showed better performance, the formation of a complex of CO and MO particles that inhibited protein aggregation, the CO-MO coacervate demonstrated a permeable network structure with heterogeneously size vacuoles intermingled, CO could improve and reduce the roughness of myosin.

5. Conclusion

Myofibrillar protein molecules' rearrangements were directly influenced by CO modification, which also altered the ancillary structure of the protein, delayed MP polymerization, inhibited protein oxidation, stabilized the molecular structure of the protein, and enhanced its quality and functional capabilities. In particular, it increased solubility, improved foaming performance, foam stability and emulsification ability. The microscopic studies of CO and myosin further illustrated the above conclusions. Overall, chitosan oligosaccharide, as a naturally active macromolecule, changed the structure and function of proteins and raised the caliber of protein-based products. Especially for those kinds of fish products which are mainly applying the functional characteristics of myofibrillar protein, such as fried fish fillets, minced fish products, fish sausages and so on. In the future, due to different sugar donors could cause diverse improvement effects of proteins, researchers could do more research about the effect of various molecular weights of the sugar donors which will promote the development of relevant special performance products in the food processing field.

Moreover, we noticed that CO had a strong antioxidant capacity, which meant we might create a kind of materials that both own the anti-inflammatory characteristic and the fish protein's nutritional value. By unexpectedly finding differences in mixing methods, as well reviewing the former studies, we learned that a way named wet-heating glycosylation showed better results, therefore we suggest future researchers could spend more effort on trying this measure and also optimize the experimental conditions to improve efficiency. Currently, 3D printing technology draws lots of attention from researchers, so we may use this emerging way to create more valuable and deeper exploration in this field. Thus, we could apply this technology to industrial production, which could significantly reduce energy consumption and production costs. Finally, it is still unclear for the mechanism of glycosylation which needs to be explored more in future studies.

Data availability statement

The original contributions presented in the study are included in the article/Supplementary files, further inquiries can be directed to the corresponding authors.

Author contributions

HC completed the writing part, scientific analysis and modification after the delivery of the manuscript, text modification, text and language editing after the review, etc. QW completed some data analysis and literature search. ZZ and HC draft the figures in the manuscript. HC, QW, ZZ, and JK revised the manuscript. HC was involved in the supervision and review of the entire experiment and thesis writing. All authors contributed to the article and approved the submitted version.

Conflict of interest

QW and JK were employed by Nutrilite Health Institute.

The remaining authors declare that the research was conducted in the absence of any commercial or financial relationships that could be construed as a potential conflict of interest.

Publisher's note

All claims expressed in this article are solely those of the authors and do not necessarily represent those of their affiliated organizations, or those of the publisher, the editors and the reviewers. Any product that may be evaluated in this article, or claim that may be made by its manufacturer, is not guaranteed or endorsed by the publisher.

References

1. Wang K, Li Y, Zhang Y, Luo X, Sun J. Improving myofibrillar proteins solubility and thermostability in low-ionic strength solution: a review. *Meat Sci*. (2022) 189:108822. doi: 10.1016/j.meatsci.2022.108822

2. Bohrer BM. Review: nutrient density and nutritional value of meat products and non-meat foods high in protein. *Trends Food Sci Technol*. (2017) 65:103–12. doi: 10.1016/j.tifs.2017.04.016

3. Oliver CM, Melton LD, Stanley RA. Creating proteins with novel functionality via the Maillard reaction: a review. *Crit Rev Food Sci Nutr*. (2006) 46:337–50. doi: 10.1080/10408690590957250

4. Liu SL, Zhao PC, Zhang JJ, Xu QH, Ding YT, Liu JH. Physicochemical and functional properties of silver carp (*Hypophthalmichthys molitrix*) myofibrillar protein glycated with konjac oligo-glucomannan. *Food Hydrocoll*. (2017) 67:216–23. doi: 10.1016/j.foodhyd.2017.01.018

5. Liu JH, Ru QM, Ding YT. Glycation a promising method for food protein modification: physicochemical properties and structure, a review. *Food Res Int*. (2012) 49:170–83. doi: 10.1016/j.foodres.2012.07.034

6. Fu LL, Wang C, Wang JB, Ni SQ, Wang YB. Maillard reaction with ribose, galacto-oligosaccharide or chitosan-oligosaccharide reduced the allergenicity of shrimp tropomyosin by inducing conformational changes. *Food Chem*. (2019) 274:789–95. doi: 10.1016/j.foodchem.2018.09.068

7. Mengíbar M, Miralles B, Heras Á. Use of soluble chitosans in Maillard reaction products with β-lactoglobulin. Emulsifying and antioxidant properties. *LWT*. (2017) 75:440–6. doi: 10.1016/j.lwt.2016.09.016

8. Zheng Z, Luo YK, Yao L, Lu J, Bu GH. Effects of Maillard reaction conditions on the functional properties of WPI chitosan oligosaccharide conjugates. *J Food Sci Technol*. (2014) 51:3794–802. doi: 10.1007/s13197-013-0946-6

9. Ping-Ping W, Wen-Duo W, Chun C, Xiong F, Rui-Hai L. Effect of fructus Mori. Bioactive polysaccharide conjugation on improving functional and antioxidant activity of whey protein. *Int J Biol Macromol*. (2020) 148:761–7. doi: 10.1016/j.ijbiomac.2020.01.195

10. Mahmood SJ, Siddique A. Ionic studies of sodium alginate isolated from sargassum terrarium (brown algea) Karachi coast with 2,1-electrolyte. *J Saudi Chem Soc*. (2010) 14:117–23. doi: 10.1016/j.jscs.2009.12.018

11. Xu W, Tang Y, Yang Y, Wang G, Zhou S. Establishment of a stable complex formed from whey protein isolate and chitosan and its stability under environmental stresses. *Int J Biol Macromol*. (2020) 165:2823–33. doi: 10.1016/j.ijbiomac.2020.10.130

12. Zhao N, Zou H, Sun S, Yu C. The interaction between sodium alginate and myofibrillar proteins: the rheological and emulsifying properties of their mixture. *Int J Biol Macromol*. (2020) 161:1545–51. doi: 10.1016/j.ijbiomac.2020.08.025

13. Liang L, Duan W, Zhang J, Huang Y, Zhang Y, Sun B. Characterization and molecular docking study of taste peptides from chicken soup by sensory analysis combined with nano-LC-Q-TOF-MS/MS. *Food Chem*. (2022) 383:132455. doi: 10.1016/j.foodchem.2022.132455

14. Yu Y, Pei FS, Li ZM. Orientin and vitexin attenuate lipopolysaccharide-induced inflammatory responses in RAW264.7 cells: a molecular docking study, biochemical characterization, and mechanism analysis. *Food Sci Human Wellness*. (2022) 11:1273–81. doi: 10.1016/j.fshw.2022.04.024

15. Li X, Liu C, Wang J, Zhou K, Yi S, Zhu W, et al. Effect of hydroxyl radicals on biochemical and functional characteristics of myofibrillar protein from large yellow croaker (*Pseudosciaena crocea*). *J Food Biochem*. (2020) 44:e13084. doi: 10.1111/jfbc.13084

16. Yang T, Geng W, Zheng Z, Wang Q, Chen S, Liu L, et al. Effects of alginate oligosaccharides on the stability, intermolecular forces and myofibrillar protein structures of silver carp surimi. *Meat Sci*. (2021) 35:1–8.

17. Xu Z-Z, Huang G-Q, Xu T-C, Liu L-N, Xiao J-X. Comparative study on the Maillard reaction of chitosan oligosaccharide and glucose with soybean protein isolate. *Int J Biol Macromol*. (2019) 131:601–7. doi: 10.1016/j.ijbiomac.2019.03.101

18. Hu J, Zhao TF, Li SJ, Wang ZY, Wen CR, Wang HT, et al. Stability, microstructure, and digestibility of whey protein isolate - tremella fuciformis polysaccharide complexes. *Food Hydrocoll*. (2019) 89:379–85. doi: 10.1016/j.foodhyd.2018.11.005

19. Meng Y, Hao L, Tan Y, Yang Y, Liu L, Li C, et al. Noncovalent interaction of cyanidin-3-O-glucoside with whey protein isolate and β-lactoglobulin: focus on fluorescence quenching and antioxidant properties. *LWT*. (2021) 137:110386. doi: 10.1016/j.lwt.2020.110386

20. Shahabadi N, Maghsudi M, Kiani Z, Pourfoulad M. Multispectroscopic studies on the interaction of 2-tert-butylhydroquinone (TBHQ), a food additive, with bovine serum albumin. *Food Chem*. (2011) 124:1063–8. doi: 10.1016/j.foodchem.2010.07.079

21. Yildiz G, Ding J, Andrade J, Engeseth NJ, Feng H. Effect of plant protein-polysaccharide complexes produced by mano-thermo-sonication and pH-shifting on the structure and stability of oil-in-water emulsions. *Innov Food Sci Emerg Technol*. (2018) 47:317–25. doi: 10.1016/j.ifset.2018.03.005

22. Zhang B, Fang C-D, Hao G-J, Zhang Y-Y. Effect of kappa-carrageenan oligosaccharides on myofibrillar protein oxidation in peeled shrimp (*Litopenaeus vannamei*) during long-term frozen storage. *Food Chem*. (2018) 245:254–61. doi: 10.1016/j.foodchem.2017.10.112

23. Li TF, Zhao JX, Huang J, Zhang WH, Huang JL, Fan DM, et al. Improvement of the quality of surimi products with overdrying potato starches. *J Food Qual*. (2017) 2017:1–5. doi: 10.1155/2017/1417856

24. Cheng J, Zhu M, Liu X. Insight into the conformational and functional properties of myofibrillar protein modified by mulberry polyphenols. *Food Chem*. (2020) 308:125592. doi: 10.1016/j.foodchem.2019.125592

25. Xu YJ, Zhao X, Bian GL, Yang L, Han MY, Xu XL, et al. Structural and solubility properties of pale, soft and exudative (PSE)-like chicken breast myofibrillar protein: effect of glycosylation. *LWT*. (2018) 95:209–15. doi: 10.1016/j.lwt.2018.04.051

26. Li Y, Liu H, Liu Q, Kong B, Diao X. Effects of zein hydrolysates coupled with sage (*salvia officinalis*) extract on the emulsifying and oxidative stability of myofibrillar protein prepared oil-in-water emulsions. *Food Hydrocoll*. (2019) 87:149–57. doi: 10.1016/j.foodhyd.2018.07.052

27. Cao L, Su S, Regenstein JM, Xiong S, Liu R. Ca 2+-induced conformational changes of myosin from silver carp (*hypophthalmichthys molitrix*) in gelation. *Food Biophys*. (2015) 10:447–55. doi: 10.1007/s11483-015-9408-1

28. Liu Z, Pan J. A practical method for extending the biuret assay to protein determination of corn-based products. *Food Chem*. (2017) 224:289–93. doi: 10.1016/j.foodchem.2016.12.084

29. Iwasaki T, Washio M, Yamamoto K. Atomic force microscopy of thermally treated myosin filaments. *J Agric Food Chem*. (2005) 53:4589–92. doi: 10.1021/jf0500381

30. Zhang F, Jiang SS, Feng X, Wang RF, Zeng MY, Zhao YH. Effect of heat treatment on physicochemical state and in vitro digestion of salt-soluble protein from Pacific oyster (*Crassostrea gigas*). *LWT*. (2020) 134:110126. doi: 10.1016/j.lwt.2020.110126

31. Lan Y, Ohm J-B, Chen B, Rao J. Phase behavior, thermodynamic and microstructure of concentrated pea protein isolate-pectin mixture: effect of pH, biopolymer ratio and pectin charge density. *Food Hydrocoll*. (2020) 101:105556. doi: 10.1016/j.foodhyd.2019.105556

32. Zhao Y, Khalid N, Shu G, Neves MA, Kobayashi I, Nakajima M. Complex coacervates from gelatin and octenyl succinic anhydride modified kudzu starch: insights of formulation and characterization. *Food Hydrocoll*. (2019) 86:70–7. doi: 10.1016/j.foodhyd.2018.01.040

33. Xu Y, Dong M, Tang C, Han M, Xu X, Zhou G. Glycation-induced structural modification of myofibrillar protein and its relation to emulsifying properties. *LWT*. (2020) 117:108664. doi: 10.1016/j.lwt.2019.108664

34. Walayat N, Xiong Z, Xiong H, Moreno HM, Niaz N, Ahmad MN, et al. Cryoprotective effect of egg white proteins and xylooligosaccharides mixture on oxidative and structural changes in myofibrillar proteins of *Culter alburnus* during frozen storage. *Int J Biol Macromol*. (2020) 158:865–74. doi: 10.1016/j.ijbiomac.2020.04.093

35. Zhang J, Liu L, Jiang Y, Shah F, Xu Y, Wang Q. High-moisture extrusion of peanut protein−/carrageenan/sodium alginate/wheat starch mixtures: effect of different exogenous polysaccharides on the process forming a fibrous structure. *Food Hydrocoll*. (2020) 99:105311. doi: 10.1016/j.foodhyd.2019.105311

36. Zhang Y-Z, Dai J, Zhang X-P, Yang X, Liu Y. Studies of the interaction between Sudan I and bovine serum albumin by spectroscopic methods. *J Mol Struct*. (2008) 888:152–9. doi: 10.1016/j.molstruc.2007.11.043

37. Wang KQ, Sun DW, Pu HB, Wei QY. Principles and applications of spectroscopic techniques for evaluating food protein conformational changes: a review. *Trends Food Sci Technol*. (2017) 67:207–19. doi: 10.1016/j.tifs.2017.06.015

38. Miao Q, Guo L, Xiangyang W, Jianying H. Study of interaction mechanism between chitosan and bovine serum albumin and emulsification of its complex. *J Nucl Agric Sci*. (2019) 33:954–61. doi: 10.11869/j.issn.100-8551.2019.05.0954

39. Wei L, Cao LW, Xiong SB, You J, Hu Y, Liu R. Effects of pH on self-assembly of silver carp myosin at low temperature. *Food Biosci*. (2019) 30:Article 100420. doi: 10.1016/j.fbio.2019.100420

40. Zhao J, Dong F, Li Y, Kong B, Liu Q. Effect of freeze–thaw cycles on the emulsion activity and structural characteristics of soy protein isolate. *Process Biochem*. (2015) 50:1607–13. doi: 10.1016/j.procbio.2015.06.021

41. Luyun C, Qing X, Ailing C. Effects of different ultrasound-assisted thawing methods on the myofibrillar protein of the sea bass (*Perca fluviatilis*). *Food Ferment. Ind*. (2020) 46:1–8. doi: 10.13995/j.cnki.11-1802/ts.024414

42. Walayat N, Xiong ZY, Xiong HG, Moreno HM, Li Q, Nawaz A, et al. The effectiveness of egg white protein and beta-cyclodextrin during frozen storage: functional, rheological and structural changes in the myofibrillar proteins of *Culter alburnus*. *Food Hydrocoll*. (2020) 105:105842. doi: 10.1016/j.foodhyd.2020.105842

43. Xu YJ, Zhao YQ, Wei ZX, Zhang H, Dong M, Huang MY, et al. Modification of myofibrillar protein via glycation: physicochemical characterization, rheological behavior and solubility property. *Food Hydrocoll*. (2020) 105:105852. doi: 10.1016/j.foodhyd.2020.105852

44. Maskan M. Production of pomegranate (*Punica granatum* L.) juice concentrate by various heating methods: colour degradation and kinetics. *J Food Eng*. (2006) 72:218–24. doi: 10.1016/j.jfoodeng.2004.11.012

45. Hunter TN, Pugh RJ, Franks GV, Jameson GJ. The role of particles in stabilising foams and emulsions. *Adv Colloid Interf Sci*. (2008) 137:57–81. doi: 10.1016/j.cis.2007.07.007

46. Fu G-M, Xu Z-W, Luo C, Xu L-Y, Chen Y-R, Guo S-L, et al. Modification of soy protein isolate by Maillard reaction and its application in microencapsulation of *Limosilactobacillus reuteri*. *J Biosci Bioeng*. (2021) 132:343–50. doi: 10.1016/j.jbiosc.2021.06.007

47. Shi C, He Y, Ding M, Wang Y, Zhong J. Nanoimaging of food proteins by atomic force microscopy. Part II: application for food proteins from different sources. *Trends Food Sci Technol*. (2019) 87:14–25. doi: 10.1016/j.tifs.2018.11.027

48. Purslow PP. Intramuscular connective tissue and its role in meat quality. *Meat Sci*. (2005) 70:435–47. doi: 10.1016/j.meatsci.2004.06.028

49. Yuan L, Kong Y, Leng W, Wang Y, Jin W, Gao R. L-glutamic acid affects myosin aggregation and the physical properties of bighead carp (Aristichthys nobilis) surimi gels. *Food Biosci*. (2021) 40:100886. doi: 10.1016/j.fbio.2021.100886

50. Hrynets Y, Ndagijimana M, Betti M. Transglutaminase-catalyzed glycosylation of natural actomyosin (NAM) using glucosamine as amine donor: functionality and gel microstructure. *Food Hydrocoll*. (2014) 36:26–36. doi: 10.1016/j.foodhyd.2013.09.001

Frontiers in Nutrition

Explores what and how we eat in the context of health, sustainability and 21st century food science

A multidisciplinary journal that integrates research on dietary behavior, agronomy and 21st century food science with a focus on human health.

Discover the latest Research Topics

See more →

frontiers

Frontiers in
Nutrition

frontiers | Research Topics